

MEASUREMENT OF e^+p
NEUTRAL CURRENT DEEP INELASTIC SCATTERING
WITH A LONGITUDINALLY POLARISED POSITRON BEAM
AND
X-RAY RADIATION DAMAGE FOR SILICON SENSORS

Dissertation

zur Erlangung des Doktorgrades
des Fachbereichs Physik
der Universität Hamburg

vorgelegt von

Friederike Januschek

aus Oldenburg (Oldb)

Hamburg

2011

Gutachter der Dissertation:	Prof. Dr. Robert Klanner Dr. Achim Geiser
Gutachter der Disputation:	Prof. Dr. Eckhard Elsen Dr. Thomas Schörner-Sadenius
Datum der Disputation:	14.11.2011
Vorsitzender des Prüfungsausschusses:	Dr. Georg Steinbrück
Vorsitzender des Promotionsausschusses:	Prof. Dr. Peter Hauschildt
Dekan der MIN Fakultät:	Prof. Dr. Heinrich Graener
Leiterin des Fachbereichs Physik:	Prof. Dr. Daniela Pfannkuche

Abstract

The cross sections for Neutral Current e^+p Deep Inelastic Scattering (NC DIS) with longitudinally polarised positron beams were measured at a centre-of-mass energy $\sqrt{s} = 318$ GeV using the ZEUS detector at HERA. Single-differential cross sections as a function of the virtuality of the exchanged boson, Q^2 , of the inelasticity, y , and of the Bjorken scaling variable, x , and reduced cross sections (as a function of x and Q^2) were measured in the phase space region defined as $Q^2 > 185$ GeV², $y < 0.9$ and $y(1-x)^2 > 0.004$.

The results, based on data corresponding to an integrated luminosity of 135.5 pb⁻¹, are given for zero polarisation for the whole sample, as well as for both positive and negative values of the longitudinal polarisation of the positron beam. The measured cross sections are compared to the predictions of the Standard Model.

The proton structure function $x\tilde{F}_3$ is measured and the interference term $xF_3^{\gamma Z}$ is extracted as a function of x at $Q^2 = 1500$ GeV² by extrapolating the measurements done at different Q^2 values.

The presented measurements of the polarised e^+p NC DIS cross sections, the $x\tilde{F}_3$ structure function and the $xF_3^{\gamma Z}$ interference term exceed the precision of previous ZEUS measurements.

The uncertainties of the Parton Density Functions (PDFs) for the gluon and the u -valence quark are expected to be reduced at high- x values when the presented results are included in the PDF fits of the proton.

A study is presented to further reduce PDF uncertainties for the gluon at very high x (above 10^{-1}) through the inclusion of DIS dijet cross sections in a ZEUS-JETS-like PDF fit.

An irradiation facility to study the X-ray-induced radiation damage of silicon sensors for the European XFEL was set up at HASYLAB. Nine gate-controlled diodes were irradiated with doses from 1 kGy to 1 GGy in several irradiation steps and the surface current I_{surf} and the flatband voltage V_{fb} were measured after each irradiation. It was found that both, I_{surf} and V_{fb} , strongly increase at low doses, but decrease at high doses (above 5 MeV). No evidence was found that this decrease was caused by temperature-induced annealing.

Kurzfassung

Die Wirkungsquerschnitte von tiefunelastischer e^+p Streuung (DIS) des neutralen Stromes (NC) mit einem longitudinal polarisierten Positronstrahl wurden bei einer Schwerpunktsenergie von $\sqrt{s} = 318$ GeV am ZEUS-Experiment bei HERA gemessen.

Die einfach differentiellen Wirkungsquerschnitte als Funktion der Bosonvirtualität, Q^2 , der Inelastizität des Ereignisses, y , und der Bjorken Skalenvariable, x , sowie die reduzierten Wirkungsquerschnitte (als Funktion von x und Q^2) wurden im Phasenraum der Analyse von $Q^2 > 185$ GeV², $y < 0.9$ und $y(1-x)^2 > 0.004$ extrahiert.

Die Ergebnisse, basierend auf Daten mit einer integrierten Luminosität von 135.5 pb⁻¹, werden mit Null-Polarisation, sowie für negative und positive Polarisation des Positronstrahls angegeben.

Es wird die Strukturfunktion $x\tilde{F}_3$ gemessen, sowie der Interferenzterm $xF_3^{\gamma Z}$, als Funktion von x bei $Q^2 = 1500$ GeV², durch Extrapolation der Messungen an verschiedenen Q^2 -Werten bestimmt.

Die präsentierten Messungen der Wirkungsquerschnitte von polarisierter NC e^+p DIS, der $x\tilde{F}_3$ Strukturfunktion und ihres $xF_3^{\gamma Z}$ Interferenzterms sind präziser als die früheren Ergebnisse von ZEUS.

Es wird gezeigt, dass durch die Einbeziehung der präsentierten Ergebnisse eine Reduzierung der Unsicherheiten der Partonverteilungsfunktionen (PDFs) bei hohem x für das Gluon und das Valenz- u -Quark erwartet wird.

Es wird eine Studie präsentiert, die zeigt, dass sich die Unsicherheiten der PDFs des Gluons bei sehr hohen x (über 10^{-1}) durch die Einbeziehung von DIS-Zweijet Wirkungsquerschnitten in einem ZEUS-JETS ähnlichen PDF-Fit weiter reduzieren lassen.

Der Aufbau eines Strahlungsstands am HASYLAB zur Untersuchung von Strahlenschäden an der Oberfläche von Siliziumsensoren für den Europäischen XFEL wird präsentiert. Neun Teststrukturen (gate-controlled diodes) wurden mit Dosen von 1 kGy bis 1 GGy schrittweise bestrahlt und der Oberflächenstrom I_{surf} , sowie die Flachbandspannung V_{fb} wurden gemessen. I_{surf} und V_{fb} steigen bei geringen Dosen stark an, um dann (bei Dosen über 5 MeV) wieder abzufallen. Dieser Effekt konnte nicht auf Ausheilung durch Temperaturerhöhung zurückgeführt werden.

"You'll find all the answers eventually, with enough time and study, and the right sort of tools. That's what you believe, isn't it...as a scientist?"

Star Trek Voyager, "Sacred Ground"

Frequently Used Abbreviations

BCAL	Barrel Calorimeter
BSM	Beyond the Standard Model
CC	Charged Current
CTD	Central Tracking Detector
CV	Capacitance-Voltage
DIS	Deep Inelastic Scattering
e^-p	electron-proton
e^+p	positron-proton
ep	electron-proton (e^-p and e^+p)
FCAL	Forward Calorimeter
FLT	First Level Trigger
IV	Current-Voltage
LH	Left-handed
MC	Monte Carlo
NC	Neutral Current
PDF	Parton Density Function
PHP	Photoproduction
QCD	Quantum Chromo Dynamics
QPM	Quark Parton Model
RCAL	Rear Calorimeter
RH	Right-handed
SLT	Second Level Trigger
SM	Standard Model
TLT	Third Level Trigger
TME	Track Matching Efficiency
TVE	Track Veto Efficiency

Contents

1. Introduction	1
2. High Q^2 Deep Inelastic Scattering at HERA	3
2.1. Deep Inelastic Scattering	3
2.1.1. Kinematic Variables	4
2.2. Electroweak Physics	5
2.3. Proton Structure	7
2.3.1. Quark Parton Model	7
2.3.2. QCD and the Quark Parton Model	8
2.3.2.a. Asymptotic Freedom and Confinement	8
2.3.2.b. Factorization and DGLAP Evolution	9
2.4. Structure Functions at HERA	11
2.4.1. Structure Functions in the QPM	11
2.4.2. Structure Functions Including QCD, Z Exchange and Polarisation	12
2.4.2.a. Generalised Structure Functions and their Contributions	12
2.4.2.b. Physics Interpretation of the Generalised Structure Functions	14
2.4.2.c. Polarisation Asymmetry and Parity Violation	15
2.5. Fits of Parton Density Functions	15
2.5.1. General Formalism	16
2.5.2. Gluon Distribution and Jets	16
2.5.3. Electroweak Fits	16
2.6. HERA's Achievements to Date	17
2.6.1. DIS Cross Sections at HERA	17
2.6.2. PDF Fits at HERA	21
3. The ZEUS Experiment at HERA	25
3.1. HERA Accelerator	25
3.1.1. Luminosity at HERA	25
3.1.2. HERA Upgrade and Running Periods	27
3.1.3. Beam Polarisation	29
3.2. The ZEUS Experiment	31
3.2.1. Luminosity Measurement	32
3.2.2. Tracking System	33
3.2.3. Calorimeters	35
3.2.4. Trigger	37
4. Event Reconstruction and Simulation	41
4.1. Data Samples	41
4.2. Monte Carlo Generation of Standard Model Events	42
4.2.1. Signal NC DIS Monte Carlo	42
4.2.2. Background Monte Carlo	43
4.3. From Raw Data and MC to Data Tables	44
4.4. ZEUS Analysis Environment	45
4.5. Calorimeter Pre-corrections	46

4.6.	Track and Vertex Reconstruction	47
4.7.	Scattered e^+ Reconstruction	47
4.7.1.	EM Finder	47
4.8.	Reconstruction of Hadronic Final State	48
4.9.	Reconstruction of Kinematic Variables	49
4.9.1.	Electron Method	49
4.9.2.	Jacquet-Blondel Method	50
4.9.3.	Double-Angle Method	50
4.9.4.	Kinematic Fitting	51
5.	Corrections Applied to the Data and MC Samples	53
5.1.	F_L Correction	53
5.2.	Polarisation Correction	54
5.3.	Different Running Periods	54
5.3.1.	Comparison of Variables	56
5.3.2.	Rates and Luminosity Measurement	58
5.4.	Trigger Variable and Rate Studies	62
5.4.1.	Trigger Variables	62
5.4.2.	Trigger Rates	62
5.4.3.	RISOE Correction	65
5.5.	Track Veto Efficiency	65
5.6.	Funnel Versions	70
5.7.	Correction of the Longitudinal Vertex Position	70
5.8.	Energy Corrections	74
5.8.1.	Cell-wise and Radial Factors in the RCAL	74
5.8.2.	Inactive Material and Non-Uniformity Corrections	77
5.8.3.	Energy Scaling and Smearing	77
5.9.	Track Matching Efficiency	81
5.10.	Summary of Applied Corrections	83
6.	NC DIS Event Selection	85
6.1.	Signal Event Characteristics	85
6.2.	Background Characteristics	88
6.2.1.	Photoproduction	88
6.2.2.	Elastic QED Compton	89
6.2.3.	Charged Current Deep Inelastic e^+p Scattering	89
6.2.4.	Beam-gas and Beam-pipe Interactions	91
6.2.5.	Halo Muons	91
6.2.6.	Cosmic Muons	91
6.3.	Preselection	91
6.3.1.	First Level Trigger	92
6.3.2.	Second Level Trigger	93
6.3.3.	Third Level Trigger	93
6.3.4.	Data Quality	94
6.4.	Selection	94
6.4.1.	Positron Selection	94
6.4.2.	Background Suppression	97
6.4.3.	Phase Space and Monte Carlo Validation	98
6.5.	Comparison of Data and SM MC Prediction	98

7. Studies of Systematic Uncertainties of the Cross Section Measurement	103
7.1. Bin Definition	103
7.1.1. Bin Definition for the $\frac{d\sigma}{dQ^2}$ Measurement	104
7.1.2. Bin Definition for the $\frac{d\sigma}{dx}$ Measurement	104
7.1.3. Bin Definition for the $\frac{d\sigma}{dy}$ Measurement	106
7.1.4. Bin Definition for the Reduced Cross Section Measurement	106
7.2. Unfolding	108
7.3. Dependence on Parton Shower Model	111
7.4. Dependence on Positron Finder	115
7.5. Dependence on Energy Scaling and Smearing	115
7.6. Correction and Photoproduction Cross Section Uncertainties	116
7.7. Cut Threshold Sensitivity	116
7.8. Major Effects	118
8. Results	125
8.1. Unpolarised Cross Sections	125
8.1.1. Unpolarised Single Differential Cross Sections	125
8.1.2. Unpolarised Reduced Cross Sections	126
8.1.3. $x\bar{F}_3$	126
8.1.3.a. $xF_3^{\gamma Z}$	126
8.2. Polarised Cross Sections	133
8.2.1. Polarised Single Differential Cross Sections	133
8.2.2. Polarised Reduced Cross Sections	133
8.2.3. Polarisation Asymmetry	133
9. PDF Fits and Outlook	139
9.1. ZEUS and HERA PDF Fits	139
9.1.1. ZEUS-PDF Fit	139
9.1.2. HERAPDF Fit	140
9.2. Influence of NC Data on PDF Fits	140
9.3. Jets in PDF Fits	141
9.3.1. How to Include Jets	141
9.3.1.a. Using Grids for Jet Cross Sections	142
9.3.2. Example: Dijets in ZEUS-JETS PDF	143
9.4. LHC and the Future of PDF Fits	150
10. Studies of Radiation Damage for Silicon Sensors for the XFEL	155
10.1. The Gated Diodes and Performed Irradiation Campaigns	155
10.2. Irradiation Procedure and Setup	157
10.2.1. HASYLAB and Beamlines F3 and F4	158
10.2.2. Spectrum	158
10.2.3. Dose and Beam Profiles	158
10.3. Measurement Techniques and Results	163
10.3.1. Measurement Setup in the Laboratory	163
10.3.2. CV Measurements	163
10.3.3. IV Measurements	166
10.3.3.a. Surface Generation Current Measurement	168
10.3.3.b. Total Diode Current Measurement	172
10.3.4. Temperature during Irradiation	172
10.4. Summary and Outlook	176
11. Conclusion	177

A. Summary of Selection Cuts	179
B. FLT Trigger Bits	181
C. Control Distributions	185
D. Trigger Rates	197
E. Track Matching Efficiency	207
F. Uncertainties of the Reduced Cross Section	213
G. Single Differential Cross Sections and A^+	229
H. Reduced Cross Section, $x\tilde{F}_3$ and $xF_3^{\gamma Z}$	249
Bibliography	263
Acknowledgements	277

1. Introduction

What is the world made of? Are there indivisible building blocks of matter? These questions have been asked by humankind for at least 2500 years¹.

In the last 100 years there have been many important findings regarding these questions. With the resolving power of the probes growing, access has been granted to smaller and smaller distance scales. Perrin confirmed the existence of molecules a bit more than 100 years ago [3] and exactly 100 years ago Rutherford published his famous explanation of the elastic scattering of alpha particles on gold nuclei [4] leading to the discovery of the nucleus.

Going from this elastic scattering process to the inelastic scattering of alpha particles on hydrogen nuclei (i. e. protons) [5], the proton was discovered. Since then the proton has been the main target of scattering experiments from which models of the proton and in general the Standard Model of particle physics have been developed.

According to the Standard Model, matter consists of fermions (particles with half-integer spin), and forces between them are mediated by bosons (with integer spins). There are three generations of fermions. Each of the generations consists of two quarks (one with a charge of $+\frac{2}{3}$ of the electron charge e and another one with a charge of $-\frac{1}{3}e$), and two leptons (an electrically neutral neutrino and a lepton with a charge of $-1e$). The first generation comprises the u - and d -quark, the electron neutrino ν_e and the electron. Almost all ordinary matter is made of first generation fermions. Every particle has an oppositely charged anti-particle.

Three of the four fundamental forces are described within the Standard Model: the electromagnetic interaction mediated by the photon, the weak interaction mediated by the W and Z bosons and the strong interaction mediated by gluons.

The Standard Model has proven very successful in the last few decades: After the discovery of the top quark [6] and of the tau neutrino [7], the Higgs particle is the last missing piece to the Standard Model of particle physics and is being intensely looked for at the *Large Hadron Collider*.

Continuing the success story of the early proton scattering experiments, the HERA accelerator at DESY (1992-2007) was built with the purpose of resolving the proton down to unprecedented small scales. Using electrons² as probes to investigate the structure of the proton at a centre-of-mass energy of $\sqrt{s} \approx 318$ GeV, the proton could be resolved down to attometer (10^{-18} m) scales.

The proton is described in terms of three structure functions. Whereas the structure function \tilde{F}_2 , which dominates most of the kinematic region at HERA, mainly describes

¹The most well-known philosophers to ask these questions were Democritus (ca. 460 BC - ca. 370 BC) and his teacher Leucippus [1], but there is evidence for atomism in the Upanishads in India in the 6th century BC, which has intensified in the Vaisheshika school [2].

²The term electron in this thesis refers to both the negatively charged electron and its antiparticle, the positively charged positron.

the electromagnetic interaction between the probing electron and the quarks in the proton, the structure function $x\tilde{F}_3$ is due to the weak interaction and is sensitive to the difference between the quark and anti-quark component in the proton. The third structure function, the longitudinal structure function F_L , quantifies the gluon content of the proton.

The processes which give the most important contribution for the determination of the proton structure at HERA are Neutral Current (NC) and Charged Current (CC) Deep Inelastic Scattering (DIS). In this thesis an analysis of the NC DIS process is presented, cross sections are measured and structure functions extracted. The analysis was done on the high statistics data sample from the ZEUS experiment, which was taken during the last period of HERA running at a centre-of-mass energy of 318 GeV. In this period the positron beam was longitudinally polarised providing good sensitivity to electroweak phenomena.

This study extends and complements previous analyses from HERA. It covers the kinematic range at high negative squared 4-momentum transferred, Q^2 , (up to about 30.000 GeV²) with better precision than any other e^+p measurement at ZEUS. In combination with the previously published e^-p data [8] it allows the most precise extraction of the structure function $x\tilde{F}_3$ at ZEUS. Taking advantage of the polarisation of the positron beam, parity violation in e^+p scattering can be directly measured.

The results of this analysis are of considerable importance for understanding the proton structure and are considered an essential part for the planned HERAPDF 2.0 fit of the proton parton distribution functions (and of other fits). In addition, they are a fundamental input for the final search for Contact Interactions at ZEUS/HERA.

This thesis is organised as follows: In Chapter 2 an overview of the theory of Deep Inelastic Scattering is given. Chapter 3 describes the experimental setup: the HERA collider and the ZEUS detector. Chapter 4 lists the data and MC samples used in the analysis and explains the reconstruction and simulation of events. In Chapter 5 results of a detailed investigation of the samples are shown and additional corrections, mainly for remaining detector effects, are derived. Chapter 6 describes the event selection and Chapter 7 discusses the cross section binning and systematic uncertainties of the measurement. The results of the analysis are presented in Chapter 8.

In Chapter 9 the influence of the data on the Parton Density Functions is assessed, and a study is presented on whether additional jet data can improve the precision of the Parton Density Functions. The further potential of the presented NC measurement and the future of fits of the Parton Density Functions in general are discussed .

Chapter 10 explores a different part of accelerator-based physics at DESY: For future experiments the radiation hardness of silicon sensors must be improved. Here a study is presented, that investigates the radiation hardness of silicon sensors as necessary for the European XFEL. The setup and first results of an irradiation campaign done at HASYLAB with synchrotron radiation doses up to 1 GGy are presented.

Chapter 11 summarises the studies presented in this thesis.

2. High Q^2 Deep Inelastic Scattering at HERA

In this chapter an overview of the theoretical background for the analysis described in this thesis is given.

As mentioned in Chapter 1, the proton is composed of quarks and gluons, which are kept together by the strong force. Since 1968, the process of Deep Inelastic Scattering (DIS) has proven to be one of the most powerful tools for the investigation of the proton structure. Section 2.1 will introduce this process and Section 2.1.1 will explain the kinematic variables used to describe it.

DIS is an electroweak process. Thus Section 2.2 will give some details on the theory of the electromagnetic and weak interaction and of their unification as electroweak theory.

Section 2.3 will give an overview of the proton models and their development with time, as more precise experimental data became available.

The remaining part of the chapter will be devoted to the definition of the proton structure functions (Section 2.4), of parton distributions (Section 2.5) and of how they are extracted. In addition, major related HERA results will be highlighted (Section 2.6).

2.1. Deep Inelastic Scattering

Using scattering experiments to learn about the structure of an object has historically been proven to be a very successful approach, the most famous example being the Rutherford experiment [4] leading to the discovery of the nucleus. Nowadays, the main subject of investigation by scattering experiments is the proton, also due to the fact that present hadron collider experiments mainly use proton beams. In order to have precise theoretical predictions and interpretations for proton-proton interactions, a precise knowledge of the proton structure is mandatory. Due to their point-like¹ structure, electrons are a perfect tool to investigate the structure of the proton.

The electron-proton collider HERA was therefore the perfect accelerator for proton structure studies. In addition, the large energies at HERA (centre-of-mass energy of 318 GeV) made it possible to resolve the proton structure down to a scale of 10^{-18} m (see Equation 2.3).

In the Deep Inelastic Scattering regime, due to the large momentum transferred between the electron and the proton, the proton is broken up and a new hadronic final state is created. According to the charge of the exchanged boson, DIS is divided into Neutral Current (NC) DIS, where the mediating boson is a γ or Z , and Charged Current (CC) DIS, where the mediating boson is a W^+ or W^- .

¹At least up-to-now there is no evidence for a substructure of electrons.

The Feynman Graph of the simplest ep DIS process is shown in Figure 2.1. In the final state of the reaction, there is the scattered lepton (e for NC and ν for CC) together with the partonic system (a scattered quark and the proton remnant), which evolves into a -partly observable- hadronic final state.

2.1.1. Kinematic Variables

In the Feynman diagram in Figure 2.1 the 4-momenta needed to describe the process kinematics are indicated:

- k : 4-momentum of the incoming electron;
- P : 4-momentum of the incoming proton;
- k' : 4-momentum of the scattered lepton;
- P' : 4-momentum of the hadronic final state;
- q : 4-momentum of the exchanged boson.

Using these variables the process can be conveniently described in terms of the following Lorentz invariants:

- the centre-of-mass energy squared, s , which is a function of the beam energies and thus an accelerator property:

$$s = (P + k)^2, \quad (2.1)$$

- the squared 4-momentum transferred from the electron to the proton, q^2 , and its negative, Q^2 , (which is the virtuality of the exchanged boson):

$$Q^2 = -q^2 = -(k - k')^2. \quad (2.2)$$

The possible Q^2 range is from 0 to s . With increasing Q^2 the proton is probed at smaller scales according to the equation

$$\lambda \approx \frac{\hbar c}{\sqrt{Q^2}} \approx \frac{0.197 \text{ fm}}{\sqrt{Q^2[\text{GeV}^2]}}. \quad (2.3)$$

where the wavelength λ of the exchanged photon represents its resolving power,

- the Bjorken scaling variable x , which is the momentum fraction of the proton carried by the struck quark (see Section 2.3.1):

$$x = \frac{Q^2}{2P \cdot q}, \quad (2.4)$$

- the inelasticity y , which in the proton rest frame represents the energy transferred from the incoming electron to the proton:

$$y = \frac{P \cdot q}{P \cdot k}. \quad (2.5)$$

The variables Q^2 , x and y characterise the event kinematics. At fixed s only two of them are independent, because (neglecting the masses²) the variables are related through the relation

$$Q^2 = s \cdot x \cdot y . \quad (2.6)$$

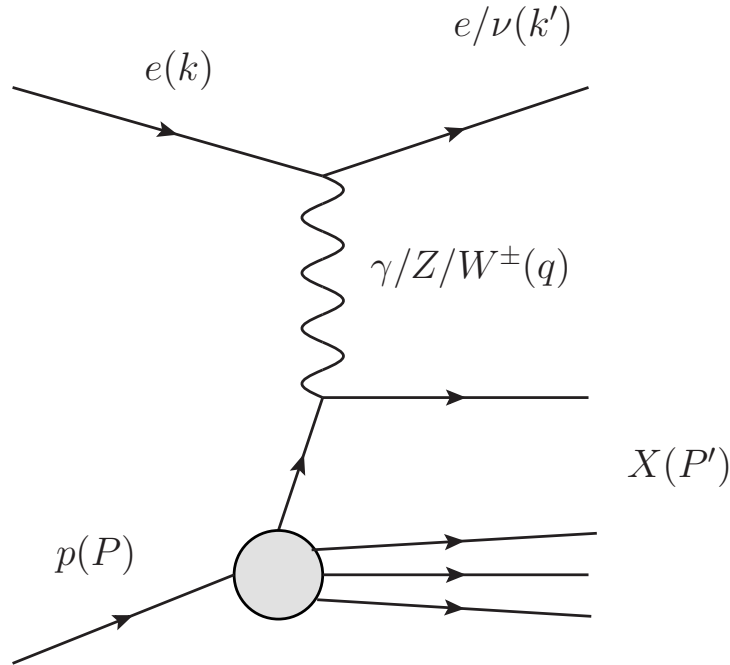


Figure 2.1: A Feynman graph for DIS at HERA including the 4-momenta of the involved particles.

2.2. Electroweak Physics

As mentioned at the beginning of this chapter, DIS is an electroweak process. The theory of electroweak interactions unifies the electromagnetic and weak forces under a $SU(2) \times U(1)$ symmetry. The mediators of the electroweak interactions are the photon, the W^\pm and the Z bosons.

The electroweak theory was introduced by Glashow, Weinberg and Salam [9,10] .

In this theory the fermions have a new quantum number, the weak isospin T , which is only carried by left-handed fermions. Its third component T_3 is conserved in all weak interactions. T_3 and the electric charge q (in units of the electron charge) combine via

$$Y = 2(q - T_3) \quad (2.7)$$

to form the weak hypercharge Y . Table 2.1 summarises these quantum numbers for all

²In the energy range of this analysis, as the masses are much smaller than the involved momenta, this is a valid assumption.

fermions. The four bosons of the electroweak theory [11, pp. 246-250] come as components of a $T = 1$ triplet of SU(2) ($W_\mu = W_\mu^{(1)}, W_\mu^{(2)}, W_\mu^{(3)}$) and a single $T = 0$ U(1) isoscalar B_μ . By the Higgs fields *spontaneous symmetry breaking* is introduced and three bosons get massive (W_μ^+, W_μ^-, Z_μ) while one (the photon A_μ) remains massless. A_μ and Z_μ are combinations of $W_\mu^{(3)}$ and B_μ mediating the neutral current:

$$\begin{pmatrix} A_\mu \\ Z_\mu \end{pmatrix} = \begin{pmatrix} \cos(\theta_W) & \sin(\theta_W) \\ -\sin(\theta_W) & \cos(\theta_W) \end{pmatrix} \begin{pmatrix} B_\mu \\ W_\mu^{(3)} \end{pmatrix}, \quad (2.8)$$

with the *weak mixing angle* or *Weinberg angle* θ_W , which has to be measured experimentally.

The charged current is mediated by

$$W^\pm = \frac{W_\mu^{(1)} \mp W_\mu^{(2)}}{\sqrt{2}}. \quad (2.9)$$

These expressions lead to the Lagrangian expressed as

$$L = \frac{g}{\sqrt{2}}(J_\mu^- W_\mu^+ + J_\mu^+ W_\mu^-) + \frac{g}{\cos(\theta_W)}(J_\mu^{(3)} - \sin^2(\theta_W) J_\mu^{em}) Z_\mu + g \sin(\theta_W) J_\mu^{em} A_\mu, \quad (2.10)$$

with the coupling strength g , the weak isospin current J_μ , the weak hypercharge current J_μ^Y , the electromagnetic current $J_\mu^{em} = J_\mu^Y + J_\mu^{(3)}$ and $J_\mu^\pm = J_\mu^{(1)} \pm J_\mu^{(2)}$. In the Lagrangian the first term is the weak charged contribution, the second term the weak neutral contribution and the third the electromagnetic neutral contribution. As the electromagnetic coupling is e , it follows that

$$e = g \sin(\theta_W). \quad (2.11)$$

From Equation 2.10 it is visible that while the weak CC consists of only weak isospin interactions (thus it only affects left-handed particles and right-handed anti-particles), the weak NC has an electromagnetic current contribution. That means that the coupling of a right-handed fermion to a Z boson g_R is not 0, but

$$g_R = -\sin^2(\theta_W)q, \quad (2.12)$$

and the coupling of a left-handed fermion to a Z boson g_L is

$$g_L = T_3 - \sin^2(\theta_W)q. \quad (2.13)$$

It follows for the vector coupling of the Z boson to a fermion v :

$$v = g_L + g_R = T_3 - 2\sin^2(\theta_W)q, \quad (2.14)$$

and for the axial vector coupling a :

$$a = g_L - g_R = T_3. \quad (2.15)$$

The theoretical values are tabulated in Table 2.1, while the measured values of v and

a are summarised in Table 2.2.

particle	q	T	T ₃	Y	v	a
u, c, t	$\frac{2}{3}$	$\frac{1}{2}$	$\frac{1}{2}$	$\frac{1}{3}$	$\frac{1}{2} - \frac{4}{3} \sin^2(\theta_W)$	$\frac{1}{2}$
d, s, b	$-\frac{1}{3}$	$\frac{1}{2}$	$-\frac{1}{2}$	$\frac{1}{3}$	$-\frac{1}{2} + \frac{2}{3} \sin^2(\theta_W)$	$-\frac{1}{2}$
e, μ , τ	-1	$\frac{1}{2}$	$-\frac{1}{2}$	-1	$-\frac{1}{2} + 2 \sin^2(\theta_W)$	$-\frac{1}{2}$
ν	0	$\frac{1}{2}$	$\frac{1}{2}$	-1	$\frac{1}{2}$	$\frac{1}{2}$

Table 2.1: Quantum numbers and couplings to the weak neutral current of left-handed fermions. [12, p. 200]

2.3. Proton Structure

The evolution of the experimental techniques and of the resolving power of the probes has allowed more and more precise models of the proton to be developed and tested with increasing precision. The Quark Parton Model (QPM, Section 2.3.1) was able to explain some of the first experimental observations. It was improved by the theory of Quantum Chromo-Dynamics (QCD), which was able to resolve some of the issues of the QPM (Section 2.3.2).

2.3.1. Quark Parton Model

The era of the investigation of the proton structure by DIS started with first results from SLAC [13], [14]. They included several surprising findings, most importantly the phenomenon that the proton structure³ in the investigated Q^2 -region (about $1 \text{ GeV}^2 < Q^2 < 10 \text{ GeV}^2$) depended only on x and hardly on Q^2 . This so-called *Bjorken scaling* (as it was predicted by Bjorken [15]) can be explained by the parton model introduced by Feynman [16]. The idea behind the parton model is that the probing electron is scattered elastically off a parton inside the proton. Due to the parton being point-like there is no dependence on Q^2 . This then leads to the interpretation of x as proton momentum carried by the struck parton. These partons were later identified as the quarks from [17, 18]⁴ constructing the *Quark Parton Model*.

The model of the proton being composed of three quarks left some unresolved issues. First of all, the quarks were treated as free in the Quark Parton Model, but could not be observed free. Secondly the momentum sum of the quarks lead to only about half of the proton's momentum [19]. Other issues related to the Quark Parton Model were the deviations from Bjorken-scaling at small and large x , the violation of the Pauli exclusion principle (in the Δ^{++} baryon there are three quarks of the same flavour) and in general the question how the quark-composed particles held together.

³The investigated variable was the cross section, divided by the cross section of an electron scattering off a point-like photon.

⁴Gell-Mann and Zweig had developed the concept of the quarks as part of an ordering scheme for the many different observed hadrons.

2.3.2. QCD and the Quark Parton Model

The problems of the Quark Parton Model were solved in the context of Quantum Chromodynamics [20,21], which is a locally gauge-invariant and renormalisable $SU(3)$ quantum field theory. It describes the strong interaction between the quarks and the gluons of the Standard Model. Both the massless gluons and the quarks carry a new degree of freedom called colour, which comes in three states (red, green, blue). According to QCD quarks carry one colour charge, gluons (which come in eight types⁵) a colour and a different anti-colour and every observable state must be colourless. Therefore the observable states comprising the lowest number of quarks are the baryons (three quarks) and the mesons (quark-anti-quark). The three "main" quarks of the proton (the quarks of the QPM) are called *valence* quarks.

The colour charge is the source of the strong interaction: not only do quarks interact by the exchange of gluons, but also gluons can interact with each other (see basic QCD vertices in Figure 2.2). This is a feature of QCD caused by its non-Abelian structure. Evidence for the existence of gluons was first found 1979 at the e^+e^- collider PETRA at DESY by the observation of three-jet events [22–25].

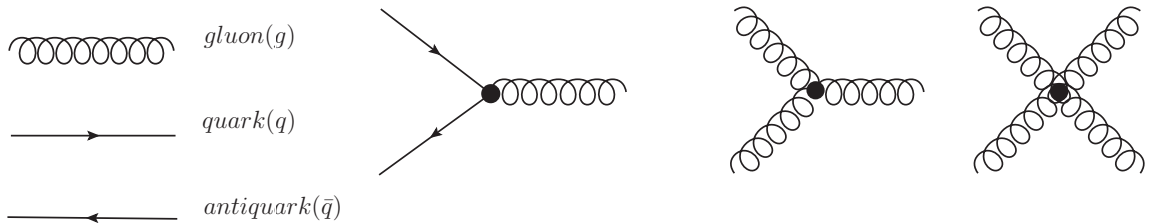


Figure 2.2: The fundamental vertices of QCD.

2.3.2.a. Asymptotic Freedom and Confinement

The coupling constant of the strong interaction, α_s , depends on the renormalization scale μ_R , which is typically taken to be the hard scale of the process. In perturbative QCD the calculation of cross sections σ is done using an expansion in powers of α_s :

$$\sigma = \sum_n C_n \alpha_s^n, \quad (2.16)$$

For each process, there is a power m , the lowest power of α_s , which contributes (i.e. $C_m \neq 0$). Calculations up to the α_s^m term are then called *leading order* (LO), up to the α_s^{m+1} term *next-to-leading order* (NLO), up to the α_s^{m+2} term *next-to-next-to-leading order* (NNLO) etc.

Perturbative QCD needs to be renormalised [26] for regulating the ultraviolet divergencies arising from the integration over all possible momenta.

⁵The ninth, totally symmetric in colour, would be colourless.

Because of its dependence on the energy scale, μ^2 , α_s is called a *running coupling constant*⁶. It can be written in leading order as [27, pp. 50-52]:

$$\alpha_s(\mu^2) = \frac{\alpha_s(\mu_R^2)}{1 + \alpha_s(\mu_R^2)b_0 \ln(\frac{\mu^2}{\mu_R^2})}, \quad (2.17)$$

where $b_0 = \frac{33-2n_f}{12\pi}$ is a function of the number of active quark flavours n_f available at the energy scale μ .

The introduction of the convenient parameter Λ_{QCD} defined as

$$\ln \Lambda_{QCD}^2 = \ln \mu_R^2 - \frac{1}{b_0 \alpha_s(\mu_R^2)}, \quad (2.18)$$

simplifies Equation 2.17 to:

$$\alpha_s(\mu^2) = \frac{1}{b_0 \ln(\frac{\mu^2}{\Lambda_{QCD}^2})}. \quad (2.19)$$

Λ_{QCD} needs to be determined experimentally. It can be interpreted as the scale at which α_s becomes large and is found to be of the order of 250 MeV [28]. Perturbation theory is only applicable, if $\mu_R \gg \Lambda_{QCD}$ is satisfied.

The running of the coupling constant explains why the quarks can be seen as free particles inside the proton, but cannot be observed free: At values of μ_R comparable to Λ_{QCD} (i.e. large distances) α_s is steeply rising, leading to the *confinement* of the quarks inside the proton. At large values of μ_R much bigger than Λ_{QCD} (i.e. at small distances) α_s becomes small and the quarks behave as (quasi-)free particles, a behaviour that is called *asymptotic freedom*. An illustration of the running of α_s (at leading order) is shown in Figure 2.3.

2.3.2.b. Factorization and DGLAP Evolution

One of the basic assumptions of the Quark Parton Model is that the short-range interactions do not interfere with the long-range interactions. The DIS cross section can therefore be described as a convolution of two independent terms: the hard scattering cross sections $\hat{\sigma}_i$, which can be calculated perturbatively and describe the scattering of the photon on the proton's constituents i , and the *parton distribution functions* f_i (the index i refers to the type of parton, so this includes the functions for the quarks q_i and for the gluon g_i), which are not calculable in perturbative QCD and describe the proton content.

The DIS cross section can then be written as

$$\sigma = \sum_i f_i(x, \mu_f) * \hat{\sigma}_i(x, \alpha_s(\mu_R^2), \mu_f^2), \quad (2.20)$$

⁶The coupling constant of the electromagnetic interaction, α_{em} , does also run, but the dependence is much smaller and in the other direction.

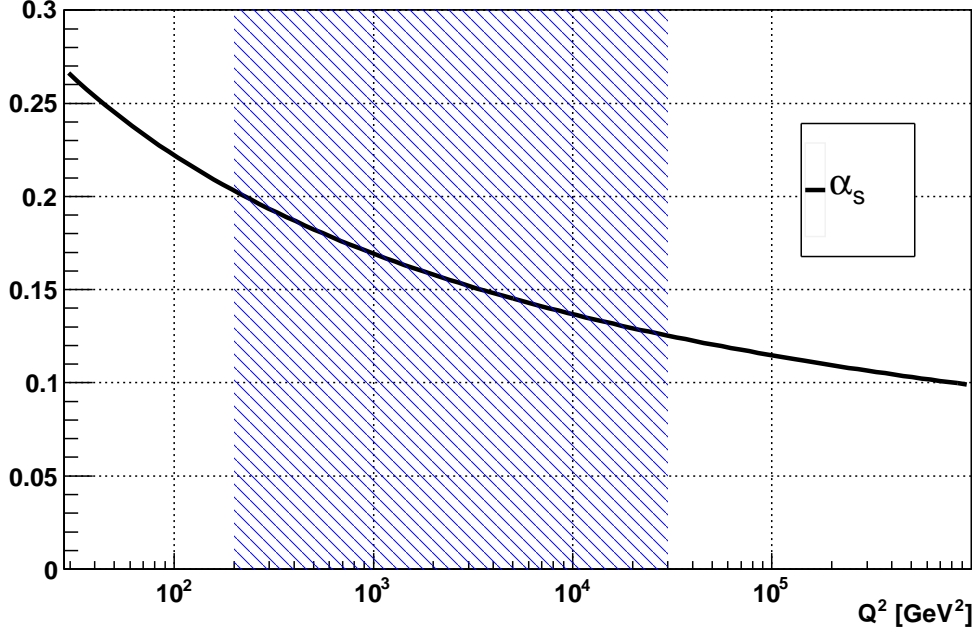


Figure 2.3: An illustration of the running of α_s at leading order with $n_f = 5$ and $\Lambda_{QCD} = 250$ MeV. The hashed blue area indicates the Q^2 region of reduced cross section extraction within this analysis.

where μ_f is called *factorization scale*⁷. It defines the boundary between $\hat{\sigma}_i$ and f_i : A parton emitted at a scale smaller than μ_f is considered part of the proton, a parton emitted at a larger scale part of the hard scatter.

As the proton is resolved better at higher scales (Q^2) there are more soft partons (quarks and gluons) visible, which are referred to as the *sea*. This is responsible for the breaking of scaling at high Q^2 . The dependence of the parton density functions on Q^2 can be calculated in QCD using the DGLAP [29], [27, pp. 79-81] equations⁸:

$$\frac{\partial}{\partial \ln Q^2} \begin{pmatrix} q_i(x, Q^2) \\ g(x, Q^2) \end{pmatrix} = \frac{\alpha_s(Q^2)}{2\pi} \sum_j \int_x^1 \frac{d\xi}{\xi} \begin{pmatrix} P_{q_i q_j}(\frac{x}{\xi}, \alpha_s(Q^2)) & P_{q_i g}(\frac{x}{\xi}, \alpha_s(Q^2)) \\ P_{g q_j}(\frac{x}{\xi}, \alpha_s(Q^2)) & P_{g g}(\frac{x}{\xi}, \alpha_s(Q^2)) \end{pmatrix} \begin{pmatrix} q_j(x, Q^2) \\ g(x, Q^2) \end{pmatrix}, \quad (2.21)$$

where the q_i (and q_j) are the quark and anti-quark distributions and g is the gluon distribution. The $P_{ab}(z)$ are the splitting functions (see Figure 2.4), which describe the probability that parton a emits parton b with the momentum fraction z of the initial parton.

On the other hand, the x dependence of the PDFs cannot be calculated perturbatively, but has to be determined experimentally (see Section 2.5).

⁷The x here, as always when it is an argument of the PDFs, refers to the fraction of the proton momentum.

⁸In the DGLAP approximation it is assumed that the partons are strongly ordered by their transverse momentum, so that only terms of the form $\alpha_s \ln(\frac{Q^2}{\mu_f^2})$ are considered.

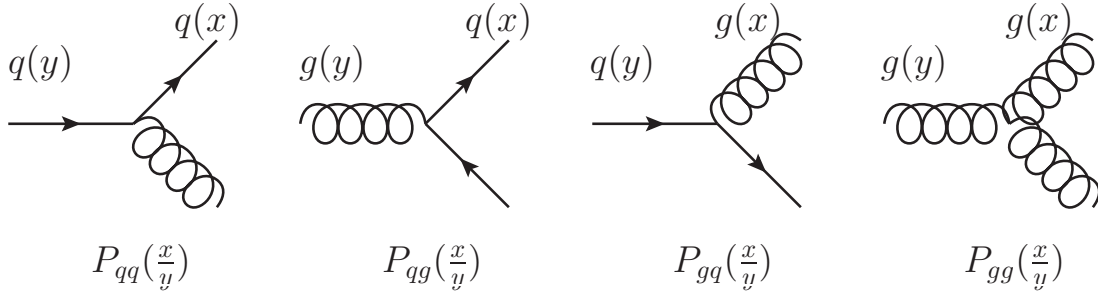


Figure 2.4: The splitting functions

2.4. Structure Functions at HERA

In elastic processes form factors describe the charge and current distribution of the scattering target. Structure functions are the extensions of the concept of form factors to include target content and dynamics in inelastic processes. As such they describe the effect of proton content on the DIS process and are what can be determined experimentally. In this section the DIS structure functions are introduced, it is explained how they reflect the parton density functions and which terms need to be considered for them.

2.4.1. Structure Functions in the QPM

In the simple Quark Parton Model (Section 2.3.1) the cross section of NC DIS can be written as [27, p. 19]

$$\frac{d^2\sigma^{e^\pm p}}{dx dQ^2} = \frac{2\pi\alpha^2}{xQ^4} \left[1 + (1-y)^2 \right] \sum_i e_i^2 x q_i(x), \quad (2.22)$$

where e_i is the electric charge and $q_i(x)$ the distribution function of the struck quark.⁹

According to the parton model with Bjorken scaling for ep NC DIS mediated by photon exchange [27, p. 6] the double differential cross section $\frac{d^2\sigma^{e^\pm p}}{dx dQ^2}$ can be expressed in terms of the proton *structure functions* $F_1(x)$ and $F_2(x)$ ¹⁰:

$$\frac{d^2\sigma^{e^\pm p}}{dx dQ^2} = \frac{4\pi\alpha^2}{xQ^4} \left[(1-y)F_2(x) + xy^2F_1(x) \right]. \quad (2.23)$$

Comparing the two equations leads to

$$F_2(x) = \sum_i e_i^2 x q_i(x) \quad (2.24)$$

⁹The term $1 + (1-y)^2$ stems from the scattering of same-handed scattering partners (isotropic, i.e. 1) and opposite-handed ($\cos^2(\frac{\theta}{2}) = (1-y)$) scattering partners.

¹⁰This is correspondent to the description of elastic scattering by form factors.

and

$$F_1(x) = \frac{1}{2x}F_2(x) , \quad (2.25)$$

the latter being referred to as the *Callan-Gross relation*.

From the Callan-Gross relation it would follow that the part of the structure functions for the absorption of longitudinal photons

$$F_L = F_2 - 2xF_1 \quad (2.26)$$

was 0.

This proposition is due to the assumption that the photon is interacting with free spin 1/2 quarks and holds as long as the exchanged boson interacts with free spin 1/2 particles exclusively.

2.4.2. Structure Functions Including QCD, Z Exchange and Polarisation

Taking into account both, electroweak and QCD effects, in an improved Quark Parton Model, the double differential cross section $\frac{d^2\sigma^{e\pm p}}{dx dQ^2}$ for ep NC DIS reads

$$\frac{d^2\sigma^{e\pm p}}{dx dQ^2} = \frac{2\pi\alpha^2}{xQ^4} \left[Y_+ \tilde{F}_2(x, Q^2) \mp Y_- x \tilde{F}_3(x, Q^2) - y^2 F_L(x, Q^2) \right] \quad (2.27)$$

with

$$Y_{\pm} = 1 \pm (1 - y)^2 \quad (2.28)$$

and the *generalised structure functions* \tilde{F}_2 , \tilde{F}_3 and F_L .

By removing the kinematic term in front of \tilde{F}_2 the *reduced cross section* $\tilde{\sigma}$ is defined:

$$\tilde{\sigma}^{e\pm p} = \frac{xQ^4}{2\pi\alpha^2} \frac{1}{Y_+} \frac{d^2\sigma_{NC}^{e\pm p}}{dx dQ^2} = \tilde{F}_2(x, Q^2) \mp \frac{Y_-}{Y_+} x \tilde{F}_3(x, Q^2) - \frac{y^2}{Y_+} F_L(x, Q^2) . \quad (2.29)$$

2.4.2.a. Generalised Structure Functions and their Contributions

For obtaining \tilde{F}_2 its terms need to be added taking the propagator and its coupling to the electron as well as to the quark (see above) into account (the vector coupling of Z to electron v_e and the axial vector coupling a_e , for χ_Z (see Equation 2.34)).

Without lepton polarisation one gets for \tilde{F}_2

$$\tilde{F}_2 = F_2^\gamma - v_e \chi_Z F_2^{\gamma Z} + (v_e^2 + a_e^2) \chi_Z^2 F_2^Z \quad (2.30)$$

and for $x\tilde{F}_3$

$$x\tilde{F}_3 = -a_e \chi_Z x F_3^{\gamma Z} + 2v_e a_e \chi_Z^2 x F_3^Z . \quad (2.31)$$

Including the polarisation of the electron P_e , additional terms have to be included:

$$\tilde{F}_2 = F_2^\gamma - (v_e + P_e a_e) \chi_Z F_2^{\gamma Z} + (v_e^2 + a_e^2 + 2P_e v_e a_e) \chi_Z^2 F_2^Z \quad (2.32)$$

and

$$x\tilde{F}_3 = -(a_e + P_e v_e)\chi_Z x F_3^{\gamma Z} + (P_e(v_e^2 + a_e^2) + 2v_e a_e)\chi_Z^2 x F_3^Z. \quad (2.33)$$

In these equations of the contributions to the generalised structure functions the variable χ_Z is of major importance, which is calculated from

$$\chi_Z = \frac{1}{\sin^2 \theta_W} \frac{Q^2}{M_Z^2 + Q^2}. \quad (2.34)$$

The mass and Q^2 dependence of χ_Z stems from the propagator term.

χ_Z accounts for the effect of the Z propagator compared to the (virtual) photon propagator, and is illustrated in Figure 2.5. While the pure photon term does not include χ_Z in any order, the photon-Z interference term includes χ_Z and the pure Z term χ_Z^2 . This gives an idea of the suppression of the photon-Z interference term with respect to the pure photon term.

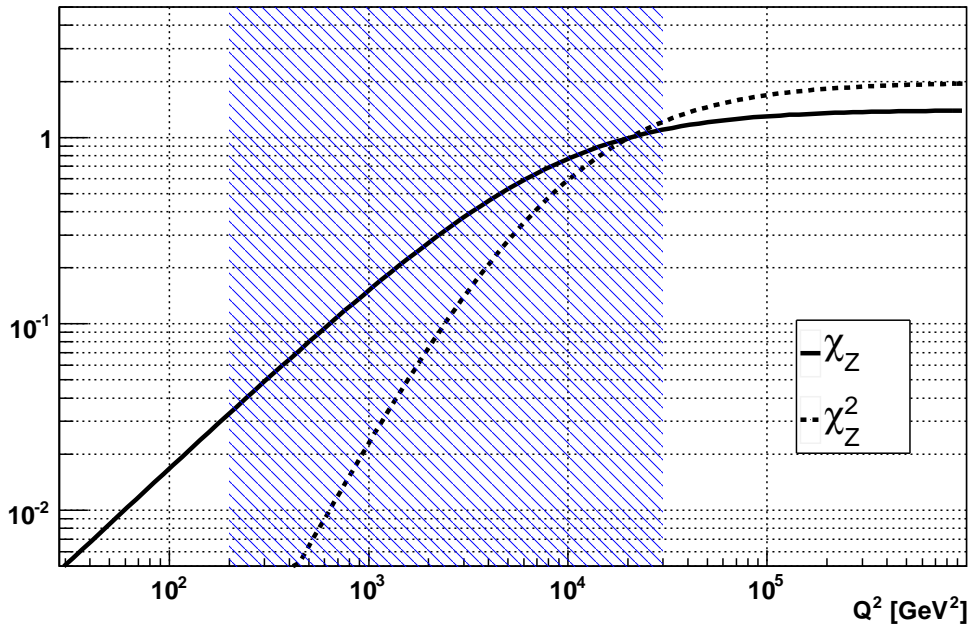


Figure 2.5: The behaviour of χ_z and its square χ_z^2 showing the order of the contribution of γZ interference and pure Z term compared to the γ exchange. The hashed blue area indicates the Q^2 region of reduced cross section extraction within this analysis.

From looking at Equations 2.32 and 2.33 it can be noticed that $x\tilde{F}_3$ is suppressed with regard to \tilde{F}_2 for $Q^2 < M_Z^2$.

Due to the y^2 term (see Equation 2.27), F_L is suppressed at low y and only sizable for high y .¹¹

Therefore \tilde{F}_2 , and more precisely its photon exchange term F_2^γ , is dominant for most of the Q^2 region of HERA.

¹¹The influence of F_L for this analysis is discussed in Section 5.1.

It can also be seen that the polarisation makes it possible to access more terms. For example, the $F_2^{\gamma Z}$ contribution nearly vanishes without the polarisation due to the smallness of v_e (see Table 2.2) (but even including the polarisation is important at high Q^2 only).

particle	vector	axial vector
u, c, t	$0.29^{+0.10}_{-0.08}$	$0.50^{+0.04}_{-0.07}$
d', s', b'	$-0.33^{+0.05}_{-0.07}$	$-0.52^{+0.05}_{-0.03}$
e, μ , τ	-0.0378 ± 0.0004	-0.5012 ± 0.0003
ν	0.5008 ± 0.0008	

Table 2.2: Measured values of vector and axial vector couplings of the Z to fermions [21].

2.4.2.b. Physics Interpretation of the Generalised Structure Functions

The generalised structure functions \tilde{F}_2 , \tilde{F}_3 and F_L are direct descriptions of the proton content as probed by electroweak projectiles. They are combinations of the parton density functions of quarks q , anti-quarks \bar{q} and gluons g .

The physics interpretation of \tilde{F}_2 being the structure function to describe the sum of all quarks is visible in

$$[F_2^\gamma, F_2^{\gamma Z}, F_2^Z] = \sum_q [e_q^2, 2e_q v_q, v_q^2 + a_q^2] x(q + \bar{q}) , \quad (2.35)$$

where F_2^γ is the photon exchange term, $F_2^{\gamma Z}$ the photon- Z interference term of \tilde{F}_2 and F_2^Z the term from pure Z exchange, v_q is the vector coupling of the Z to the quark q and a_q the axial-vector coupling (see Table 2.2).

F_2 is also sensitive to the gluon contribution via its dependence on Q^2 :

$$\frac{\partial F_2}{\partial \log Q^2} \propto \alpha_s g(x) \quad (2.36)$$

\tilde{F}_3 describes the valence quark distributions and has only photon- Z interference ($x F_3^{\gamma Z}$) and pure Z exchange ($x F_3^Z$) terms:

$$[x F_3^{\gamma Z}, x F_3^Z] = \sum_q [e_q a_q, v_q a_q] x(q - \bar{q}) . \quad (2.37)$$

As seen above, F_L would be 0, if the proton was constituted from spin-1/2 particles only. It becomes non-zero due to the presence of gluons, and thus is a direct measure of the gluon content of the proton:

$$F_L \approx \frac{\alpha_s}{8.3} xg(x) . \quad (2.38)$$

2.4.2.c. Polarisation Asymmetry and Parity Violation

The polarisation asymmetry of e^+p scattering, A^+ , can be defined as (A^- for e^-p scattering is defined in the same way):

$$A^+ = \frac{2}{P_e^+ - P_e^-} \frac{\sigma(P_e^+) - \sigma(P_e^-)}{\sigma(P_e^+) + \sigma(P_e^-)}, \quad (2.39)$$

where P_e^+ and P_e^- are the average polarisations of the positively and negatively polarised lepton beam, and

$$P_e = \frac{N_{rh} - N_{lh}}{N_{rh} + N_{lh}} \quad (2.40)$$

is calculated from the number of right-handed, N_{rh} , and the number of left-handed, N_{lh} , electrons. $\sigma(P_e^\pm)$ is the respective cross section.

As A^+ measures the difference between cross sections with positively and negatively polarised lepton beams, it is a direct measure of parity violation. To a good approximation, the asymmetry is proportional to the ratio of the pure photon and photon- Z interference term of the structure function F_2 . Using Equation 2.35 one gets

$$A^+ \approx -\chi_Z a_e \frac{F_2^{\gamma Z}}{F_2^\gamma} \sim a_e v_q, \quad (2.41)$$

showing that the asymmetry measures parity violation with a minimum sensitivity to the PDFs and provides a direct test of the electroweak sector of the Standard Model.

2.5. Fits of Parton Density Functions

It was stated in Section 2.3.2.b, that, while the Q^2 evolution of the Parton Density Functions (PDFs) can be predicted by perturbative QCD, the x dependence needs to be obtained experimentally. As described in the previous sections, NC and CC DIS provide direct information on the structure of the proton. In the *PDF fits*, the parameters describing the parton distributions are determined. The results are usually quoted in terms of distributions of valence (u_v, d_v) and sea quarks (the u, d, s and c quarks¹² and their anti-partners $\bar{u}, \bar{d}, \bar{s}$ and \bar{c} of the quark sea) and of the gluon. Parton distribution functions are extracted from the data by a fitting procedure involving the following steps:

- Choice of data to be included: PDF-sensitive data with a precise theory description.
- Parametrisation of the PDFs as a function of Q^2 at a small, but perturbatively describable, Q_0^2 .
- Evolution of the PDFs to the Q^2 of the data using DGLAP equations.
- Choice of the starting values of the parameters¹³.

¹²The b and t quark contributions are small due to their high masses.

¹³The starting values of the parameters should not influence the final results. The dependence on the starting values of parameters is normally tested by the fitting groups.

- Fitting the parameters (using χ^2 minimisation method).

The choice of the data sets to use for the fitting is very important. The most precise PDFs would be expected from using the maximal available input. The major drawbacks with this approach are that some data sets were shown not to be consistent with each other [27, p. 142], and that for some data of heavy target scattering nuclear binding corrections are needed, which add additional uncertainties. Using inconsistent data sets renders the method of χ^2 minimisation problematic.

2.5.1. General Formalism

The parametrisation used at Q_0^2 for the PDFs is different in the various approaches used by different groups of fitters. A typical example (from HERAPDF 1.0 [30]) is

$$xf(x) = Ax^B(1-x)^C(1 + \eta\sqrt{x} + Dx + Ex^2), \quad (2.42)$$

where $f(x)$ is the PDF and A , B , C , D , E and η are the parameters to be determined in the fit. For HERAPDF 1.0 the starting scale Q_0^2 was fixed at 1.9 GeV².

In addition, there are requirements on the PDFs, which are typically physics-driven. Examples are sum rules, that all PDFs should be positive, that $xd_v > x\bar{d}$ at large x and possibly that in the sea there should be symmetry between quarks and anti-quarks.

2.5.2. Gluon Distribution and Jets

As the gluon PDF contributes mostly indirectly to the inclusive DIS cross sections through the scaling violation (see Equation 2.36), it is not very well constrained by them. To access the gluon PDFs directly through the HERA data other processes need to be investigated. In principle there are several possibilities: jet production and open charm production (both through the boson-gluon fusion (BGF) process, see left part of Figure 2.6), the longitudinal structure function (see Section 2.4.2), prompt photon production (through the dominant subprocess $gq \rightarrow \gamma q$) and elastic (diffractive) J/Ψ production (depends on the square of the gluon distribution).

At present, the process that has been proven to provide the most useful input to the PDF fits is jet production. Jets help to remove the correlation between α_s and the gluon distribution present in the inclusive data. This is due to the fact that the QCD Compton process (right part of Figure 2.6) only depends on α_s , but not on the gluon content of the proton. In this way α_s does not need to be fixed anymore in the fit, but can be treated as a free additional parameter. As a consequence, the fit provides as an output both the gluon distribution and the value of α_s . The uncertainty on the extracted PDFs is similar to that obtained from the fit to the inclusive data with fixed α_s .

2.5.3. Electroweak Fits

The measurement of polarised cross sections in HERA-II data makes it also possible to extract precise values of the electroweak couplings in the PDF fit¹⁴. The Charged

¹⁴For fits using only unpolarised HERA-I data the precision is much smaller [31], especially for the vector couplings.

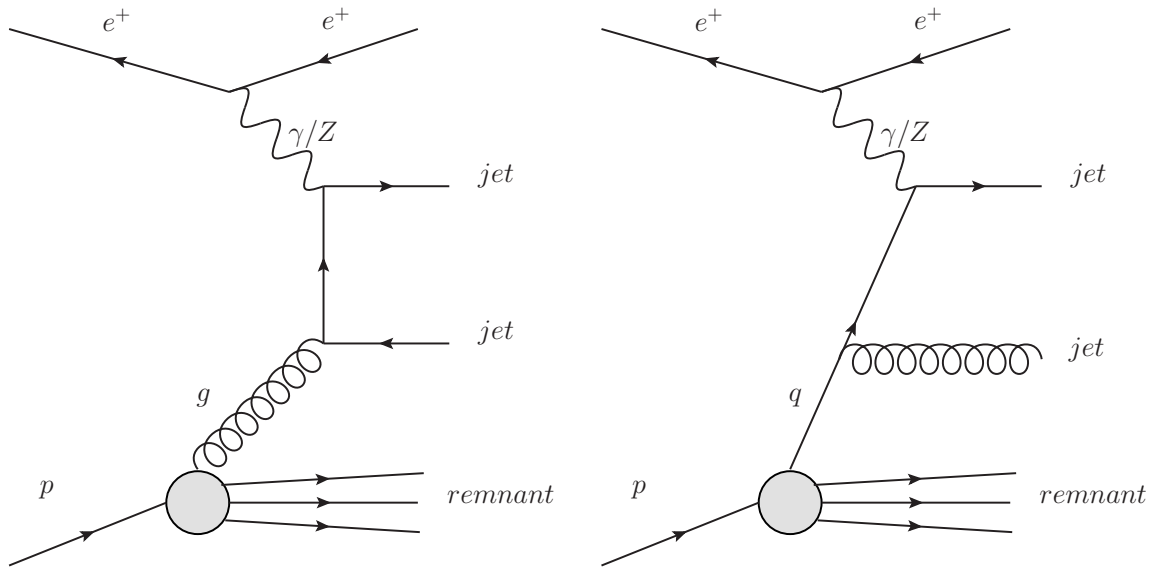


Figure 2.6: The boson-gluon fusion process (left) and the QCD Compton process (right).

Current cross section provides information about the mass of the W bosons and the strength of the weak coupling while the Neutral Current cross section depends on the couplings of the Z boson to the quarks (see Sections 2.2 and 2.4.2). The confidence intervals extracted for the couplings are complementary to the ones measured at e^+e^- and $p\bar{p}$ colliders.

2.6. HERA's Achievements to Date

Many important results come from HERA, which cannot be exhaustively described in this section. Here only the current status of the results with direct connection to the analysis described are highlighted: DIS cross sections, structure functions and parton density functions.

2.6.1. DIS Cross Sections at HERA

At HERA, the CC and NC cross sections have been measured over a large range of Q^2 up to about 30000 GeV^2 . Through these results the generalised structure functions \tilde{F}_2 and (through the difference of e^+p and e^-p NC DIS) $x\tilde{F}_3$ were precisely measured. One of the textbook results is shown in Figure 2.7: the cross sections of NC and CC DIS measured as a function of Q^2 , where electroweak unification at about $Q^2 = M_Z^2$ is confirmed.

Also the third structure function F_L has been measured at HERA. This was made possible by dedicated running periods for the measurement of the cross section at different centre-of-mass energies (see Figure 2.8).

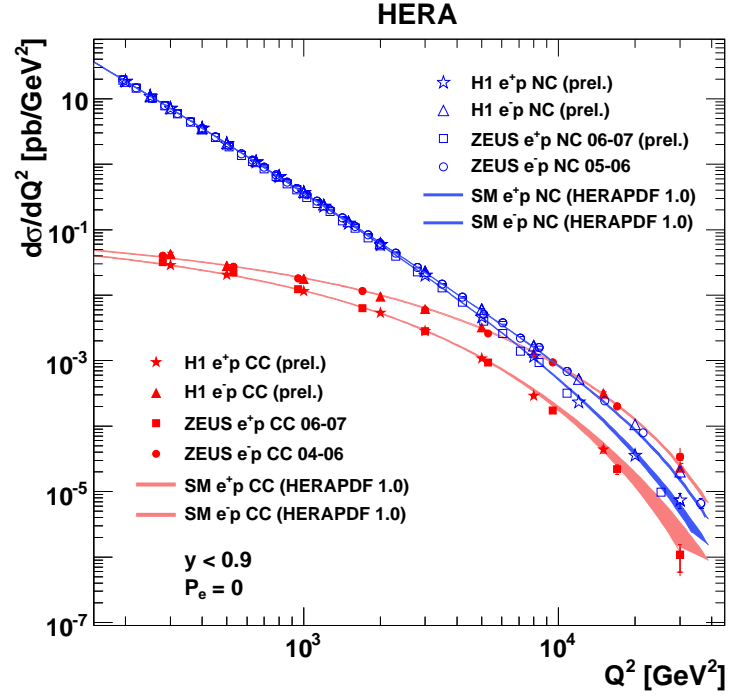


Figure 2.7: The $\frac{d\sigma}{dQ^2}$ cross sections of Neutral and Charged Current Deep Inelastic Scattering measured at HERA. From [32].

The scaling violation has been quantified impressively using the NC DIS measurements at different x values (see Figure 2.9). In addition the measurement of CC DIS at different polarisation values (see Figure 2.10) made it possible to determine the polarisation dependence of CC DIS very precisely and to exclude the existence of right-handed charged currents up to the experimental sensitivity.

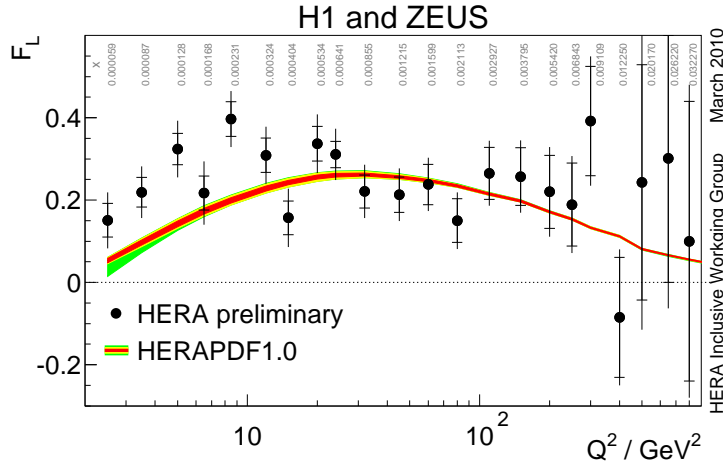


Figure 2.8: The longitudinal structure function F_L as a function of x as measured at HERA. From [33].

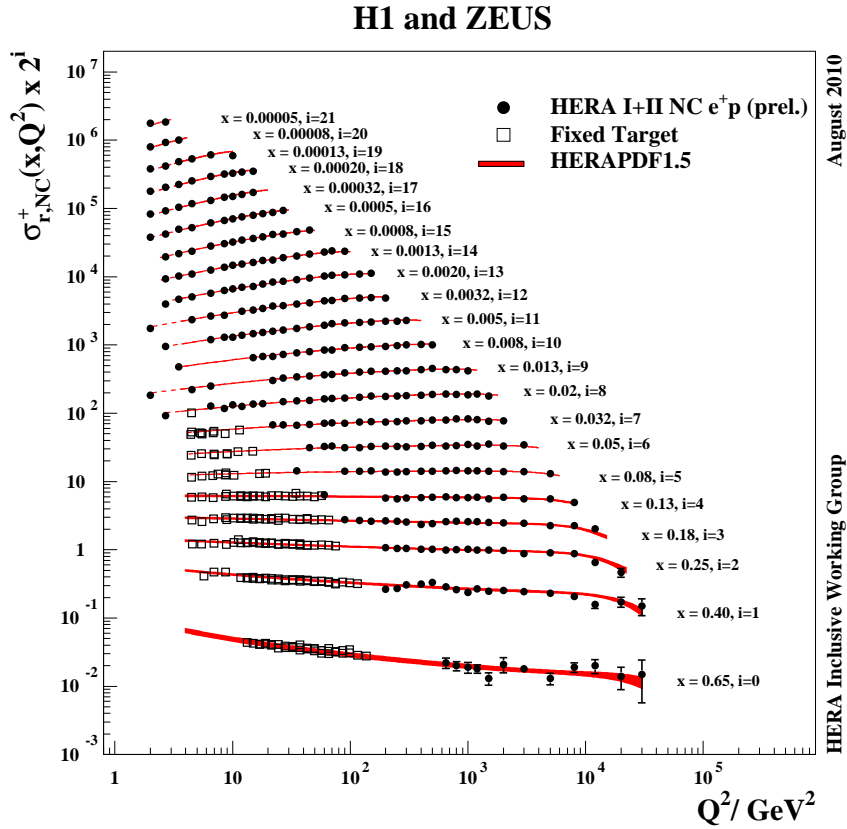


Figure 2.9: The reduced cross sections of Neutral Current Deep Inelastic e^+p Scattering measured at HERA and fixed target experiments shown as a function of Q^2 at different x values. From [34].

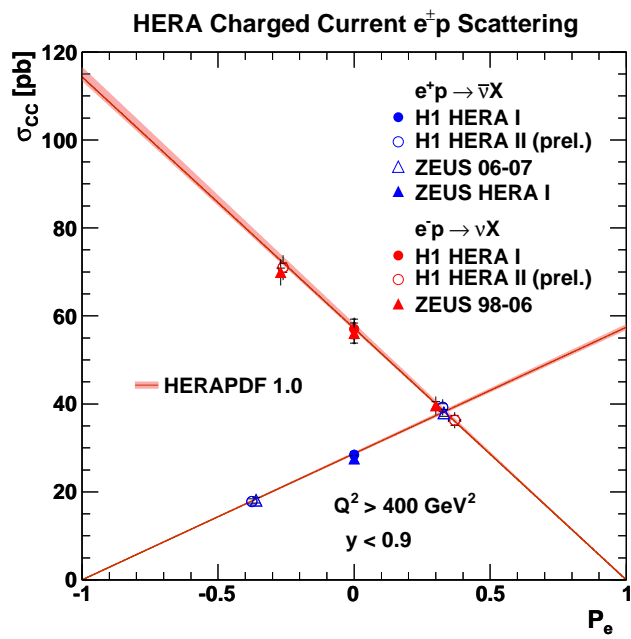


Figure 2.10: Charged Current Deep Inelastic Scattering total cross sections measured at HERA as a function of lepton polarisation. From [32].

2.6.2. PDF Fits at HERA

While several groups extract PDFs using data sets from many different experiments (e.g. CTEQ [35,36], MSTW [37,38] and the NNPDF [39], which uses a different (Neural Network) approach), H1 and ZEUS have fitted the Parton Density Functions based only on HERA data [30, 34, 40]. That has several advantages, most importantly that the problem of inconsistency of data sets is under much better control, but also that the correlation between the different systematic uncertainties is well understood and that the fitters are in general much more knowledgeable about the data sets used than in a fit of data from many different experiments.

Figure 2.11 shows that HERA data cover nearly the whole x range of the displayed important experiments.¹⁵

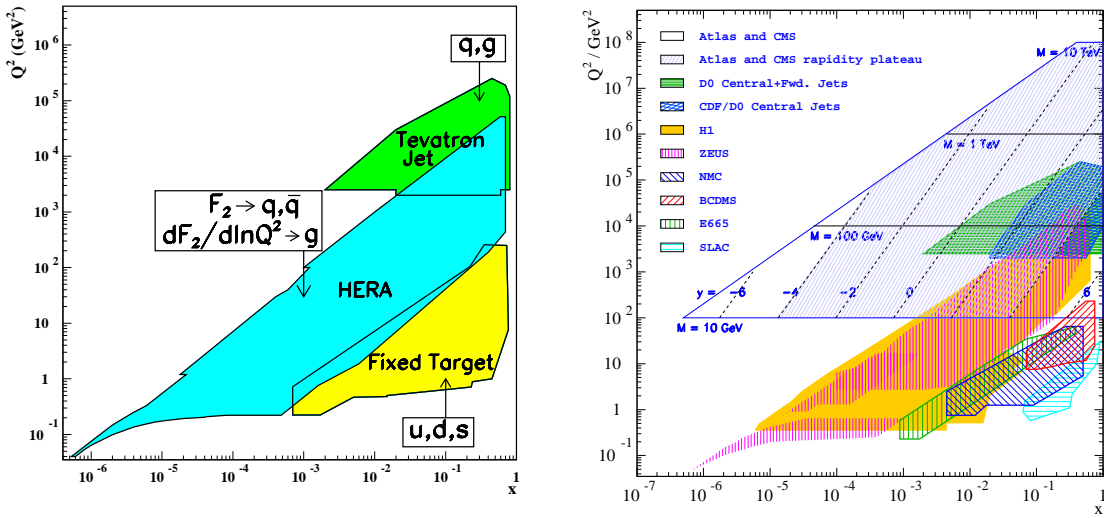


Figure 2.11: Kinematic range in x and Q^2 covered by different collider and fixed-target experiments. On the left plot from [21, Fig. 16.3] in addition, the most important regions for the various parton distributions are indicated. On the right plot from [41] the coverage of LHC is indicated.

The parton distribution functions as a function of x from the HERAPDF 1.5 fit [34] are shown for 10 and 10000 GeV² of Q^2 in Figure 2.12.

In 2005 ZEUS started using jet data in PDF fits [40], and the most recent (preliminary) results of the HERA PDF fit (HERAPDF 1.7) [42] include jet and charm data. This is discussed in more details in Section 9.3.

¹⁵Not covered by HERA is mainly the very high x -region above ≈ 0.6 .

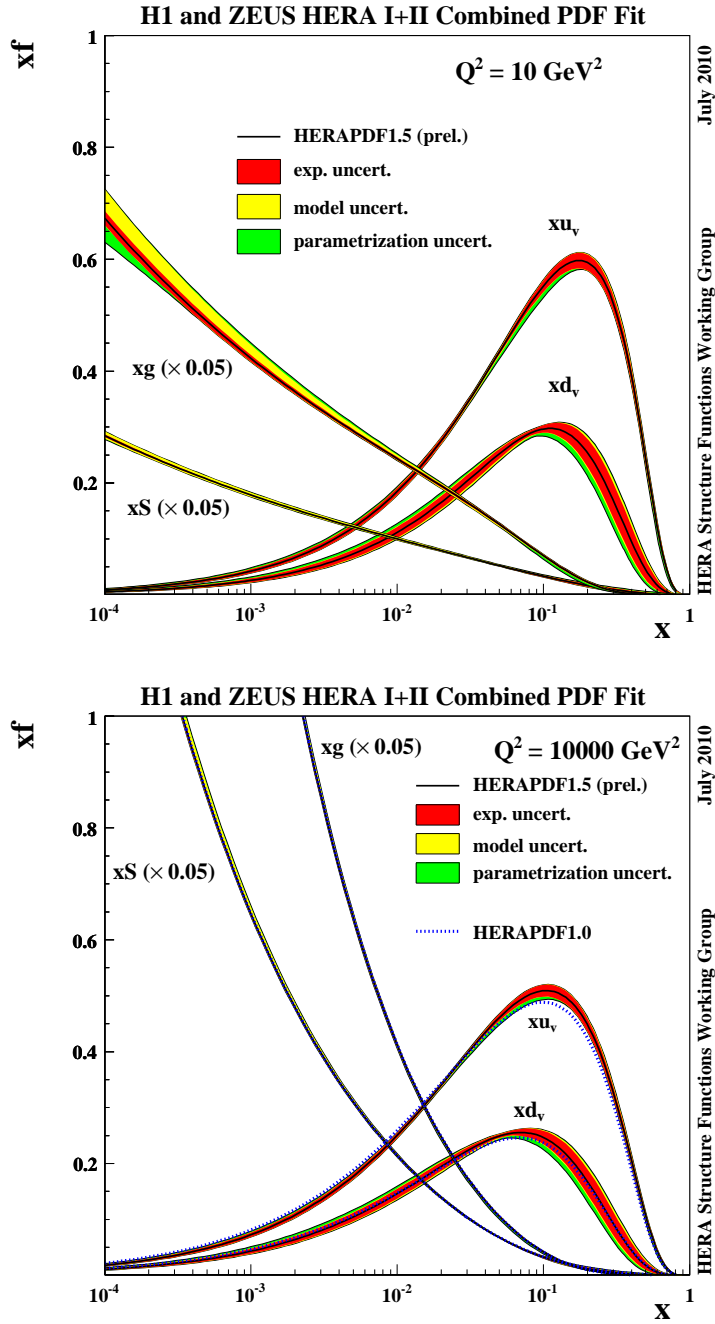


Figure 2.12: Parton density functions as extracted from HERA inclusive DIS data with the HERAPDF1.5 fit at $Q^2 = 10 \text{ GeV}^2$ (top) and $Q^2 = 10000 \text{ GeV}^2$ (bottom) [34]. u_v refers to the u valence quark, d_v refers to the d valence quark, g to the gluon and S to the sum of all sea quarks (the last two are suppressed by a factor 20 for the plot).

ZEUS [43] and H1 [44] have both performed electroweak fits extracting values of the couplings of the Z boson to the quarks a_u , a_d , v_u , v_d . The result of these fits is shown in Figure 2.13. Especially the uncertainties of the u quark couplings are reduced compared to measurements from other experiments and to the HERA results based only on unpolarised data.

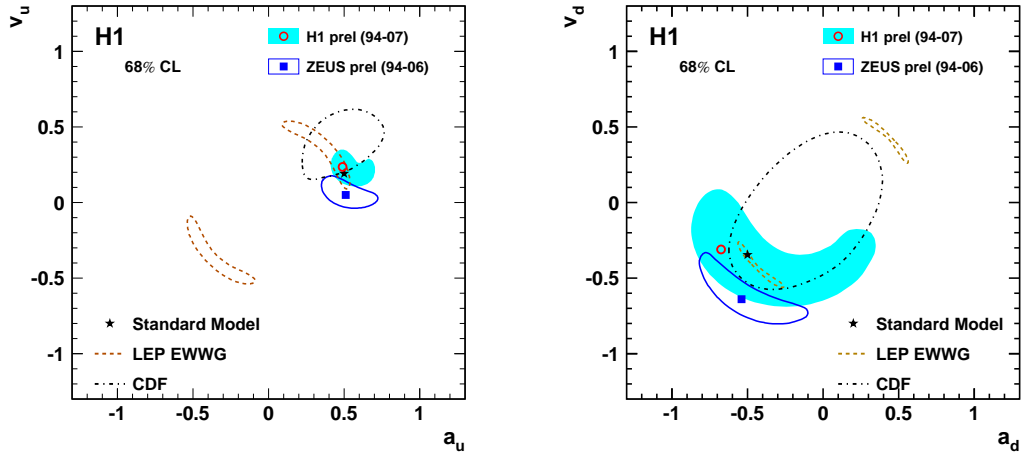


Figure 2.13: Contours at 68% confidence level for the couplings of the Z boson to the u (left) and d (right) quark. The results from ZEUS and H1 as well as results from LEP and CDF are shown. [44, Fig. 1]

3. The ZEUS Experiment at HERA

This chapter introduces the experimental setup, i.e the ep -collider HERA and the general purpose detector ZEUS, which provided the data analysed here. Special emphasis is placed on detector components with particular importance for the presented analysis, namely the calorimeter, the central tracking detector, the polarisation detectors and the luminosity detectors. Major parts of this chapter are taken from the author's diploma thesis [45], which uses [46] as main source of information.

3.1. HERA Accelerator

HERA (**H**adron-**E**lektron-**R**ing-**A**nlage) was the main accelerator facility at DESY (**D**eutsches **E**lektronen **S**ynchrotron) and the only Multi-GeV electron-proton particle collider in the world. It was situated in a tunnel about 15 to 20 m underground in Hamburg, Germany. An aerial view of the site can be seen in Figure 3.1.

HERA's main components were the two storage rings, one for the protons and one for the electrons, which were built between 1984 and 1990. The total circumference of the HERA ring was approximately 6.3 km. Before being injected into HERA there was a system of pre-accelerators, which accelerated the electrons to 12 GeV and the protons to 40 GeV. In HERA they finally reached the energy of 27.5 GeV (electrons) and 920 GeV (protons).¹ Thus the centre-of-mass energy was

$$\sqrt{s} = \sqrt{4E_p E_e} \approx 318 \text{ GeV} . \quad (3.1)$$

Figure 3.2 shows the HERA accelerator, the four experiments and the system of pre-accelerators.

Out of the four experiments the ZEUS and the H1 experiment were collider experiments which used both the electron and the proton beam. Particle collisions were taking place at a rate of approximately 96 ns. The ZEUS detector was located in the Southern experimental hall and the H1 detector in the Northern hall. HERMES (Eastern Hall) and HERA-B (Western Hall) were fixed target experiments. The HERA-B experiment [47], which used the proton beam to investigate CP-violation, had already stopped taking data in 2003. HERMES [48] used the electron beam to investigate the nucleon spin structure.

3.1.1. Luminosity at HERA

Through the reaction rate,

$$R = \sigma L , \quad (3.2)$$

¹Proton energy was limited by the strengths of the superconducting magnets whereas the electron energy was limited due to synchrotron radiation.



Figure 3.1: Aerial view of the DESY laboratory in Hamburg. The HERA collider is marked with the dashed line. In addition the pre-accelerator PETRA (enclosing the main DESY site) is shown in the foreground. The ZEUS detector was situated off the main DESY campus at the south side of HERA.

(where σ is the cross section of the reaction) the (instantaneous) luminosity L is a key component of the accelerator. It can be expressed as

$$L = n_1 n_2 \frac{f}{A}, \quad (3.3)$$

where f is the bunch-crossing rate, n_1 and n_2 are the number of particles per bunch for each beam and A is the effective transverse area of the overlap of the beam and can be expressed as (assuming Gaussian beams)

$$A = 4\pi\sigma_x\sigma_y, \quad (3.4)$$

where σ_x and σ_y are the transverse dimensions of the beam.

The design values at HERA² for these key parameters were [27, p. 139]: $n_1=4.18\cdot 10^{10}$ (electron), $n_2=10\cdot 10^{10}$ (proton), $f=8.2\cdot 10^6 \text{ s}^{-1}$ (174 bunches at a revolution frequency of $4.7\cdot 10^4 \text{ s}^{-1}$), $\sigma_x = 118 \mu\text{m}$ and $\sigma_y = 32 \mu\text{m}$ leading to an instantaneous luminosity of $7\cdot 10^{35} \text{ m}^{-2}\text{s}^{-1}$.

The integrated luminosity,

²This is for the HERA-II running period as explained in 3.1.2, which is relevant for the analysis described in this thesis.

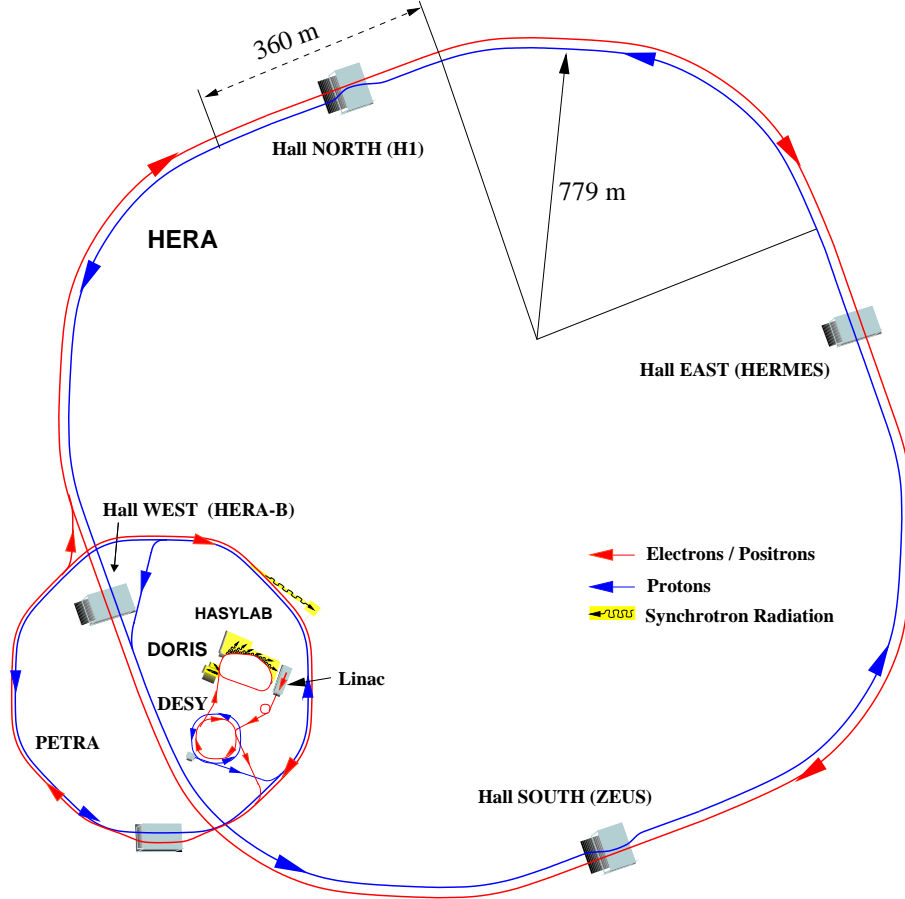


Figure 3.2: Schematic view of HERA and its experiments including the pre-accelerator systems. The four experiments are ZEUS (Southern Hall), HERA-B (Western Hall), H1 (Northern Hall), and HERMES (Eastern Hall).

$$\mathcal{L} = \int L dt = \frac{N}{\sigma}, \quad (3.5)$$

relates the number of observed events N to the cross section σ of a given process and is a measure of the amount of data taken, which has been about 0.5 fb^{-1} for the H1 and ZEUS experiment each over the whole HERA running.

3.1.2. HERA Upgrade and Running Periods

At HERA data was taken from 1992 to 2007. During this period the polarity of the electron ring was switched (electron and positron running) several times. Six high-energy running periods can be distinguished from each other. Additionally, there were two running periods with lower proton energies in 2007, which were dedicated to the study of the F_L -structure function. This running period will not be discussed here as F_L is not the focus of this analysis.

During the shutdown between the years 2000 to 2002 HERA was upgraded to increase

the luminosity significantly and to provide longitudinally polarised lepton beams for H1 and ZEUS. The period before the upgrade is referred to as HERA-I, and the period after the upgrade as HERA-II. This analysis is based on the e^+p -data collected from 2006 to 2007 by the ZEUS experiment during the HERA-II running period. Thus the analysis of this thesis was done with polarised positron beam. In Table 3.1 details about the different running periods can be found. The integrated luminosity delivered by HERA is shown as a function of time in Figure 3.3 and is summarised in the table, along with the luminosity available for physics analyses recorded by ZEUS during the same period. The achieved luminosity increase is clearly seen, when one compares HERA-I and HERA-II running periods.

Period	94 - 97	98 - 99	99 - 00	03-04	04-06	06-07	07 LER	07 MER
Mode	e^+p	e^-p	e^+p	e^+p	e^-p	e^+p	e^+p	e^+p
E_p [GeV]	820	920	920	920	920	920	460	575
E_e [GeV]	27.5							
E_{CMS} [GeV]	301	318	318	318	318	318	225	251
\mathcal{L} (HERA) [pb^{-1}]	70.9	25.2	95.0	84.5	290.9	180.5	15.69	9.36
\mathcal{L} (ZEUS) [pb^{-1}]	48.3	16.7	65.9	40.6	213.5	145.9	13.18	7.77

Table 3.1: Main parameters of the HERA collider and its electron and proton beams for the eight running periods.

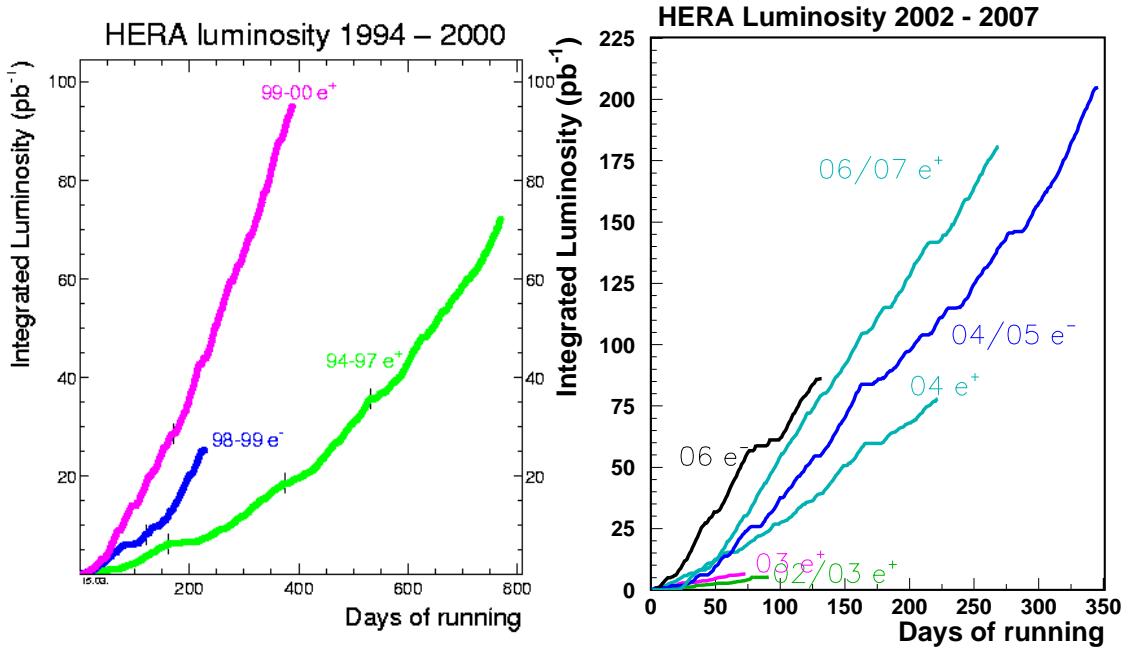


Figure 3.3: Integrated luminosity delivered by HERA during all HERA-I (1994-2000, left plot) and HERA-II (2003-2007, right plot) running periods.

3.1.3. Beam Polarisation

As mentioned in Section 3.1.2 one of the main achievements of the HERA upgrade [49–51] was the longitudinal polarisation of the electron beam as it gives access to polarisation dependent physics.

The electron beam was unpolarised when it was injected into HERA. The first step of the polarisation happened automatically through the Sokolov-Ternov effect [52]: Electrons become gradually transversely polarised through asymmetric spin flips due to emission of synchrotron radiation. Thus electrons will become anti-parallel (and positrons parallel) aligned to the external magnetic field. This effect builds up over time according to

$$P_T(t) = P_{max}(1 - e^{-\frac{t}{\tau}}), \quad (3.6)$$

where

$$P_T = \frac{N_{up} - N_{down}}{N_{up} + N_{down}} \quad (3.7)$$

is the transverse polarisation (N_{up} : number of spin-up electrons, N_{down} : number of spin-down electrons), P_{max} is the theoretically possible maximum polarisation of 0.924, t the time and τ the time constant of about 40 min at HERA [53, pp. 5-6].

To change the transverse polarisation into longitudinal there were spin rotators installed in front of (and behind) the ZEUS and H1 experiments for HERA-II running (see Figure 3.4) [54]³. They used a combination of horizontal and vertical dipole magnets for rotating the polarisation axis. As they also have depolarisation effects, they were one of the reasons for limiting the achieved maximum to approximately 40-50% of maximum longitudinal polarisation and an average of about 30%.

Polarisation was measured using two independent polarimeters: the longitudinal polarimeter, LPOL, [55] and the transverse polarimeter, TPOL, [56], both indicated in Figure 3.4. Both polarimeters used Compton scattering on the lepton beam of circularly polarised photons, TPOL measuring the spatial asymmetry of the Compton photons and LPOL measuring the energy asymmetries of converted e^+e^- pairs. The error on the polarisation measurement is approximately 4%. [57]

³For HERMES spin rotators had been installed before.

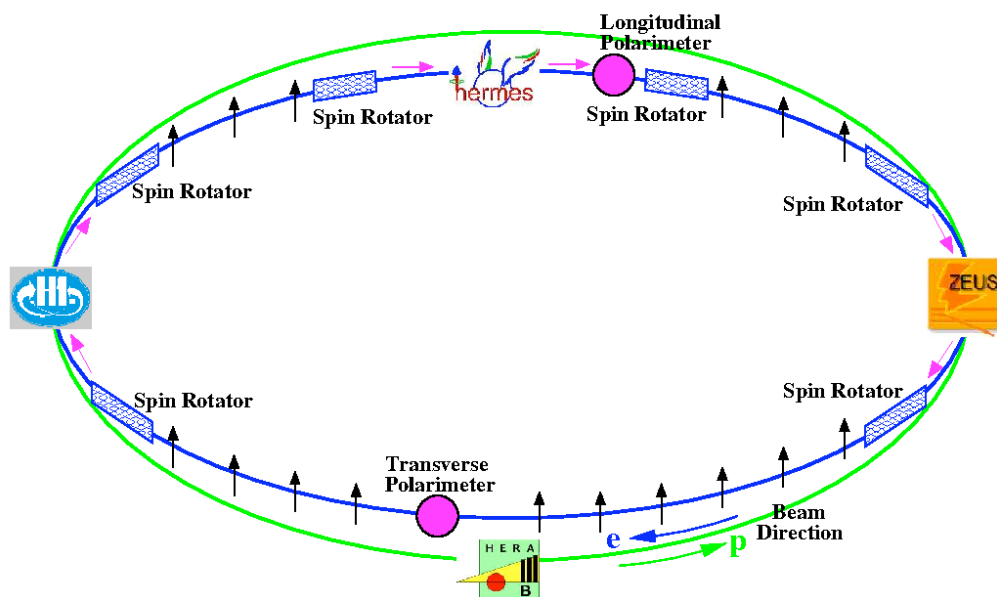


Figure 3.4: Electron spin configuration (indicated by the arrows), spin rotators and polarimeters at HERA. From [53, p. 7].

3.2. The ZEUS Experiment

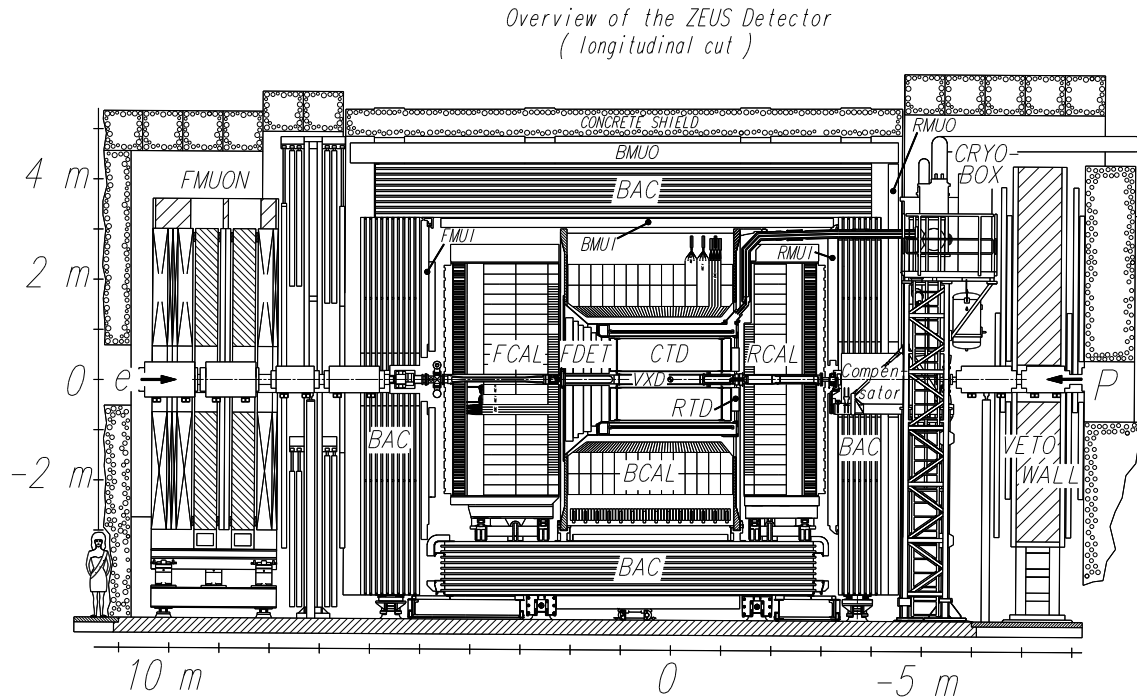


Figure 3.5: Schematic view of the ZEUS detector along the beam direction.

The ZEUS detector [46] was a multi-purpose particle detector designed to measure final state particles in ep -collisions. It has been dismantled in 2008 after the HERA running ended.

Due to the imbalance in the beam energies at HERA⁴, the detector was asymmetric in z -direction as is visible in Figure 3.5.⁵

The main detector components from the interaction point (IP) to the outer detector surface (see Figure 3.6) were the Microvertex Detector (MVD), the Central Tracking Detector (CTD), the Uranium Calorimeter (UCAL) and the muon detectors (Muon Chambers and Backing Calorimeter). Between the CTD and the UCAL there was a super-conducting solenoid producing a magnetic field of 1.43 T. The iron yoke outside the UCAL was used as return path for the magnetic field.

In order to remove background from beam-gas events and secondary collisions there were several detectors to veto such events. The Veto Wall (VETO) and the C5 Counter (C5) were two of these detectors.

The main luminosity monitor was located 104 m away from the detector.

The sub-detectors most relevant to this analysis are described in detail in the following sections.

⁴Due to this imbalance, the forward detector part generally contained more particles of higher average energy than the rear part.

⁵The forward and barrel regions have extra instrumentation compared to the rear region.

Overview of the ZEUS Detector
(cross section)

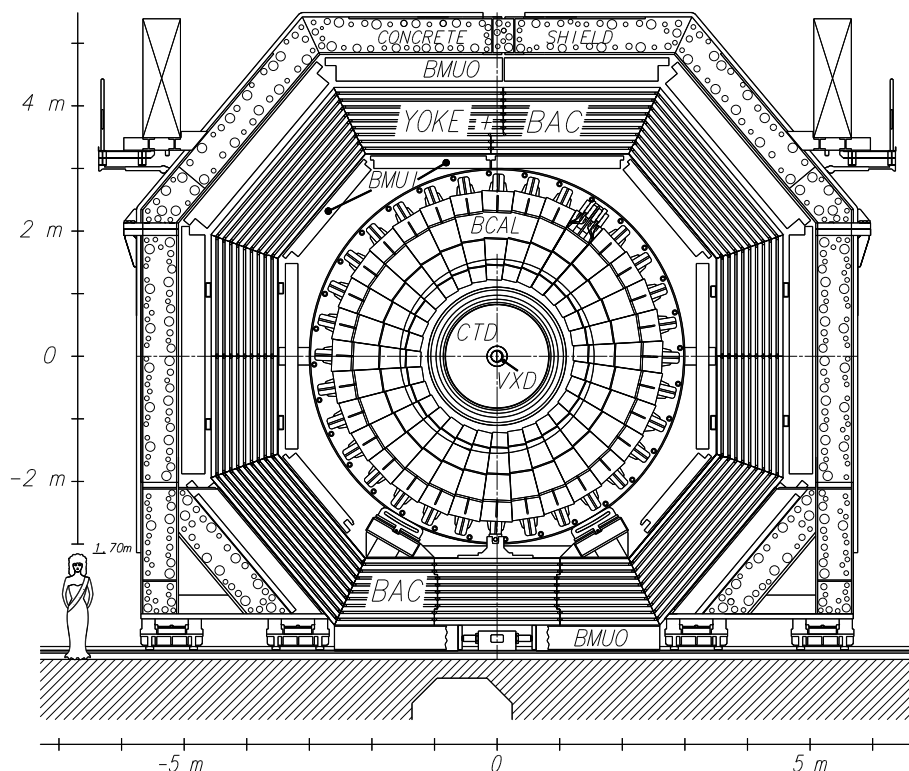


Figure 3.6: Schematic view of the ZEUS detector perpendicular to the beam direction.

3.2.1. Luminosity Measurement

At accelerators, the luminosity is usually determined using a reaction with a well-known cross section. At ZEUS it was measured using the bremsstrahlung process $ep \rightarrow ep\gamma$, for which the cross section is known to the order of 0.5% as it is a pure QED process. Luminosity monitors were used for measuring the event rate of this process by counting photons. For HERA-I the photon detector was a lead-scintillator sandwich calorimeter [58, 59].

To handle the larger luminosity at HERA-II, the luminosity measurement was improved. The two main components at ZEUS for detecting the photons from bremsstrahlung were the luminosity spectrometer SPEC [60] and the photon calorimeter PCAL [61], [62] about 100 m away from the interaction point. Other new components including a 6m-Tagger (≈ 6 m from the IP), which detected scattered electrons from bremsstrahlung, were installed.

The layout of the upgraded ZEUS luminosity system is shown in Figure 3.7. The beam was separated from the photons from bremsstrahlung through a bending magnet. At the exit window approximately 9% of the photons convert into e^+e^- pairs. The SPEC measured these electrons (the e^+ and e^- are separated from the photons and

each other through a magnet), whereas the PCAL measured the showers and positions of the non-converted photons.

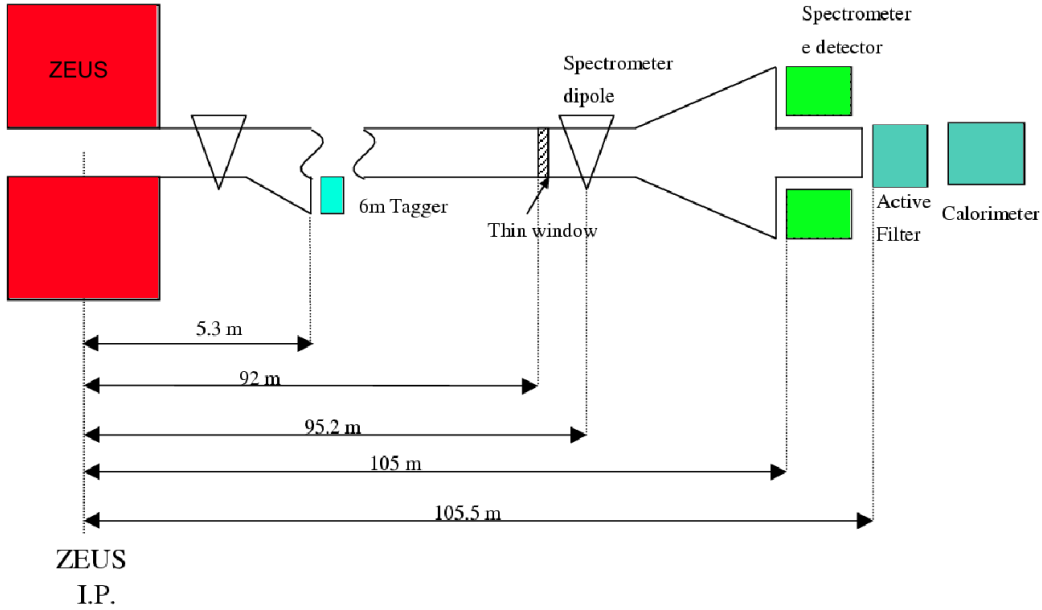


Figure 3.7: The ZEUS system for luminosity measurement during the HERA-II data-taking period.

As the PCAL was more stable and its instantaneous luminosity measurement more precise, luminosity values were taken from the PCAL, but the systematic error⁶ and the normalisation⁷ from the SPEC were used.

More details on the luminosity measurement for the 06/07 e^+p period relevant for this thesis and possible problems are discussed in Section 5.3.2. The achieved precision for the period of the measurement described in this thesis is around 1.8% [63].

3.2.2. Tracking System

The ZEUS tracking system for the HERA-II data-taking period consisted of three detectors: the **M**icro-**V**ertex **D**etector (MVD) [64], the **S**traw-**T**ube **T**racker (STT) and the **C**entral **T**racking **D**etector (CTD) [65]. They were designed to measure the momentum and direction of charged particles with high precision and provide a reconstruction of the event vertex position.

The main tracking device at ZEUS was the CTD, which was a cylindrical drift chamber surrounding the beam pipe at the **I**nteraction **P**oint (IP). As it was inside the magnetic field of 1.43 T from the solenoid, the momenta of charged particles can be reconstructed from the trajectories measured by the CTD. The precise vertex position is reconstructed from the measured particle trajectories. The CTD covered the polar

⁶Because it was better understood, see e.g. [63].

⁷That means that results from the PCAL but multiplied by an average factor of $\frac{\mathcal{L}_{SPEC}}{\mathcal{L}_{PCAL}} \approx 1.01$.

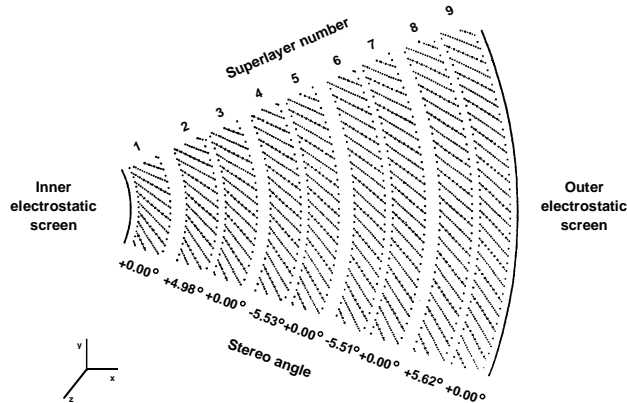


Figure 3.8: One octant of the CTD.

angle region from $11.3^\circ < \theta < 168.2^\circ$ and had full azimuthal coverage.⁸ The CTD extended from an inner radius of 18.2 cm to an outer radius of 79.4 cm, stretching out from $z=-100$ cm to $z=104$ cm. The chamber was filled with a mixture of argon, carbon dioxide and ethane⁹.

The CTD was divided into nine superlayers (counted from inside to outside) and eight octants (see figure 3.8). Each octant consisted of 72 drift cells, each with eight $30 \mu\text{m}$ thick sense wires, leading to the number of 4608 sense wires for the whole CTD. The sense wires were surrounded by the field wires. Odd numbered superlayers had their wires parallel to the z -axis whereas the even numbered ones had their wires tilted by 5° to achieve a z -measurement for the tracks.

When a particle passed through the CTD ionizing the gas mixture, the electrons drifted to the positively charged sense wires and the ionized atoms to the field wires. The drift velocity of the electrons was almost constant over most of the drift cell. Close to the signal wires the number of electrons was amplified by avalanche multiplication. The read-out electronics recorded both the amplitude and the time of the signal. From these measurements the xy -position could be determined with an accuracy of $200 \mu\text{m}$. From the tilted wires a z -resolution of approximately 2 mm could be obtained. Using a fit to all reconstructed tracks, the position of the interaction vertex can be reconstructed with a resolution of about 0.1 cm in x and y and with around 0.4 cm in z .

The nominal resolution of the transverse momentum, p_t , of a particle for vertex-fitted tracks passing a minimum of three superlayers and having a minimal transverse momentum of 170 MeV can be described by [66]:

$$\frac{\sigma(p_t)}{p_t} = 0.0058 \cdot p_t[\text{GeV}] \oplus 0.0065 \oplus \frac{0.0014}{p_t} . \quad (3.8)$$

The first term depends on the CTD hit resolution, while the second and third arise due

⁸The precision at the edge is not as good as for the central region. Results of further studies relevant for the analysis of this thesis are shown in Section 5.9.

⁹The mixing ratio was 85 parts of Ar, 5 parts of CO_2 , 1 part C_2H_6 .

to multiple scattering in material between the interaction point and the CTD.¹⁰

The resolution for a particle with a transverse momentum of 10 GeV is around 6.5% and 3.6% for one with a p_t of 5 GeV.

The CTD can also be used for particle identification by measurements of the mean energy loss $-\frac{dE}{dx}$ of charged particles in the gas of the active volume, which is described by the Bethe-Bloch [67] equation.

The original **VerteX Detector** (VXD) inside the CTD was removed during the 95/96 shutdown due to high voltage problems and synchrotron radiation damage. It was replaced in 2000/01 by the MVD, which was a silicon strip detector having a hit resolution of 20 μm and a track separation better than 200 μm . The tracking system also had additional components in the forward and backward direction: the FTD (Forward Tracking Device) and the STT (replacing the Transition Radiation Detector TRD in 2000) in the forward and the RTD (Rear Tracking Device) in the rear part of the detector.

3.2.3. Calorimeters

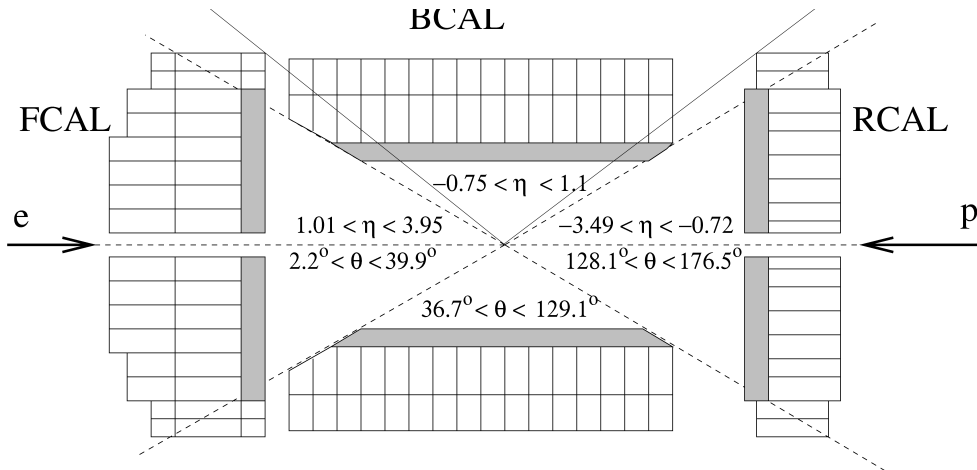


Figure 3.9: Schematic representation of the three sections of the ZEUS Uranium-Scintillator Calorimeter (UCAL).

The high resolution **Uranium-Scintillator CALorimeter** (UCAL) was an almost hermetic calorimeter with a coverage of 99.7% of the 4π solid angle. A schematic view is shown in Figure 3.9. It was a sampling calorimeter using uranium plates for absorption and scintillator layers for optical readout. The 3.3 mm thick depleted uranium plates (98.1% ^{238}U , 0.2% ^{235}U and 1.7% Nb) alternated with the 2.6 mm thick layers of organic scintillator (SCSN-38 polystyrene). The thickness was chosen to achieve a good hadronic energy resolution through the method of *compensation*. That means that nearly equal responses to electromagnetic and hadronic showers were achieved ($\frac{EM_{resp}}{Had_{resp}} = 1.00 \pm 0.02$ in the UCAL). This worked through the specific characteristics of uranium as an absorber for hadronic activity: It provides a high yield of neutrons from spallation which transfer their energy to the hydrogen nuclei (protons - nearly same mass as the neu-

¹⁰ \oplus stands for the quadratic sum.

trons) of the scintillator. This and the photons from neutron capture in the Uranium compensate for energy losses due to nuclear excitations in hadronic cascades, which are not present for electromagnetic cascades from electrons and photons - thus leading to a different response for electromagnetic and hadronic showers in non-compensating sampling calorimeters.

The energy resolution achieved for electromagnetic showers is

$$\frac{\sigma(E_{em})}{E_{em}} = \frac{18\%}{\sqrt{E}} \oplus 2\% . \quad (3.9)$$

And the resolution for hadrons is

$$\frac{\sigma(E_{had})}{E_{had}} = \frac{35\%}{\sqrt{E}} \oplus 1\% . \quad (3.10)$$

The worse resolution for the hadronic showers is due to the fluctuation of the electromagnetic part of the hadronic shower.

In addition to this, for the resolution it is very important to take inactive (dead) material and non-uniformities into account as they influence the energy measurement considerably (see Section 5.8 for details). Pre-samplers, which measured the particle multiplicity in front of the RCAL and the FCAL, were installed to help estimate the inactive material energy loss.

As visible from Figure 3.9 the UCAL is divided into three parts [68–70]:

- the **F**orward **C**ALorimeter (FCAL) at $z = 234.4$ cm covering $\theta = 2.2^\circ$ to 39.9° ,
- the **B**arrel **C**ALorimeter (BCAL) at $R_{in} = 134.5$ cm covering $\theta = 36.7^\circ$ to 129.1° and
- the **R**ear **C**ALorimeter (RCAL) at $z = 162.2$ cm covering $\theta = 128.1^\circ$ to 176.5° ,

Due to the much higher proton energy, more of the energy was deposited in +z than in -z-direction and the thickness of these three parts was different: the FCAL has a depth of around 7 interaction lengths, the BCAL of around 5 and the RCAL of around 4.

Each of these CAL parts was divided into modules and each module was subdivided into one **E**lectro**M**agnetic **C**alorimeter (EMC) section and two **H**Adronic **C**alorimeter (HAC) sections (only one HAC section in the RCAL). As an example this is shown in Figure 3.10 for the FCAL. The sections consisted of cells, which were 20 cm long in x-direction and extended 5 cm (EMC FCAL & EMC BCAL), 10 cm (EMC RCAL) or 20 cm (HAC) in y-direction depending on the calorimeter part. This and some other important characteristics of the different calorimeter parts are summarised in Table 3.2.

After the deposition of energy in the calorimeter the light produced in the scintillator plates of each cell was read out by 2 mm thick **W**ave**L**ength**S**hifters (WLS), which were attached to both sides of the module. Then it was transferred to the **P**hoto **M**ultiplier **T**ubes (PMT) where the light signal was transformed into an electric signal. These

¹¹This is the depth for one of the HCAL sections, so it has to be multiplied by two in case of FCAL and BCAL. Additionally for the whole radiation lengths λ_0 of the UCAL section one also has to take into account the ECAL. This leads then to the above mentioned values of approximately 7 for FCAL, 5 for RCAL and 4 for RCAL.

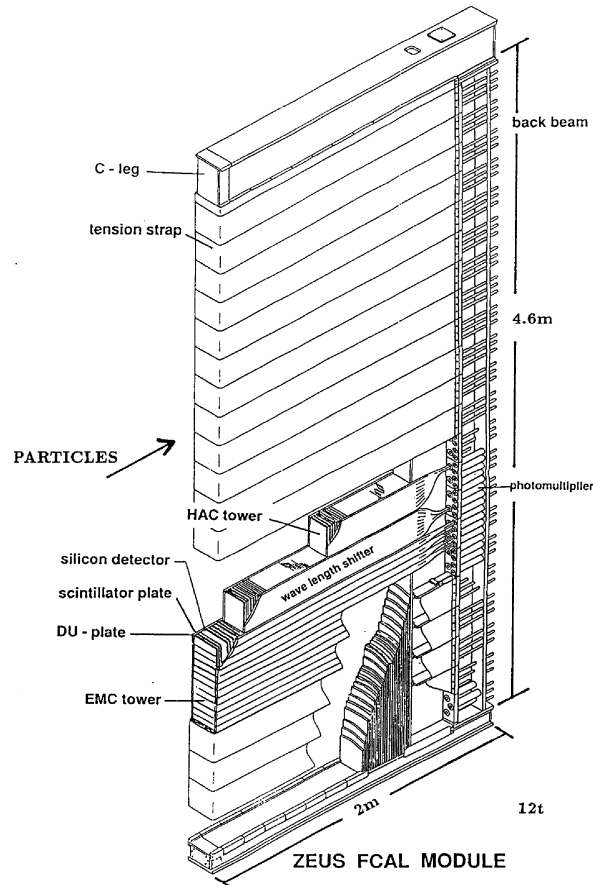


Figure 3.10: FCAL module, which is divided into electromagnetic (EMC) and hadronic (HAC) section.

signals could be used for energy, position and time measurement. The timing was measured with a precision of about 1 ns for a signal with an energy deposition of at least 1 GeV.

3.2.4. Trigger

At HERA the bunch-crossings took place at a rate of about 10 MHz. This exceeded the data storage possibilities by far. Additionally the total interaction rate (any signal in the detector) was dominated by background events (beam-gas collisions, cosmic showers etc). Therefore an efficient and very fast trigger system was required to select ep physics events of interest and reduce the event rate.

At ZEUS a three-level trigger was used. An overview of the trigger and data acquisition system is shown in Figure 3.11.

First Level Trigger The **F**irst **L**evel **T**rigger (FLT) [71] was a hardware trigger designed to reduce the input rate from the 10 MHz of the bunch-crossing to below 1 kHz, which was the design rate of the **S**econd **L**evel **T**rigger (SLT). The data of each bunch

UCAL part	FCAL	BCAL	RCAL
Region	$2.2^\circ < \theta < 39.9^\circ$	$36.7^\circ < \theta < 129.1^\circ$	$128.1^\circ < \theta < 176.5^\circ$
EMC sections	1	1	1
HAC sections	2	2	1
EM depth [X_0]	26	21	26
Had depth ¹¹ [λ_0]	3.1	2.0	3.1
EMC section [cm^2]	20 x 5	20 x 5	20 x 10
HAC section [cm^2]	20 x 20	20 x 20	20 x 20

Table 3.2: Important Parameters of the UCAL Sections.

crossing was stored in a pipe which was 46 events deep. This gave the FLT around $4.4 \mu s$ to decide about the value of the event. For that there were two steps. In the first step each detector component provided its FLT information and sent it to the **Global First Level Trigger** (GFLT). This took around $2.5 \mu s$. Then the GFLT reached a final decision within the left-over $1.9 \mu s$. For the FLT only very general information like track multiplicity¹², muon chamber hits and regional energy sums could be used.¹³

Second Level Trigger Whenever an event was accepted by the FLT it was sent to the SLT, which had more time and information to decide on the event. It had an input rate of approximately 1000 Hz and an output rate of around 50 to 100 Hz. Analogously to the FLT each component had a component SLT which passed the data to the GSLT [72], where the decision about the event was taken. One of the most important information on this trigger level was the timing information from UCAL. Naturally most non- ep background events are off the expected timing and can be filtered out through timing criteria (see Section 6.2).

Third Level Trigger If an event was accepted by the GSLT the complete data of each component was sent to the Event Builder, which combined the data for an event and wrote it into the ADAMO [73] database tables. The combined data was sent to the **Third Level Trigger** [74] (TLT), which was based on the offline reconstruction code and selected special classes of interesting ep events. Unlike the FLT and the SLT the TLT was run on highly configurable computer server clusters. The input rate of the TLT was the 50 to 100 Hz coming from GSLT, whereas the output rate was 3 to 5 Hz.

¹²This is of outermost importance for the track veto efficiency discussed in Section 5.5.

¹³For details on the FLT bits used in this analysis refer to Appendix B.

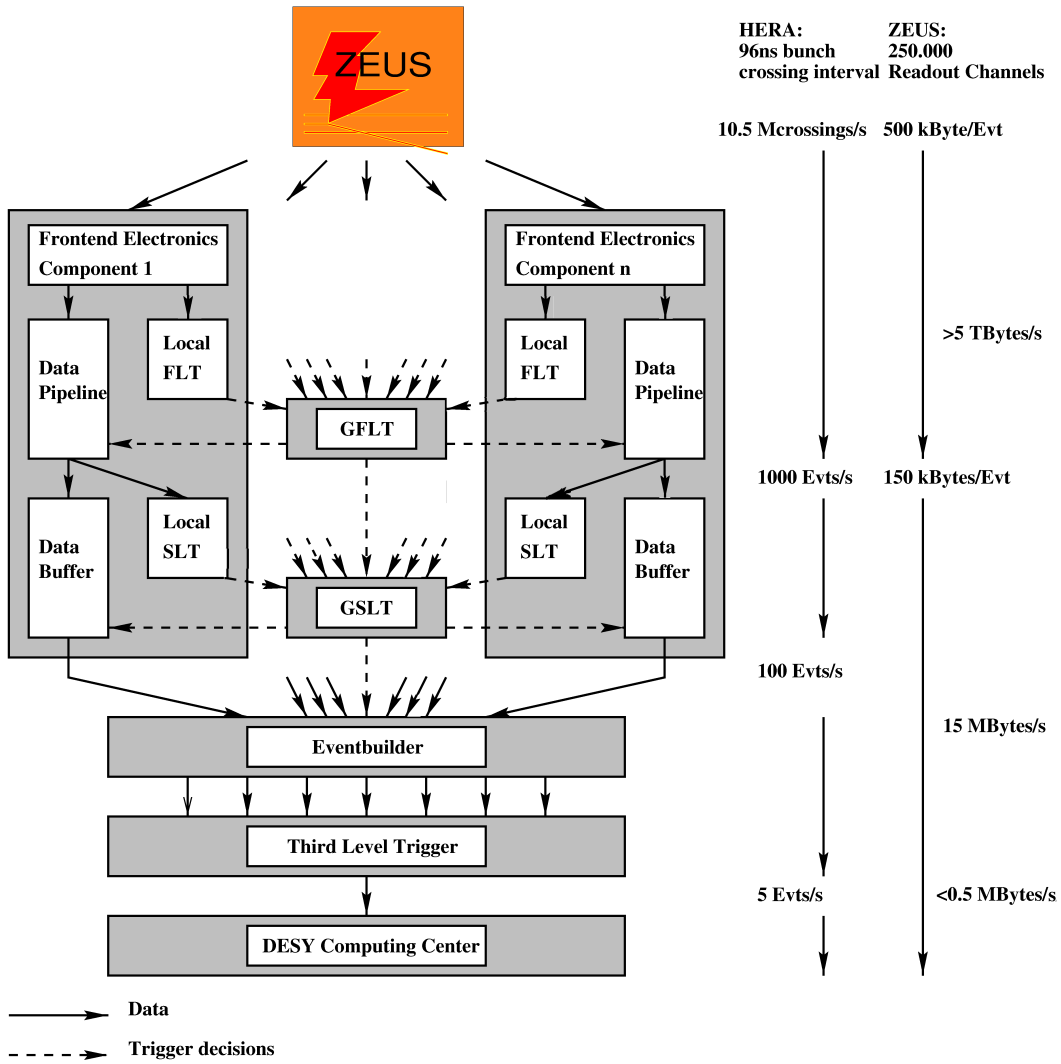


Figure 3.11: Data flow through the three-leveled ZEUS trigger and the data acquisition systems.

4. Event Reconstruction and Simulation

This chapter¹ describes which data and Standard Model Monte Carlo samples were used in the presented analysis and how they were processed before the analysis. This includes a description of the event reconstruction methods and of the first level of detector-related corrections needed for an accurate NC cross section measurement.

4.1. Data Samples

The ZEUS data from 06/07 e^+p -running at nominal proton beam energy of 920 GeV was used for the analysis described in this thesis. This is the last HERA period with full energy.² Only runs with a good data quality³ were used. This data set has an integrated luminosity of 135.5 pb^{-1} , out of which 78.8 pb^{-1} are of positive and 56.7 pb^{-1} of negative polarisation (see Equation 2.40) respectively. The polarisation of the different periods is shown in Figure 4.1. A summary of the integrated luminosity and polarisation values for the different sub-periods is shown in Table 4.1.

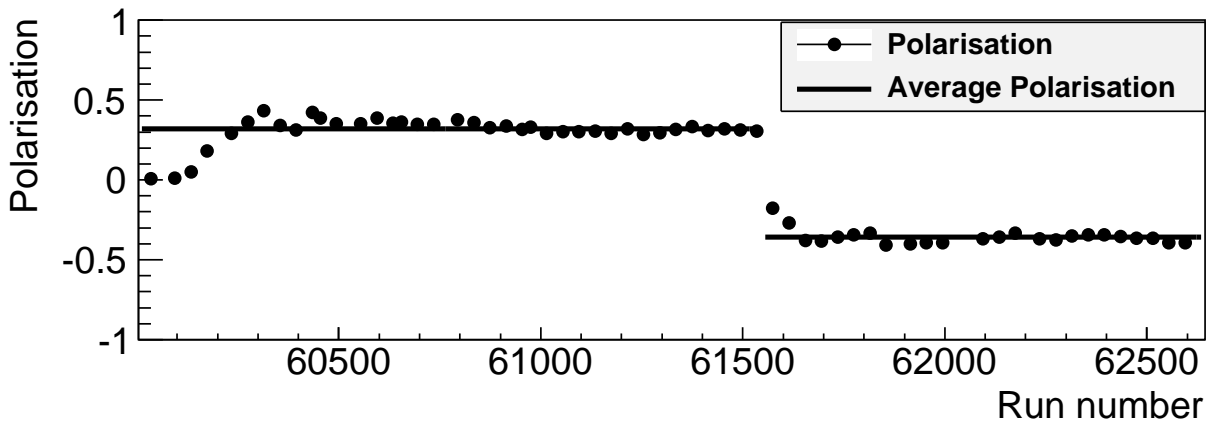


Figure 4.1: The lepton beam polarisation as a function of run intervals (points) and the average polarisation for the right-handed and left-handed period.

The period in the beginning, when the positron beam was positively polarised, is referred to as *RH* (right-handed) period in the following, the later period⁴ with negative

¹Some parts on general event reconstruction, the ZEUS analysis environment and the scattered e^+ reconstruction are taken over from the author's diploma thesis [45].

²The run range is from run 60005 to 62639.

³The exact requirements are described in Section 6.3.4.

⁴from run 61548 onwards

	Luminosity [pb^{-1}]	Polarisation
All	135.5	+3.5%
RH	78.8	+31.8%
LH	56.7	-35.9%
LH1	33.2	-35.5%
LH2	23.5	-36.5%

Table 4.1: Integrated luminosities and average polarisation for each investigated subperiod.

polarisation as *LH* (left-handed) period.

The LH period has been further subdivided into two sub-periods referred to as LH1 and LH2. They are separated by an extended shutdown in early 2007.⁵ This sub-division was proven necessary based on studies from this analysis (see Section 5.3).

4.2. Monte Carlo Generation of Standard Model Events

The main aim of the analysis described here is the NC DIS cross section measurement. For extracting the cross section, the correction of different effects is needed, which are mainly detector- and selection-related. For that purpose (that includes also selection criteria optimisation and background contribution subtraction) an acceptance correction based on Monte Carlo events is used. That means the Standard Model prediction is transformed into a pseudo-data sample mimicking as close as possible what data would look like if the Standard Model would perfectly describe the data. This section explains the generation of Monte Carlo events for Standard Model signal and background. How these samples are treated after the generation is discussed in Section 4.3.

The MC samples are luminosity-weighted to be directly comparable to data. For that

$$w_{\mathcal{L}} = \frac{\mathcal{L}_{data}}{\sum_i \mathcal{L}_{MC}^i} \quad (4.1)$$

is used, where $w_{\mathcal{L}}$ is the weight calculated from the integrated luminosity of data \mathcal{L}_{data} and the sum of the integrated luminosities of all MC samples below the Q^2 of the event \mathcal{L}_{MC}^i .⁶

4.2.1. Signal NC DIS Monte Carlo

In this analysis the main sample of signal NC DIS events were generated with DJANGO 1.6 [75] using PDFs from CTEQ5D [76]. DJANGO is an interface of the programs HERACLES [77] generating the event kinematics and ARIADNE⁷ [78] simulating the parton cascade based on the Colour Dipole Model [79]. Instead of using ARIADNE,

⁵Last physics run before the shutdown was 62003 and first after 62050.

⁶For the photoproduction there is just one sample for resolved and direct photoproduction, so Equation 4.1 becomes $w_{\mathcal{L}} = \frac{\mathcal{L}_{data}}{\mathcal{L}_{MC}}$.

⁷ARIADNE version 4.12 was used.

LEPTO [80], which uses the Matrix Element and Parton Shower (MEPS) approach, can be chosen.⁸ The LUND string fragmentation model from JETSET [81] is used for simulation of hadronisation.

HERACLES does include emission of one photon from the electron⁹, self-energy corrections and all electroweak one-loop corrections. The processes included are depicted in Figure 4.2.

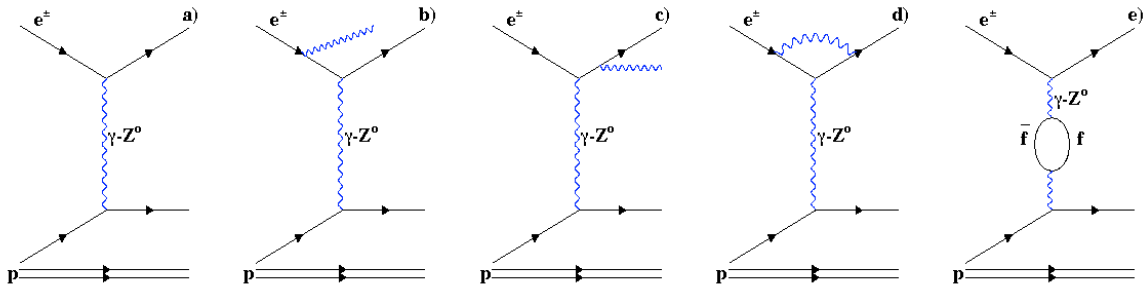


Figure 4.2: Processes included in HERACLES: a) Born-level process, b) initial state radiation, c) final state radiation, d) vertex correction, e) self-energy correction. From [82, p. 59].

DJANGO was set up to include diffractive [83] events.

The main sample of this analysis has about 8 million events and a lower Q^2 -limit of 100 GeV^2 . Additional samples were generated with minimum Q^2 of 400, 1250 and 10000 GeV^2 to keep the statistical uncertainty of MC insignificant across the whole kinematic range of the analysis. The samples are summarised in Table 4.2. As shown, even just the MC sample with $Q^2 > 100 \text{ GeV}^2$ has more than 7 times more statistics (i.e. luminosity and thus approximately events after selection) than the complete data sample. Thus the statistical uncertainty due to MC can be neglected.

minimum Q^2 [GeV^2]	generated events	σ [pb]	Luminosity [pb^{-1}]
100	7999056	8111	986.2
400	1999958	1168	1712
1250	999993	198.1	5047
10000	260000	2.83	91990

Table 4.2: Details of the NC DIS MC samples used in this analysis.

4.2.2. Background Monte Carlo

The main background process for the NC DIS process as shown in previous analyses (e.g. [84], [85], [82], [86]) is photoproduction, the Feynman diagram of which is shown

⁸The effect of this on the cross section measurement is discussed in Section 7.3.

⁹Thus including initial and final state radiation.

in Figure 6.4. Its characteristics are discussed in Section 6.2.

The direct and resolved photoproduction (see Feynman diagrams shown in Figure 6.4) samples were generated by HERWIG [87]¹⁰ using CTEQ4D [88] PDFs. Due to the high photoproduction cross section, the following cut was applied on the generator level: $E_t > 30$ GeV or $p_t > 6$ GeV.

The samples used in the analysis are summarised in Table 4.3. On top of the given luminosity a factor of 1.56 was applied, which was extracted for this sample in a previous study [86, pp. 63-65].

	maximum Q^2 [GeV ²]	generated events	σ [pb]	Luminosity[pb^{-1}]
direct	4	530000	2830	187.28
resolved	4	630000	11900	52.94

Table 4.3: Details of the photoproduction MC samples used in this analysis.

4.3. From Raw Data and MC to Data Tables

Data In order to reconstruct an event fully, the raw data of the TLT-selected events described in Section 3.2.4 are processed using the reconstruction software package ZEPHYR (**Z**Eus **P**Hysics **R**econstruction) [89], which does data calibration and correction (e.g. for dead cells, see Section 4.5), runs the reconstruction codes for the components and then relates the information to each other and reconstructs the event globally. Finally it processes the events through physics filters and writes events passing at least one physics filter to **Data Summary Tapes (DST)**. Information about the physics filters selecting the events is also saved. These are the so-called DST-bits. This is in effect a fourth level trigger and events with a common DST bit can be easily selected saving CPU time.

Monte Carlo For MC events to be comparable to data, there has to be a different approach. The output of the MC event generators consists of a list of the 4-vectors of all final state particles. These enter a simulation of the ZEUS detector that describes the response of all the components and the efficiency of the triggers.

This simulation of the detector is performed by the MOZART [90] [91] package, which is based on GEANT [92]. Trigger simulation is done by the ZGANA (**Z**eus **G**eant **A**nalysis) package [90] [93] with the same trigger logic as for the real data. Afterwards the response of the detector to the passage of the individual particles is simulated, for which an identical reconstruction code as for data is used (ZEPHYR). Hence, the output is given in the same format as for the data, allowing a direct comparison between MC and data. In addition, information about the generated particles is saved.

The ZEUS detector and trigger simulations as well as the ZEUS reconstruction program for MC are done using the ZEUS Monte Carlo production facility FUNNEL [94]. For the analysis described in this thesis funnel version num07t3.6 was utilised.

¹⁰HERWIG version 5.9 was used.

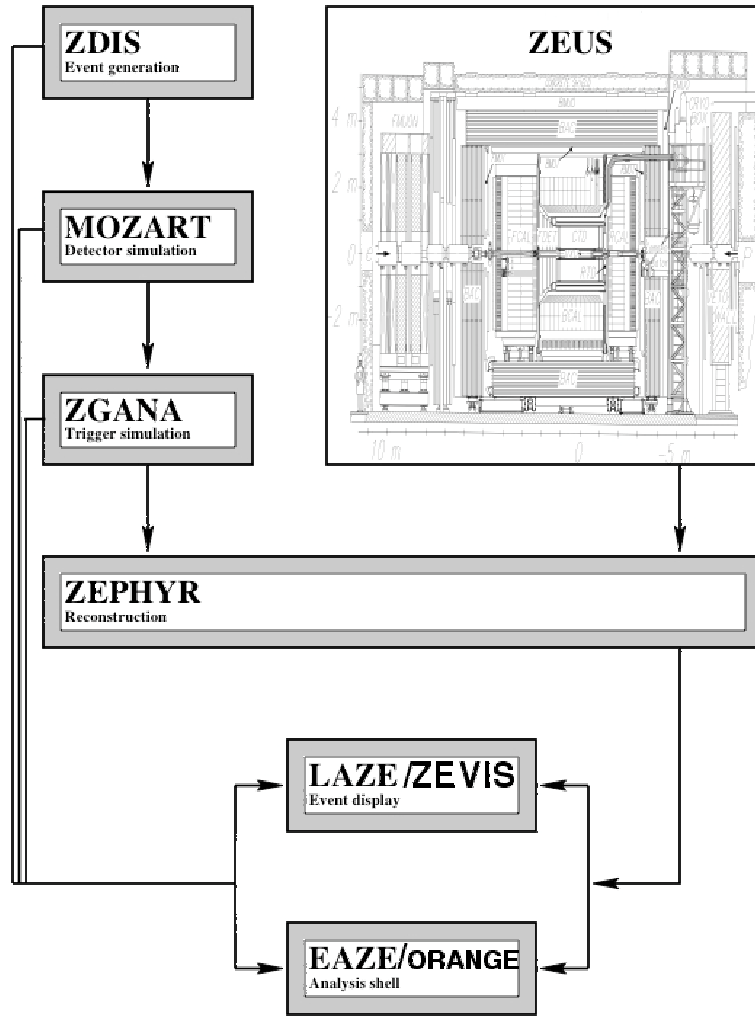


Figure 4.3: Diagram of the ZEUS offline and MC simulation programs.

4.4. ZEUS Analysis Environment

The data and MC from the ADAMO tables can be analysed using either an ORANGE job or an EAZE job and analysis code in C^{++} or FORTRAN¹¹.

In this analysis the software package ORANGE (**O**verlying **R**outine for **A**nalysis **N**tuple **G**eneration) [95,96] is used to analyse the real data (as well as MC) of the ZEUS experiment. It contains the basic techniques and methods to perform standard parts of a physics analysis which are common for many research projects and creates Ntuples with specific variables appropriate for an analysis. The subroutines of the ORANGE and related PHANTOM libraries can be adjusted and variables selected for the specific requirements of each analysis. With data preservation and easy access to the data becoming more and more important for ZEUS, the Common Ntuple project has been developed, where ORANGE Ntuples suitable for an as-broad-as-possible range of anal-

¹¹EAZE jobs and FORTRAN have been extensively used in the past, but are hardly used nowadays.

yses are produced and can be used for analysis now and in the future. The analysis presented here was done on analysis Ntuples from ORANGE created specifically for this analysis, but was compared to a Common Ntuple analyses [97].

Offline selection of detector data as well as of simulated events is based on ROOT [98] using C⁺⁺-code in the analysis described here.

Additionally the event display ZEVIS (**Z**eus **E**vent **V**ISualization)¹² [100] can give a visual impression of what a specific event "looks like" in the detector. Sometimes checking peculiar events by eye-scanning is still of advantage.¹³

A flow-diagram of the processing of ZEUS data and simulated events is shown in Figure 4.3.

4.5. Calorimeter Pre-corrections

Before reconstruction of the event the calorimeter information should be pre-processed removing fake signals due to noise and aligning the calorimeter with respect to the CTD.

Noise Sources for noise in the calorimeter can be faulty photomultipliers or electronics, photomultiplier sparks and the inherent uranium radioactivity of UCAL.

The **radioactivity noise** was suppressed by requiring a minimum energy in the cells and the threshold is increased if surrounding cells have no energy deposited.

Photomultiplier sparks are a spontaneous discharge of photomultiplier tubes faking a large energy deposit. The second photomultiplier tube of the same cell is not affected by that and the energy balance of the two photomultiplier tubes can be used for rejection of the sparks.

Noisy and dead cells were found looking at their long-term behaviour and corrected for.

The energy scale of the three calorimeter parts (RCAL, BCAL, FCAL) was pre-corrected on a cell-by-cell basis for the EMC section of RCAL and by an overall correction factor for the other UCAL parts.

Alignment The CTD is used as frame-of-reference for alignment at ZEUS. For a good-quality reconstruction the position of the calorimeter with regard to the CTD needs to be known very precisely as e.g the match of the track and a calorimeter cluster of an electron depends on it.

The positions were measured by optical survey during shutdowns and checked and refined using NC event electrons. The principle in using NC DIS events was comparing the positions of the scattered electron using track position information from CTD and cluster position information from calorimeter.

The precision reached for the data period of this analysis was about 1 mm and 1 mrad for RCAL and BCAL and about 2 mm for FCAL. [86, p. 43]

¹²LAZE (**L**ogical **A**ccess to **Z**EOS **E**vents) [99] is an older ZEUS event display.

¹³This is especially the case for halo muons and cosmic muons, as there is no MC generated for these background events.

4.6. Track and Vertex Reconstruction

The tracks of each event are reconstructed based on the hit information from the CTD and the MVD (and STT for the forward tracks). The **R**igorous **T**rack **F**it method (RTFIT) [101] is used for the track reconstruction. Within this method a weight is assigned to each hit depending on the component it originated from. The weight is based on the component's resolution. The track fit itself is based on the Kalman filter technique [102].

The vertex position was determined by extrapolation of the reconstructed tracks.¹⁴

4.7. Scattered e^+ Reconstruction

For the analysis described here the identification of the scattered electron, on which the event selection and kinematic reconstruction is based, is most important. Electron candidates are characterised by a localized energy deposit in the electromagnetic part of the calorimeter with no or little energy leakage into the hadronic part and usually a track pointing towards it. Hadronic showers are on average transversally much broader and longitudinally much deeper. In addition the scattered electrons should be well separated from the hadronic system.

Extensive studies were done on the topic of electron identification and two sophisticated algorithms have been developed at ZEUS to identify electrons and to quantify their quality: EM [103] and Sinistra [104].

Both work in a similar way, but Sinistra is optimized for lower Q^2 , i.e. for the rear region, whereas EM is better suited for FCAL/BCAL¹⁵ with high Q^2 than Sinistra. A detailed comparison of the finders can be found in [105]. In this analysis EM is used.

4.7.1. EM Finder

EM calculates many different sub-probabilities for each calorimeter cluster (e.g. for the calorimeter shape of the electron) to calculate the likelihood of the cluster to be an electron. These sub-probabilities are then combined to the so-called *Grand Probability*. The seven sub-probabilities are based on:

1. The fraction of the energy in the HAC layers.
2. The fraction of the EMC energy outside the highest energy cell strip pair.
3. The fraction of the energy in the highest energy module pair.
4. The energy not associated to the candidate in an $\eta\phi$ -cone of radius 0.8.
5. The difference of the polar angle θ for the calorimeter cluster and the track.
6. The difference of the azimuthal angle ϕ for the calorimeter cluster and the track.

¹⁴Also possible secondary vertices were reconstructed.

¹⁵EM is optimized for BCAL and FCAL separately for avoiding problems due to the crack between the two.

7. $\frac{1}{E} - \frac{1}{P_{trk}}$, where E is the energy from calorimeter and P_{trk} the momentum from the track.

As 1-4 are calorimeter variables and 5-7 include tracking, the last three sub-probabilities can only be calculated, if a track is matched to the calorimeter cluster. The distributions of the subprobabilities are shown in Figure 4.4 for the selected scattered positrons of the NC DIS sample of this analysis.

From all available N sub-probabilities the Grand Probability is calculated using following formula:

$$P_{Grand} = P \sum_{k=0}^{N-1} \frac{(-\log P)^k}{k!}, \quad (4.2)$$

where P is the product of the sub-probabilities: $P = \prod_{i=1}^{N-1} p_i$. If no track is matched, but the electron is found in the CTD acceptance region ($0.3 < \theta < 2.85$), the probability is reduced by a suppression factor.

As the Grand Probability is a kind of multiplication of several probabilities below 1, any value above 0.001 still corresponds to a good electron candidate.

The EM Calorimeter Probability is calculated in the same way, but only taking into account the calorimeter variables (1-4), even if a track is associated to the candidate.

The Selection Probability P_{Sel} of the EM finder is a tool to find a candidate with not only a high probability to be an electron, but to be the scattered electron. It is calculated as

$$P_{Sel} = P_{Grand} \cdot \frac{1}{Q^4} \cdot P_{pt}, \quad (4.3)$$

where P_{pt} is the probability calculated that it is not a fake scattered electron with another candidate with high transverse momentum being the correct one ($P_{pt}=1$, if there is no other candidate).¹⁶ The term $\frac{1}{Q^4}$ comes from the DIS cross section and suppresses candidates with a Q^2 that is higher, as events with higher Q^2 happen less often and thus the probability of that electron to be the DIS electron is lower. The EM electron candidates are ordered according to their Selection Probability.

4.8. Reconstruction of Hadronic Final State

The hadronic final state (HFS) is reconstructed from all anergy deposits (and tracks) except for the ones associated with the scattered electron.

¹⁶ P_{pt} is

1. 1, if there is no other electron candidate;
2. based on the p_t of the candidate p_t^{true} and the p_t of the candidate with the second highest p_t (then taken as p_t^{fake}), if the candidate is the one with the highest p_t ;
3. based on the p_t of the candidate p_t^{true} and the p_t of the candidate with the highest p_t (then taken as p_t^{fake}), if the candidate is not the one with the highest p_t .

In the second and third case the value of P_{pt} is calculated using a formula depending on the bin of p_t^{true} and $r(p_t^{fake}, p_t^{true}) = \log\left(\frac{p_t^{fake}}{\sqrt{(p_t^{true})^2 + 1}}\right)$. This formula is of the form $A \cdot e^{(-B \cdot (r(p_t^{fake}, p_t^{true}) + C))^D}$, where the parameters A , B , C and D depend on the bin.

For the analysis described in this thesis the CorAndCut [106] algorithm was used for the reconstruction of the HFS. CorAndCut uses calorimeter and vertex information. It calculates the angle of the clustered calorimeter energies as an energy-weighted mean. CorAndCut suppresses bias from the "backsplash" (energy deposits, which are not from the ep interaction point and are mostly due to back scattering from the calorimeter)¹⁷. Thus CorAndCut improves the measurement of γ_{had} , which is important for the reconstruction of kinematic variables in this analysis. In addition CorAndCut includes energy corrections leading to an agreement of data and MC simulation on a few percent level.

4.9. Reconstruction of Kinematic Variables

The kinematic variables of the events must be accurately reconstructed in order to measure the cross sections precisely. The main kinematic variables of DIS are Q^2 , x and y (see Section 2.1.1). They are related through Equation 2.6, $Q^2 = xys$, and the squared centre-of-mass energy s is known. Therefore, two measured variables are sufficient to reconstruct Q^2 , x and y . In this section different methods to reconstruct the event kinematically are described. They differ in the choice of measured variables used for reconstruction, and are employed to correct for various detector effects.

They are all based on the four-vectors of the electron and the hadronic system after the scattering (k' and p') as well as the knowledge about the four-vectors of the beam electron and proton (k and p) and momentum and energy conservation. The four-vectors are¹⁸

$$k = \begin{pmatrix} E_e \\ 0 \\ 0 \\ -E_e \end{pmatrix}, \quad k' = \begin{pmatrix} E'_e \\ E'_e \sin(\theta_e) \cos(\phi_e) \\ E'_e \sin(\theta_e) \sin(\phi_e) \\ E'_e \cos(\theta_e) \end{pmatrix}, \quad p = \begin{pmatrix} E_p \\ 0 \\ 0 \\ E_p \end{pmatrix}, \quad p' = \begin{pmatrix} E_{had} \\ E'_{had} \sin(\gamma_{had}) \cos(\phi_{had}) \\ E'_{had} \sin(\gamma_{had}) \sin(\phi_{had}) \\ E'_{had} \cos(\gamma_{had}) \end{pmatrix}, \quad (4.4)$$

where E_e is the energy of the incoming electron and E'_e the energy, θ_e the polar angle and ϕ_e the azimuthal angle of the scattered electron. E_p is the proton beam energy and E_{had} , γ_{had} and ϕ_{had} are the energy, polar and azimuthal angle of the hadronic system respectively. Additional useful observable quantities are the transverse momenta of electron and hadronic system p_t^e and p_t^{had} and the difference of the energy and longitudinal momentum component $E - p_z$.¹⁹

4.9.1. Electron Method

In the Electron Method the measurements of the energy and the polar angle of the scattered electron are used for the reconstruction of the kinematic variables²⁰:

$$Q_{el}^2 = 2E_e E'_e (1 + \cos(\theta_e)), \quad (4.5)$$

¹⁷For HERA-II study and update see [85, 65-68].

¹⁸The masses are neglected.

¹⁹In Section 6.1 the importance of $E - p_z$ for the NC DIS measurement is explained.

²⁰The equations assume no initial and final state radiation.

$$x_{el} = \frac{E_e}{E_p} \cdot \frac{E'_e(1 + \cos(\theta_e))}{2E_e - E'_e(1 - \cos(\theta_e))} , \quad (4.6)$$

$$y_{el} = 1 - \frac{E'_e}{2E_e}(1 - \cos(\theta_e)) . \quad (4.7)$$

The Electron Method is well suited for high-y measurements, at small y the resolution in x is not sufficient.

4.9.2. Jacquet-Blondel Method

In the Jacquet-Blondel Method the measurements of the energy and the polar angle of the hadronic system are used for the reconstruction of the kinematic variables:

$$Q_{JB}^2 = \frac{(p_t^{had})^2}{1 - \frac{(E-p_z)_{had}}{2E_e}} = \frac{(p_t^{had})^2}{1 - y_{JB}} , \quad (4.8)$$

$$x_{JB} = \frac{\frac{(p_t^{had})^2}{1 - \frac{(E-p_z)_{had}}{2E_e}}}{s \cdot \frac{(E-p_z)_{had}}{2E_e}} = \frac{Q_{JB}^2}{s \cdot y_{JB}} , \quad (4.9)$$

$$y_{JB} = \frac{(E - p_z)_{had}}{2E_e} . \quad (4.10)$$

At low y and low Q^2 this method is less reliable due to low hadronic energy in the detector. The Jacquet-Blondel Method is used for the reconstruction of CC DIS events, where the scattered neutrino is not detected.

4.9.3. Double-Angle Method

The Double-Angle Method combines information from the scattered electron and the hadronic final state and uses the angles of the electron and the hadronic system for the reconstruction of the kinematic variables:

$$Q_{DA}^2 = E_e^2 \frac{\sin(\gamma_{had})(1 + \cos(\theta_e))}{\sin(\gamma_{had}) + \sin(\theta_e) - \sin(\gamma_{had} + \theta_e)} , \quad (4.11)$$

$$x_{DA} = \frac{E_e}{E_p} \cdot \frac{\sin(\gamma_{had}) + \sin(\theta_e) + \sin(\gamma_{had} + \theta_e)}{\sin(\gamma_{had}) + \sin(\theta_e) - \sin(\gamma_{had} + \theta_e)} , \quad (4.12)$$

$$y_{DA} = \frac{\sin(\theta_e)(1 - \cos(\gamma_{had}))}{\sin(\gamma_{had}) + \sin(\theta_e) - \sin(\gamma_{had} + \theta_e)} . \quad (4.13)$$

The major advantage of the Double-Angle Method is that it does not depend on the absolute calorimeter energy measurement in the detector, so it is almost insensitive to the calorimeter energy scale and its uncertainty. It has been shown that the Double-Angle Method is the best-suited two-variable method (i.e. all described methods except for Kinematic Fitting) for the kinematic region of this analysis [107], [85, pp. 49-54] and therefore it is used as main method for reconstruction of the kinematic variables

in this thesis.²¹

4.9.4. Kinematic Fitting

In Kinematic Fitting [108] the energy and angle of the scattered electron and the hadronic system are used. As all available information is taken into account, improvement of the precision of the measurement is expected. In addition, this method gives the possibility to extract the energy of an initial-state-radiation photon, E_γ . At HERA it has recently been tested for high-x NC DIS analysis [109] and will be explained in more detail in [110].

The aim of the fit is to get the set of x , y and E_γ ($\lambda = (x, y, E_\gamma)$) values with the highest probability. For that, during the fit λ -points are supplied and from it the values $D = (E'_e, \theta_e, E_{had}, \gamma_{had})$ are calculated and compared to the measured values D_{meas} . Then the probability for λ to be true if D_{meas} is measured $P(\lambda|D)$, is calculated according to Bayes' theorem:

$$P(\lambda|D) \propto P(D|\lambda) \cdot Q(\lambda) . \quad (4.14)$$

$P(D|\lambda)$ (the likelihood to measure D, if λ is the true value) and $Q(\lambda)$, the prior for λ ²², need to be supplied.

Finding $P(D|\lambda)$ is the central point of the Kinematic Fitting Method. In the simplest case it is a Gaussian distribution centered at the true values for all measured variables.

At ZEUS the λ of the highest probability was calculated using BAT [111].

Resolution for very high x (greater than 0.1) is shown to be better for Kinematic Fitting [109], but for the phase space of the analysis described in this thesis the reconstruction using the Double-Angle Method is of about the same quality as using Kinematic Fitting.

²¹The resolution of the Double-Angle Method worsens for small values of either angle, but that is not a severe problem for the presented analysis.

²²In case of the high-x NC DIS analysis [109] $Q(\lambda) = (1-x)^5 \cdot \frac{1+(1-\frac{E_\gamma}{E_e})^2}{y^2 x^2 \frac{E_\gamma}{E_e}}$ was used, but the dependence on the choice of prior was shown to be small.

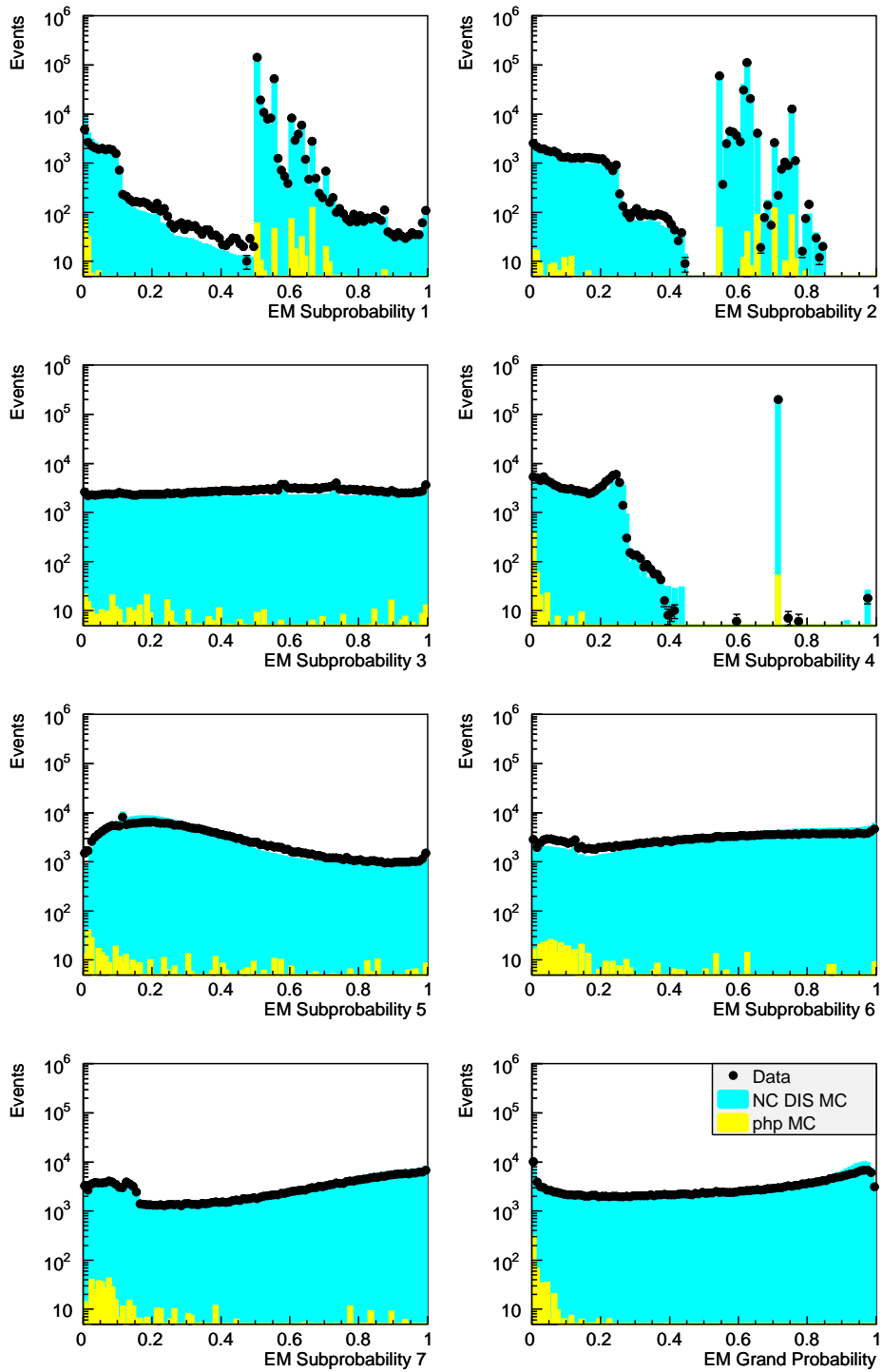


Figure 4.4: Control distribution of the EM subprobabilities (explained in Section 4.7.1) and the EM Grand Probability for data (black data points) compared to NC DIS MC (cyan histograms) and the php background from MC (yellow histogram). The selection is the one described in Chapter 6.

5. Corrections Applied to the Data and MC Samples

Even though the event kinematics are already well-reconstructed and the Standard Model Monte Carlo describes the distributions reasonably after the procedures described in Chapter 4, for the high-statistics and high-precision measurement of NC DIS described in this thesis an improvement is highly desirable. Therefore additional studies were done and corrections were developed to improve the understanding of the samples, the precision of the reconstructed variables and the description of data by the Monte Carlo simulation. As for the extraction of cross sections the acceptance correction is required (which is extracted from the MC prediction) this description is vital for a precise measurement.

The studies described in this chapter were done with NC DIS events selected with a similar selection as the one described in Chapter 6.

5.1. F_L Correction

The cross section for NC DIS does depend on the longitudinal structure function F_L (see Section 2.4). For this high- Q^2 analysis the influence of F_L is rather small compared to the influence from \tilde{F}_3 and especially \tilde{F}_2 , but it cannot be completely neglected. From Equation 2.27 it is easily visible that the main influence of F_L is for high values of the inelasticity y . The influence of F_L for NC DIS at HERA is for example discussed in [112, pp. 79-82], where it is quoted as up to 10% at high y and small x .

The MC used in this analysis has F_L set to 0. The reason is that for unfolding cross sections from HECTOR [113] were used, where F_L is set to 0, so that for cancellation reasons the MC needs to have $F_L = 0$ as well (see Section 7.2).

It follows that for obtaining a good description of the data by MC (i.e. for the control plots mainly) a correction is needed to take F_L into account. For that purpose the MC is reweighted in bins of simulated x and Q^2 using a factor extracted from dividing a prediction of CTEQ5D with (σ_{F_L}) and without (σ_0) F_L in each bin [114] [115]:

$$w_{F_L} = \frac{\sigma_{F_L}}{\sigma_0} . \quad (5.1)$$

The result is the reweighting factor w_{F_L} used for the distribution comparison only.¹ The effect is especially visible in y and related variables and is illustrated in Plot 5.1, where the influence and better description of the data at high y after inclusion of F_L is visible. The overall effect on normalisation of this correction is 1% for the investigated sample.

¹All other corrections are applied both for distribution comparison and acceptance correction.

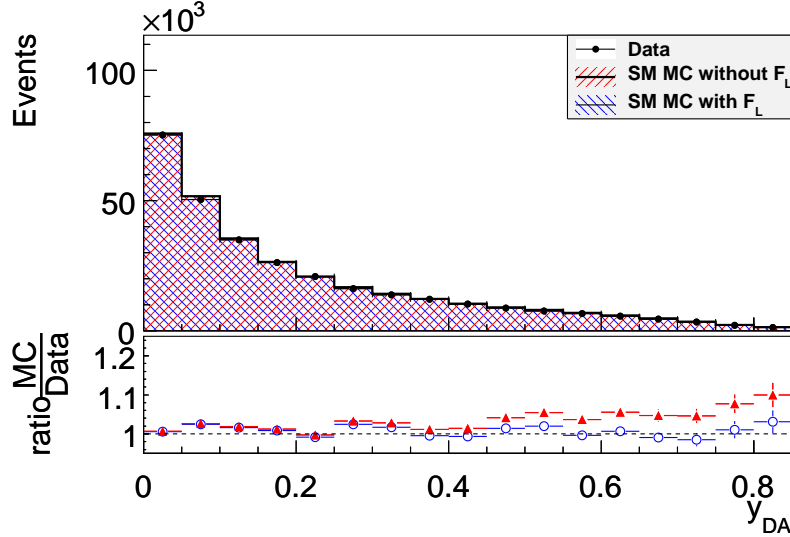


Figure 5.1: Distribution of y_{DA} with data (black data points) and SM MC (NC and php) with (blue hashed histogram) and without (red hashed histogram) F_L included. In addition the ratio of data and MC is shown in the lower part of the plot: red filled triangles for the SM predictions without and blue open circles for the predictions with F_L .

5.2. Polarisation Correction

As the NC DIS MC used (see Section 4.2.1) does not include polarisation, a correction was needed to take into account the effects of the positron beam polarisation. For that HECTOR interfaced to BASES [113,116] was used: Integrated cross sections were predicted for bins in Q^2 without polarisation (σ_{unpol}) and with the average polarisation (σ_{pol}) for the data period. In each bin a correction factor w_p was calculated by dividing the two and this factor was applied to the MC events generated with a Q^2 value within this bin:

$$w_p = \frac{\sigma_{pol}}{\sigma_{unpol}} . \quad (5.2)$$

The influence on the total number of events is about 1% upwards for RH and 1% downwards for LH data. In the lowest Q^2 bins (of the cross section) the influence is of the order of half a percent, in the highest bins of the order of 10%.

5.3. Different Running Periods

In Section 4.1 it was already mentioned that there is a sub-division of the LH period. The decision to divide the samples originates from observed differences regarding the events per integrated luminosity (called rate in this section) of NC events within the sub-periods: Looking at the rates of NC events the drop of event numbers going from the RH to the LH period can be clearly seen (see Figure 5.2). In addition there is a

drop after the shutdown in early 2007².

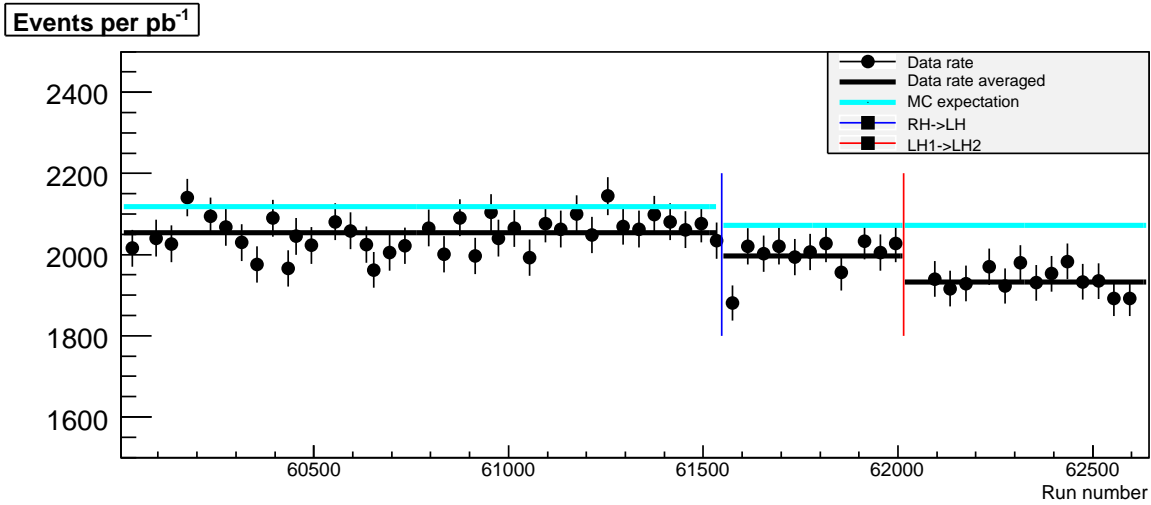


Figure 5.2: The rate (events per integrated luminosity) of NC events in the final sample (black points, bar is error on luminosity measurement) compared to the expectation of the Standard Model. The blue line indicates the switch of polarisation from RH to LH, the red line the shutdown in early 2007. Here the MC prediction only includes the polarisation correction and selection is without the loosened cut on track requirement.

Whereas a rate drop is expected from the RH period compared to the LH period due to polarisation effects (see MC prediction in the Figure), there is no obvious explanation for the difference between the LH1³ and the LH2⁴ period.

Subdividing the LH period into LH1 and LH2 is thus motivated by three reasons:

- The rate difference between the two sub-periods
- The fact that there was the extended shutdown between these runs, which might have affected detector conditions [117]
- The differences in distributions as shown in this section

The following possible reasons were investigated to account for the rate drop and are finally able to explain it reasonably well:

1. General trigger inefficiencies and problems with trigger variables (see Section 5.4)
2. Track Veto Efficiency (see Section 5.5)
3. Track Matching Efficiency (see Section 5.9)
4. Differences in the Z_{vtx} distribution (see Section 5.7)
5. Problems with the luminosity measurement (see Section 5.3.2)

²The last physics run before the shutdown was 62003 and the first after 62050.

³Runs from 61548 to 62003

⁴Runs from 62050 till 62639

5.3.1. Comparison of Variables

The distributions of all variables on which cuts were applied and of some important other variables were compared between the LH1 and the LH2 data period (and RH for cross check). Mostly the difference of the shape of the variable distributions between LH1 and LH2 was about the same size (or less) as the difference between RH and LH1, so a usual fluctuation related not only to statistics, but also due to minor detector changes (changes with time and due to shutdowns)⁵. As an example, the plot for the comparison of the positron angle ϕ is shown in Figure 5.3. The only significant differences found were in the tracking variables (see Figure 5.4) and the Z_{vtx} (see Figure 5.5) distributions.

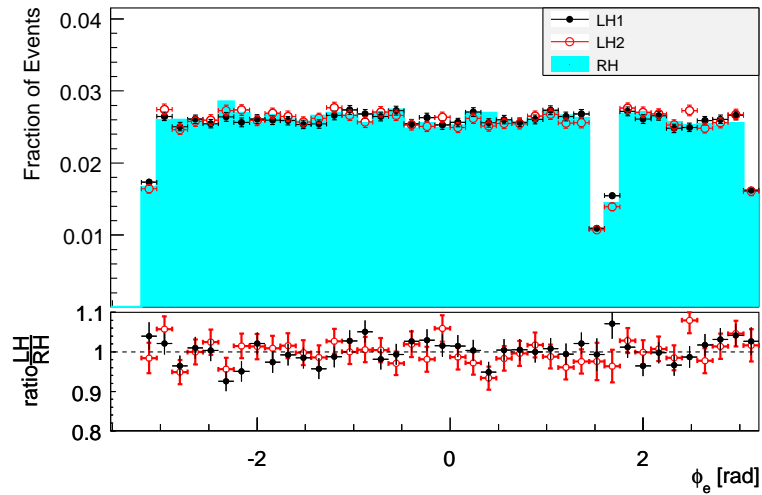


Figure 5.3: Distribution of the angle ϕ of the positron for the different data periods RH (cyan histograms), LH1 (red data points) and LH2 (black filled data points). In the lower part of the plot the ratio of the two LH periods and the RH period is shown (LH1/RH (red data points) and LH2/RH (black filled data points)).

The tracking variables seem to indicate that the tracking was somehow worse for LH2 compared to LH1. The tracks being reconstructed by few superlayers are more, the ones with more superlayers are less.⁶ This supports strongly the described need to do corrections for tracking and to do them separately for LH1 and LH2. This difference is as much as possible resolved by the sub-period dependent TVE and TME corrections described in Sections 5.5 and 5.9.

The Z_{vtx} distribution of LH2 period shows that there are more satellite and less nominal events. This proves the point of doing the Z_{vtx} -reweighting for the periods separately, which makes MC mimic this behaviour and thus resolves the problem. This procedure is described in Section 5.7.

⁵Comparing RH to LH one needs to be very careful though as the polarisation effects come into play. So the normalisation is different and in many cases also the shape of the distribution of the variable. The polarisation of LH1 and LH2 is within the error of the polarisation measurement the same (see Table 4.1).

⁶It should be mentioned that the plot shows the fraction of selected events, not the number of events.

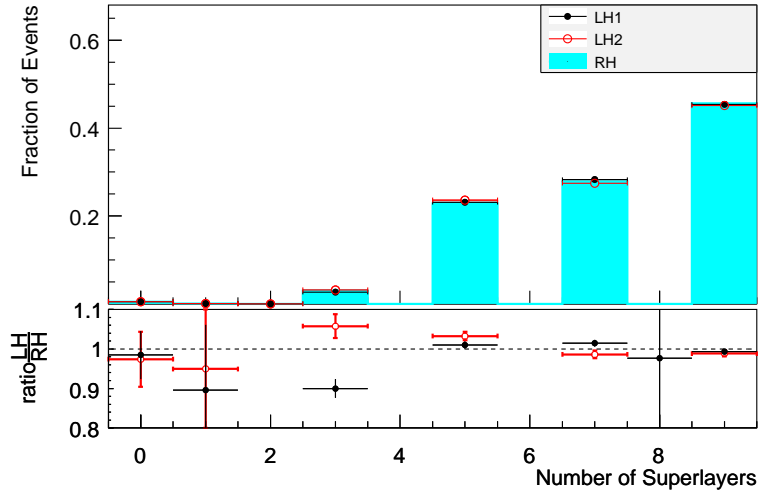


Figure 5.4: Distribution of the number of superlayers detecting the track associated with the positron for the different data periods RH (cyan histograms), LH1 (red data points) and LH2 (black filled data points). In the lower part of the plot the ratio of the two LH periods and the RH period is shown (LH1/RH (red data points) and LH2/RH (black filled data points)).

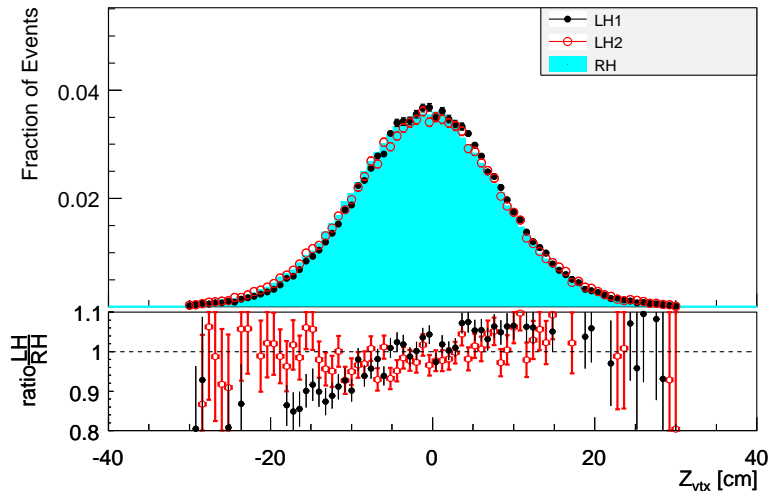


Figure 5.5: Distribution of the longitudinal vertex position (in cm) for the different data periods RH (cyan histograms), LH1 (red data points) and LH2 (black filled data points). In the lower part of the plot the ratio of the two LH periods and the RH period is shown (LH1/RH (red data points) and LH2/RH (black filled data points)).

5.3.2. Rates and Luminosity Measurement

A drop of the event rate (events per integrated luminosity) could also be caused by a mis-measurement of the luminosity (see Equation 3.5). After all corrections it is about the size (1%) that luminosity measurement could vary between periods⁷ [118]. As the MC is reweighted according to luminosity, the event numbers from MC scale linearly with the luminosity, so that difference could be explained by luminosity mismeasurement.⁸

For run-dependent luminosity measurements (see descriptions in Section 3.2.1) values from PCAL are used, which are rescaled by 1% based on the longterm ratio of $\frac{\mathcal{L}_{SPEC}}{\mathcal{L}_{PCAL}}$. PCAL uses for its acceptance calculation the beam widths measured by SPEC, as they are more precise. For the run period in question (LH2), SPEC was offline for a considerable time (see Figure 5.6) and for PCAL luminosity calculation average values from other periods were used for the beam widths. It is of course not clear, whether these values are correct within the needed precision (normally every three minutes they are updated), especially since there was a shutdown in-between and the beam positions at the interaction points have changed (see Figures 5.7 and 5.8). The acceptance correction is described in detail in [59, Ch. 4.3]. Figure 5.9 illustrates the need for a geometrical acceptance correction. As one can see from that figure, the dependence on the y-position and width is much smaller than the one for x, where one can expect a difference of the result in the luminosity measurement of 1% for a width increase of 1 mm [119].

During later runs in the LH2 period, SPEC was partially working (without the down-x part, this is the so-called noDX period) [121] [118] and it is possible to reconstruct σ_x and σ_y with another method. A study was done of how much the reconstructed values are biased through this method. (Results are shown in [120], where there are also details about the technical reasons for the noDX period and the reconstruction method.) It was found that σ_x is measured 0.6 mm too large and σ_y is measured 0.5 mm too large on average using the new method. As for this analysis even small luminosity differences are important, approximate values of the beam widths for the available period were calculated:

- Approximate value of σ_x = 21.5 mm (as measured with the new method) - 0.6 mm (influence of the new method) = 20.9 mm
- Approximate value of σ_y = 10.2 mm (as measured with the new method) - 0.5 mm (influence of the new method) = 9.7 mm

The influence of σ_y is considered negligible, but the value of σ_x is significantly off the value of 2.2 cm used as average for PCAL [119]⁹. The above approximation would lead to the statement that luminosity might be overestimated by about 1% for LH2 period.

Another approach for approximating the error of the LH2 luminosity measurement is to look at the typical fluctuation of σ_x . Judging from Figure 5.6, there seems to

⁷LH1 and LH2 are not separate periods though. And as shown later the error might actually have different reasons than what is the cause for this 1% uncertainty between periods.

⁸Finally after all found differences between the LH1 and LH2 period have been corrected, there is still a slightly larger rate drop between the two periods than can be accounted for (see Figure 6.12 and Table 6.1).

⁹This value is not directly comparable though as the value from SPEC would need to be geometrically corrected for SPEC.

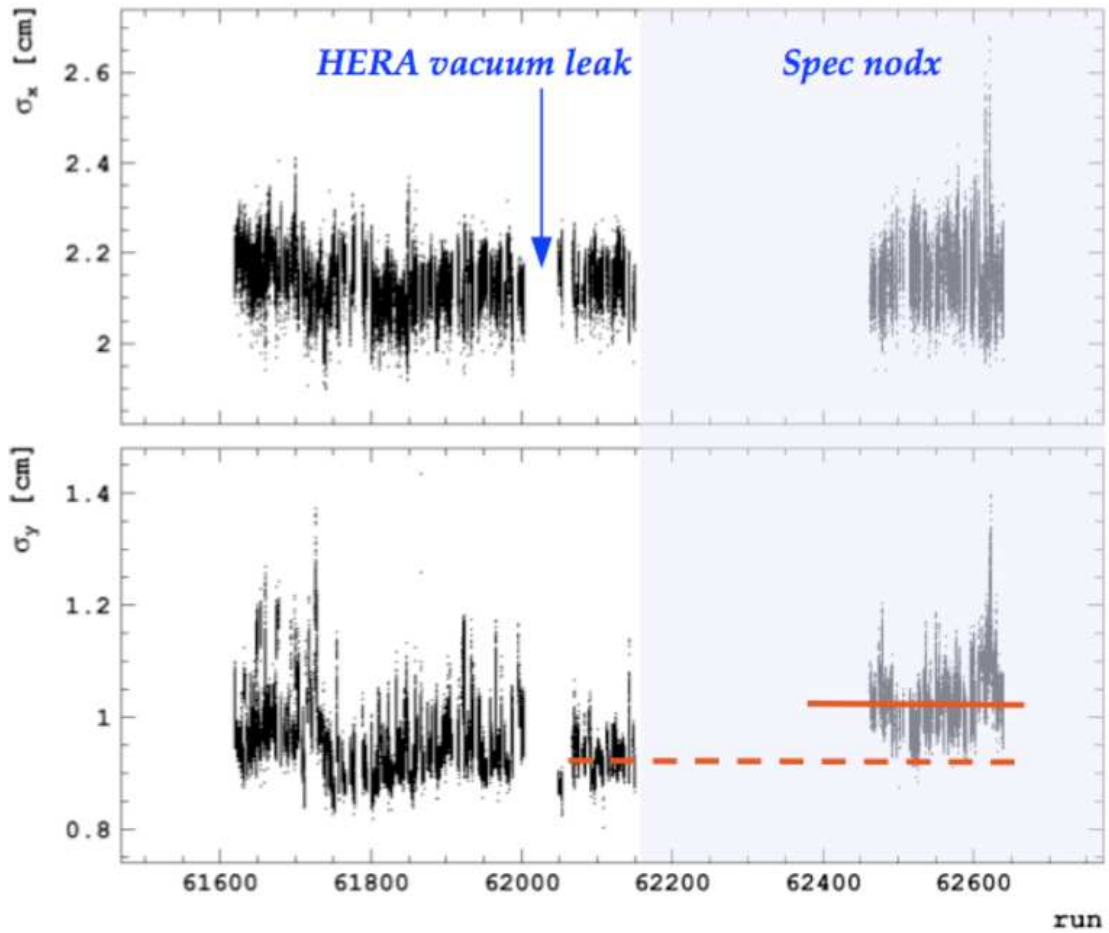


Figure 5.6: Change of σ_x (upper plot) and σ_y (lower plot) from SPEC with time/run number. The arrow labelled vacuum leak indicates the transition from LH1 to LH2 (LH2 period is also indicate by dashed red line). The light blue shaded part is the part, where SPEC was (partially) offline and PCAL used average values for the acceptance correction. The solid red line is the noDX period of the spectrometer. The plot is taken from [120].

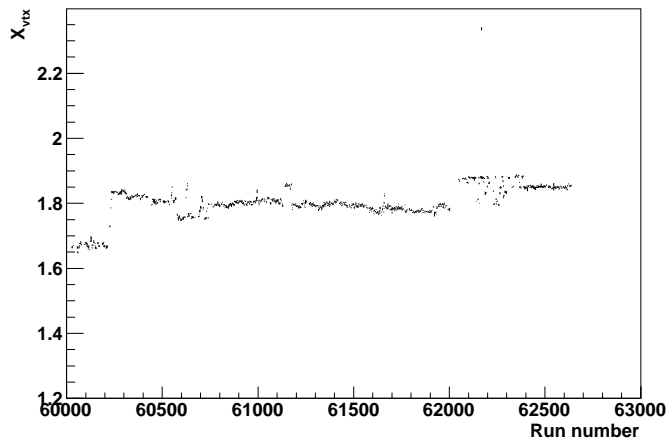


Figure 5.7: Change of X_{vtx} (in cm) with time/run number: Shown is the mean value of X_{vtx} and its RMS for each run. LH1 sub-period starts at 61548, LH2 sub-period at 62050.

be a variation of σ_x of about 1 mm, which is (according to above's approximation) equivalent to a luminosity value variation of about 1%. So the additional systematic error on the luminosity measurement of the affected period (without up-to-date values of σ_x from SPEC for acceptance correction) is about 1%. This is in good agreement with the number from the calculation from noDX period and done for this analysis. For final values, it would be necessary to feed the new σ_x (and σ_y) values into the acceptance correction for PCAL and get more precise luminosity values for the LH2 period and reduce its error.

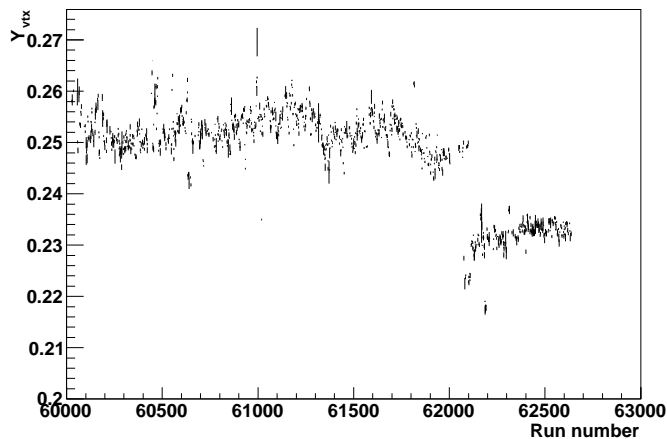


Figure 5.8: Change of Y_{vtx} (in cm) with time/run number: Shown is the mean value of Y_{vtx} and its RMS for each run. LH1 sub-period starts at 61548, LH2 sub-period at 62050.

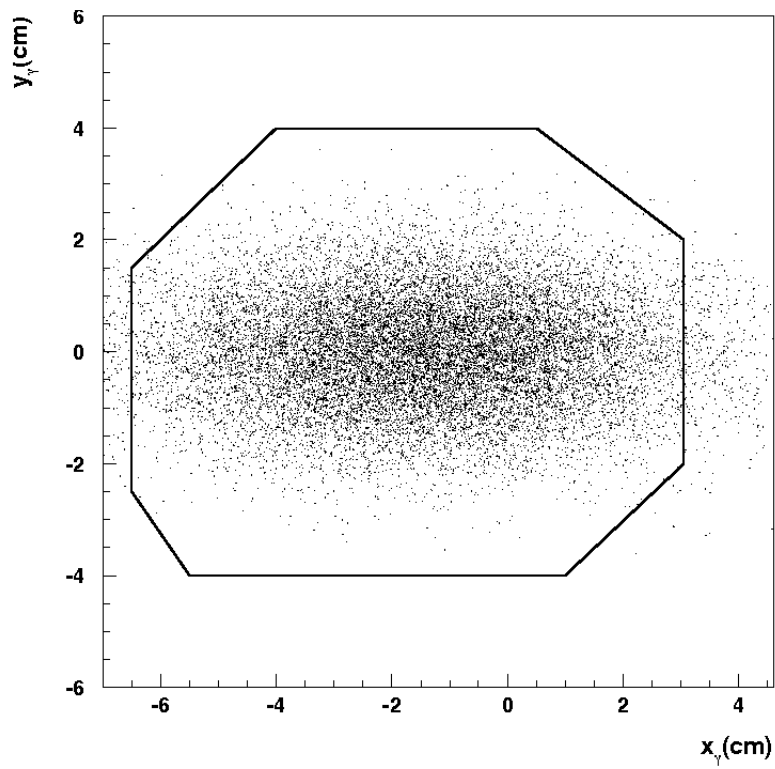


Figure 5.9: Projection of the acceptance contour (black lines) due to the HERA beam line and simulated spatial distribution (points) of the photons on PCAL [59, Figure 14].

5.4. Trigger Variable and Rate Studies

One of the reasons why there are less events for a period than expected from comparing to other periods could be event loss at the trigger level. Thus it is very important to know the trigger efficiency precisely and implement this precise knowledge into the MC simulation.

5.4.1. Trigger Variables

Here two very basic things were studied on FLT level: whether the events triggered really satisfied exactly the criteria (described in Appendix B) they should, and whether the trigger rate stayed within the expected fluctuations constant over time.

All variables used on FLT level were investigated and plotted for all NC events triggered by this FLT bit. An efficiency was then calculated through division by all NC events satisfying the supposed criteria. Though the sample is biased due to the selection of NC events¹⁰, problems with the trigger bits should show up. An example plot is shown in Figure 5.10, where the efficiency of FLT 40 is shown as a function of the EMC energy in the calorimeter. It can be clearly seen that the investigation of FLT bit 40 shows results in accordance with the description of the bit (see Appendix B), which requires events with more than 20 GeV of CAL_EMC ¹¹ and really triggers the events satisfying this criterium (as the efficiency is close to 1 for events with $CAL_EMC > 20$ GeV).

Most of the bits were shown by this study to behave as expected, only bits with a requirement on $RCAL_EMC$ do show a problem. This can be seen especially well for FLT 30 of which a plot is shown in Figure 5.11. Not all events which should be triggered, are triggered for data (efficiency is lower than 1). In contrast, the MC shows the expected behaviour, the limit on $RCAL_EMC$ for FLT 30 being about 4 GeV. That means that for the data there is a clear problem. A correction routine will be described in Section 5.4.3.

5.4.2. Trigger Rates

The number of events per pb^{-1} for each trigger bit used in this analysis (FLT, SLT and TLT) was plotted as a function of run number to check for periods in which the trigger was not working in the expected way. For most of the bits no peculiarity was found (see Figure 5.12 for an example and Appendix D for the other bits).

The problem for the bits depending on $RCAL_EMC$ (the so-called RISOE bug), which was described above, is visible here as well though. In Figure 5.13, which shows the rate of FLT 30, there is for part of the right-handed period¹⁴ some runs for which the rate is considerably lower. This is visible by a kind of double-line: some of the runs are along a line of about 0.0015 events per attobarn as for the other periods, but some are along a line of about 0.0009 events per attobarn. These are the bug-affected runs.

¹⁰As there is no possibility of having a non-trigger biased sample, a sample with NC selection was used for this study. That made it also possible to compare to MC.

¹¹All the subtriggers used and their variables are explained in Appendix B.

¹²See Appendix B for explanation.

¹³See Appendix B for explanation.

¹⁴runs 60226 till 60778

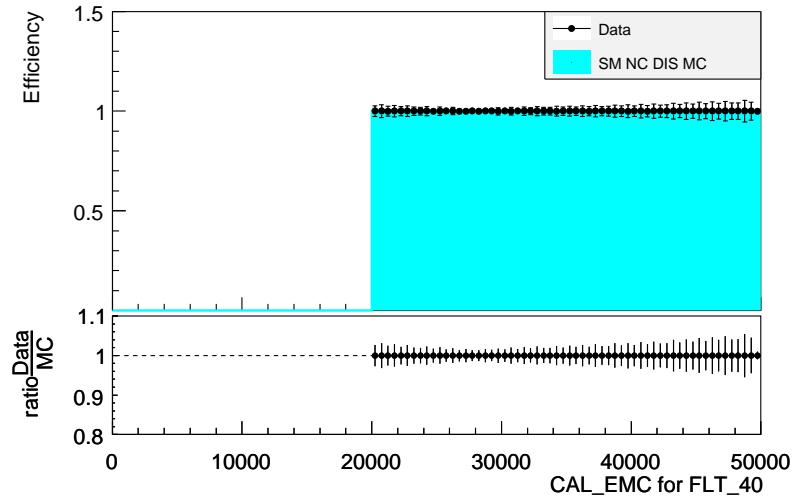


Figure 5.10: Efficiency of the FLT variable CAL_EMC^{12} [in MeV] for FLT 40 with data (black data points) and NC MC (cyan histograms). In addition the ratio of data and MC is shown in the lower part of the plot.

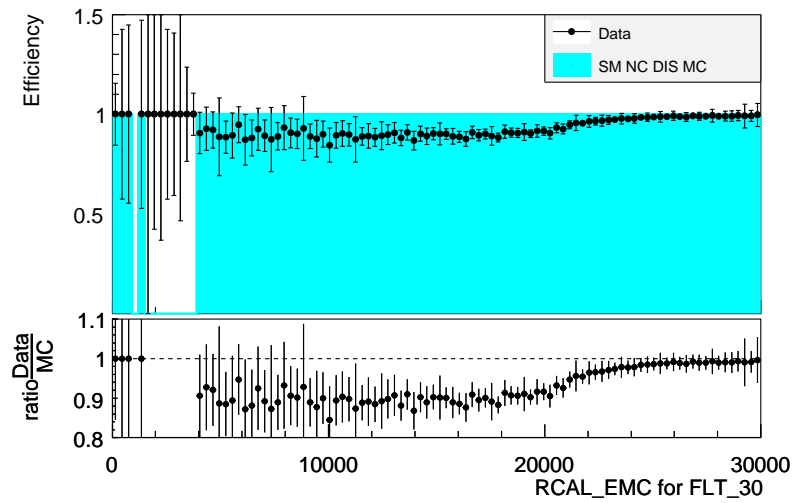


Figure 5.11: Efficiency of the FLT variable $RCAL_EMC^{13}$ [in MeV] for FLT 30 with data (black data points) and NC MC (cyan histograms). In addition the ratio of data and MC is shown in the lower part of the plot. The efficiency below unity for data is due to the RISOE bug explained in Section 5.4.3.

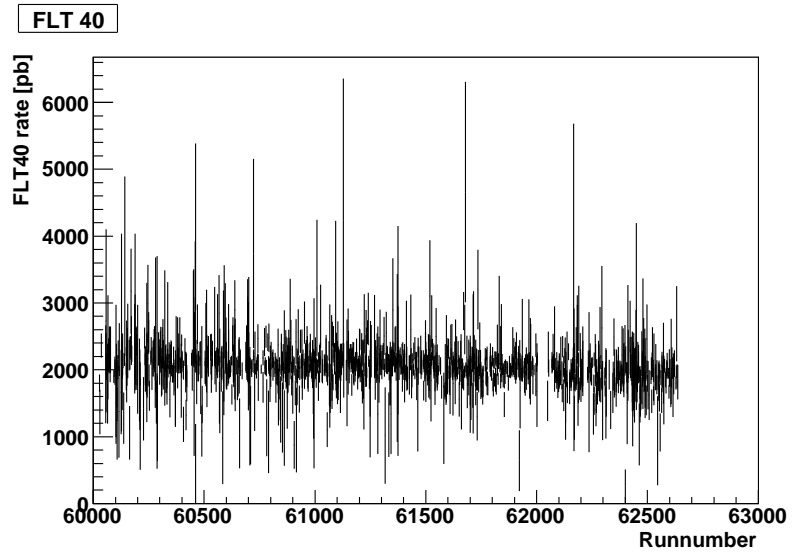


Figure 5.12: Rate (Events divided by run luminosity) for NC DIS events triggered by FLT 40.

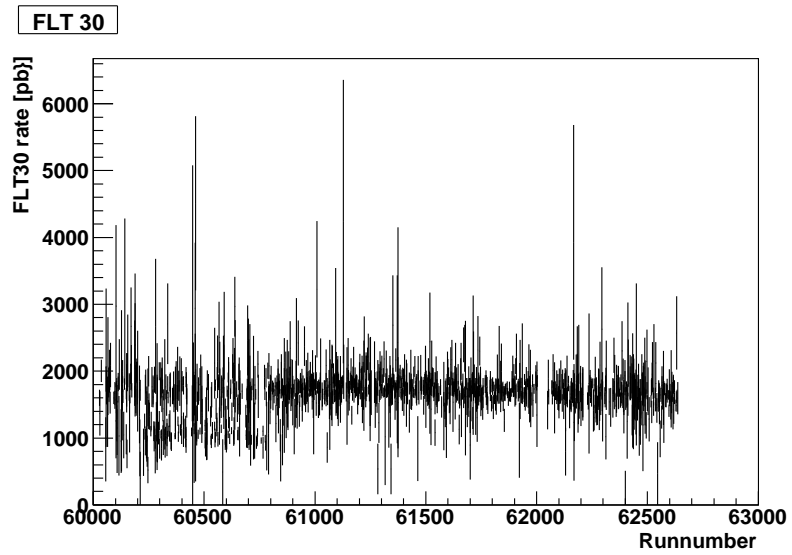


Figure 5.13: Rate (Events divided by run luminosity) for NC DIS events triggered by FLT 30.

5.4.3. RISOE Correction

The reason for the RISOE bug, which can be clearly seen in the FLT bits based on RCAL electrons (30 and 36 for this selection), has been first described in [122].

Within the period of runs 60226 till 60778 for specific trigger settings¹⁵ the threshold of *RCAL_EMC* used for the bits in question was not set properly (i.e. to about 4 GeV) but to infinity. As the logic of these bits is an OR of requirements on *RCAL_EMC* and *RCAL_EMC_TH*, events were still passing the trigger slot through the *RCAL_EMC_TH* criteria, so the rate did not drop to 0 and the problem was not immediately spotted. About 15 pb⁻¹ of data were affected. The double-line feature of Figure 5.13 can be explained by only some trigger configurations being affected¹⁶.

Though the influence is small as the bug only biases events which are exclusively triggered by FLT 30 and 36 (i.e. about 3.5% of events) of about one tenth of the sample, a correction routine was applied to compensate for this effect.

The correction routine (see [122], [86, p.100] for details), does select data events of the same kind as the affected events and gives them a weight higher than 1 to compensate for the lost events. The total effect for this analysis is about 0.15% on total number of events from data (about 0.25% of RH data, LH is unaffected).

5.5. Track Veto Efficiency

On FLT level most of the trigger bits do have a track veto (for details on the FLT bits see Appendix B). That means that events with a special track topology are not selected even if they satisfy the other criteria. Track vetoing is based on the so-called track classes, which are a function of the number of all tracks and vertex-fitted tracks¹⁷ and which are shown in Figure 5.14. For the FLT bits used in this analysis there are the following track vetoes:

1. Track class 2 is rejected (FLT bits 36, 41 and 47)
2. Track class 2 is rejected and track class 8 if there are at least 26 tracks (FLT bit 40 and 28 if isolated electron is found in FCAL)
3. Track classes 0, 1, 2 and 8 are rejected (FLT bit 44)
4. Track classes 0, 1, 2 are rejected (FLT bits 39, 43 and 46)
5. Track classes 0, 1, 2 are rejected and track class 8 if there are at least 26 tracks (FLT bit 28 if isolated electron is found in BCAL)
6. No track veto (FLT bit 30)

The problem is that tracking is not well described in the MC simulation (as has been seen in Section 6.5). This is unfortunately true for the tracking classes as well (see Figure 5.15), which leads to different efficiencies for the trigger selection based on these track classes.

¹⁵affected were STD_060801_High/Low, STD_060823_High

¹⁶not affected were STD_060801_Low_LER, STD_060823_Low

¹⁷Here number of all tracks and vertex-fitted tracks refers to these variables on FLT level. After the whole reconstruction chain the numbers are often different.

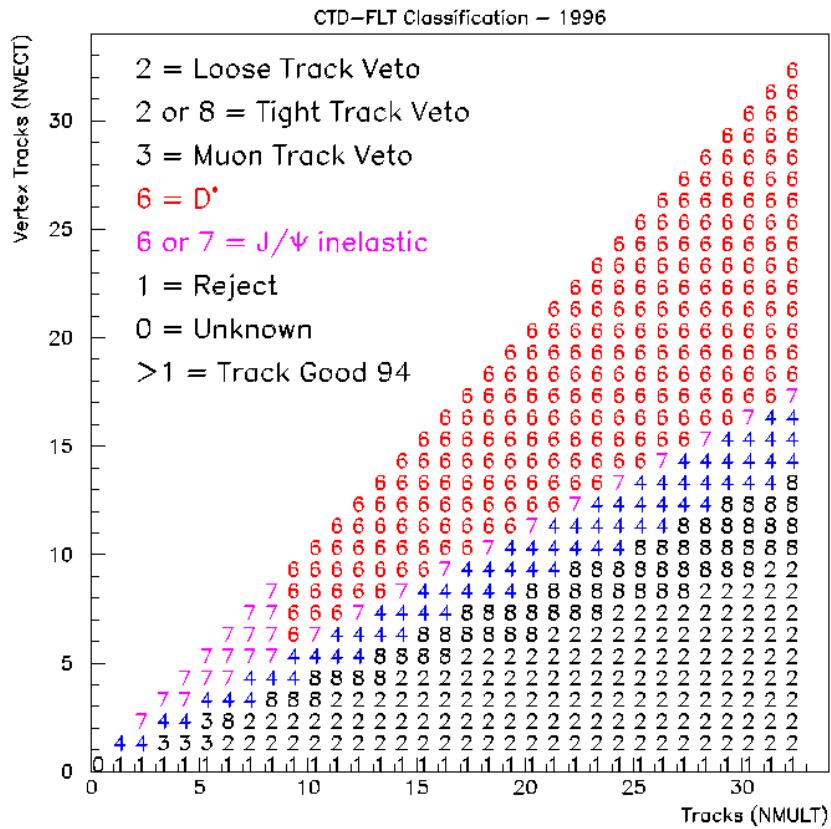


Figure 5.14: Definition of track classes from [123].

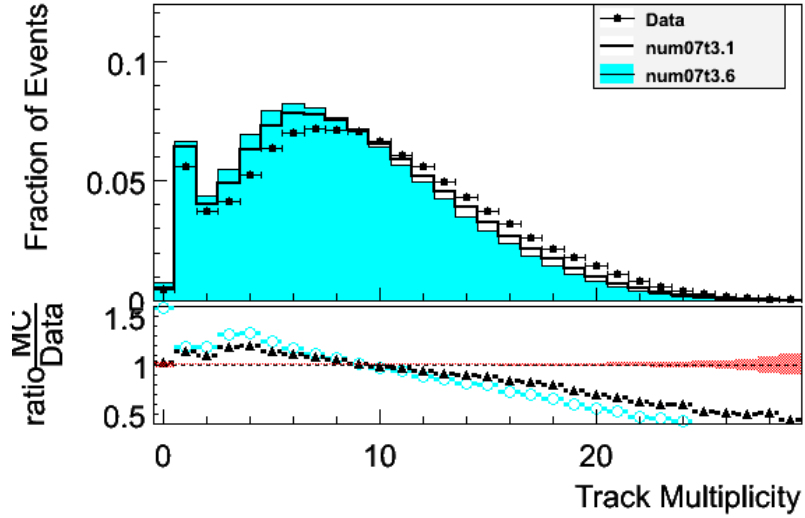


Figure 5.16: Distribution of the track multiplicities on FLT level for data events (black data points), NC MC from funnel version num07t3.6 (cyan histograms) and NC MC from funnel version num07t3.1 (empty histograms with wider black line). In addition the ratio of MC and data is shown in the lower part of the plot.

- There are considerable differences between the different data (sub-)periods, so the correction needs to be done sub-period dependently (see Figure 5.17).
- There is a dependence on other variables, most notably γ_{had} (also visible in Figure 5.17), so a correction factor should be variable-dependent.

To take all these points into account the efficiency ratio of data and MC was fitted for each sub-period (and all data) for the (semi-)loose and tight track veto as a function of γ_{had} . γ_{had} was chosen as it is highly correlated with the number of tracks, but correcting on it avoids a direct bias due to the difference in the distributions of number of (vertex) tracks for data and MC.²¹ A fourth degree polynomial was found to describe the efficiency reasonably well and was used for fitting. The results for loose track veto can be found in Figure 5.1 and for tight track veto in Figure 5.2.

The weight for each MC event was then multiplied by the track veto efficiency (TVE) weight w_{TVE} , separately for the following three cases:

- If FLT 30 triggered the event $w_{TVE}=1$, i.e. no correction as FLT 30 does use no track veto.²²
- If the event was not triggered by FLT 30, but by any event with a (semi-)loose veto, w_{TVE} was calculated by Equation 5.4 using the (semi-)loose parameters

can be seen from Figures 5.15 and even more importantly 5.16, the number of these events is very small.

²¹Due to the problematic simulation of the tracking variables, there are events of different physics topology in data and MC in a bin of a direct tracking variable (e.g. number of tracks). Thus when comparing events from data and MC in a tracking bin, you compare apples and oranges and bias the correction.

²²FLT 30 triggers about 75% of the events in the final selection.

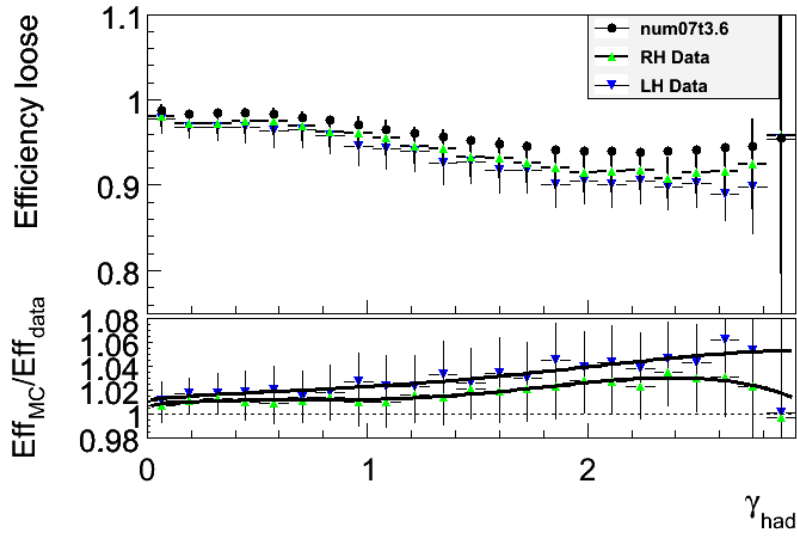


Figure 5.17: Loose track veto efficiency as a function of γ_{had} for MC (black points), RH data (green upward triangles) and LH data (blue downward triangles). In addition the ratio of MC and data efficiency is shown in the lower part of the plot.

tabulated in Table 5.1.

- If the event was neither triggered by FLT 30, nor by any event with a (semi-)loose veto, w_{TVE} was calculated by Equation 5.4 using the tight parameters tabulated in Table 5.2.²³

The weight applied was calculated using the following equation:

$$w_{TVE} = \frac{1}{p_0 + p_1 * \gamma_{had} + p_2 * \gamma_{had}^2 + p_3 * \gamma_{had}^3 + p_4 * \gamma_{had}^4} . \quad (5.4)$$

Period	p_0	p_1	p_2	p_3	p_4
All	1.008927	0.020829	-0.030502	0.021778	-0.004404
RH	1.006749	0.024269	-0.043516	0.030723	-0.006285
LH	1.011914	0.016892	-0.014096	0.010123	-0.001924
LH1	1.011645	0.010865	-0.014184	0.016096	-0.003931
LH2	1.012364	0.025045	-0.012312	0.000068	0.001311

Table 5.1: The parameters of the fourth degree polynomial (semi-)loose efficiency correction function of Track Veto Efficiency for each sub-period.

The overall effect on the number of events is about 0.4% for RH and 0.7% for LH data. For the discussion of the error of this efficiency extraction, refer to Section 7.6.

²³This is only the case for the very small number of events being triggered exclusively by FLT 44.

Period	p_0	p_1	p_2	p_3	p_4
All	1.017347	0.089308	-0.094140	0.061045	-0.012465
RH	1.014636	0.093528	-0.116458	0.072666	-0.014321
LH	1.020805	0.086463	-0.067830	0.046565	-0.010079
LH1	1.022110	0.052672	-0.022951	0.029992	-0.008566
LH2	1.018845	0.136703	-0.135377	0.071864	-0.012481

Table 5.2: The parameters of the fourth degree polynomial tight efficiency correction function of Track Veto Efficiency for each sub-period.

5.6. Funnel Versions

The funnel version (see Section 4.3 for explanation of funnel) used in this analysis is num07t3.6. Results have been cross-checked with num07t3.1 and num07t4.1. The most important difference between the versions is the CTD gas gain settings. In neither of the versions are they simulated perfectly (which is the main reason for the necessity of TVE correction), but the description in num07t3.6 is significantly improved compared to num07t3.1 (see trigger plot in Figure 5.18 still without corrections).

The final analysis (including all corrections) has been cross checked using num07t4.1 and been proven to agree well within the expectation. In num07t4.1 it is possible to have run-depedent settings (that means MC simulates the time-dependent differences), but as within this analysis the whole sample is used and our corrections take into account the sub-period-dependencies, num07t3.6 is sufficient. The only important difference seen in the distributions of variables is for the trigger bits, especially 44 (see Figure 5.19). As described in Section 5.5 (details in Appendix B) 44 is the only trigger bit with tight track veto used in this analysis and thus the difference is expected due to the CTD gas gain differences. The only trigger bit where no difference is seen is the FLT bit 30, which is the one without any track veto, thus the above interpretation is confirmed. To conclude: it is expected that the results from num07t3.6 would be reproduced very exactly with num07t4.1 if the corrections were re-extracted based on them.²⁴ As by far the main difference of the different funnel version is due to the track vetoes, the systematic uncertainty of the choice of funnel version is accounted for by the uncertainty of the TVE correction (see Section 7.6).

5.7. Correction of the Longitudinal Vertex Position

The interaction vertex is reconstructed for each event using tracks from charged particles measured by the tracking system of the ZEUS detector (see Section 3.2.2). The longitudinal vertex position Z_{vtx} does affect the reconstructed kinematics as the angle in the coordinate system of the detector is a function of the scattering angle and the vertex position. Thus it is very important to have a good consistency of vertex distributions of real data and simulation to be able to use the simulation for the acceptance correction. In addition it is necessary to impose restrictions on the Z_{vtx} position to

²⁴Similarly it would probably be possible to use num07t3.1 with the proper set of extracted corrections.

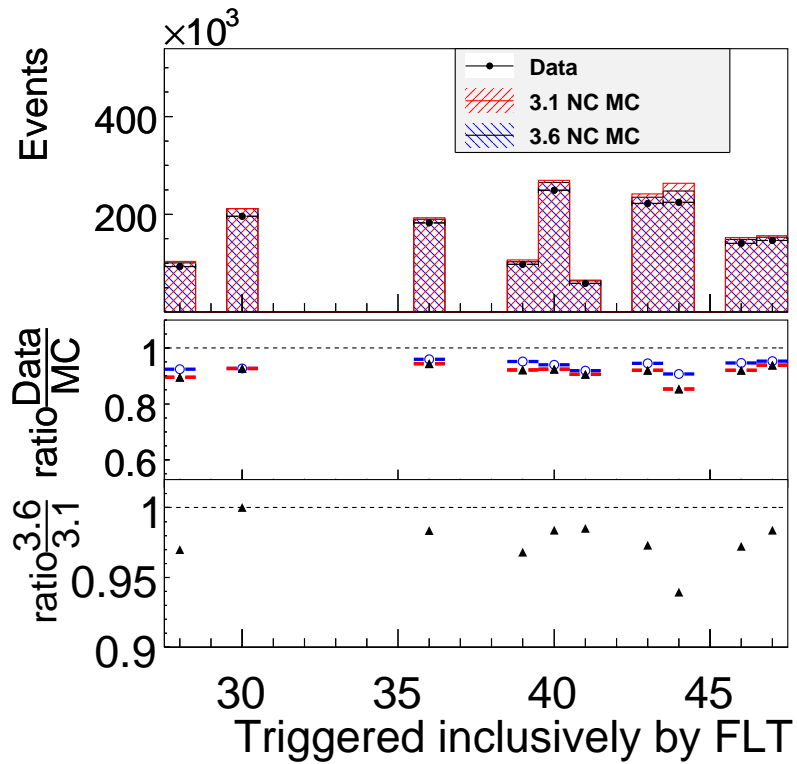


Figure 5.18: Distribution showing the number of weighted events triggered by each FLT bit used in this analysis (the number on the x-axis refers to the number of the FLT bit) within data (black points), num07t3.1 MC (red hashed histogram) and num07t3.6 MC (blue hashed histogram). The upper plot shows the absolute event numbers, the middle plot the ratio of data and MC prediction (3.1: filled triangles, 3.6: empty circles) and the lower plot the ratio of the different MC funnel versions.

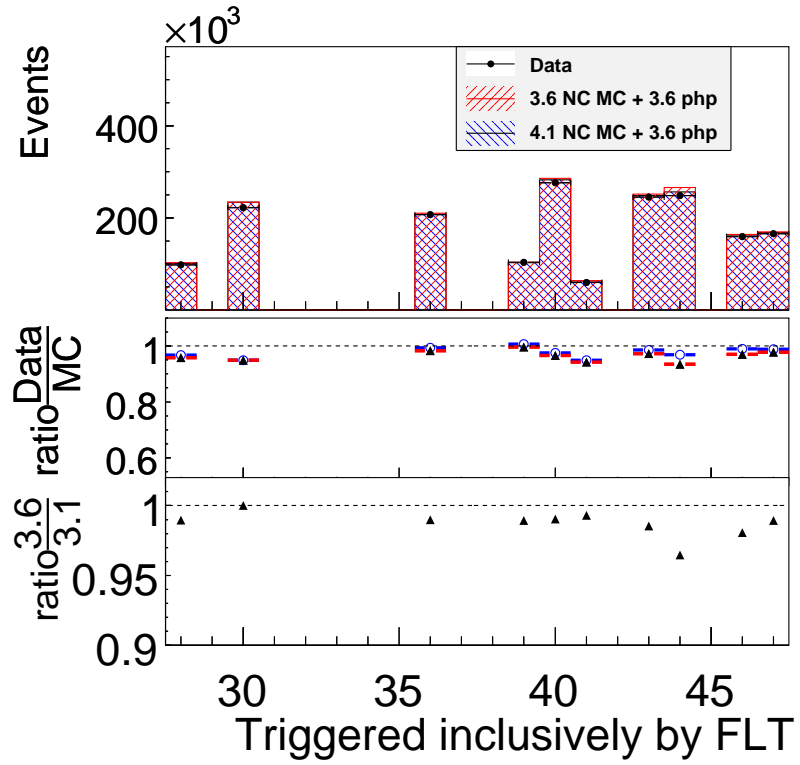


Figure 5.19: Distribution showing the number of weighted events triggered by each FLT bit used in this analysis (the number on the x-axis refers to the number of the FLT bit) within data (black points), num07t3.6 MC (red hashed histogram) and num07t4.1 MC (blue hashed histogram). The upper plot shows the absolute event numbers, the middle plot the ratio of data and MC prediction (3.6: filled triangles, 4.1: empty circles) and the lower plot the ratio of the different MC funnel versions.

remove non- ep background, which necessitates a good description of the vertex position in MC as well. As the vertex position changes for different runs (i.e. accelerator and detector conditions) as depicted in Figure 5.20, it is necessary to do the extraction of the Z_{vtx} distributions anew for each period one wants to measure separately. In case of this analysis it was done for the whole 06/07 e^+p -running as well as RH period, LH1 and LH2 (for description of this periods see Section 4.1) alone. Comparing the whole set to adding RH, LH1 and LH2, results were consistent.

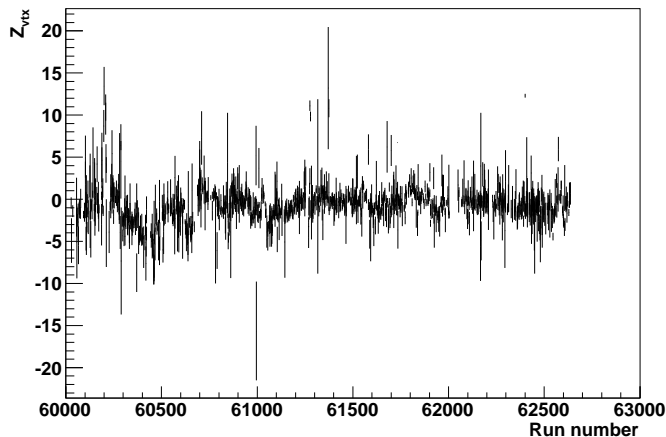


Figure 5.20: Change of Z_{vtx} with time: Shown is the mean value of Z_{vtx} (in cm) and its RMS for each run. LH1 sub-period starts at 61548, LH2 sub-period at 62050.

The method of extracting the Z_{vtx} distributions is described e.g. in [124] and the extraction for this period in more detail in [97]. As the trigger and detector are biased towards events in the central region, this bias needs to be taken into account and compensated as well as possible to describe the event vertex properly. The region of -100 cm to 100 cm, in which the distribution is extracted, is thus divided in three parts, where the efficiency is then measured and fitted. Based on that a Z_{vtx} distribution is reconstructed from the measured events and fitted with the sum of seven Gaussians (1 central peak, 4 electron satellite peaks, 2 proton satellite peaks).²⁵ The fit is shown in Figure 5.21.

The result is shown in Figure 5.22 for one sub-period. It can be clearly seen that the description of the longitudinal vertex distribution has been improved much compared to the previously extracted distributions.

The Z_{vtx} -reweighting shows significant differences between the different periods, which can account for a considerable part of the rate drop between LH1 and LH2 seen in Figure 5.2. The different Z_{vtx} -distributions are the reason for nearly 3% of rate difference between the LH1 and LH2 data period.

²⁵Other fits e.g. with 5 Gaussians were found to describe the distribution only slightly worse. The difference on the final NC analysis is extremely small.

²⁶The period shown is the LH2 period with the highest influence of the Z_{vtx} reweighting on normalisation.

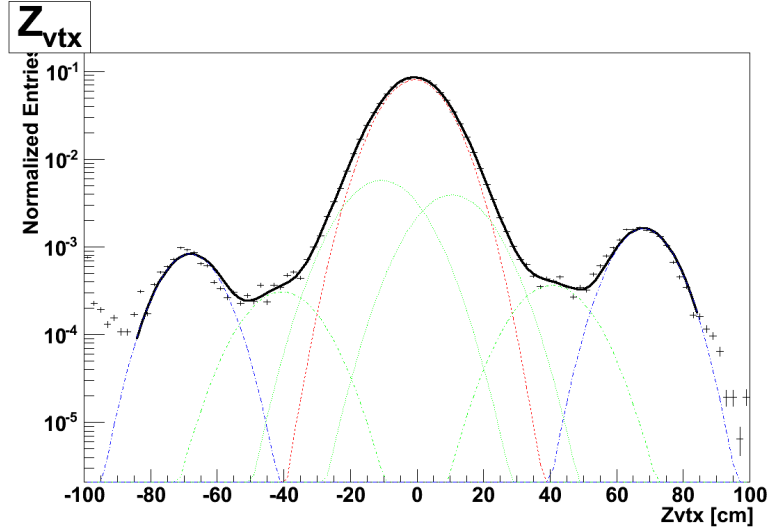


Figure 5.21: Fit of the Z_{vtx} distribution: Data is shown in black points, the central peak in red, the electron satellites in green and the proton satellites in blue. The black line is the fit (sum of the seven Gaussians). From [125].

5.8. Energy Corrections

A precise measurement of the electron energy is highly relevant for this analysis. Starting on the raw energy measurement from the calorimeter there are different effects which have to be taken into account and corrected for to get as close as possible to the true energy of the electron and to have the detector response well-modeled in the Monte Carlo events. The steps taken in this process are described in this section. The measurement of NC DIS is much less sensitive to the hadronic energy (see Section 7.5 for details). As one can see from Figure C.5 the hadronic angle (which is the variable of the most importance that is directly related to the hadronic energy) the hadronic energy was already described precisely enough for this analysis. It is based on the *CorandCut* correction routine described in [106] and included in the ORANGE [95] environment. Thus only the electron energy measurement was optimised in course of this analysis. As statistics are very low for the FCAL, the energy of the FCAL electrons was taken from past studies included in the ZEUS analysis environment, whereas for the RCAL and the BCAL the raw measured energy was taken and calibrated specifically for this period and analysis in several steps.

5.8.1. Cell-wise and Radial Factors in the RCAL

The cell-wise and radial correction factors²⁷ (for the RCAL) were extracted comparing the measured energy to the energy from the Double-Angle method described in Section 4.9.3²⁸. Using this method the energy of the scattered lepton is written as a function of

²⁷They were applied during Ntuple creation and optimised iteratively.

²⁸In addition Kinematic Peak method was used. For details refer to [126].

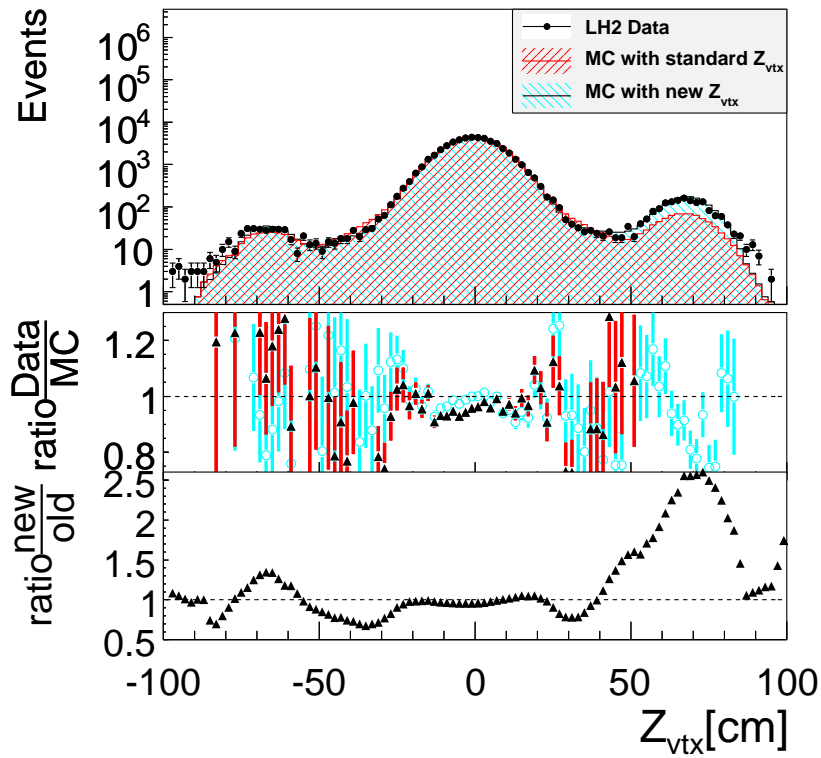


Figure 5.22: The longitudinal vertex distribution without the limitation to $|30\text{ cm}|$ for one data sub-period²⁶ showing the number of weighted events from data (black points), SM MC with Z_{vtx} reweighting as standard before the study for this analysis (red hashed histogram) and SM MC with new Z_{vtx} reweighting (cyan hashed histogram). The upper plot shows the absolute event numbers, the middle plot the ratio of data and MC predictions and the lower plot the ratio of the differently reweighted MC.

the scattering angles of the lepton and the hadronic system alone²⁹:

$$E_{DA} = 2E_{e^+}^{beam} \frac{\sin(\gamma_{had})}{\sin(\gamma_{had}) + \sin(\theta_{e^+}) - \sin(\gamma_{had} + \theta_{e^+})}. \quad (5.5)$$

As E_{DA} is independent of the calorimeter energy scale it can be used to cross check the energy measured in the calorimeter.

Factors were extracted cell-wise whenever possible. In case of statistical limitations radial factors were extracted. Originally for the data from the data-taking period of this analysis, these factors were extracted based on the (limited) data for the analysis of the longitudinal structure function F_L (i.e. low Q^2 and x). Investigations showed (see Figure 5.23), that the existing factors from this subsample were not sufficient for this analysis.

Based on a wider range of kinematics by combining samples (from this analysis and the F_L analysis) new factors were extracted (see [110]).

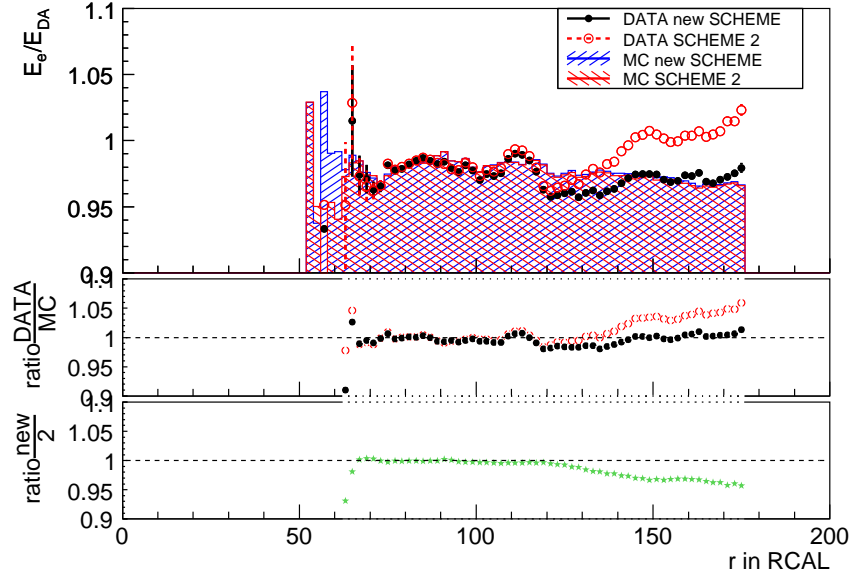


Figure 5.23: The averages of $\frac{E_{meas}}{E_{DA}}$ as a function of radius (in cm) in the the RCAL. Compared are values with the factors extracted from previous samples (SCHEME 2, red data points and MC histogram) to values after extraction from bigger sample including Ntuples from this analysis: data points in black and Monte Carlo prediction in blue histogram. The middle ratio of data and MC clearly shows improved agreement with the new settings (black ratio points) compared to the old one (red ratio points). The bottom green ratio points show that the two schemes differ mainly for large radii. The accuracy of the values for very small radii are statistically limited.

²⁹Only the beam energy is needed, but no energy measured from the detector.

5.8.2. Inactive Material and Non-Uniformity Corrections

Corrections for inactive (also called dead) material and non-uniformities in the detector need to be applied for precise energy measurements. The method for extracting both corrections is the same for data and MC, but the values were extracted separately and do differ.

Dead material corrections are necessary as the particles produced loose energy passing through inactive material like cables, beam-pipe and magnets before reaching the calorimeter. For taking this into account a dead material map was available, so that the amount of dead material in units of radiation lengths (X_0) can be calculated as function of the position and angle of the electron.³⁰ The corrected energy E_{cor} is then calculated from the energy before this correction E_{before} with the formula

$$E_{cor} = 2E_{before} \cdot \left(1 + \frac{A(X_0)}{E_{before}^{B(X_0)}}\right). \quad (5.6)$$

$A(X_0)$ and $B(X_0)$ are calibrated with the help of test beam results for data [127] [128].

Non-uniformity corrections are needed because of the different response of the calorimeter with regard to the position of the electron in the calorimeter due to gaps and structures in the calorimeter itself. In the RCAL they are done as a function of x - and y -position of the electron, in the BCAL the correction routine depends on position and angles, but also directly on distance to cell and module edges. For both corrections existing routines were used, which were found applicable to this analysis with minor modifications.³¹ The improvement due to the corrections is sizable, an example plot is shown in Figure 5.24. As the corrections are different for data and MC, not well tuned corrections do have a big effect in the description of data by the MC for this analysis, which depends very much on the electron energy measurement.

5.8.3. Energy Scaling and Smearing

After the corrections described in the previous sections³², the measured energies of the data and the simulated events were compared to the energies reconstructed with the Double-Angle Method (see Section 4.9.3, an illustration of the used distributions is shown in Figure 5.25). A Gaussian was then fitted on the ratio of E_{meas} and E_{DA} in bins of E_{DA} . From these, global factors were extracted for the RCAL and the BCAL (for the FCAL statistics were too low): A straight line was fitted through the MC-Data ratio of the center values of the Gaussians to extract a factor of scaling the energy of the events for MC. In addition the resolution was compared for data and Monte Carlo (i.e. the width of the distribution) and a factor extracted to compensate for the slightly better resolution in the simulation.³³ The extracted factors were then used on top of

³⁰In the RCAL it is also possible to use the PRES to measure the produced particle multiplicity of an event, which is closely correlated to the energy loss due to dead material.

³¹They are described in more detail elsewhere: see [110] for the RCAL and [129] for the BCAL. Originally they were developed for the high-x NC DIS analysis in e^-p (BCAL) and e^+p data.

³²The routine used for the correction of dead material and non-uniformities in the BCAL already includes an overall scaling factor.

³³The extraction procedure will be described in more detail in [97].

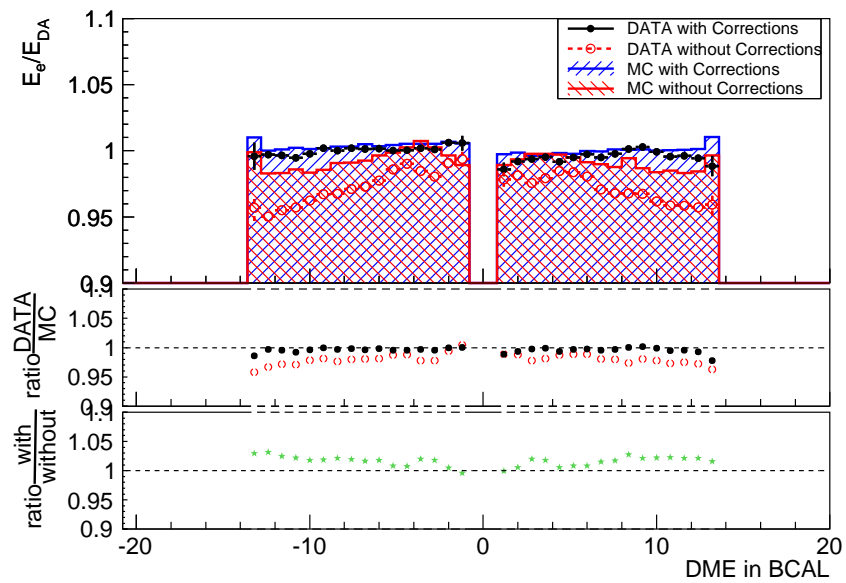


Figure 5.24: The averages of $\frac{E_{meas}}{E_{DA}}$ as a function of distance to calorimeter module edge (in cm) in the BCAL. Compared are values without the correction of dead material and non-uniformities (red data points and MC histogram) to values after correction: data points in black and Monte Carlo prediction in blue histogram. The ratio clearly shows an improved agreement with the new settings (black ratio line) compared to the old one (red ratio line). The bottom green ratio line shows the amount of change by the corrections.

the other corrections to shift and smear the reconstructed energies. The influence of this correction is shown in Figure 5.26, the extracted numbers are summarized in Table 5.3.

	RCAL	BCAL
Shift	-0.7%	-1.1%
Smear	3.22%	2.93%

Table 5.3: Factors extracted for scaling and smearing of electron energy after the other correction routines.

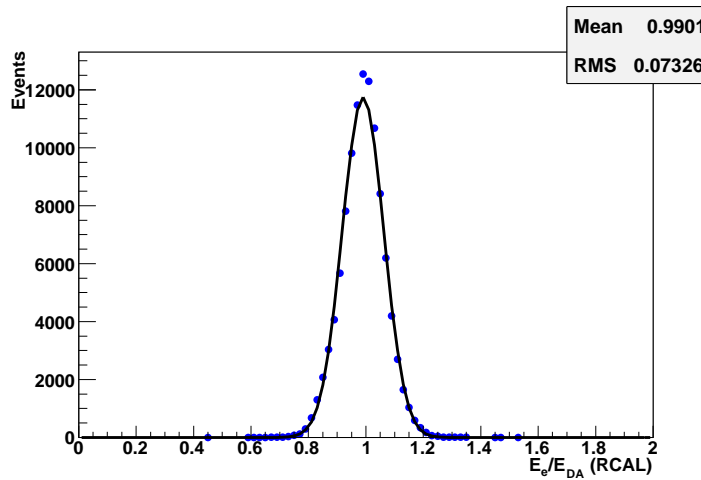


Figure 5.25: Example plot from which information about scaling and smearing factors can be extracted by fitting a Gaussian (black line): Histogram of the ratio of the measured energy of scattered electrons (in the RCAL) to the electron energy reconstructed using the Double-Angle Method.

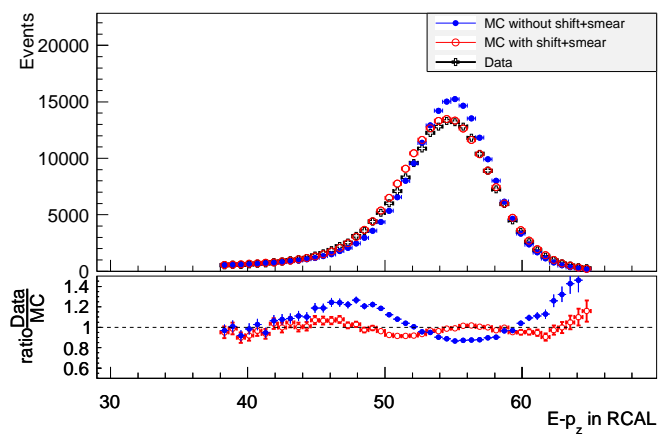


Figure 5.26: Comparison of the $E - p_z$ (in GeV) distribution with the positron reconstructed in the RCAL from data (black crosses), MC with (red circles) and without (blue squares) shifting and smearing factors applied. In addition the lower part of the plot shows the ratio of data and MC (red circles) and without (blue squares) the additional shifting and smearing.

5.9. Track Matching Efficiency

The selection of NC DIS events includes numerous track-related selection criteria (see Sections 6.4.1 and 6.4.3). Thus the validity of the acceptance correction depends on the tracking efficiency in the MC simulation to reproduce the real efficiency from the data.

To investigate how well the MC describes the track matching efficiency of the data, a sample was selected with the NC DIS selection criteria excluding all track-related restrictions, namely:

- Matched track in CTD acceptance region
- Track momentum in the CTD acceptance > 3 GeV
- $DCA(\text{Track}, \text{Cluster}) < 10$ cm in CTD acceptance
- Distance to module edge > 1.5 cm in CTD acceptance
- At least one good track ($p_t > 0.2$ GeV, outer superlayer ≥ 3 , inner superlayer ≤ 1 , primary vertex fitted)

All restrictions except for the last one depend directly on whether the positron candidate is found within the so-called CTD acceptance region. Historically this acceptance region was defined as $0.3 < \theta < 2.85$, which was also used for this study³⁴. The track matching efficiency TME was then defined in each investigated bin as

$$TME = \frac{N_{all\ cuts}}{N_{wo\ track}}, \quad (5.7)$$

where $N_{all\ cuts}$ is the number of events satisfying all criteria including the track-related criteria³⁵ and $N_{wo\ track}$ is the number of events satisfying the selection criteria without track requirements (i.e. a less tight selection).

Figures 5.27 and 5.28 show the result as a function of θ and positron energy. More Figures can be found in Appendix E. It can be clearly seen that the efficiency of track matching is not the same in data and MC³⁶. There are actually two separate effects: a major one in the RCAL and a less prominent one in the BCAL.

RCAL The effect in the RCAL (visible at high θ in Figure 5.27, and at energies around 25 GeV in Figure 5.28) gets worse the closer the polar angle is to the cut-off value 2.85, from which onwards no track is required. It was decided to resolve the disagreement of data and MC in this region through removing the track requirement in this region completely. There was hardly any influence on purity observed as the increase of background events was relatively small. Also the effect on resolution was found to be negligible [97] [130]. Thus the CTD acceptance region was defined as $0.3 < \theta < 2.5$ for this analysis as used in Chapter 6.

³⁴Due to the requirement of $Q^2 = 185$ GeV², $\theta \approx 2.85$ was not reached for positrons in this analysis.

³⁵That responds to the standard selection used in this analysis with higher upper θ -value for CTD acceptance.

³⁶The photoproduction background is subtracted from data here and compared to the NC DIS MC as there is no track expected in the majority of photoproduction events, so the term track matching efficiency is not applicable in case of photoproduction.

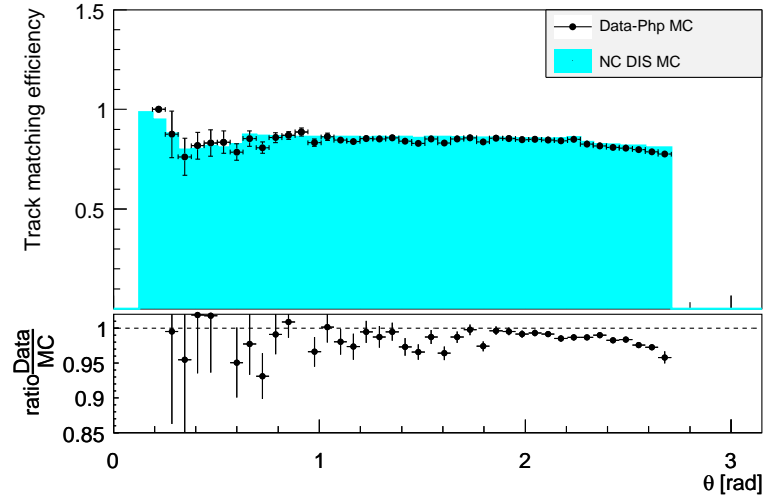


Figure 5.27: Track matching efficiency as a function of the angle θ of the scattered positron from data (black data points, php contribution subtracted from SM prediction) and NC MC (cyan histograms). In addition the ratio of data and MC is shown in the lower part of the plot.

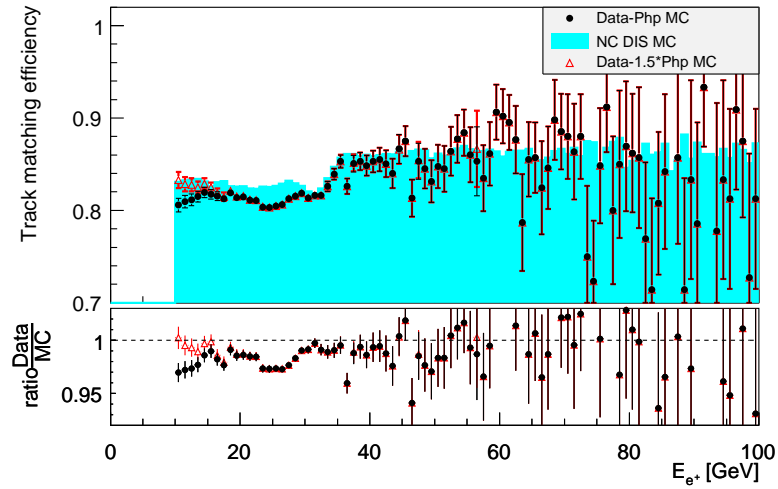


Figure 5.28: Track matching efficiency as a function of the energy of the scattered positron with data (black data points, php contribution subtracted from SM prediction) and NC MC (cyan histograms). The red triangles show the TME of data assuming a 50% higher photoproduction contribution. In addition the ratio of data and MC is shown in the lower part of the plot.

BCAL The effect in the BCAL (visible at medium θ in Figure 5.27, and at energies around 15 GeV in Figure 5.28) is rather of a different nature: It spreads among a large angular range basically central in the detector, where no inefficiency due to e.g. thresholds is expected. Interestingly the drop in $\frac{TME_{Data}}{TME_{MC}}$ thereby is situated in the same regions in which the contribution from photoproduction background is expected to be high. Looking at the TME in other variables (see Appendix E) shows the same: $\frac{TME_{Data}}{TME_{MC}}$ is lower for low positron energy, where the photoproduction contribution is comparably high.³⁷.

Furthermore the relatively high uncertainty on the photoproduction cross section (50%) could account for the difference seen in TME in data and MC as shown in Figure 5.28. Thus the option of reweighting the NC DIS MC in this region was disfavored (though proven to give reasonable results as well).

5.10. Summary of Applied Corrections

It was found to be necessary to apply the following corrections to the samples:

- **F_L correction**, which mainly influences the high y region. The overall effect on the number of MC events is about -1%.
- **Polarisation correction**, which changes the MC mainly at high Q^2 in opposite ways for the opposite lepton beam polarisations.
- **Luminosity uncertainty correction**, the uncertainty has been increased by an additional 1% for the LH2 period.
- **RISOE correction**, which only has a tiny influence.
- **Track veto efficiency correction**, which was applied as a function of γ_{had} and which is very period-dependent.
- **Z_{vtx} reweighting**, which explains a major part of the rate difference between the periods.
- **Energy smearing/scaling**, which improves the ability of the MC to describe the measured positron energy.
- **TME: change of region in which track is required**, there are two separate effects: one in the RCAL and one in the BCAL.

In this way, a good description of the variables by the Standard Model MC, necessary for a reliable acceptance correction, is achieved.

The differences in events per luminosity between the different data-periods can be understood by the sum of the corrections .

The uncertainties of the corrections and their influence on the systematic error are discussed in Section 7.6.

³⁷Of course, positron θ and energy are closely correlated, but also in less correlated variables, there seems to be a correlation of lower $\frac{TME_{Data}}{TME_{MC}}$ and higher photoproduction contribution.

6. NC DIS Event Selection

In this chapter it is described which characteristics signal NC DIS events and background events do exhibit in the detector and how the NC DIS events were selected in this analysis.

6.1. Signal Event Characteristics

NC DIS events at high Q^2 have a clear signature of a well-isolated electromagnetic cluster in the calorimeter with a track pointing towards it from the scattered electron and a hadronic final state which compensates the transverse momentum of the scattered electron.

A typical NC event as recorded by the ZEUS detector is shown in Figure 6.1. In the XY view it can be seen, that the hadronic transverse momentum balances the transverse momentum of the electron. A Feynman graph of NC DIS is shown in Figure 6.2. The proton remnant is usually either detected very close to the forward beam pipe or escaping detection in the beam pipe.

The scattered electron is usually detected as a well-isolated shower in the electromagnetic part of the calorimeter to which a track is pointing from the interaction point. As the scattering angle of the electron is closely connected to Q^2 of the event (see Equation 4.5) and the cross section drops with $\frac{1}{Q^4}$ most of the events are recorded at large angles¹, thus with the scattered electron in the RCAL². Events above approximately 500 GeV^2 are found in the BCAL and the rare NC DIS events with the electron in the FCAL are of very high Q^2 . Furthermore it can be seen from the equation that the energy of the scattered electron increases with Q^2 and x . The angle of the hadronic system (corresponding to the scattered quark in the QPM picture) is directly related to x . It is scattered to the rear direction at low x and to the forward direction for high x . The event topology and its dependence on x and Q^2 is illustrated in Figure 6.3.

Momentum conservation requires that the transverse momentum of the electron is balanced by the hadronic transverse momentum in NC DIS.

A very important variable for the selection of NC DIS events stemming from energy and momentum calculation is $\delta = E - p_z$.

The total energy is the sum of the proton and electron beam energy $E = E_p + E_e$ and the longitudinal momentum is (neglecting the masses) $p_z = E_p - E_e$ as there is no transverse momentum of the beams and the electron and the proton move in opposite directions. This leads to

¹As the angle is measured from the direction of the proton, a large angle is actually a small electron scattering angle.

²The selection requirement on a lower cut of Q^2 thus is also a cut on the angle.

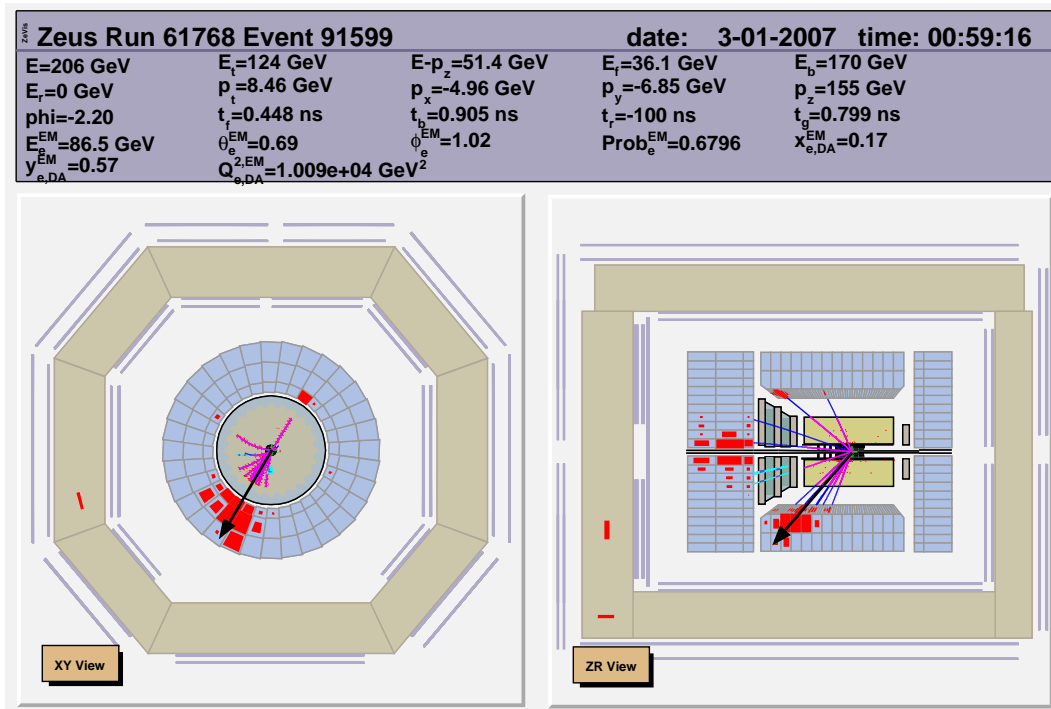


Figure 6.1: A NC DIS event in the ZEUS detector as visualised by the ZEVIS [100] event display. This event was reconstructed with the scattered electron at $\theta \approx 0.69$, $\phi \approx 1.02$ and $Q^2 \approx 10000 \text{ GeV}^2$, $y \approx 0.57$ and $x \approx 0.17$.

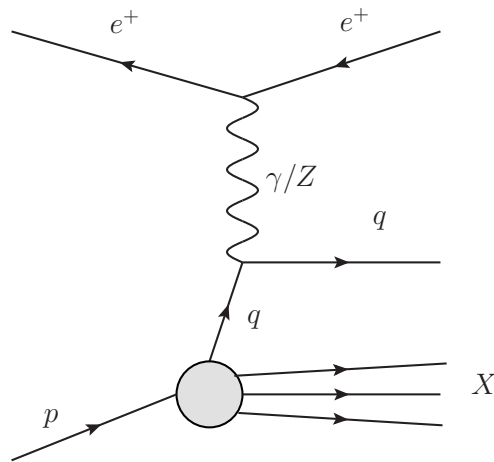


Figure 6.2: A Feynman graph of Neutral Current Deep Inelastic e^+p Scattering.

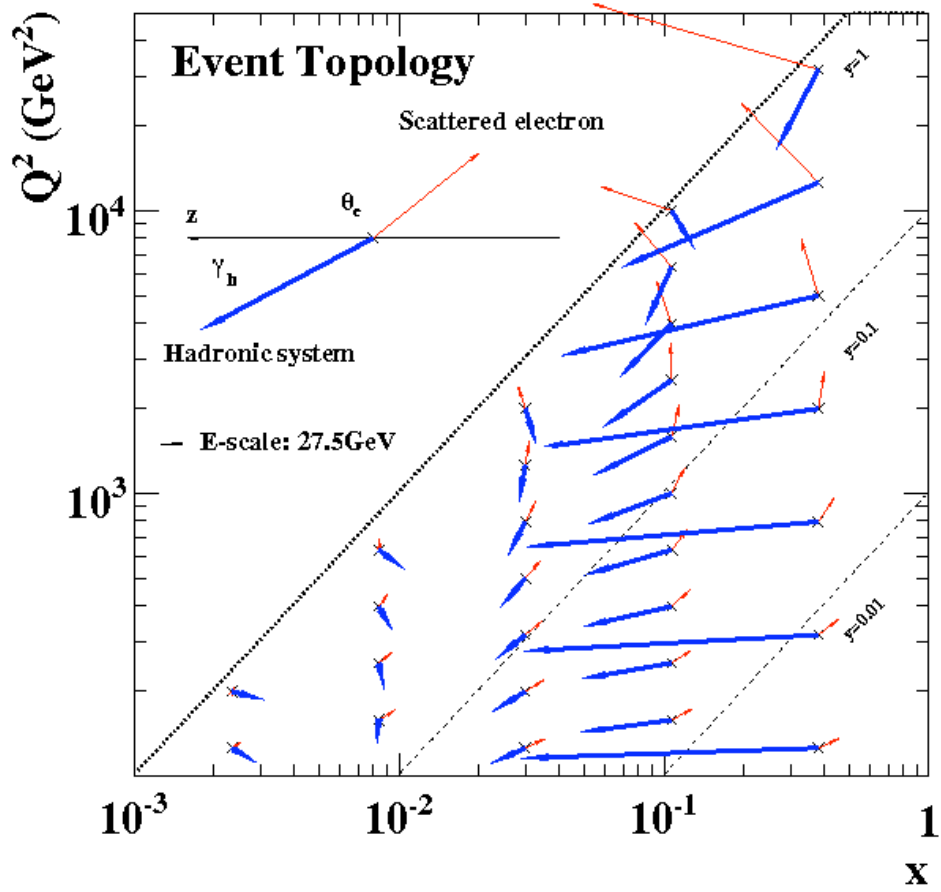


Figure 6.3: Topology of NC DIS events depending on their Q^2 and x values. The thick blue arrow shows the direction and energy (arrow length) of the hadronic system, the thin blue arrow corresponds to the scattered electron. The figure is taken from [85, p. 45].

$$\delta = E - p_z = E_p + E_e - (E_p - E_e) = 2E_e . \quad (6.1)$$

Assuming energy and momentum conservation and cancellation for the particles escaping detection through the forward beamhole (mainly the proton remnant) as $E^i - p_z^i = E^i(1 - \cos\theta_i) \approx 0$ ³ δ is conserved and a value of δ around 55 GeV (twice the energy of the positron beam) is expected for well-reconstructed NC events (without e.g. initial state radiation).

6.2. Background Characteristics

6.2.1. Photoproduction

The most important background for NC DIS is photoproduction due to its huge cross section. In Figure 6.4 the Feynman graphs are shown for direct and resolved photoproduction.

In photoproduction in ep scattering, the electron emits a quasi-real photon, which scatters off the proton. The electron is scattered by such a small angle (large θ) that it remains in the beam-pipe and is not detected.

Misidentification as a NC DIS event can happen if a fake electron is found by misidentification e.g. the overlay of a charged hadron and a photon. Rejection of these events is possible by different cuts, which depend on the kinematic variables of the electron. Requiring the electron to be isolated is helpful as well as the cut on the electron energy. Furthermore, as the real electron escapes without detection, the cut on δ suppresses most photoproduction events.

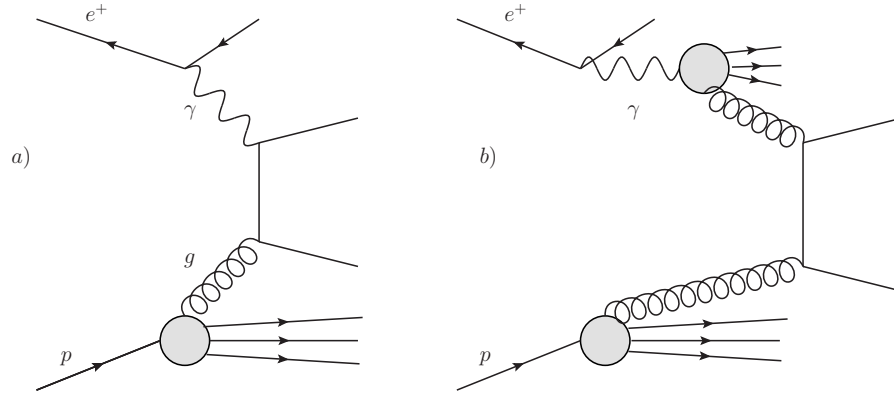


Figure 6.4: Feynman graphs of a) direct and b) resolved photoproduction.

³The index i here refers to the escaping particles.

6.2.2. Elastic QED Compton

The Feynman graph for QED Compton scattering is shown in Figure 6.5: the initial or the scattered electron emits a hard photon, which biases the reconstruction of the kinematic variables. The inelastic QED Compton process (proton dissociates) is well-simulated by Monte Carlo, but the elastic process is not and thus needs to be removed from the sample (see 6.4.2 for details on elastic QED Compton removal).

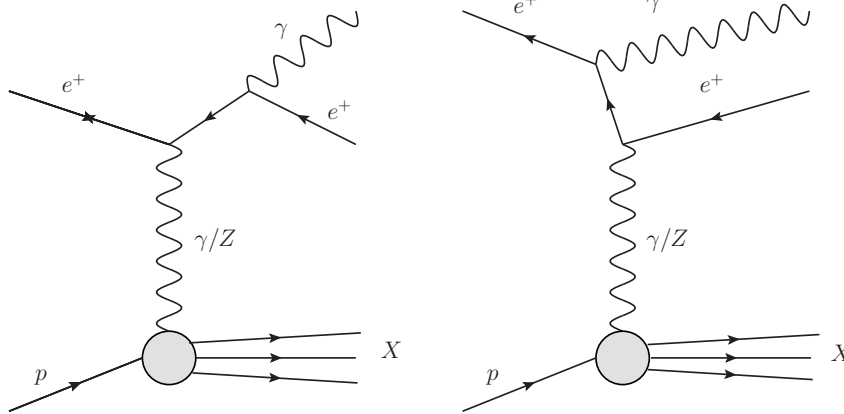


Figure 6.5: Feynman graphs of QED Compton processes: initial (right) or scattered (left) electron emits a hard photon.

6.2.3. Charged Current Deep Inelastic e^+p Scattering

CC DIS events, where a W-Boson is exchanged instead of a photon or Z-Boson are a background to NC DIS events as well. As through this interaction the electron is changed into a neutrino, which escapes the detector undetected, the signature of these events is clearly different: There is no scattered electron, but missing transverse momentum. This also leads to a $E - p_z$ distribution, which is very different to the NC DIS one.

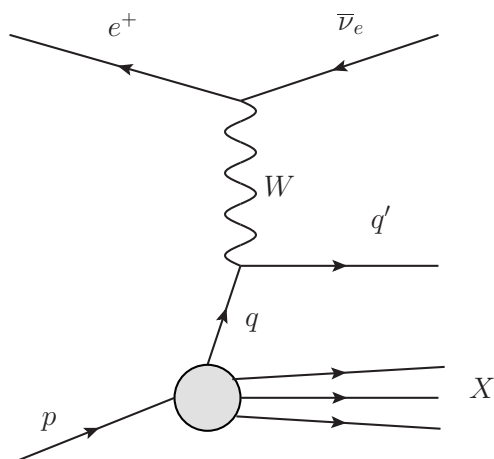


Figure 6.6: A Feynman graph of Charged Current Deep Inelastic e^+p Scattering.

ZEUS

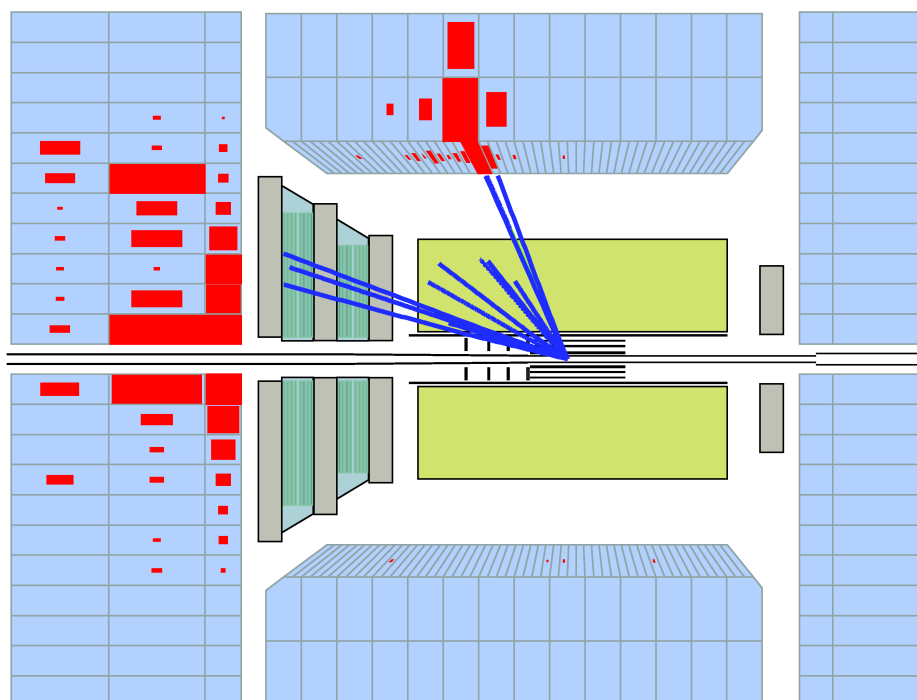


Figure 6.7: A CC DIS event in the ZEUS detector as visualised by the ZEVIS [100] event display. This event was reconstructed with $Q^2 \approx 53000 \text{ GeV}^2$ and $x \approx 0.59$.

6.2.4. Beam-gas and Beam-pipe Interactions

As the vacuum in the beam-pipes was not perfect, the beam electrons and protons could interact with the remaining molecules of the beam gas. Similarly interactions with the beam-pipe could also happen if the beam particles are not perfectly positioned. Already on trigger basis, such events were mostly rejected e.g. by the information from the Veto Wall.

Additionally they often create an imbalance of the transverse momentum and can be rejected by a cut on δ .

6.2.5. Halo Muons

“Halo” muons originate from the decay of hadrons which are produced by an interaction of the stored beam particles with residual beam gas (beam gas events) or with the beam pipe outside of the ZEUS detector. These muons are produced within the beam-pipe and move (nearly) parallel to it. They can create a fake electron signal in the calorimeter. In contrast to the signal events, halo muon events do often show an imbalance of the total transverse momentum due to interacting mainly in a located region of the calorimeter. Halo muons can also be rejected by calorimeter timing as they travel horizontally through the detector, so the timing of their arrival in the RCAL and the BCAL is different from particles coming from a vertex in the centre of the detector.

6.2.6. Cosmic Muons

“Cosmic” muons are produced in the atmosphere by the decay of e.g. pions which are created by the interaction of cosmic particles with the atoms of the atmosphere. They are part of cosmic showers and have often a very high energy and velocity leading to a quite long lifetime in the frame of the earth. In general, the transverse momentum of a cosmic muon event is not transversely balanced and the track does not go through a vertex in the centre of the detector. In addition, the timing of cosmic muons is naturally not in any way correlated with the bunch crossings. Thus timing is a good method to remove most of the cosmic muon background.⁴

6.3. Preselection

Event preselection consists of requirements of trigger bits (on FLT, SLT and TLT level) and the rejection of periods in which a detector component important for the analysis was not working properly.

Technically, before the creation of the analysis Ntuples possible suitable events were selected based on TLT bit DIS03 (explanation see Section 6.3.3). This preselection of events from the ZEUS 06/07 e^+p data was done using zesLite [131]. Based on the output of zesLite, Ntuples were created and the remaining preselection was done offline.

⁴For more information on cosmic muon rejection see [45, 46].

6.3.1. First Level Trigger

The FLT trigger bits (explanation of the FLT see Section 3.2.4) used for this analysis can be divided into two sub-categories: bits based on the detection of a possible isolated electron (FLT 28, FLT 30, FLT 36, FLT 39, FLT 46, FLT 47) and inclusive bits based on calorimeter energies mainly (FLT 40, FLT 41, FLT 43, FLT 44).

A detailed explanation of the trigger bits can be found in Appendix B. Here only a rough summary is given. On most of the trigger bits there are veto conditions from the Veto Wall, the C5 counters⁵, the SRTD, tracking conditions and others. For this analysis only the tracking vetoes necessitate further discussion and were described in Section 5.9. The logic required for the analysis is an OR of all the following FLT bits:

- **FLT 28:** Isolated electron in the FCAL or the BCAL and some track requirements⁶
- **FLT 30:** Isolated electron in the RCAL, more than 4 GeV⁷ in the EMC section of the RCAL or more than 15 GeV very close to beampipe (first inner ring)
- **FLT 36:** Isolated electron in the RCAL, more than 4 GeV⁸ in the EMC section of the RCAL or more than 5 GeV very close to beampipe (first inner ring) and some track requirements
- **FLT 39:** Isolated electron in the BCAL, more than 3.5 GeV in the EMC section of the BCAL and some track requirements
- **FLT 40:** More than 20 GeV of energy in the electromagnetic part of the calorimeter and some track requirements
- **FLT 41:** More than 30 GeV of total transverse energy in the calorimeter and some track requirements
- **FLT 43:** More than 15 GeV of total transverse energy in the calorimeter and some track requirements
- **FLT 44:** More than 5 GeV in the EMC section of the BCAL or more than 3.5 GeV in the EMC section of the FCAL and some track requirements
- **FLT 46:** Isolated electron in one of three quadrants of the RCAL⁹ and more than 2 GeV in the EMC section of the RCAL or more than 4 GeV if very close to beampipe (first inner ring) and some track requirements
- **FLT 47:** Isolated electron in one of three quadrants of the RCAL and more than 2 GeV in the EMC section of the RCAL or more than 4 GeV if very close to beampipe (first inner ring) and some track requirements in addition to a veto related to total calorimeter energy

⁵Veto Wall and C5 counters do check the timing of the event, which is necessary for rejection of non-ep backgrounds as described in Sections 6.2.4, 6.2.5 and 6.2.6.

⁶The requirements for tracks in the FLT and its consequences have been discussed in Section 5.9.

⁷The limit is only about 3.5 GeV for part of the investigated period.

⁸As for FLT 30 limit is only about 3.5 GeV for part of the investigated period.

⁹In the fourth quadrant, contribution from background sources was comparably high.

The above described sums of calorimeter energies exclude the first inner ring of CAL towers for the RCAL and the FCAL and by that avoid counting most of the energy from proton remnants and beam-gas events.

6.3.2. Second Level Trigger

The SLT (explanation of the SLT see Section 3.2.4) requirements are based on the FLT bits described above plus some additional information. On SLT level there is also vetoes, most importantly further timing vetoes against cosmic and halo muons and beam-gas events.

- **EXO 1:** Total transverse energy of more than 35 GeV
- **EXO 2:** Total transverse energy of more than 15 GeV if triggered by FLT 28 or total transverse energy of more than 25 GeV and $E - p_z > 15$ GeV
- **EXO 3:** Total transverse energy of more than 16 GeV and $E - p_z > 34$ GeV
- **DIS 7:** Triggered by a DIS FLT bit (28, 30, 31, 36, 39, 40, 41, 43, 44, 46, 47 or 62), an electron candidate with energy of more than 5 GeV, $(E - p_z) + 2 \cdot E_{Lumimonitor} > 29$ GeV ($E_{Lumimonitor}$ is the energy detected in the luminosity monitor originating from a radiated photon) and more than 2.5 GeV of energy in the EMC section of the BCAL or the RCAL or more than 10 GeV in the FCAL

The DIS bit is supposed to trigger most NC DIS events on SLT level. For triggering very high Q^2 events, the EXO bits, which are based on high transverse energy (excluding most of the proton remnant due to the the RCAL inner ring exclusion), are used.

6.3.3. Third Level Trigger

On the TLT (explanation of the TLT see Section 3.2.4) level only bit DIS03 was used for the selection. Its requirements are based on the FLT and SLT bits described above plus again some additional information not available at lower trigger levels. For DIS03 it is required

- Certain FLT and SLT bits (including requirements on CAL energy, an electron candidate or high transverse energy and a lower $E - p_z$ -cut)
- $(E - p_z) + 2 \cdot E_{Lumimonitor} > 30$ GeV
- $E - p_z < 100$ GeV
- Reconstruction of a primary vertex
- An electron candidate (outside a radius of 35 cm if in the RCAL) with an energy of more than 4 GeV

6.3.4. Data Quality

It was required that all detector components used in the NC DIS analysis were in good working condition. This was done using a requirement of EVTAKE bit (requires CTD, CAL, LUMI and the magnet to be working and at least 100 events in the run) as well as MVDTAKE and STTTAKE for the MVD and the STT.

In addition, it was required that the polarisation measurement was working. In contrast to the data quality bits described above, LPOLTAKE and TPOLTAKE are event-based bits and can change within a run. For the polarisation measurement it is enough if either LPOL or TPOL are working, but as luminosity numbers are only available for LPOL and TPOL separately (i.e. how much luminosity was recorded during all the time LPOLTAKE (TPOLTAKE) was TRUE for this run), it was not possible to require a simple OR of TPOLTAKE and LPOLTAKE as then the luminosity sum could not be calculated. Thus it was decided for each run whether to use LPOL or TPOL and all events within this run which were recorded during time the corresponding polarimeter was not working were discarded. To maximize luminosity always the polarimeter with the higher luminosity was chosen.¹⁰

6.4. Selection

The final selection criteria for the NC DIS events can be divided in the sub-categories trigger chain, data quality, positron selection (including detector-related geometry), background suppression, Monte Carlo validation and phase space. In the specific subsections these criteria are discussed in detail.¹¹ All selection criteria (including the trigger and data quality criteria described in the previous Section 6.3) are summarised for convenience in Appendix A.

6.4.1. Positron Selection

This subsection describes in detail the criteria used to find the scattered positron with high efficiency and purity. The EM finder [103] (see Section 4.7.1) is used to find suitable candidates on which the following requirements are imposed¹²:

- If more than one electron candidate is found, the one with the highest *EM Selection Probability* is selected.
- The *EM Grand Probability* should be greater than 0.001 to ensure that the candidate is most probably an electron.
- Scattered electron energy E'_e greater than 10 GeV selects a large kinematic range of NC DIS events and removes much background (most photoproduction events with fake scattered electron (e.g. from pions) have lower electron energies as can be seen in Figure 6.8).

¹⁰A summary of luminosity and polarisation numbers for the investigated periods is given in Table 4.1.

¹¹This set of selection requirements has been developed and improved over many years of analysing ZEUS NC DIS events (see e.g. [84], [85], [82], [86]).

¹²Any event in which there is no EM candidate is of course rejected.

- Requiring a matched track in CTD acceptance $0.3 < \theta < 2.5$ is a good tool to select electrons, where tracking detectors are available, in order to reject photons with a similar shower in the EMC part of calorimeter. The CTD acceptance range is discussed in Section 5.9.
- The track momentum of an associated track in CTD acceptance region should be higher than 3 GeV to increase the purity by lowering the probability that the track belongs to another particle.
- The track association is more refined by requiring the distance of closest approach (DCA) between the track and the calorimeter to be less than 10 cm (if the track is found in CTD acceptance region).
- A minimum distance to module edges of 1.5 cm is required (if the track is found in CTD acceptance region), as the energy measurement close to the edge of calorimeter modules is less reliable.
- The positron should be isolated: Energy not belonging to the positron within a cone of radius of $R = \sqrt{(\Delta\phi)^2 + (\Delta\eta)^2} = 0.8$ should be less than 5 GeV. This requirement improves the reliability of the energy measurement and reduces the number of fake positron candidates from the overlay of a hadron track and a photon deposit.

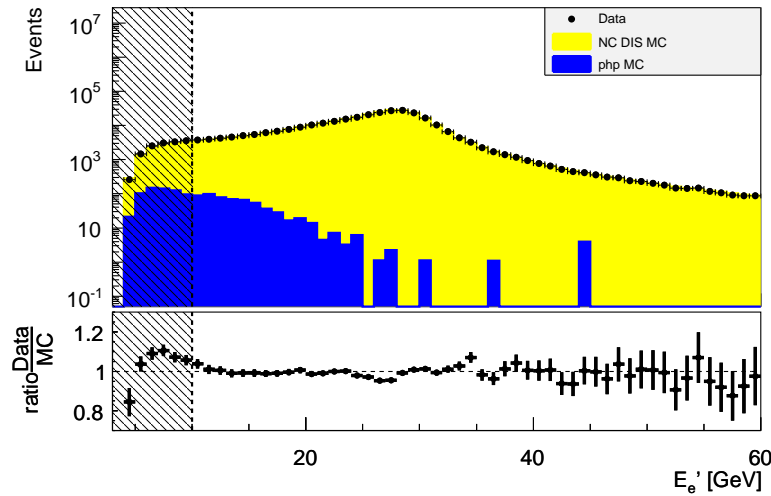


Figure 6.8: Positron energy E'_e , with data (black data points) and NC MC (yellow histograms) and the php background from MC (blue histogram). The selection includes all cuts and corrections except for the cut on the positron energy, for which the rejected part is indicated by the grey hashed area. In addition the ratio of data and MC is shown in the lower part of the plot.

Detector Geometry

This subsection describes in detail the selection criteria for the scattered positron due to detector constraints. The removal of some of the specific geometric regions from the sample can be seen in Figure 6.9.

- Events where the positron goes into one of the so-called supercracks between the RCAL and the BCAL or the BCAL and the FCAL pose problems to the precise energy measurement and simulation in the MC. Thus they are rejected by a cut on the z-position of the positron in calorimeter, rejecting events with the positron between -104.0 cm and -98.5 cm or between 164.0 cm and 174.0 cm.
- In upper central part of the RCAL there were pipes carrying liquid helium to and from the superconducting solenoid. There some CAL cells are missing and thus energies in this so-called chimney region are not precisely measured. Thus events with the positron were rejected if the absolute of their calorimeter x position was within 12 cm and their y position above 80 cm.
- The most outer part of the RCAL is screened by the BCAL, which leads to imprecise energy measurement [132, p. 89] and is not well simulated in MC, especially in the trigger simulation (shown in [132, p. 64]). Therefore events with the scattered positron in the RCAL are rejected if the radius of 175 cm is exceeded.

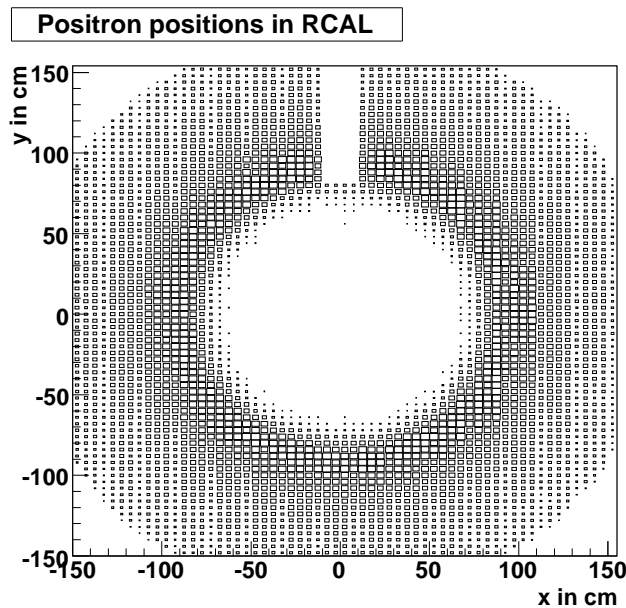


Figure 6.9: A plot showing the reconstructed positions of positrons in the RCAL. The size of the boxes is proportional to the number of events in this area. The prominent empty space in the upper central part is the chimney region.

6.4.2. Background Suppression

This subsection describes in detail the cuts mainly used for suppression of the backgrounds discussed in Section 6.2.

- As discussed in Section 6.1 the $E - p_z$ of NC DIS events should be around 55 GeV. As this is not the case for the background sources the cut $38 \text{ GeV} < E - p_z < 65 \text{ GeV}$ is very valuable for background reduction as visible for photoproduction in Figure 6.10.
- y is large for events in the FCAL, where tracking is not available, with low energies (see Equation 4.7). Without a track the probability of misidentifying a photon for an electron is very high, so $y_{el} < 0.9$ is required.
- The transverse momentum should be balanced for NC DIS events, so the global p_t should be 0 except for the limited resolution which is approximated as \sqrt{E} . So $p_t/\sqrt{E_t} < 4 \text{ GeV}^{0.5}$ is used to impose a transverse momentum balance. In addition $p_t/E_t < 0.7$ is required. Background which does not satisfy these criteria (e.g. cosmic and halo muons, beam-gas and beam-pipe events) are often not even simulated by the Monte Carlo, so it is important to remove them to be able to do a MC-based acceptance correction.
- Elastic QED Compton rejection¹³ is done according to [85] as elastic QED Compton events are neither well simulated nor rejected. Rejected are events by the following criteria which have two good electron candidates (one of them the misidentified photon in a QEDC event)
 - Two good electron candidates being back-to-back (azimuthal angle difference of more than 3 rad);
 - these candidates having balanced transverse momentum (ratio between 0.8 and 1.2),
 - and hardly any other activity in detector (less than 3 GeV of CAL energy from other sources)

Vertex

- The longitudinal vertex position is important for the reconstruction of the event and its kinematic variables. Best results and simulations are achieved for events with the vertex at the nominal interaction point. In addition most NC DIS events (of the primary bunches) do happen there, which is not true for non-ep background sources. Thus it is required that a vertex is found (according to $\chi_{vtx}^2 < 100$) and a cut on $|Z_{vtx}| < 30 \text{ cm}$ is done.
- For a good vertex it is required that at least one good track, associated to this vertex, is found. This track should satisfy having a transverse momentum of more than 0.2 GeV and pass through at least three superlayers.

¹³This cut does also reject di-electron events.

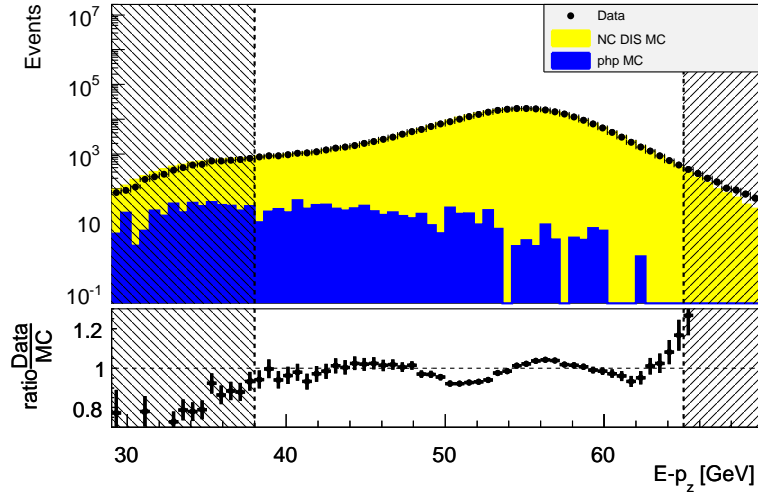


Figure 6.10: Control distribution of $E - p_z$ with data (black data points) and NC MC (yellow histograms) and the php background from MC (blue histogram). The selection includes all cuts and corrections except for the cut on the positron energy, for which the rejected part is indicated by the grey hashed area. In addition the ratio of data and MC is shown in the lower part of the plot.

6.4.3. Phase Space and Monte Carlo Validation

In this subsection the phase space selection is described.

- Events, where the hadronic final state is found very close to the beam pipe are not simulated very well due to the particles escaping detection through the beam hole. Then the measurement of the angle γ_{had} is not reliable, which is important for the kinematics calculation with the Double-Angle Method. Thus events where the γ_{had} -projection on the FCAL gives a value of less than 18 cm are rejected.
- At very low y and high x the MC is not valid due to missing higher order QED corrections [75], [133]. Thus a cut of $y_{JB}(1 - x_{DA})^2 > 0.004$ was used to remove this region.
- The phase space was limited to $Q_{DA}^2 > 185 \text{ GeV}^2$. The exact value was chosen to be consistent with previous measurements, especially [8] for the direct extraction of x_{F_3} and the easier input into the PDF fits. The lower Q^2 -limit made it also possible to use the Double-Angle Method reliably.

6.5. Comparison of Data and SM MC Prediction

In total 301428 events are selected from the data, which correspond to a reweighted 301851 events due to the correction of the RISOE trigger inefficiency (see Section 5.4.3). Whereas out of the 11,259,007 NC DIS MC events 4,156,683 are selected, which are

reweighted to 304562 including all corrections. From the photoproduction MC only 353 events (out of 1,160,000) were selected, which are reweighted to 602, so the background contribution is very small (about 0.2%).

The total event numbers, summarised in Table 6.1, (reweighted to the integrated luminosity and with all described corrections) do agree well within the uncertainty of the error on luminosity measurement (1.8% for RH and LH1, 2.1% for LH2) for all periods. The MC prediction is only based on leading order calculations and a difference of about 1.5% on total normalisation is expected to arise compared to next-to-leading order calculations.

	Data	NC MC	php MC	difference in %
All	301851	304562	602	1.10
RH	178697	179711	353	0.76
LH1	73132	73832	148	1.16
LH2	50022	50871	101	1.90

Table 6.1: Selected reweighted events from data and Standard Model prediction (signal NC MC and php background) for the whole sample and each subperiod. In addition the relative difference of prediction to data ($\frac{N_{MC}}{N_{Data}} - 1$) is shown. The numbers include all corrections described in this and the next chapter.

In Figure 6.12, the rate of NC DIS events over time is shown after implementation of all corrections. The changes of the rate are now described well by the MC prediction. The effect of the corrections is especially visible comparing Figure 6.12 to Figure 5.2, which shows the prediction without track veto efficiency (see Section 5.5), Z_{vtx} (see Section 5.7) and track matching efficiency (see Section 5.9) related changes.

Figure 6.11 shows an overview of the distributions of important kinematic variables. Agreement between data and SM prediction (including F_L correction) is good.

As the cross sections are measured in the kinematic variables Q^{214} , x and y , looking at the agreement for these variables is especially insightful. Control plots including ratio plots of all important variables can be found in Appendix C. As the description of the data is overall good (problems with the description of the tracking variables are described in 5.9 and 5.5 and are dealt with by the respective corrections) it is possible to use the MC for determining a reliable acceptance correction and unfold the cross sections.

¹⁴The bin around $\log(Q_{DA}^2) \approx 4.2$ has 6 data events, where approximately 16 are predicted. This is a deviation of about 2.5σ , which is not significant. Such a deviation is expected due to the large number of investigated bins.

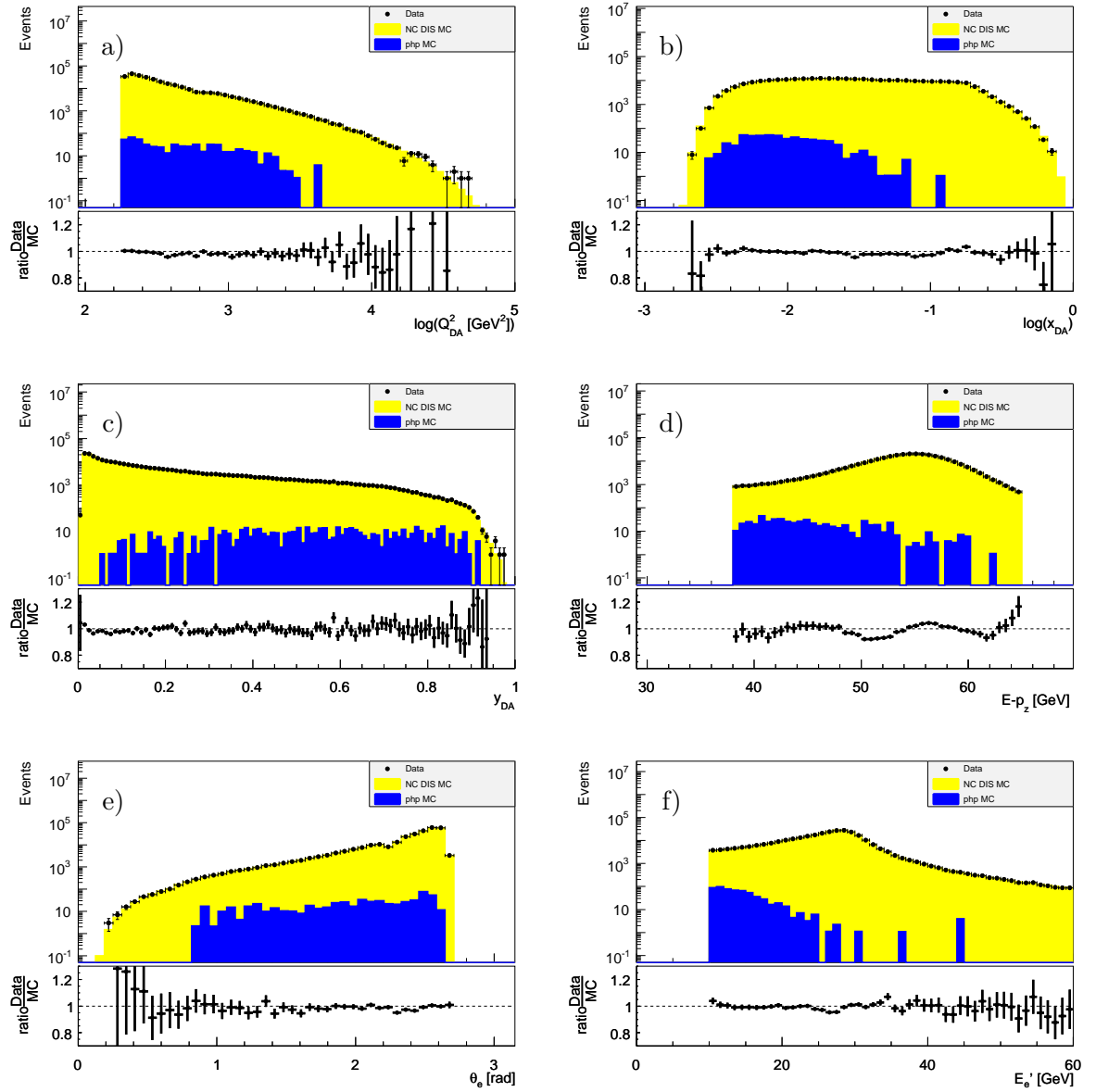


Figure 6.11: Distributions of important variables from high Q^2 NC selection. Data is represented by black points, the NC DIS MC by yellow histograms and the photoproduction background MC by blue histograms. a) shows $\log(Q_{DA}^2)$, b) $\log(x_{DA})$, c) y_{DA} , d) $E - p_z$, e) θ of the scattered positron and f) the energy of the scattered positron. In addition the ratio of data and MC is shown in the lower part of each plot.

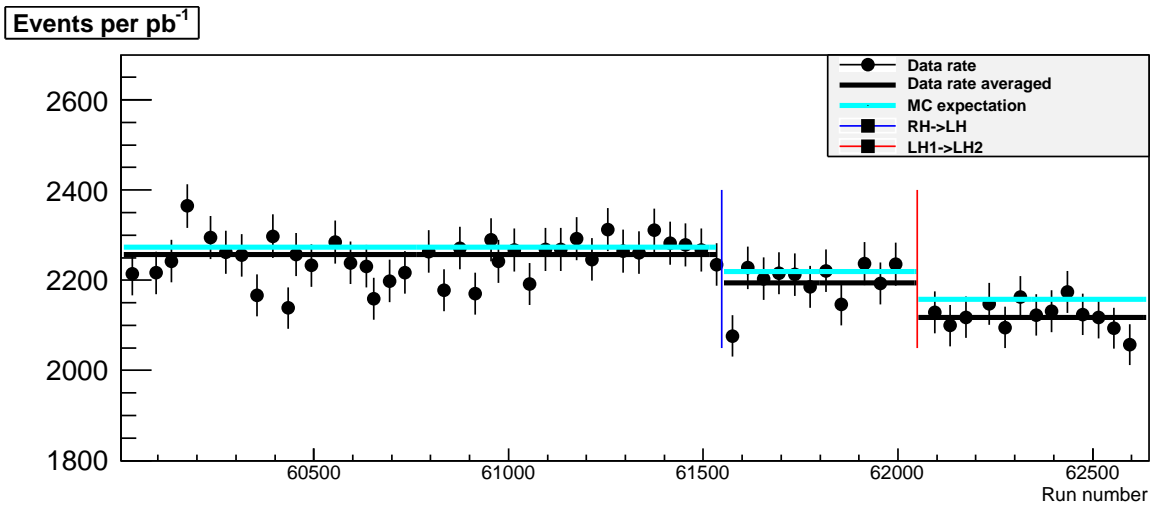


Figure 6.12: The number of NC events in the final sample per integrated luminosity (black points, error is error on luminosity measurement) compared to the expectation of the Standard Model. The blue line indicates the switch of polarisation from RH to LH, the red line the shutdown in early 2007. Here the MC prediction includes all corrections and selection is with the loosened cut on track requirement.

7. Studies of Systematic Uncertainties of the Cross Section Measurement

In this chapter the studies done to investigate systematic effects of the measurement, that can influence and bias the unfolding of the cross sections, are described. They must be taken into account for the uncertainty calculation.

For that first the cross section bins of the polarised and unpolarised cross section measurements are defined and their applicability is shown (Section 7.1, they are tabulated in Appendix G and H.). Next the cross section unfolding method is explained (Section 7.2).

Then systematic effects of the cross section measurement are discussed: Possible effects stem from the parton shower model of the MC, the algorithm used for identifying the scattered positron, the choice of selection thresholds and the corrections (described in Chapter 5). Each of these effects has been investigated and will be described. At the end of this chapter plots are shown that summarise the individual uncertainties in the same bins as used for the cross section measurements, which allows comparing them to each other, to the statistical uncertainty and to the uncertainty of the luminosity measurement.

7.1. Bin Definition

The size of the bins, in which the cross sections are extracted, is limited by mainly two factors: statistics (i.e. number of data events in the bin) and resolution of the variable as a function of which the cross section is measured. In addition for the extraction of xF_3 (and for the PDF fits) it is convenient to have the cross section extracted in the bins of the previous e^-p measurement [8]. As the measurement was done with the same detector and similar luminosity (169.9 pb^{-1}), the bins and their sizes were taken and checked for applicability within this analysis.

The quality of a bin can be expressed in terms of the purity P , efficiency E and acceptance A calculated from the MC according to

$$P = \frac{N_{gen, i}^{meas, i}}{N_{meas, i}}, \quad (7.1)$$

$$E = \frac{N_{gen, i}^{meas, i}}{N_{gen, i}}, \quad (7.2)$$

$$A = \frac{N_{meas, i}^{meas, i}}{N_{gen, i}}, \quad (7.3)$$

where $N_{gen, i}^{meas}$ is the number of events generated and measured in bin i , $N_{meas, i}$ is the number of events measured in bin i (regardless of where the events originated from) and $N_{gen, i}$ is the number of events generated in bin i (regardless of whether they were selected and in which bin they ended up reconstructed).¹

The purity quantifies the effect of migration between kinematic bins. A low purity values indicates that the bin is very much affected by migration from other bins into it and indicates that the bin is too small for the given resolution. In the cross section measurement low purity means you are endangered by not measuring the cross section of the bin region itself well enough, but are biased by the neighbouring bins.

The efficiency quantifies the fraction of signal events selected. Low efficiency means that you reject many events. It is not problematic in itself, but means that your statistics is much reduced and thus the statistical uncertainty increases.

The acceptance also counts the selected events, but regardless of whether they are signal events and correctly reconstructed. Other than for purity and efficiency values larger than 1 are possible for acceptance if more events migrate from other bins to the bin under investigation than are not selected in this bin though they were generated in it. The value of acceptance is needed for the bin-by-bin unfolding method described in Section 7.2.

From Equations 7.1, 7.2 and 7.3 it follows that acceptance, efficiency and purity are connected via the equation

$$A = \frac{P}{E} . \quad (7.4)$$

7.1.1. Bin Definition for the $\frac{d\sigma}{dQ^2}$ Measurement

For the single differential cross section $\frac{d\sigma}{dQ^2}$ 34 bins of Q^2 were defined covering Q^2 values from the analysis' cut-off value of 185 GeV² up to 51,200 GeV². The sizes of Q^2 bins up to about 2000 GeV² are similar in $\log(Q^2)$, for higher ones the size is increased due to statistical limitations.

The acceptances, purities and efficiencies within the bins are shown in Figure 7.1. The purity is about 70% on average and never below 60%. It is slightly increasing with Q^2 (where bin limits are determined not from the resolution but mainly from statistics). The dip at about 650 GeV² in efficiency and acceptance (i.e. less selected events) is due to the crack between RCAL and BCAL (see first detector geometry cut in 6.4.1).

7.1.2. Bin Definition for the $\frac{d\sigma}{dx}$ Measurement

For the extraction of single differential $\frac{d\sigma}{dx}$ cross sections there were two measurements done: one with the selection's lower Q^2 cut of 185 GeV² and one with a higher cut of 3000 GeV². The latter was done to extend the measurement to higher x and especially y (see Section 7.1.3) with reasonable values of acceptance, efficiency and purity.

For the measurement with Q^2 greater than 185 GeV² 8 x bins were defined starting from 0.0063 and going up to 0.25. For the measurement with Q^2 greater than 3000 GeV² 6 x bins were defined starting from 0.04 and going up to 0.75. For both cases, bins were of approximately logarithmically equal widths.

¹An event being generated in a bin refers to its true values.

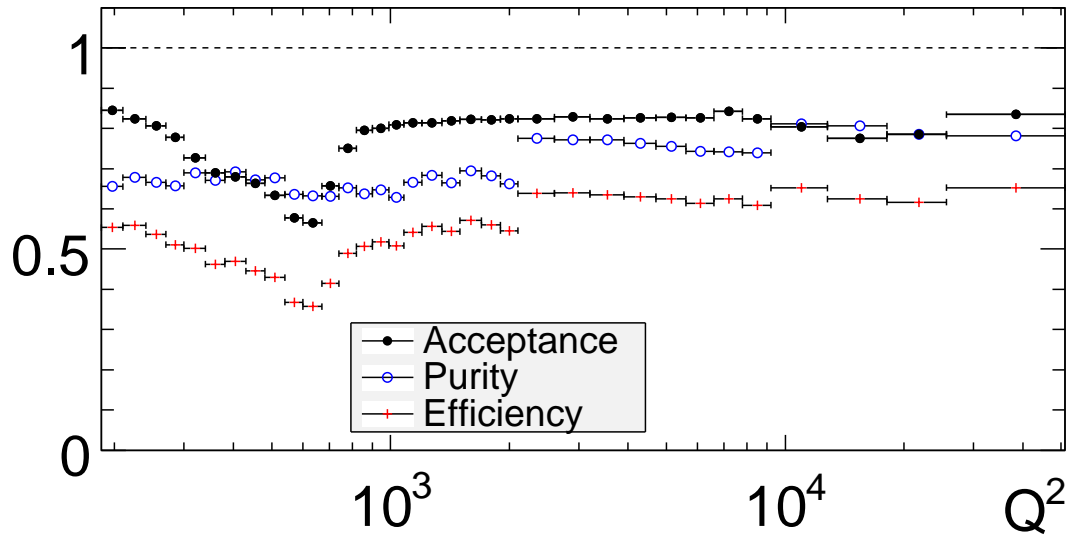


Figure 7.1: Acceptance (black filled dots), purity (blue empty dots) and efficiency (red crosses) in the bins of the $\frac{d\sigma}{dQ^2}$ measurement.

The acceptances, purities and efficiencies within the bins are shown in Figures 7.2 and 7.3. The purity is about 65% on average for $Q^2 > 185 \text{ GeV}^2$ and about 75% for $Q^2 > 3000 \text{ GeV}^2$, where it is increasing with x (where bin limits are mainly determined from statistics, not from resolution).

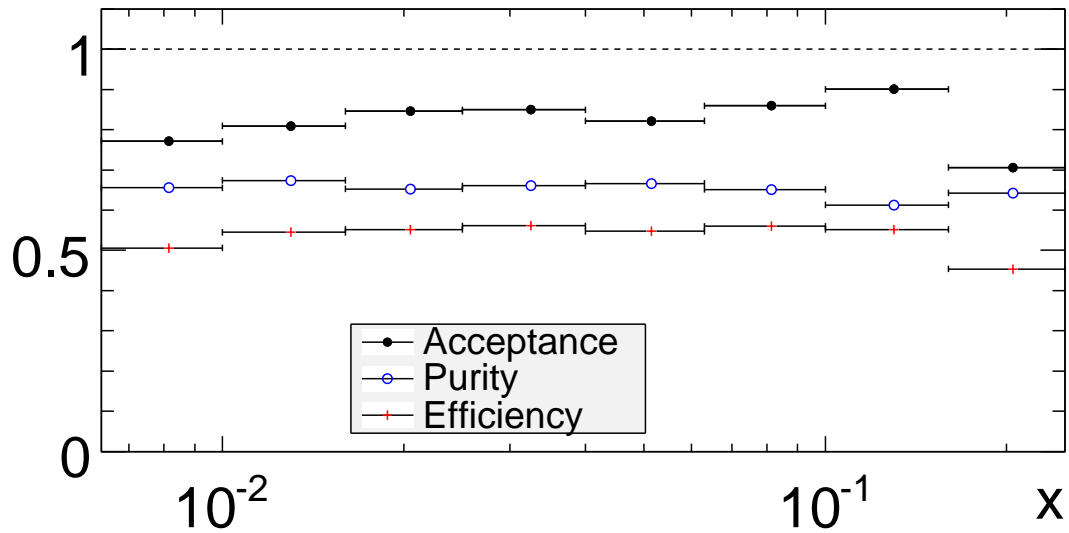


Figure 7.2: Acceptance (black filled dots), purity (blue empty dots) and efficiency (red crosses) in the bins of the $\frac{d\sigma}{dx}$ measurement with $Q^2 > 185 \text{ GeV}^2$.

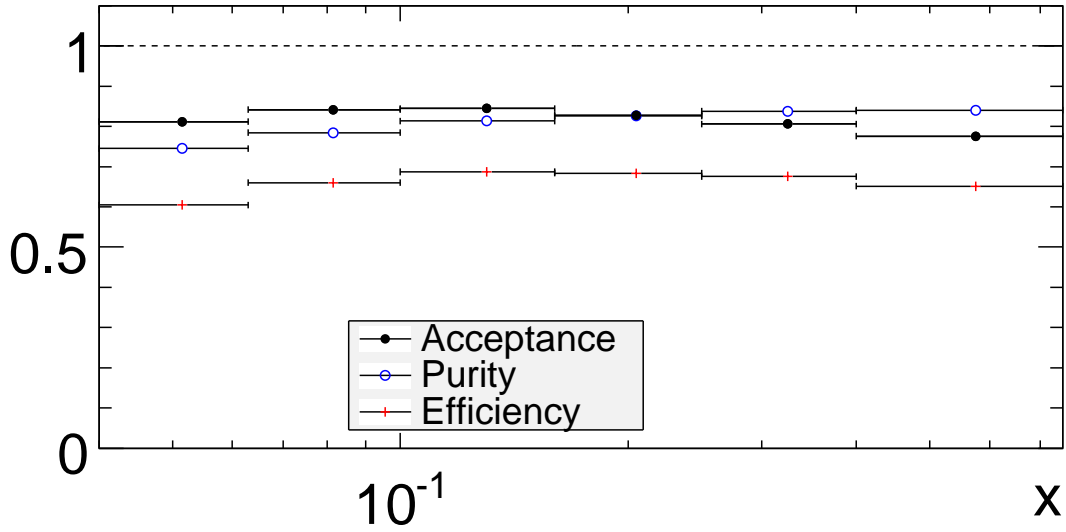


Figure 7.3: Acceptance (black filled dots), purity (blue empty dots) and efficiency (red crosses) in the bins of the $\frac{d\sigma}{dx}$ measurement with $Q^2 > 3000 \text{ GeV}^2$.

7.1.3. Bin Definition for the $\frac{d\sigma}{dy}$ Measurement

For the extraction of $\frac{d\sigma}{dy}$ there were equally two measurements done: one with the selection's lower Q^2 cut of 185 GeV^2 and one with a higher cut of 3000 GeV^2 .

For the Q^2 greater than 185 GeV^2 measurement 15 y bins were used, the lowest starting from 0 and the highest going up to 0.75. For the Q^2 greater than 3000 GeV^2 measurement 17 y bins of were used starting from 0.05 and going up to 0.9. For both cases, bins were of equal widths of 0.05.

The acceptances, purities and efficiencies within the bins are shown in Figures 7.4 and 7.5. The purity is about 55% on average for $Q^2 > 185 \text{ GeV}^2$ and about 65% for $Q^2 > 3000 \text{ GeV}^2$.

In both cases the purity decreases with y considerably, but less for the measurement with $Q^2 > 3000 \text{ GeV}^2$. For the measurement with $Q^2 > 185 \text{ GeV}^2$ it starts with a purity of larger than 80%, then the purity drops to only slightly above 40% at $y \approx 0.5$. This is due to the efficiency of the selection, which drops because of very tight selection criteria in this region to remove photoproduction background - mainly the lower cut on the energy of the scattered positron, which puts an upper limit on y^2 (see Equation 4.7).

7.1.4. Bin Definition for the Reduced Cross Section Measurement

90 bins are defined with a Q^2 between 185 and 50000 GeV^2 and x between 0.0037 and 0.75. The purity is above 50% in all bins, on average it is about 65%. It is rising with Q^2 .

²The limit on y is a function of $\cos(\theta_e)$ or (using Equation 4.5 in addition to Equation 4.7) a function of Q^2 : $y = 1 - \frac{Q^2}{4} \cdot E_e'^2$.

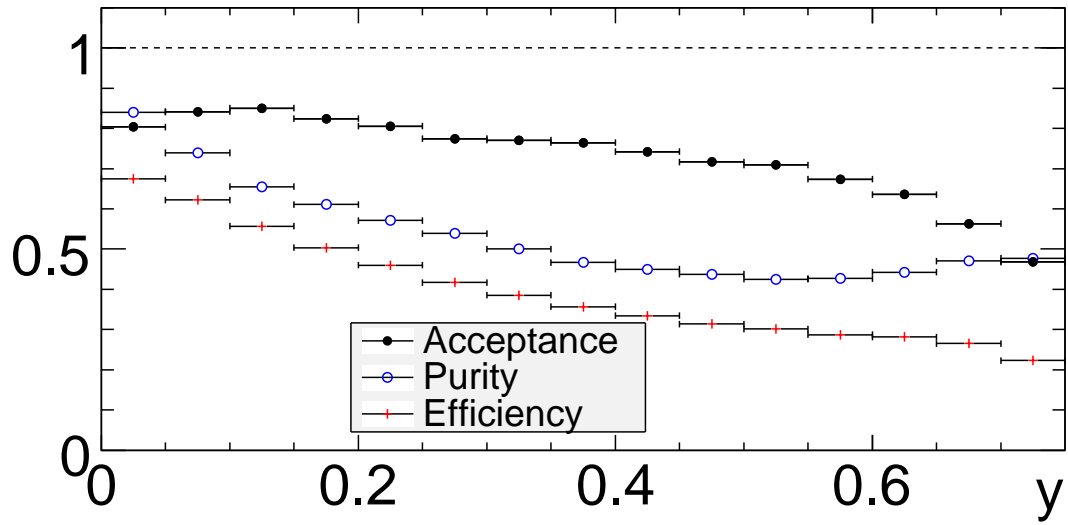


Figure 7.4: Acceptance (black filled dots), purity (blue empty dots) and efficiency (red crosses) in the bins of the $\frac{d\sigma}{dy}$ measurement with $Q^2 > 185 \text{ GeV}^2$.

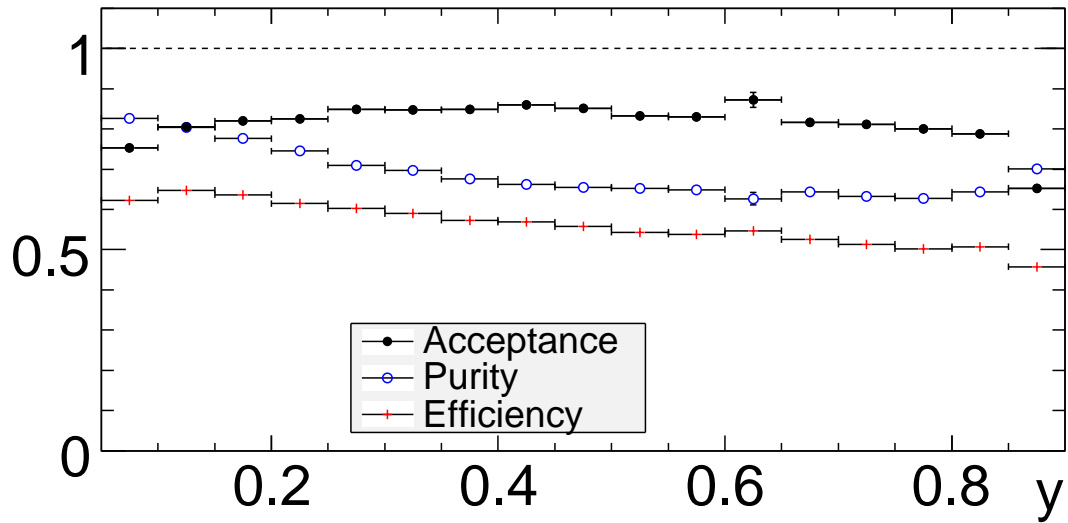


Figure 7.5: Acceptance (black filled dots), purity (blue empty dots) and efficiency (red crosses) in the bins of the $\frac{d\sigma}{dy}$ measurement with $Q^2 > 3000 \text{ GeV}^2$.

In the highest Q^2 bins, it is much higher (as there the bin size is limited by statistics and not by resolution).

7.2. Unfolding

What has been shown in the previous chapters is how to get the number of events and the values of acceptance in the bins described. To obtain the cross sections from those numbers a bin-by-bin unfolding method is used.

In general, in addition to Equation 3.5, for extracting the Born-level cross section at a specific point one needs to take into account

- background subtraction,
- acceptance correction,
- radiative corrections and
- bin-centering correction.

Background Subtraction

As the measured data events do not only include NC DIS events, the background contribution (estimated from photoproduction MC) needs to be subtracted and Equation 3.5 gives for the NC DIS cross section in the bin σ_i

$$\sigma_i = \frac{N_i^{data} - N_i^{php}}{\mathcal{L}} \cdot C_i^a, \quad (7.5)$$

where N_i^{data} is the number of data events in the bin, N_i^{php} the number of photoproduction MC events in that bin and \mathcal{L} is the integrated luminosity of the data sample. C_i^a are the remaining correction factors described below.

Acceptance Correction

The cross section needs to be corrected for the measurement's acceptance (see Equation 7.3). This leads to

$$\sigma_i = \frac{N_i^{data} - N_i^{php}}{\mathcal{L} \cdot A_i} \cdot C_i^b, \quad (7.6)$$

with the acceptance value of the bin A_i and the remaining correction factor C_i^b .

Radiative Corrections

As the data include electroweak radiative effects, there needs to be a radiative correction (calculated from theory corrections) to get to the cross section at Born level

$$\sigma_i = \frac{N_i^{data} - N_i^{php}}{\mathcal{L} \cdot A_i} \cdot \frac{\sigma_i^{born}}{\sigma_i^{rad}}, \quad (7.7)$$

where σ_i^{born} is the theoretical cross section at Born-level and σ_i^{rad} is the theoretical cross section including radiative corrections.

Bin-centering Correction

The events are measured in a bin. To get the differential cross section of a variable w at a specific point w_{point} the theoretical prediction has to be used:

$$\frac{d\sigma_i}{dw}(w_{point}) = \frac{N_i^{data} - N_i^{php}}{\mathcal{L} \cdot A_i} \cdot \frac{\sigma_i^{born}}{\sigma_i^{rad}} \cdot \frac{\frac{d\sigma_i^{born}}{dw}(w_{point})}{\sigma_i^{born}}, \quad (7.8)$$

where $\frac{d\sigma_i^{born}}{dw}(w_{point})$ is the theoretical prediction at w_{point} .

As visible from Equation 7.8, as long as the theoretical predictions are done in the same order and the cross sections are evaluated using the same PDFs this equation becomes

$$\frac{d\sigma_i}{dw}(w_{point}) = \frac{N_i^{data} - N_i^{php}}{\mathcal{L} \cdot A_i} \cdot \frac{\frac{d\sigma_i^{born}}{dw}(w_{point})}{\sigma_i^{rad}}. \quad (7.9)$$

Using MC prediction for Unfolding

If the NC DIS MC includes radiative processes and is of the same order and uses the same PDFs as the theoretical prediction for $\frac{d\sigma_i^{born}}{dw}(w_{point})$ the relation

$$\mathcal{L} \cdot \sigma_i^{rad} \cdot A_i = N^{NC \text{ DIS MC}}, \quad (7.10)$$

with the number of events from NC DIS MC, $N^{NC \text{ DIS MC}}$, holds.

The conditions are met for the NC DIS MC used in this analysis (see Section 4.2.1), which is based on HERACLES, and the used HECTOR prediction also based on HERACLES. [134], [85, p. 96]

Thus Equation 7.9 can be simplified and finally the cross section can be extracted using the following expression

$$\frac{d\sigma_i}{dw}(w_{point}) = \frac{N_i^{data} - N_i^{php}}{N^{NC \text{ DIS MC}}} \cdot \frac{d\sigma_i^{born}}{dw}(w_{point}). \quad (7.11)$$

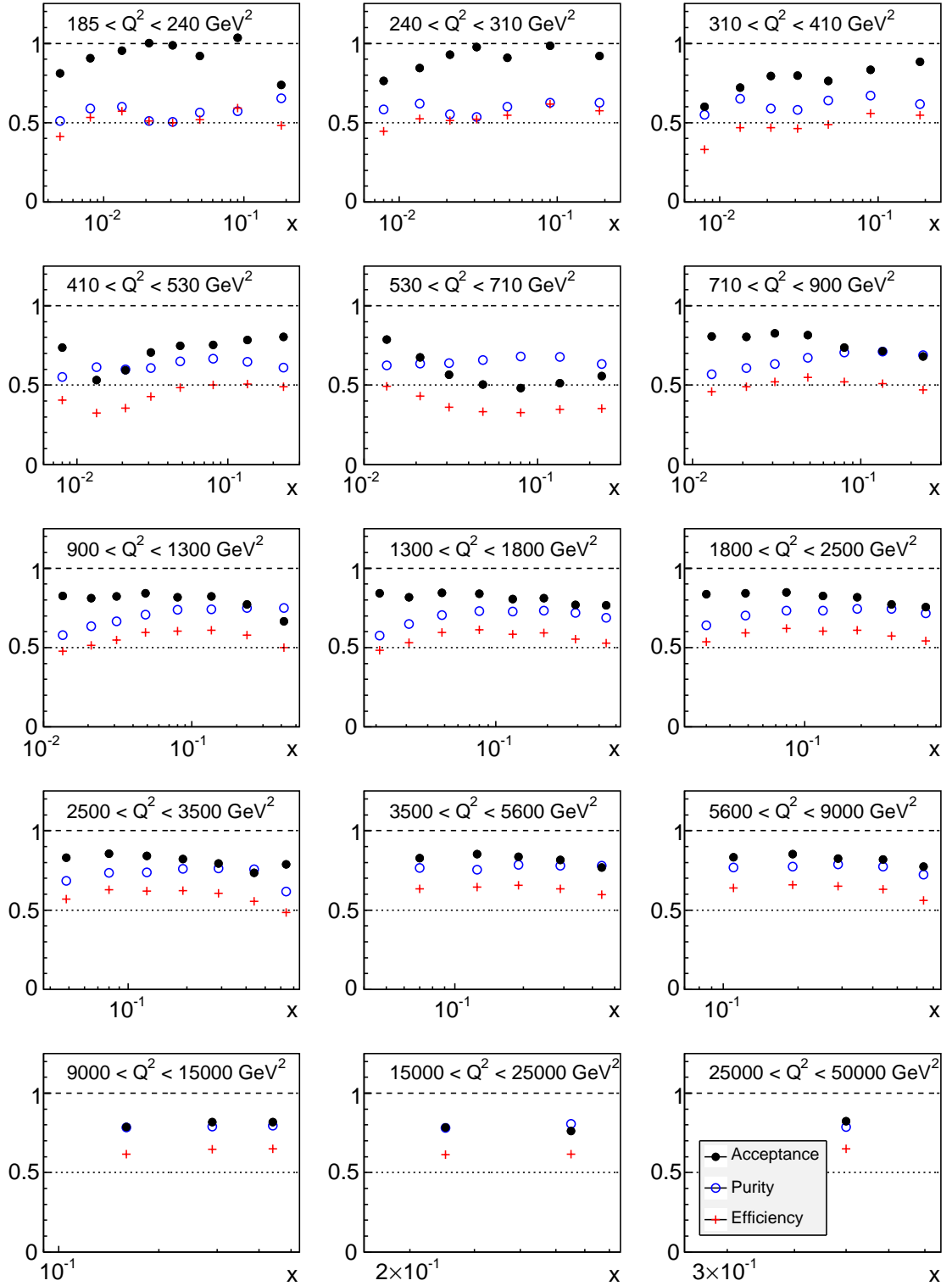


Figure 7.6: Acceptance (black filled dots), purity (blue empty dots) and efficiency (red crosses) in the bins of x and Q^2 for the double differential cross section measurement.

7.3. Dependence on Parton Shower Model

As the acceptance corrections are calculated from the MC simulation the measured cross section directly depends on them. Thus this dependence needs to be accounted for in the uncertainties. This was done using a different MC using the MEPS model from LEPTO [80] instead of ARIADNE (see Section 4.2). The main difference of the two programs is that MEPS uses the matrix element parton shower model whereas ARIADNE employs the colour-dipole model of the hadronic shower. In addition, using two Monte Carlo simulations also accounts for the overall uncertainties in setting up a MC simulation.

Comparing the results from both samples in this analysis the main differences between MEPS and ARIADNE are in the variables directly connected to the hadronic final state as expected (see e.g. the comparison of the total sum of the transverse momentum $\sum \vec{p}_t$ in Figure 7.7), but a difference can also be seen in variables such as the number of EM electron candidates to which the differences propagate indirectly (see Figure 7.8) which MEPS over- and ARIADNE underestimates. In comparison much smaller differences are in the variables in which the cross sections are measured (see Q^2 plot in Figure 7.9). In general both MC samples describe the data reasonably well and neither is considerably worse/better than the other.

Overall the MEPS MC leads to 0.3% less expected events than the ARIADNE MC. The uncertainty on the cross section in the bins used for the measurement is of the order of 0.5-2% reaching up to 7% in low statistics bins.³

³This could possibly be improved by including more or bigger MC samples at higher Q^2 , but as in this region the statistical error is by far dominant, it is not necessary.

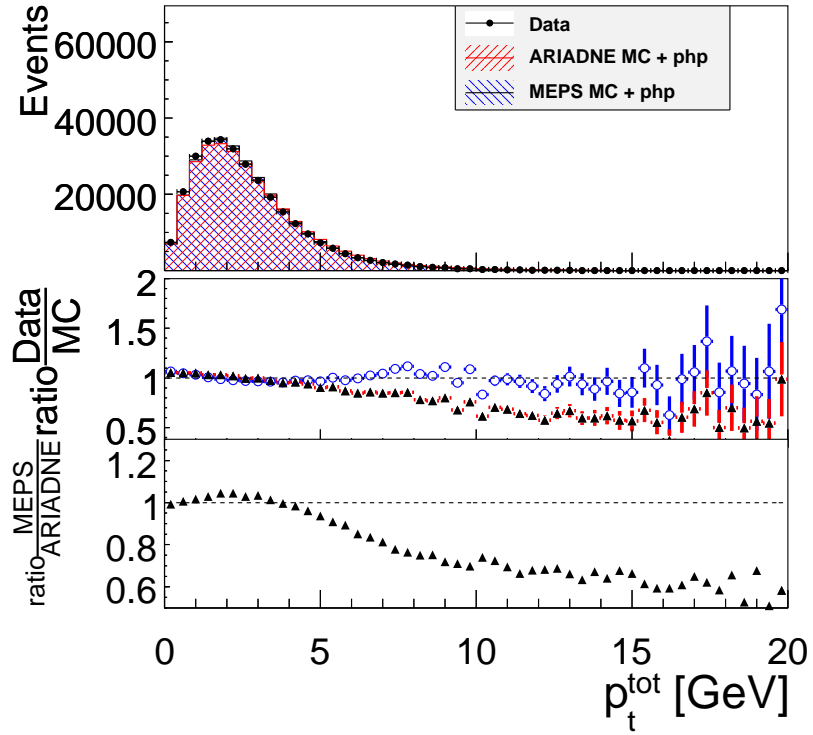


Figure 7.7: Distribution of the total transverse momentum showing the number of data events (black points) compared to the ARIADNE NC DIS MC (red hashed histogram) and the MEPS NC DIS MC (blue hashed histogram). The upper plot shows the absolute event numbers, the middle plot the ratio of data and MC predictions and the lower plot the ratio of the different MC generators.

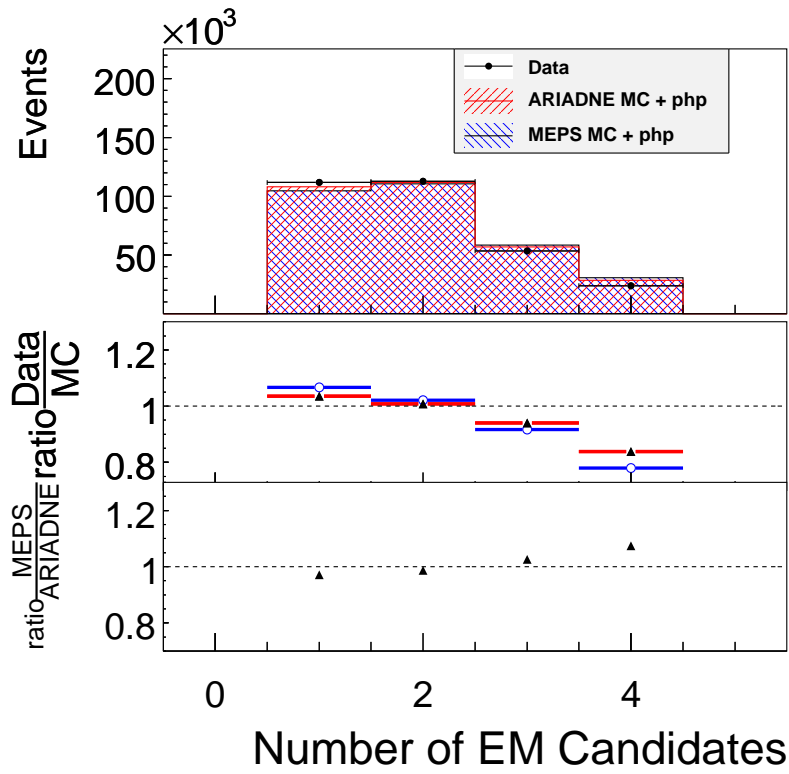


Figure 7.8: Distribution of the number of electron candidates from the EM finder showing the number of data events (black points) compared to the ARIADNE NC DIS MC (red hashed histogram) and the MEPS NC DIS MC (blue hashed histogram). The upper plot shows the absolute event numbers, the middle plot the ratio of data and MC predictions and the lower plot the ratio of the different MC generators.

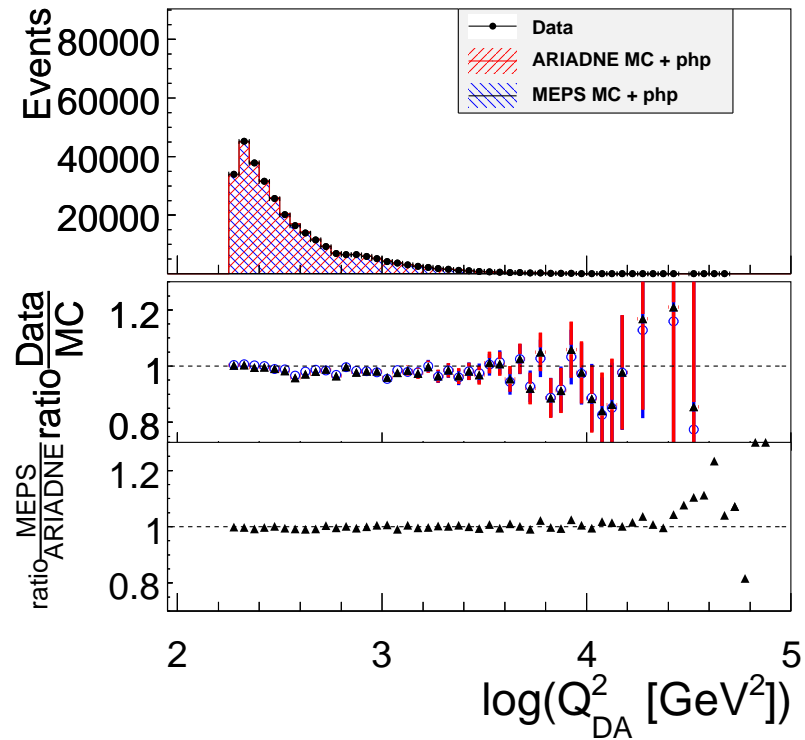


Figure 7.9: Distribution of $\log(Q_{DA}^2)$ showing the number of data events (black points) compared to the ARIADNE MC (red hashed histogram) and the MEPS MC (blue hashed histogram). The upper plot shows the absolute event numbers, the middle plot the ratio of data and MC predictions and the lower plot the ratio of the different MC generators.

7.4. Dependence on Positron Finder

For investigation of the effects due to characteristics of the EM electron finder [103] (see description in Section 4.7.1) the analysis was done with the SINISTRA electron finder [104], which is based on a neural-network algorithm, instead of EM. As the BCAL energy corrections in the current format were not available when using SINISTRA they were switched off for EM for this study as well to allow a direct comparison. Using SINISTRA resulted typically in a higher cross section, the difference being about 0.5-2%, but reaching about 10 times as much in high y and high Q^2 bins. Similar effects have been observed in past analyses (see e.g. [84]) and studies regarding the differences of the electron finders can be found in [105] and in [84, App. C] with regard to the NC DIS analyses. The exact reason of the higher cross section and the shape of the difference remains unclear.

Within the course of this analysis another study was done to investigate the uncertainty due to the electron finding: instead of the EM candidate with the highest selection probability the candidate with the highest EM grand probability is used (see Section 4.7.1 for an explanation of EM probabilities). The shape of the differences due to this change are indeed very similar to the changes due to changing to SINISTRA including the bump at medium Q^2 . Thus it looks like the main difference is within the $\frac{1}{Q^4}$ suppression factor or the P_{pt} probability (see Section 6.4.1).⁴

Due to the strong correlation of both effects, only the uncertainty due to the change to SINISTRA was included in the computation of the total systematic error.

7.5. Dependence on Energy Scaling and Smearing

The energy of the positron influences the measurement in different ways, most significantly through the selection cut requiring at least 10 GeV. The precision of the energy measurement and its description by MC simulation were described in Section 5.8. The error on the overall scale after this procedure is below 0.5%, but differs in different kinematic regions (non-uniformity effects), so that a 1% uncertainty is a reasonable choice to use for the uncertainty of the cross section measurement. A variation of 1% leads to less than 0.5% uncertainty in most cross section bins, but reaching up to 3% in high- y bins (see Figure 7.13).

Also the error on smearing was considered and the MC energy smeared by 1% more or 1% less. The effect was found to be negligible (about 0.1%, maximum of 0.3% in a single bin of the double-differential cross section).

The hadronic energy was shifted by 1% in both directions as well. Due to the weak dependence of this measurement on the hadronic energy (discussed in Section 5.8) the effect was comparably small, mostly less than 0.1%, nowhere reaching more than 0.7%.

⁴It should be mentioned though that the medium Q^2 region is also the region of BCAL and this study was done without BCAL corrections, but (as mentioned before) for both electron finders.

7.6. Correction and Photoproduction Cross Section Uncertainties

To improve the description of the data by the MC simulation the following correction methods were applied (described in Chapter 5)⁵:

- Track veto efficiency correction (TVE)
- Track matching efficiency correction (TME)
- Polarisation correction
- RISOE correction
- Z_{vtx} correction

The uncertainty coming from the Z_{vtx} reweighting procedure is indirectly accounted for by the variation of the Z_{vtx} cut (see Section 7.7).

The RISOE correction itself is so small, that its uncertainty can be neglected.

Also the uncertainty of the polarisation correction is not considered. It would only be sizable for the higher Q^2 regions in which the statistical uncertainty by far dominates.

The TVE correction uncertainty is important and the error of the fit is considerable. Thus it is varied by 50% in both directions to calculate the systematic uncertainty. The main influence of TVE is for medium Q^2 . The uncertainty due to the TVE there is about 1.5% (see Figure 7.10 and e.g Figure F.6).

For TME purposes the cut value of the positron polar angle θ for track requirement was changed to 2.5 due to the dropping of the TME in this region. Figure 5.27 shows that varying this cut value by 0.1 is a reasonable choice for uncertainty calculation. Overall the uncertainty due to the TME is below 1%, but reaching up to 2% in the low Q^2 region (see Figure 7.10 and Figure F.1).

As the uncertainty of the photoproduction cross section might be related to the TME in BCAL they are treated as a combined systematic effect by variation of the photoproduction cross section of 50%. The resulting uncertainty on the cross section measurement reaches up to 1.4% in the middle Q^2 region (which is the BCAL region), but for most bins is about 0.1-0.2%.

7.7. Cut Threshold Sensitivity

The selection criteria, where a sizable difference could occur from the cut variation, were varied within a region of reasonable cut variation. The following criteria (see Section 6.4 for detailed description of the criteria) were varied by the mentioned amount:

- Track momentum of the scattered positron in the CTD acceptance region $p_{trk} > 3$ GeV varied by 1 GeV in both directions

⁵As the F_L correction was not needed for the cross section extraction, there is no systematic error originating from it.

- Distance of closest approach between positron track and cluster $DCA(\text{Track,Cluster}) < 10$ cm in the CTD acceptance region set to 8 cm
- Energy not assigned to the e^+ in $R = \sqrt{(\Delta\phi)^2 + (\Delta\eta)^2} = 0.8$ cone < 5 GeV varied by 2 GeV in both directions
- $38 \text{ GeV} < E - p_z < 65 \text{ GeV}$: making the boundaries tighter or looser by 2 GeV on each side
- $p_t/\sqrt{E_t} < 4 \text{ GeV}^{0.5}$ varied by $1 \text{ GeV}^{0.5}$ in both directions
- $p_t/E_t < 0.7$ varied by 0.1 in both directions
- $|Z_{vtx}| < 30$ cm varied by 5 cm in both directions
- γ_{had} -projection onto FCAL > 18 cm varied by 2 cm in both directions

Using this as systematic uncertainty the arbitrariness of the exact cut value is taken into account. The difference caused by the cut threshold variation on the measured cross section is shown in Table 7.1.⁶

Cut	variation	\approx influence in %	highest DD influence
p_{trk}	± 1 GeV	0.3%	6%
DCA	-2 cm	0.2%	6%
E_{cone}	± 2 GeV	neg.	5%
$E - p_z$	± 2 GeV	0.5%	5%
$p_t/\sqrt{E_t}$	± 1 GeV	neg.	0.1%
p_t/E_t	± 0.1	neg.	2%
$ Z_{vtx} $	± 5 cm	0.3%	7%
$Proj_{\gamma_{had}}$	± 2 cm	0.1%	6%

Table 7.1: Amount of variation and approximate change of the cross section for cut variation. Selection criteria where the variation shows that the influence on cross section is completely negligible are marked as *neg.*. The last column denotes the highest influence in any of the double-differential cross section bins.⁷

The main effect from the cut variation comes from the $E - p_z$, followed by the $|Z_{vtx}|$ and the p_{trk} cut variation. In general the systematics due to the cut variations are very small though, which shows the good choice of selection criteria and good description of the data by the MC simulation.

⁶The threshold sensitivity is also a measure of the description of the data variable in question by MC.

⁷The highest influence is normally in a low statistics bin, where the systematics is completely dominated by statistics and the reason for the systematic being so high is most probably statistics as well.

7.8. Major Effects

From the above sections it can be concluded that the effect of the different systematics is of very different sizes. The Figures 7.10, 7.11, 7.13 and 7.12 and 7.14 summarise them for the single-differential cross sections and Figure 7.15 shows an example for the double-differential case, for which plots of the other bins are shown in Appendix F.

It can be concluded that the dominant sources of the systematic uncertainties are the change of EM electron finder to SINISTRA (0.5-2% on average) and using MEPS MC including a different parton shower model instead of ARIADNE MC (0.5-2% on average). In addition there is the bin-to-bin correlated uncertainty on the luminosity (1.8% for the RH and the LH1 period, 2.1% for the LH2 period), which is not shown on the plots, but is not negligible. The TME and TVE correction uncertainties are important for the low Q^2 region. $E - p_z$ cut variation (mainly for higher Q^2) and shifting of the positron energy are important as well.

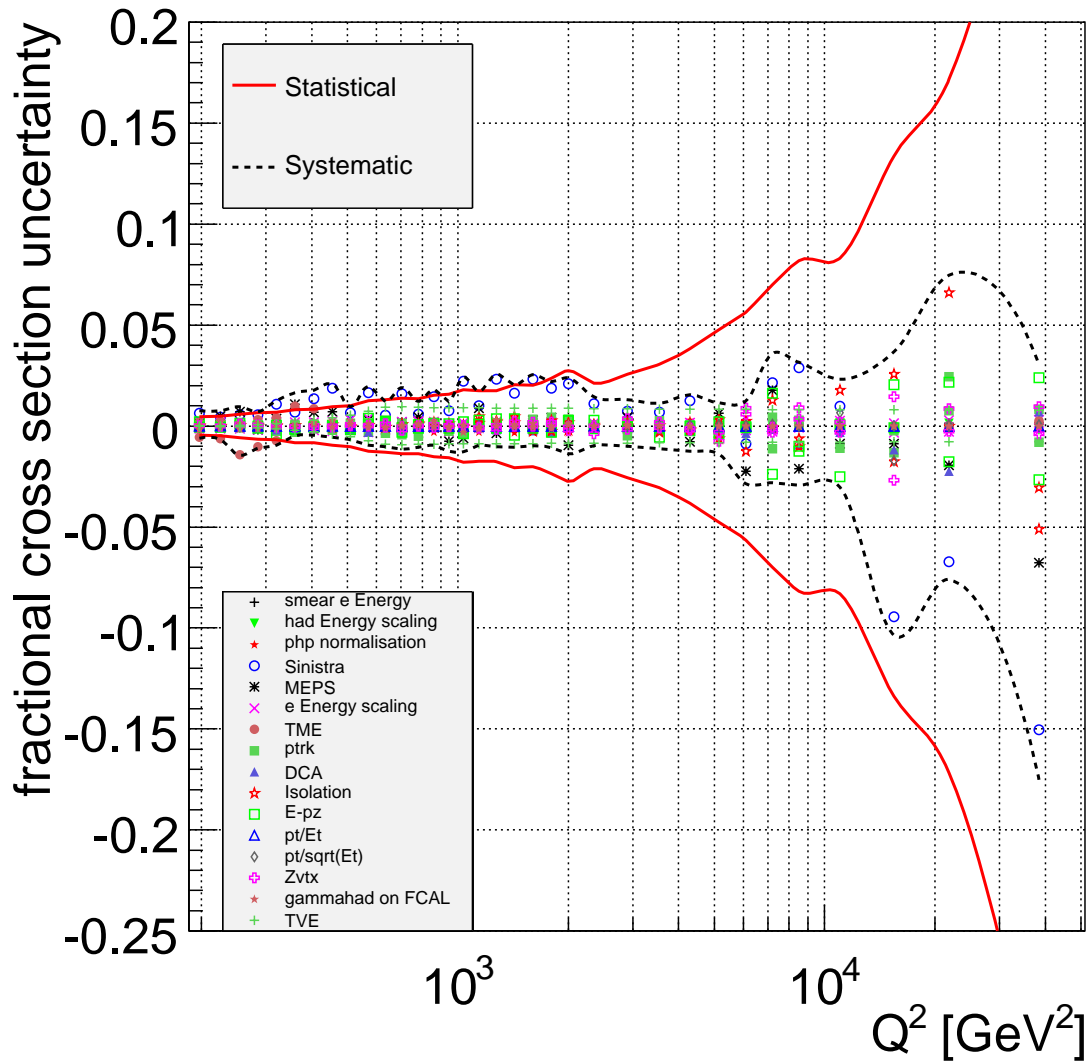


Figure 7.10: The fractional systematic and statistical uncertainties of the differential cross section $\frac{d\sigma}{dQ^2}$ for $y < 0.9$. Indicated by the symbols are the individual systematic uncertainties. Red lines show the statistical and dashed black lines the quadratic sum of all systematic uncertainties.

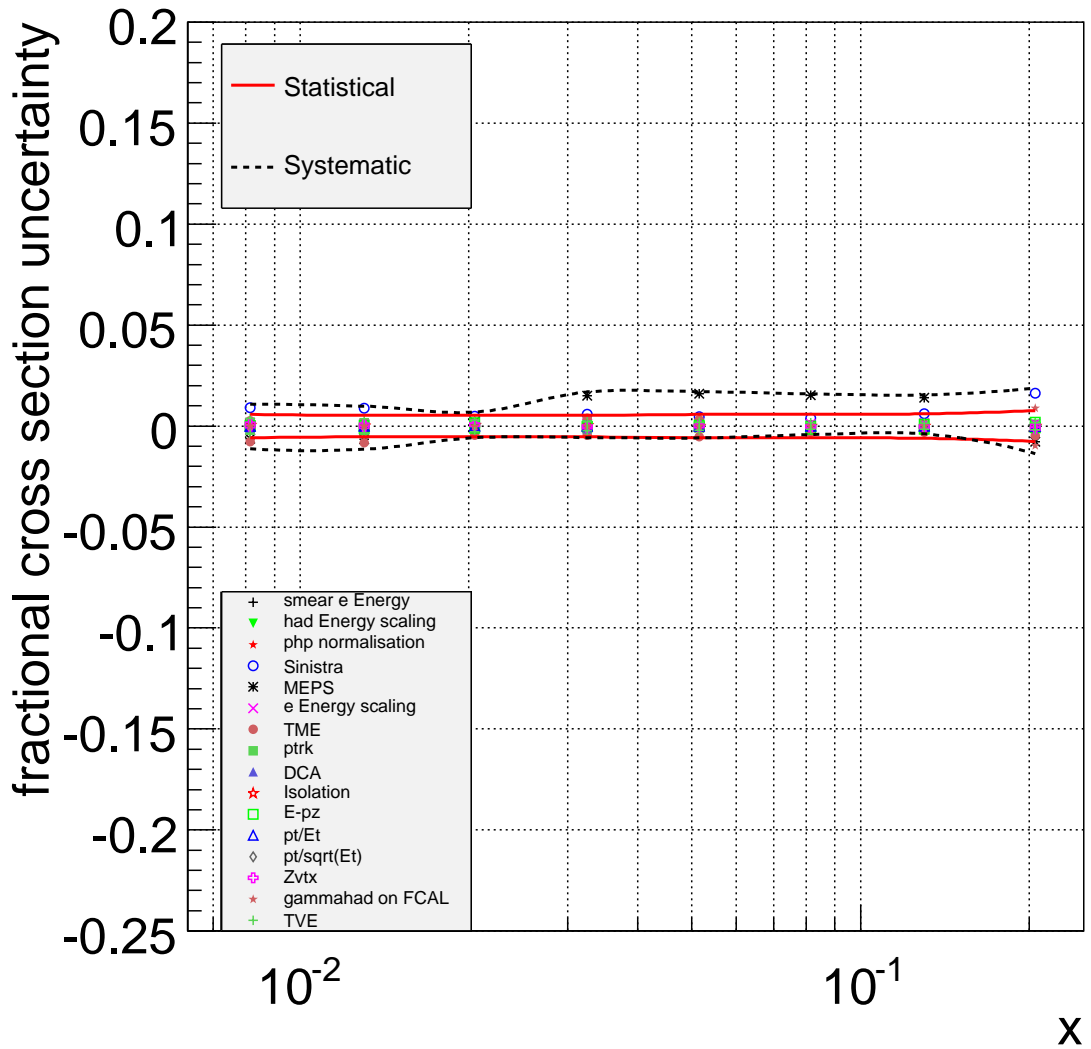


Figure 7.11: The fractional systematic and statistical uncertainties of the differential cross section $\frac{d\sigma}{dx}$ for $Q^2 > 185 \text{ GeV}^2$ and $y < 0.9$. Indicated by the symbols are the individual systematic uncertainties. Red lines show the statistical and dashed black lines the quadratic sum of all systematic uncertainties.

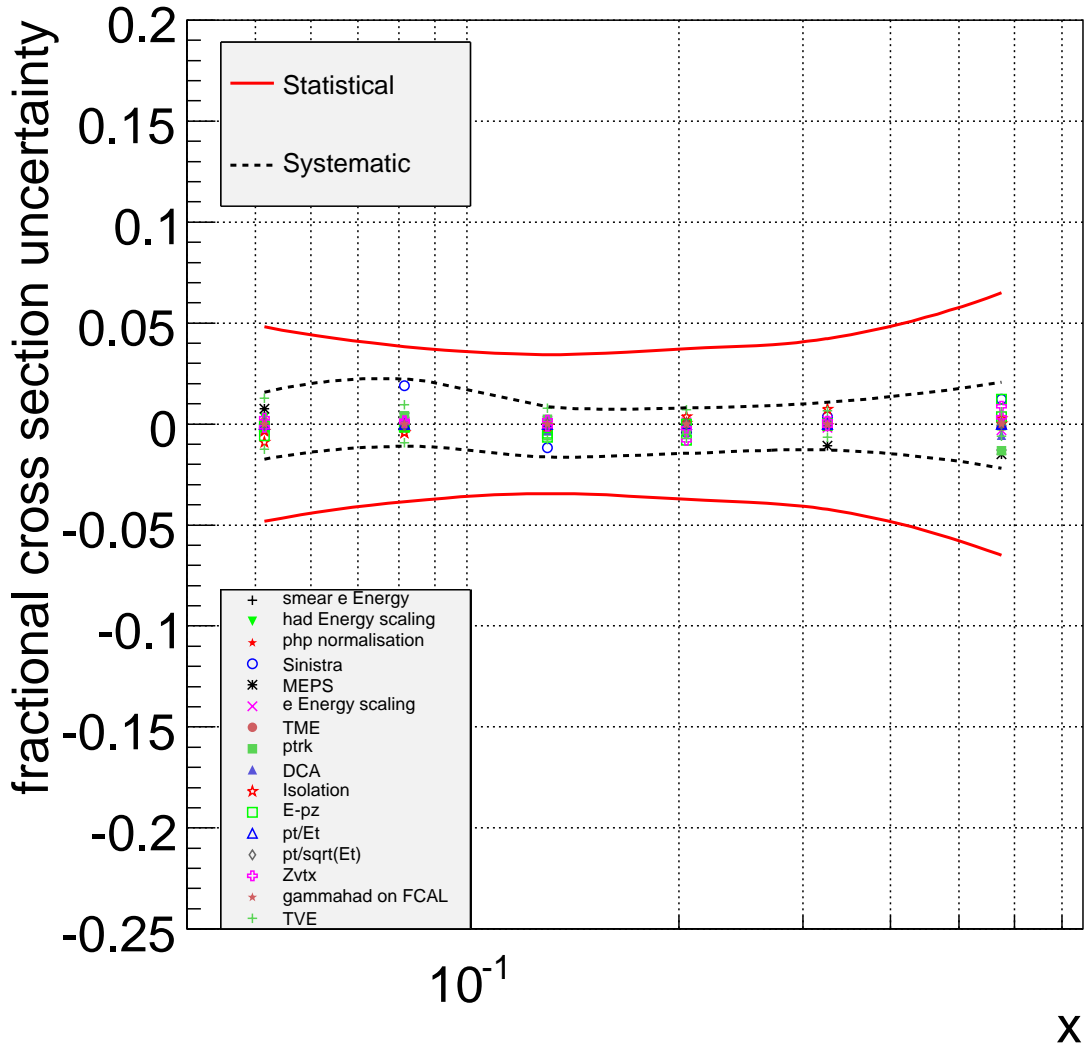


Figure 7.12: The fractional systematic and statistical uncertainties of the differential cross section $\frac{d\sigma}{dx}$ for $Q^2 > 3000 \text{ GeV}^2$ and $y < 0.9$. Indicated by the symbols are the individual systematic uncertainties. Red lines show the statistical and dashed black lines the quadratic sum of all systematic uncertainties.

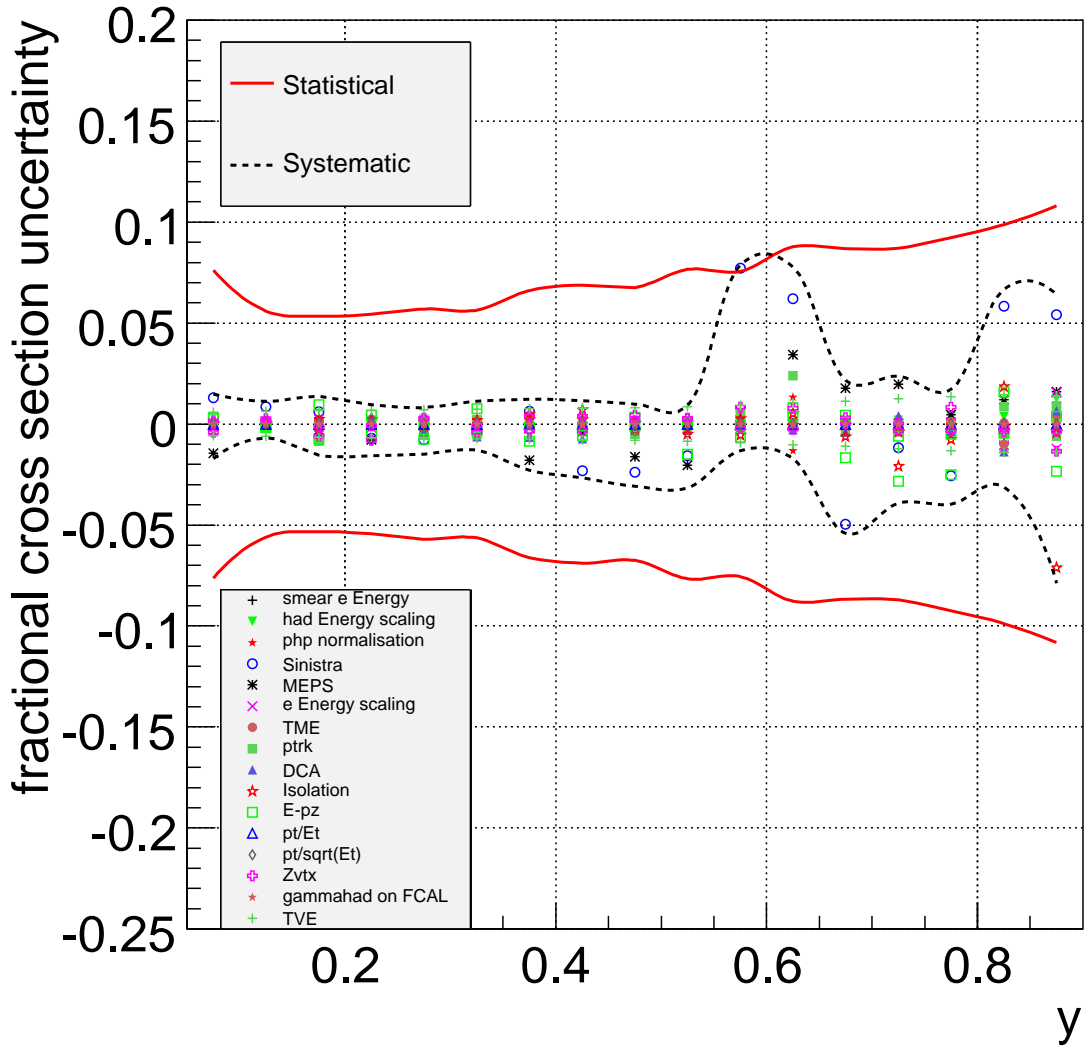


Figure 7.14: The fractional systematic and statistical uncertainties of the differential cross section $\frac{d\sigma}{dy}$ for $Q^2 > 3000 \text{ GeV}^2$. Indicated by the symbols are the individual systematic uncertainties. Red lines show the statistical and dashed black lines the quadratic sum of all systematic uncertainties.

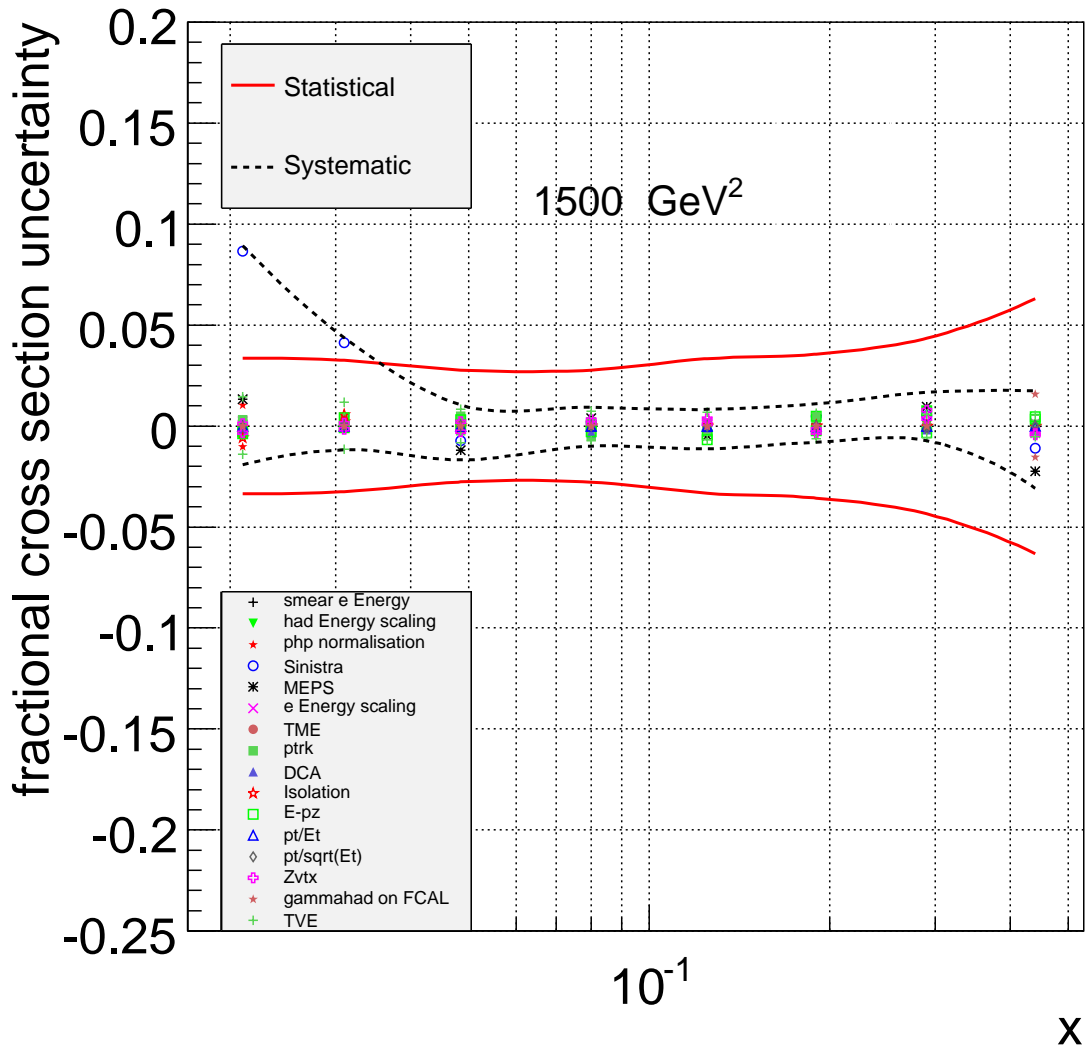


Figure 7.15: The fractional systematic and statistical uncertainties of the double-differential cross section $\frac{d\sigma}{dx dQ^2}$ in the bin of $Q^2 = 1500 \text{ GeV}^2$. Indicated by the symbols are the individual systematic uncertainties. Red lines show the statistical and dashed black lines the quadratic sum of all systematic uncertainties.

8. Results

In this chapter the results extracted using the selection described in Chapter 6 are presented. The cross sections are presented in the bins described in Section 7.1. They include the statistical and systematic uncertainties (see Chapter 7).

The unpolarised cross sections together with the published e^-p measurement are used to extract the structure function xF_3 (Section 8.1). Finally the polarised cross sections (separate cross sections for positive and negative polarisation) are used for extracting the polarisation asymmetry (Section 8.2) and the asymmetry A^+ , a measure of the parity violation of NC DIS.

8.1. Unpolarised Cross Sections

The average lepton beam polarisation of the e^+p sample is $P_e = +0.03$, which has very small influence on the NC cross sections. So the complete selected sample is basically unpolarised. The remaining polarisation is corrected for by the theory prediction using HECTOR:

$$\frac{d\sigma_i}{dw}(w_{point})_0 = \frac{d\sigma_i}{dw}(w_{point}) \cdot \frac{\frac{d\sigma_i^{born}}{dw}(w_{point})_0}{\frac{d\sigma_i^{born}}{dw}(w_{point})_{0.03}}, \quad (8.1)$$

where $\frac{d\sigma_i}{dw}(w_{point})$ is the measured cross section without correction of remaining polarisation, $\frac{d\sigma_i}{dw}(w_{point})_0$ is the measurement corrected for the polarisation, $\frac{d\sigma_i^{born}}{dw}(w_{point})_0$ is the unpolarised theoretical prediction and $\frac{d\sigma_i^{born}}{dw}(w_{point})_{0.03}$ the prediction at a polarisation of 0.03.

In the following the results of unpolarised cross sections are shown. The numbers are tabulated in Appendix G and Appendix H.

8.1.1. Unpolarised Single Differential Cross Sections

Figure 8.1 shows the measured single differential cross sections $\frac{d\sigma}{dQ^2}$, $\frac{d\sigma}{dx}$ and $\frac{d\sigma}{dy}$ in the phase space of the analysis ($Q^2 > 185 \text{ GeV}^2$, $y < 0.9$, $y(1-x)^2 > 0.004$). The results show the completely unpolarised ($P_e = 0$) cross sections, corrected for the remaining polarisation (see Equation 8.1). The measurement spans about 3.5 orders of magnitude of Q^2 in which $\frac{d\sigma}{dQ^2}$ decreases by about seven orders as expected due to the Q^{-4} dependence of the Standard Model NC DIS cross section (see Equation 2.27).

Confirming the Standard Model prediction $\frac{d\sigma}{dx}$ drops with increasing x and $\frac{d\sigma}{dy}$ drops with increasing y , very steeply so at small y .

All the measured cross sections confirm the Standard Model predictions. They all have very small uncertainties and thus the measurement is a precision measurement,

which can be used to test the Standard Model and extract Standard Model parameters.

8.1.2. Unpolarised Reduced Cross Sections

Figure 8.2 shows the measured reduced cross sections $\tilde{\sigma}$ as a function of x at fixed Q^2 values. In addition the published ZEUS e^-p results [8] are shown. Both are corrected to unpolarised values. The differences between the e^-p and e^+p cross sections become clearly visible at high Q^2 , where the structure function $x\tilde{F}_3$ (see Equation 2.27) becomes sizable. At low Q^2 $x\tilde{F}_3$ is negligible as it does not have a pure photon exchange term. Thus $x\tilde{F}_3$ is relevant only in high- Q^2 regions where γZ interference and Z exchange become important (see Figure 2.5).

The data are well described by the Standard Model prediction evaluated using HERAPDF 1.5¹. Furthermore the errors are so small that using the data in PDF fits is expected to be able to improve the precision of the PDFs (see Chapter 9).

8.1.3. $x\tilde{F}_3$

The reduced cross sections of this analysis together with the ones from the published e^-p analysis [8] can be used to extract the structure function \tilde{F}_3 . Due to the different sign in front of $x\tilde{F}_3$ for e^+p and e^-p in Equation 2.27 it can be extracted as:

$$x\tilde{F}_3 = \frac{Y_+}{2Y_-}(\tilde{\sigma}^{e^-p} - \tilde{\sigma}^{e^+p}) . \quad (8.2)$$

The result is shown in Figure 8.3 using a conservative approach for the uncertainties treating the systematic errors as uncorrelated between the e^-p and the e^+p analysis. Especially in the highest Q^2 bins the leading systematic errors are mostly correlated between the e^-p and the e^+p analysis. There the uncertainty is better approximated by the statistical error only. For the lower Q^2 bins uncorrelated systematics like the TVE and TME (as these corrections are not included in the e^-p analysis) are important, so the systematic uncertainty cannot be treated as correlated for all bins as that would mean underestimation of the errors.

8.1.3.a. $xF_3^{\gamma Z}$

Equation 2.31 for the unpolarised case of $P_e = 0$ states for xF_3

$$x\tilde{F}_3 = -a_e\chi_Z xF_3^{\gamma Z} + 2v_e a_e\chi_Z^2 xF_3^Z . \quad (8.3)$$

From Figure 2.5 in combination with the small value of v_e (see Table 2.2) it can be seen that the $F_3^{\gamma Z}$ term by far dominates in the Q^2 region of this analysis. So $F_3^{\gamma Z}$ can be approximated as:

$$xF_3^{\gamma Z} \approx -\frac{x\tilde{F}_3}{a_e\chi_Z} . \quad (8.4)$$

¹The e^-p data is included in the fit for HERAPDF 1.5. The description of the data by CTEQ6D was found to be good as well.

This makes it possible to extract $xF_3^{\gamma Z}$ using of the data of this analysis together with the published e^-p data. The results are shown in Figure 8.4. It is visible that the Q^2 dependence is not very strong. To improve the precision of the $xF_3^{\gamma Z}$ measurement as a function of x , $xF_3^{\gamma Z}$ is re-extracted at $Q^2 = 1500 \text{ GeV}^2$ using - in addition to the $Q^2 = 1500 \text{ GeV}^2$ values - the $xF_3^{\gamma Z}$ values from points at the same x , but different Q^2 , which are corrected via

$$xF_3^{\gamma Z}(1500) \approx -\frac{x\tilde{F}_3(\text{point})}{a_e\chi_Z} * \frac{xF_3^{\gamma Z}(1500)_{THEO}}{xF_3^{\gamma Z}(\text{point})_{THEO}}, \quad (8.5)$$

where $xF_3^{\gamma Z}(1500)_{THEO}$ is the theoretical prediction at $Q^2 = 1500 \text{ GeV}^2$ and $xF_3^{\gamma Z}(\text{point})_{THEO}$ the theoretical prediction at the Q^2 point from which the measurement is taken.

The results of the combination of the values is shown in Figure 8.5. It is more precise than previous measurements of $F_3^{\gamma Z}$ at ZEUS as it uses the two large statistics periods of HERA-II ZEUS data. The errors are calculated from the fit of all $xF_3^{\gamma Z}$ values² at the same x value.

²The errors of e^+p and e^-p are treated as uncorrelated.

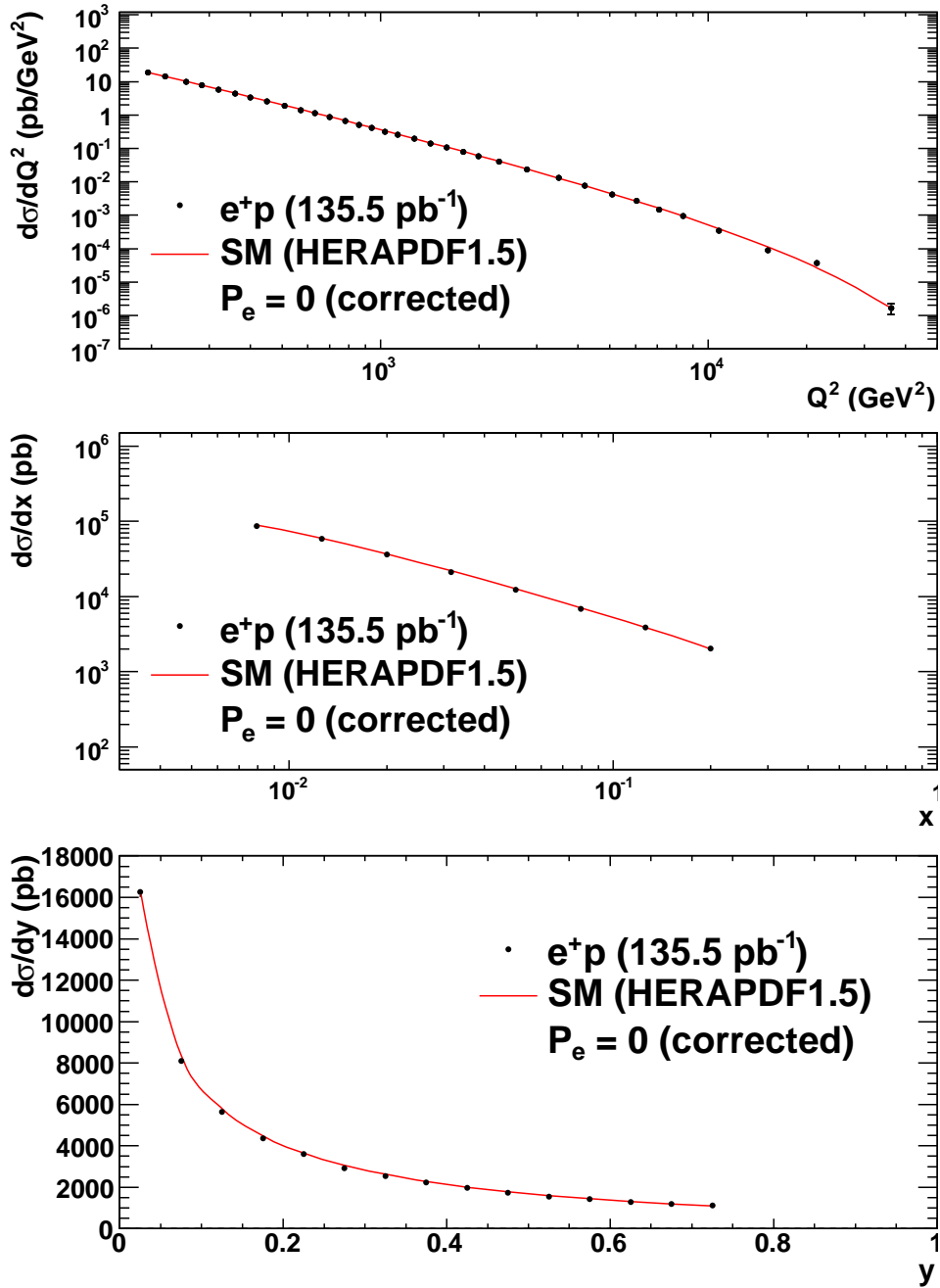


Figure 8.1: The unpolarised e^+p single differential cross sections $\frac{d\sigma}{dQ^2}$ (top), $\frac{d\sigma}{dx}$ (middle) and $\frac{d\sigma}{dy}$ (bottom) for $Q^2 > 185 \text{ GeV}^2$, $y < 0.9$, $y(1-x)^2 > 0.004$. The closed circles represent the data points and the curves show the predictions of the Standard Model evaluated using the HERAPDF 1.5 PDFs. The outer error bars represent the full uncertainty including systematics, the inner error bars the statistical uncertainty only.

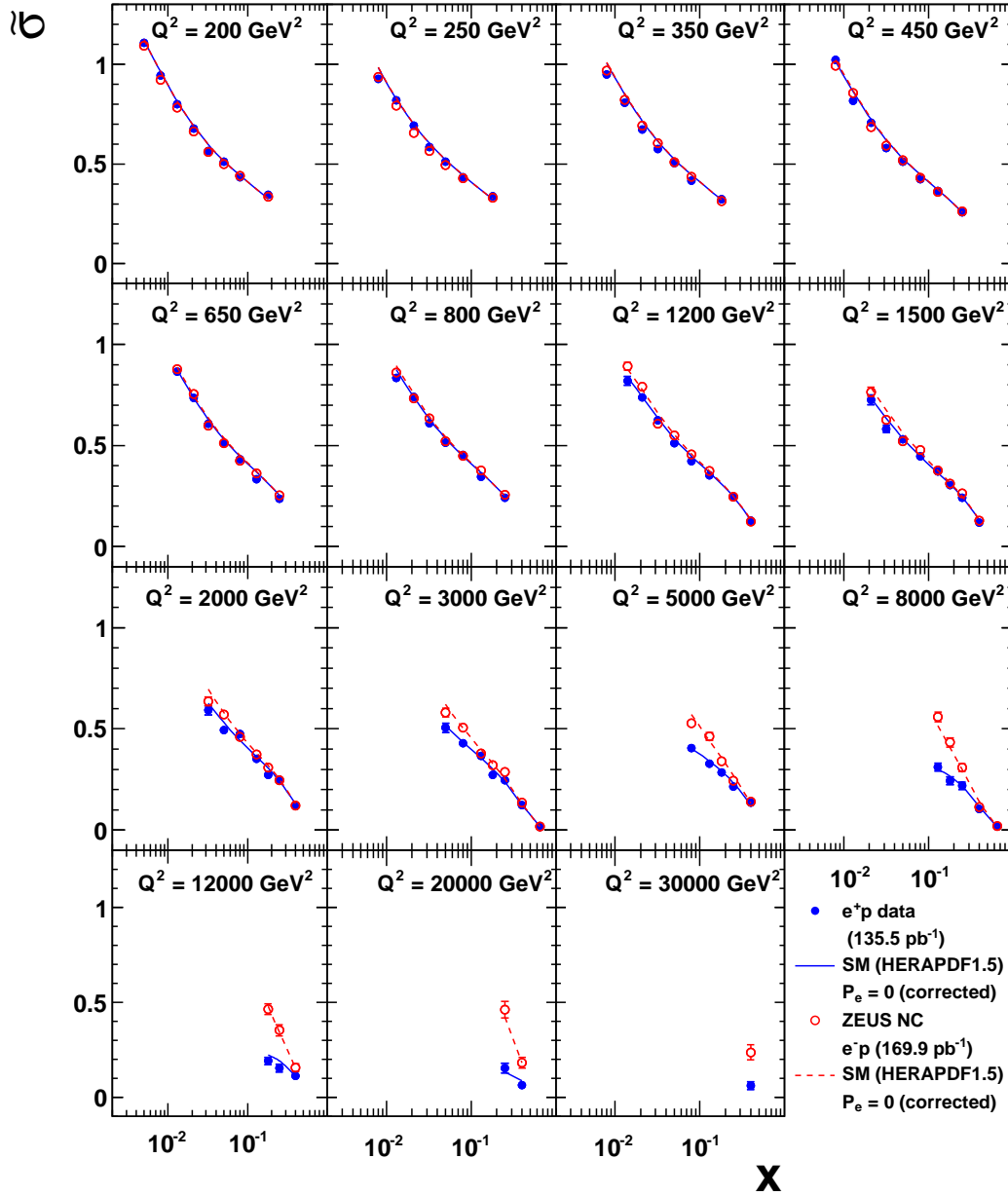


Figure 8.2: The reduced cross sections $\tilde{\sigma}$ as a function of x at fixed Q^2 values: shown are the data of this analysis (closed blue circles) and its Standard Model predictions obtained using HERAPDF 1.5 PDFs (blue solid lines) as well as the published e^-p results [8] (red open circles) and its Standard Model predictions obtained using HERAPDF 1.5 PDFs (red dashed lines). In many bins the errors are too small to be visible, but the outer error bars represent the full uncertainty including systematics, the inner error bars show the statistical uncertainty only.

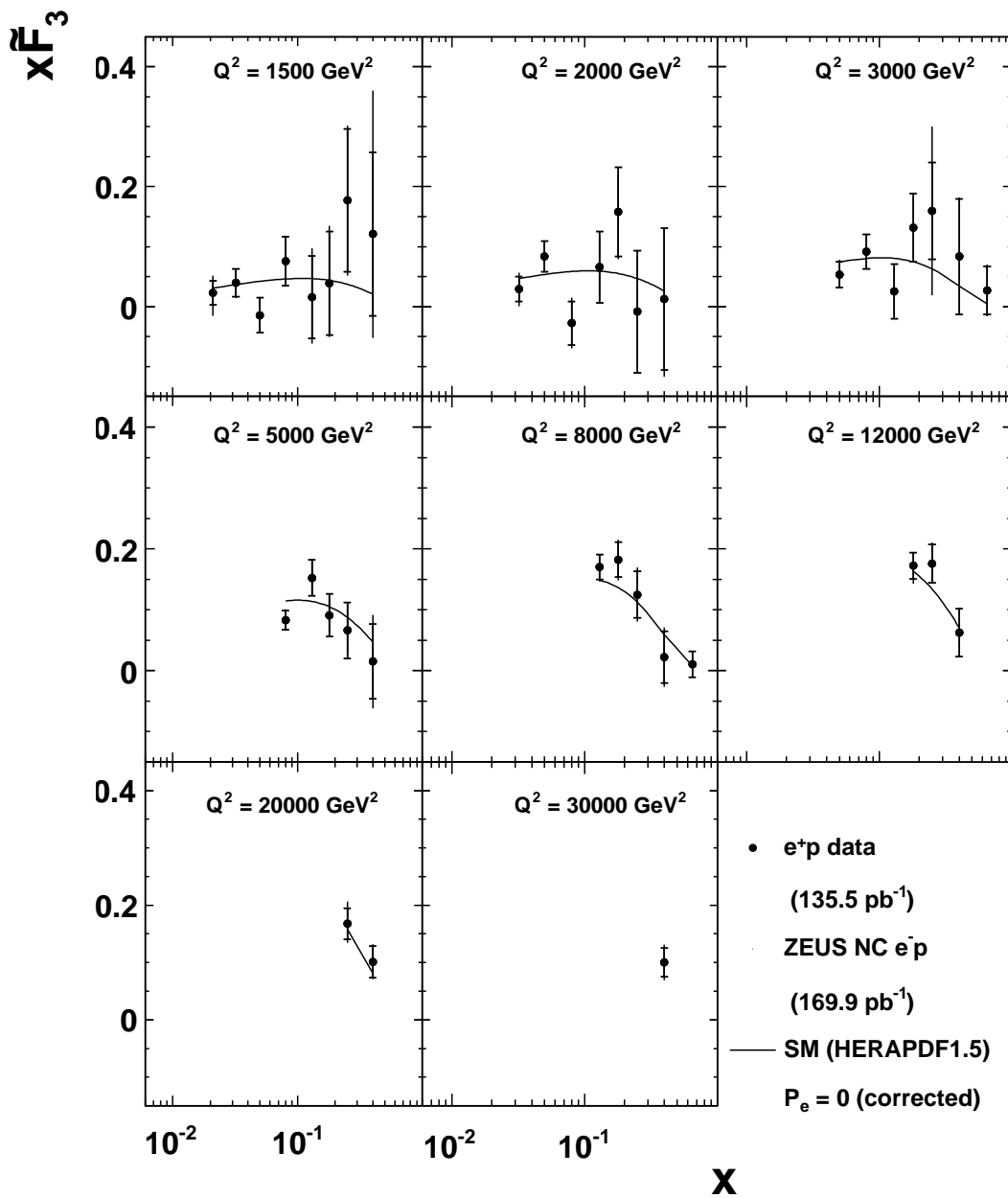


Figure 8.3: The structure function $x\tilde{F}_3$ as a function of x at fixed Q^2 values. The black points represent the data, the black line shows the Standard Model prediction evaluated using the HERAPDF 1.5 PDFs. The outer error bars represent the full uncertainty including systematics, the inner error bars show the statistical uncertainty only.

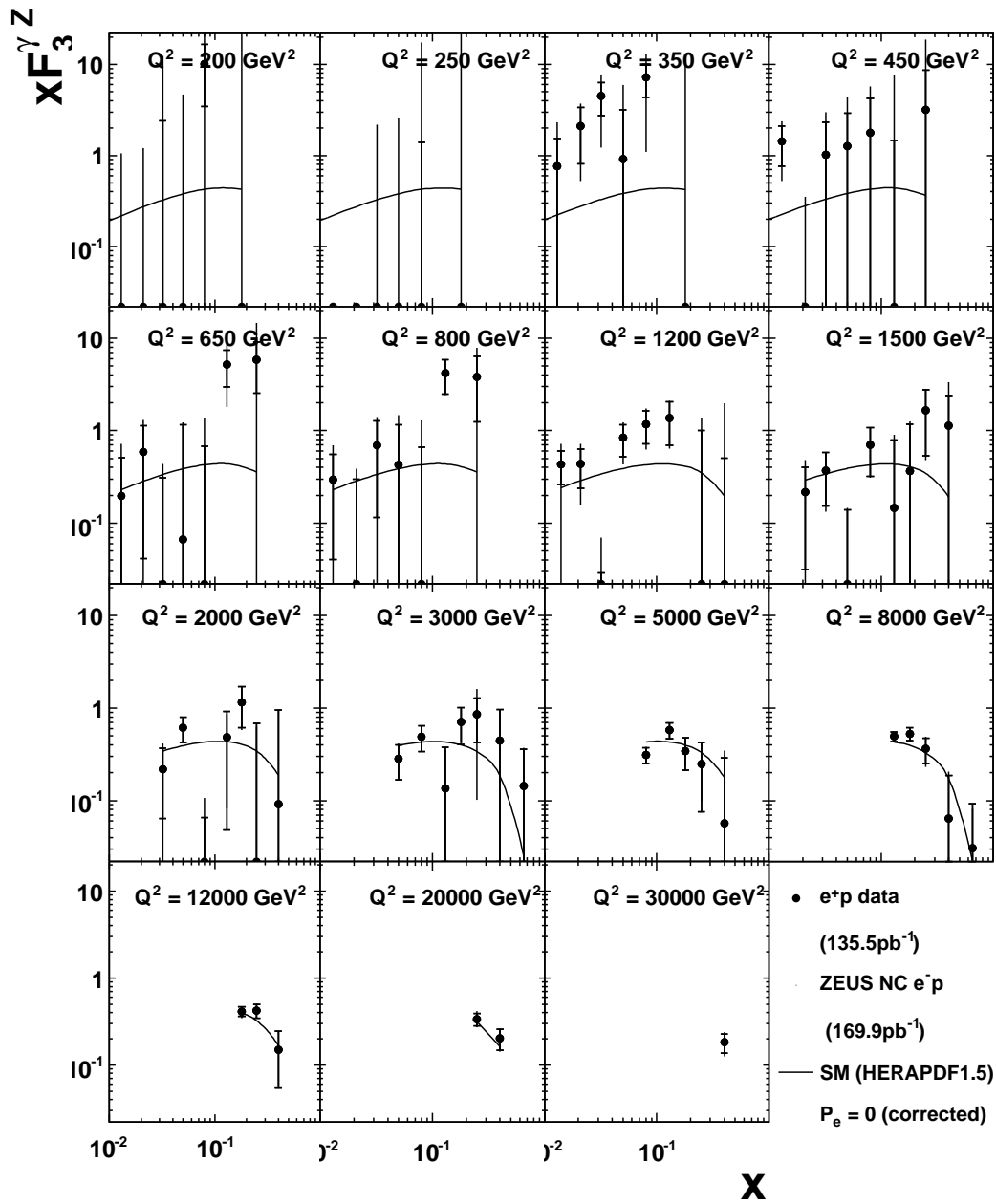


Figure 8.4: The structure function $x F_3^{\gamma Z}$ as a function of x at fixed Q^2 values. The black points represent the data, the black line the Standard Model prediction evaluated using the HERAPDF 1.5 PDFs. The outer error bars represent the full uncertainty including systematics, the inner error bars show the statistical uncertainty only.

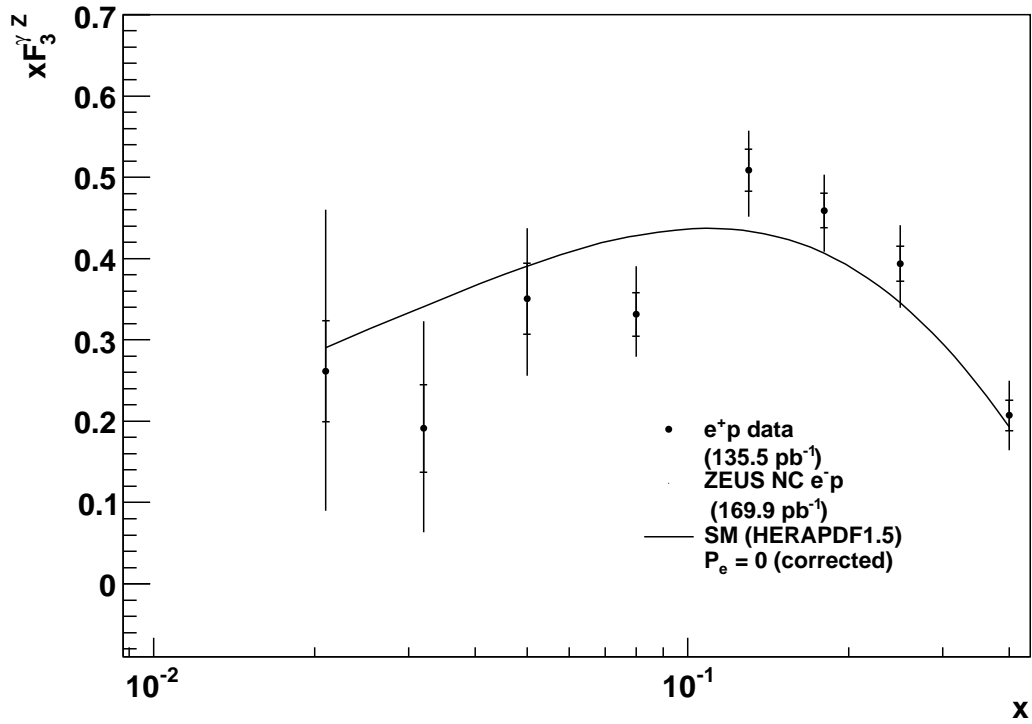


Figure 8.5: The structure function $xF_3^{\gamma/Z}$ at $Q^2 = 1500 \text{ GeV}^2$ as a function of x . The black points represent the data, the black line the Standard Model prediction evaluated using the HERAPDF 1.5 PDFs. The outer error bars represent the full uncertainty including systematics, the inner error bars show the statistical uncertainty only.

8.2. Polarised Cross Sections

The data sample used in this analysis makes it possible to investigate electroweak effects, because the polarisation of the lepton beam is of opposite sign in the first and second part of the running period.

For that purpose, the cross sections were extracted separately for the samples with positive and negative lepton beam polarisation. The γZ -interference term becomes important at the order of $Q^2 \approx 1000 \text{ GeV}^2$ ³, which is thus the order from which onwards a visible separation of the differently polarised cross sections is expected (see the single-differential $\frac{d\sigma}{dQ^2}$ cross section in Section 8.2.1 and the reduced cross sections in Section 8.2.2). The numbers are tabulated in Appendix G and Appendix H.

To see directly the amount of parity violation in the NC the polarisation asymmetry can be extracted (see Section 8.2.3).

8.2.1. Polarised Single Differential Cross Sections

The single differential cross sections $\frac{d\sigma}{dx}$ and $\frac{d\sigma}{dy}$ are shown separately for right-handed and left handed polarisation in Figure 8.6. In Figure 8.7 they are shown for $Q^2 > 3000 \text{ GeV}^2$ in addition. The shape of these cross sections with a higher Q^2 cut looks considerably different compared to the $Q^2 > 185 \text{ GeV}^2$ ones in confirmation of the Standard Model prediction. Especially in Plot 8.7 with $Q^2 > 3000 \text{ GeV}^2$ it is clearly visible that the cross section of the right-handedly polarised sample is higher. The increase of parity violation with Q^2 is confirmed and investigated in more detail in Section 8.2.3.

The difference of the e^+p NC DIS cross sections with positive and negative polarisation is even more obvious in Figure 8.8, which shows the $\frac{d\sigma}{dQ^2}$ cross section and the ratio of the right-handed and left-handed cross sections.

8.2.2. Polarised Reduced Cross Sections

Figure 8.9 shows the measured reduced cross sections as a function of x at fixed Q^2 values separately for the samples with positive and negative lepton beam polarisation. The separation between the two becomes clearly visible at high Q^2 , where the γZ -interference terms (see Equation 2.27) become sizable. The data confirm the Standard Model prediction evaluated with HERAPDF 1.5 PDFs. The results are so precise that they should be able to constrain the PDFs and electroweak couplings further (see Chapter 9).

8.2.3. Polarisation Asymmetry

From the differences in $\frac{d\sigma}{dQ^2}$ for the oppositely polarised data the asymmetry A^+ is extracted (according to Equation 2.39) and shown in Figure 8.10.⁴

The results show clearly and directly the parity violation in Neutral Current DIS with minimal PDF dependence.

³The suppression due to the χ^2 term leads to a below 1% contribution before (see Figure 2.5).

⁴The systematic error is not considered, as it is mainly (except for influences due to period-dependent corrections) correlated between the samples and thus cancels in the ratio.

$Q^2 > 185 \text{ GeV}^2$

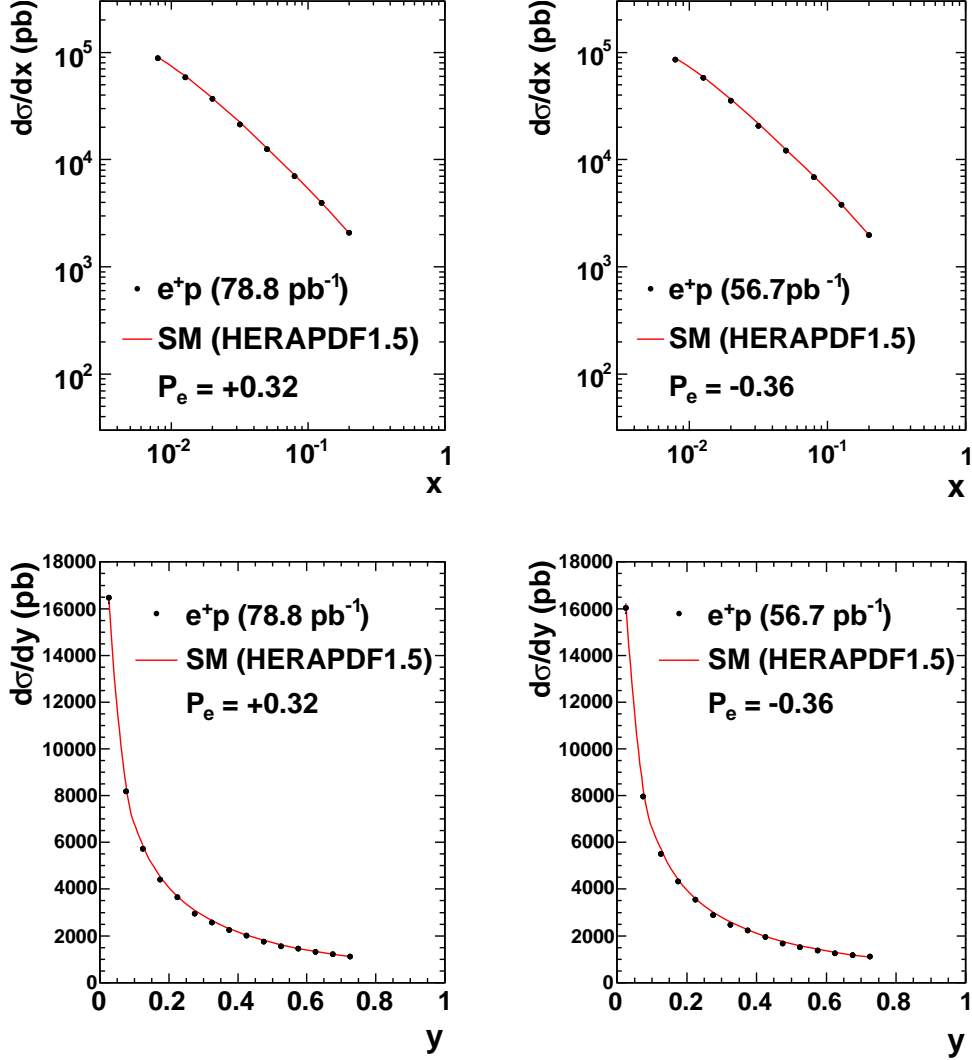


Figure 8.6: The polarised single differential cross sections for $Q^2 > 185 \text{ GeV}^2$, $y < 0.9$, $y(1-x)^2 > 0.004$: data (black points) compared to the Standard Model prediction evaluated using HERAPDF 1.5 PDFs (red lines). The left plots show the data with positive lepton beam polarisation ($P_e = +0.32$), the right plots show the data with negative lepton beam polarisation ($P_e = -0.36$). The top plots show $\frac{d\sigma}{dx}$ and the bottom plots $\frac{d\sigma}{dy}$. The errors are mostly too small to be visible, but outer error bars represent the full uncertainty including systematics, the inner error bars show the statistical uncertainty.

$Q^2 > 3000 \text{ GeV}^2$

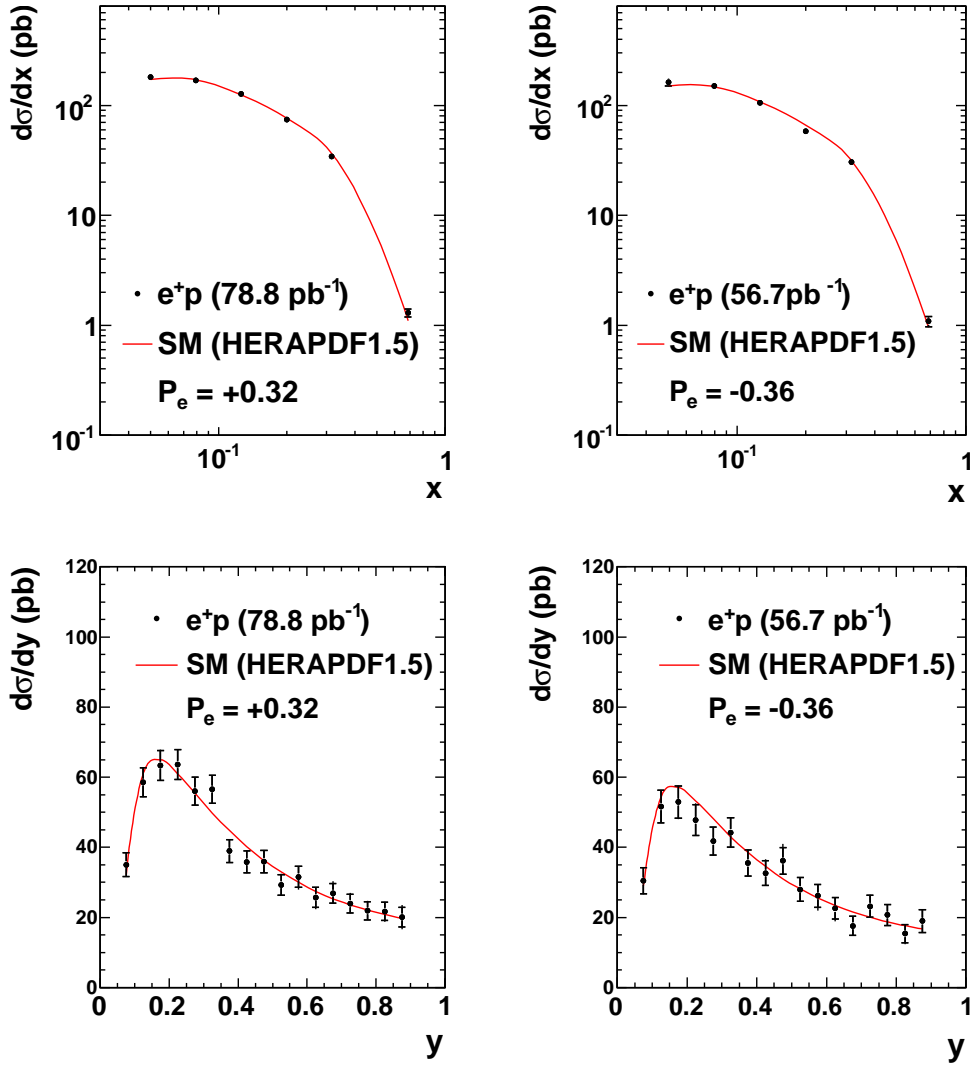


Figure 8.7: The polarised single differential cross sections for $Q^2 > 3000 \text{ GeV}^2$, $y < 0.9$, $y(1-x)^2 > 0.004$: data (black points) compared to the Standard Model prediction evaluated using HERAPDF 1.5 PDFs (red lines). The left plots show the data with positive lepton beam polarisation ($P_e = +0.32$), the right plots show the data with negative lepton beam polarisation ($P_e = -0.36$). The top plots show $\frac{d\sigma}{dx}$ and the bottom plots $\frac{d\sigma}{dy}$. The outer error bars represent the full uncertainty including systematics, the inner error bars show the statistical uncertainty.

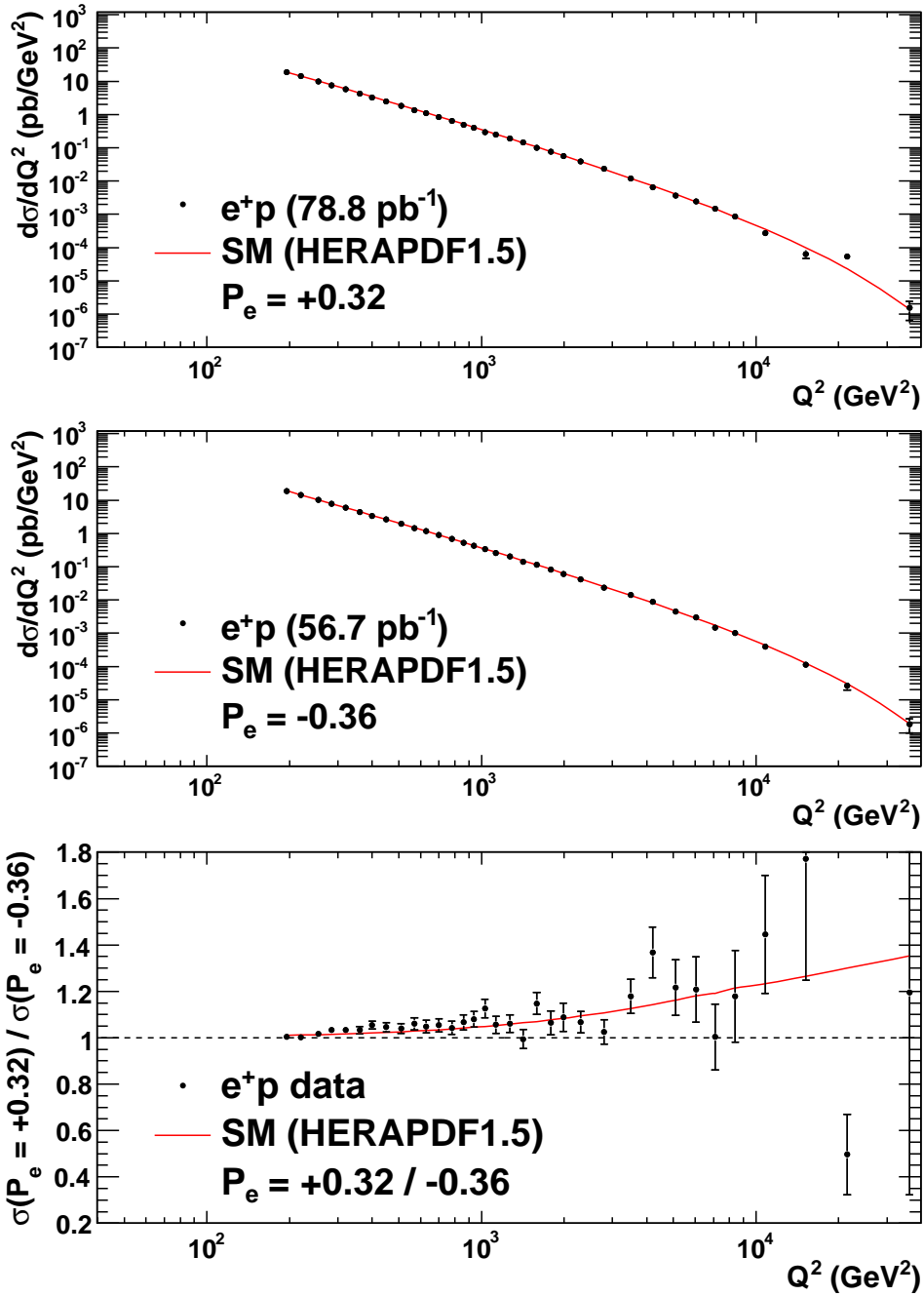


Figure 8.8: The polarised single differential cross section $\frac{d\sigma}{dQ^2}$ for $y < 0.9$, $y(1-x)^2 > 0.004$: data (black points) compared to the Standard Model evaluated using HERAPDF 1.5 PDFs (red lines). The top plot shows the data with positive lepton beam polarisation ($P_e = +0.32$), the middle plot shows the data with negative lepton beam polarisation ($P_e = -0.36$). The bottom plot shows the ratio of the oppositely polarised cross sections. The outer error bars represent the full uncertainty including systematics, the inner error bars the statistical uncertainty.

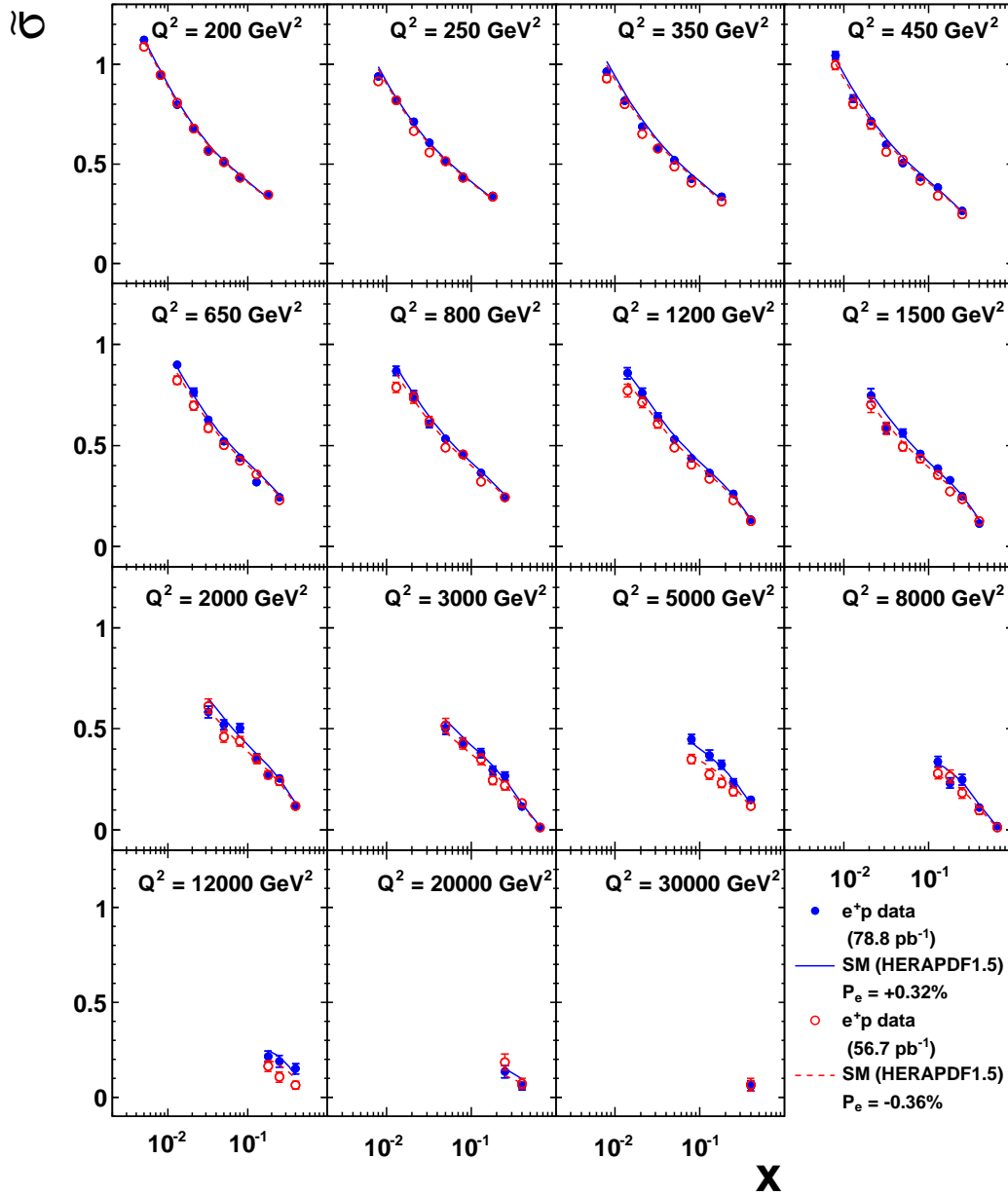


Figure 8.9: The polarised reduced cross sections as a function of x at fixed Q^2 values: shown are the data with positive lepton beam polarisation (filled blue circles) and its prediction from the Standard Model evaluated using HERAPDF 1.5 PDFs (blue solid lines) as well as the left-handed data (red open circles) and its prediction from the Standard Model evaluated using HERAPDF 1.5 PDFs (red dashed lines). The outer error bars represent the full uncertainty including systematics, the inner error bars the statistical uncertainty only.

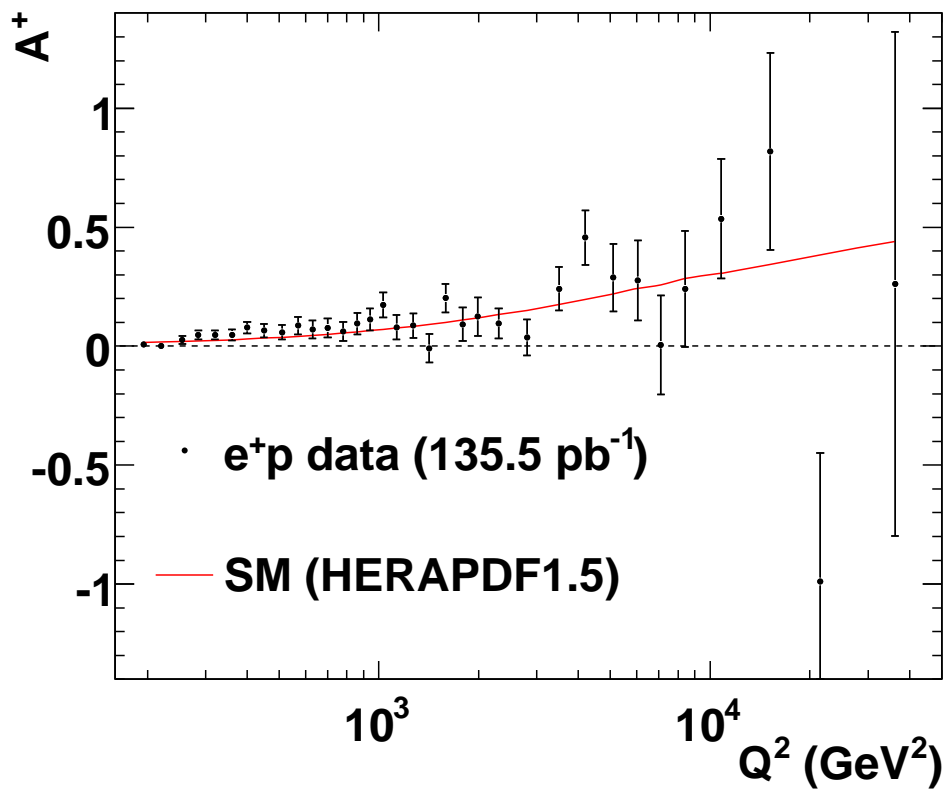


Figure 8.10: The polarisation asymmetry A^+ as a function of Q^2 extracted from the presented e^+p data. The black circles represent the data, the red curve shows the Standard Model prediction evaluated using PDFs from HERAPDF 1.5. The error bars represent the uncertainty.

9. PDF Fits and Outlook

In Chapter 8 the results of the main analysis of this thesis have been presented. This chapter describes how these results can improve our knowledge of the parton density functions (PDFs) of the proton and the inclusion of which other results would be insightful.

For this purpose, first the ZEUS (Section 9.1.1) and HERA (Section 9.1.2) PDF fits are described. Then, using the example of a PDF fit with ZEUS data, it is shown how the uncertainty of the PDFs is affected by the results of this thesis (Section 9.2).

In Section 9.3 the importance of including jet data into the PDF fits is discussed. In Section 9.3.1 it is discussed how this can be achieved and was done in a study by the author. Section 9.3.2 shows the results obtained from the additional inclusion of dijet cross sections measured by ZEUS.

Finally Section 9.4 discusses the importance of PDF fits for the determination of cross sections at the LHC, and how additional measurements from different accelerators can contribute to the precise knowledge of the parton density functions.

9.1. ZEUS and HERA PDF Fits

ZEUS and H1 started doing their own PDF fits, based on their data only, directly after the HERA-I running period in 2002 [135] and 2003 [136]¹. The reasons for providing fits with HERA data only have been given in Section 2.6.2. Later on, ZEUS and H1 combined their data and started extracting PDFs from these data (HERAPDF fits). HERAPDF 1.0 [30] was published in 2009 and since then there have been several improvements (mainly including additional data) which will lead to HERAPDF 2.0 in the near future. The following subsections will discuss the ZEUS-PDF and the HERAPDF fits in more detail, as they were used for the analysis described here.

9.1.1. ZEUS-PDF Fit

The so-called *ZEUS-O* fit of [135] was the first fit to use only ZEUS data in a next-to-leading-order QCD PDF fit. It includes CC DIS data and NC DIS data from HERA-I, both for e^+p and e^-p running [139–142]. In the same paper a fit was also presented including fixed target data in addition to ZEUS data to determine the valence quark distributions more precisely. This fit is called *ZEUS-S* fit. In addition to the fit with fixed α_s , the fit was repeated with free α_s making it possible to determine the gluon density and the strong coupling constant simultaneously. In the ZEUS-PDF fits the correlation of uncertainties was taken into account, the *Offset* method [27, pp. 167-168] being used for error treatment.

¹There have been fits of PDFs before at both H1 [137] and ZEUS [138], but on very limited data and thus with rather limited results only.

The PDFs were parametrised at the starting scale $Q_0^2 = 7 \text{ GeV}^2$ as

$$xf(x) = Ax^B(1-x)^C(1+Dx), \quad (9.1)$$

where $f(x)$ is the PDF and A , B , C , and D are the parameters of the fit. The valence distributions $xu_v(x)$ and $xd_v(x)$, the total sea distribution $xS(x)$, the gluon distribution $xg(x)$ and the difference of the u and d contributions to the sea $x\Delta = x(\bar{d}-\bar{u})$ were fitted. Nine of the parameters were fixed e.g due to sum rules, leading to 11 free parameters (12 for free α_s). The heavy quarks were treated according to the *Roberts-Thorne* general-mass variable flavour-number scheme [143]. The resulting PDFs are available for the *LHAPDF* [144] PDF set interface.

9.1.2. HERAPDF Fit

HERAPDF 1.0 [30] was published in 2009. The fit included the H1 and ZEUS combined inclusive NC and CC $e^\pm p$ DIS data of HERA-I. The cross section results from each experiment, H1 and ZEUS, were first extrapolated to a common (x, Q^2) -grid² and then combined. This leads to a reduction of the statistical uncertainty. In addition, the use of different detectors, kinematic reconstruction methods and in general different experimental techniques to measure the same cross sections by H1 and ZEUS allows the systematic uncertainties to be reduced. The data span six orders of magnitude both in Q^2 and x .³

For the PDF fit the parametrisation of Equation 2.42 ($xf(x) = Ax^B(1-x)^C(1 + \eta\sqrt{x} + Dx + Ex^2)$) was used at the starting scale of $Q_0^2 = 1.9 \text{ GeV}^2$. First a fit was done with nine parameters, setting all η , D and E to 0. Then additionally η , D and E were freed, and the resulting fit was compared to the fit with only nine free parameters. It was found that only $E_{u_v} \neq 0$ led to a significant improvement of the fit. So this ten-parameter fit was used, giving a χ^2 per degree of freedom of $636.5/656 \approx 0.97$.⁴

The correlation of systematic uncertainties was taken into account and the *Hessian* method [27, pp. 168-169] was used for error treatment. The heavy quarks were treated according to an improved general-mass variable flavour-number scheme [143, 146].

HERAPDF 1.5 [34, 147] is a very similar fit to HERAPDF 1.0, including in addition part of the results of the HERA-II running period. HERAPDF 1.0 and HERAPDF 1.5 were also done at NNLO [147, 148] (with slightly worse χ^2 per degree of freedom).

All described PDFs are included in the *LHAPDF* [144] PDF set interface. The current recommendation of the HERA fitting group is that HERAPDF 1.5 should be used for cross section predictions.

9.2. Influence of NC Data on PDF Fits

The results from the analysis presented here will have an impact on the PDF fits and will help to determine the parton densities more precisely. The preliminary results [149]

²The method is described in [145].

³For the PDF fit only data points above $Q^2 = 3.5 \text{ GeV}^2$ were used in order to ensure the applicability of perturbative QCD.

⁴There were 1402 data points combined to 741 cross sections out of which 656 were used for the fit.

can already be used in preliminary PDF fits, waiting for the final publication⁵.

The expected influence of these data can be seen in Figure 9.1, where the data were included into a fit of inclusive ZEUS data. Clearly an improvement can be seen. This is most visible at high- x for the gluon and u_v distributions, where the precision of the data is especially important.⁶ The error reduction is impressive considering that only a single additional data sample (90 cross section points) is included in addition.

9.3. Jets in PDF Fits

An asset of including jet cross section measurements into the PDF fits is that with the jet data it is possible to free α_s without the uncertainty on the PDFs becoming very large. This is because the jet data reduces the correlation between the gluon PDF and α_s through the QCD Compton process (see Section 2.5.2).

Even with the high precision inclusive HERA data there are still kinematic regions for which specific PDFs are not very well constrained. This is especially true for the gluon in a fit with free α_s . Whereas the low- x gluon can be constrained by low- Q^2 NC data, the middle- and high- x gluon is not sufficiently constrained by inclusive data. In this region jet data can be used to improve the precision of the PDFs considerably.⁷

In 2005 ZEUS began using jet data and successfully reduced the uncertainty on the gluon PDF [40] (see Figure 9.2). The fit was done using the same premises as the previous ZEUS-S and ZEUS-O fits (see Section 9.1.1), only with more inclusive data [139–142,151,152] and two additional HERA-I jet samples: inclusive jets in NC DIS [153] and dijets in photoproduction [154]. This fit was used for the study in Section 9.3.2.

Most recently jets have also been preliminarily included in the HERAPDF fit. [155] HERAPDF 1.7 [42] also uses charm data to establish a proper treatment of heavy flavours in the PDF fits.⁸

Figure 9.3 shows a χ^2 scan for a fit with free α_s including (HERAPDF 1.6) and excluding (HERAPDF 1.5f) jet data. It is clearly visible that the fit without jet data has only a very shallow minimum and thus a large uncertainty on α_s .

Other fitting groups do include *Tevatron* jet data [35, 37], the impact of which is discussed in Section 9.4.

9.3.1. How to Include Jets

For the calculation of jet cross sections factorisation (Equation 2.20) and the expansion series of α_s (Equation 2.16) from perturbative QCD is used. In the description of jet kinematics, ξ takes the role of x , being the proton's momentum fraction entering into

⁵Publication is expected beginning of 2012.

⁶The slight increase of the high- x sea quark uncertainties is due to slight tensions with past measurements, most probably the e^-p data.

⁷Jet data can provide considerable improvement for x above 10^{-2} approximately. Constraints from only inclusive data get very loose from about $x = 10^{-1}$ onwards. See Figure 9.2.

⁸Through the BGF process the charm data is also sensitive to the gluon, but the uncertainty reduction is dominated by the jet data.

the hard scattering.⁹ The cross section can therefore be written as

$$\sigma = \sum_n \alpha_s^n \sum_i f_i * \hat{\sigma}_{i,n} = \sum_n \alpha_s^n(\mu_R) \sum_i \int_x^1 f_i(\xi, \mu_f) \cdot \hat{\sigma}_{i,n}\left(\frac{x}{\xi}, \mu_R, \mu_f\right) d\xi. \quad (9.2)$$

The calculation of these cross sections does take comparably long due to the time-consuming calculation of the phase-space integrals. The long calculation time does not allow the usage of this calculation in PDF fits (where the cross section would need to be calculated anew for each iteration¹⁰) at present. For making it feasible to include the jets a "grid" (look-up tables) method can be applied that utilises the assumption that the PDFs $f_i(\xi, \mu_f)$ are approximately constant within a small range of ξ and μ_f .

9.3.1.a. Using Grids for Jet Cross Sections

The "grid" method of fast NLO calculation was first described in [157, App. C]. The PDFs are divided into bins of ξ and μ_f and

$$f_i(\xi, \mu_f) \approx f_i(\xi^l, \mu_f^m), \quad (9.3)$$

is used, where ξ^l and μ_f^m denote the representative value of ξ and μ_f in the correspondent bins l and m . As μ_f and μ_R are not always equal, in the analysis described here bins of the renormalization scale μ_R were used in addition to ξ and μ_f and Equation 9.2 can be written as

$$\sigma \approx \sum_{n,i} \sum_{k,l,m} \alpha_s^n(\mu_R^k) f_i(\xi^l, \mu_f^m) \cdot \hat{\sigma}_{i,n}^{k,l,m}(\xi^l, \mu_R^k, \mu_f^m). \quad (9.4)$$

The weights,

$$\hat{\sigma}_{i,n}^{k,l,m} = \int_{\xi^l} \hat{\sigma}_{i,n}\left(\frac{x}{\xi}, \mu_R^k, \mu_f^m\right) d\xi, \quad (9.5)$$

need to be computed only once using standard NLO QCD techniques and are then saved in the "grids". As mentioned above, these phase-space integrals are the most time-consuming part of the cross section calculation. As the PDFs are outside the integrals, the cross sections can be calculated much faster for different PDFs enabling the inclusion of jet data in PDF fits.

The grids of this analysis were calculated using the DISENT [158, 159] program for NLO QCD calculation. For renormalization and factorization scales binning in Q^2 and E_T (transverse jet energy) was used. This makes it possible to choose any combination of Q^2 and E_T as the renormalization scale. For the factorization scale Q^2 is used. The interface for the PDF fits was written by the author and was based on the *FORTRAN* program *ASSEMBLE* [160, 161].

Important tools using "grid" methods for fast pQCD calculations are *FastNLO* [162] and more recently *APPLGRID* [163], which also allows the variation of renormalization and factorization scale as well as the calculation of other processes (electroweak boson production).

⁹Details about jet physics at HERA can e.g. be found in [156].

¹⁰A typical PDF fit as done by the author needed 500 to 800 iterations.

¹¹ n goes from 1 to 2 for the NLO calculations used here.

9.3.2. Example: Dijets in ZEUS-JETS PDF

For this thesis a study of the impact of the inclusion of additional jet data in the ZEUS-JETS PDF fits was performed. The aim was to check whether the uncertainty on the gluon PDF could be further reduced by including more jet data. Here results of the inclusion of additional cross section data from DIS dijets with Q^2 between 10 and 10000 GeV² [164] are shown as an example.¹²

PDF fits were done by the author of this thesis with the data of the ZEUS-JETS PDF fits and the above described settings *a)* without any jet data, *b)* with the jet data included in the ZEUS-JETS data, and *c)* with these jet data and in addition with the results of [164]. The PDFs and their uncertainties were then compared to each other with special emphasis on the gluon uncertainty.

Figure 9.4 shows the parton density functions as a function of x as they were extracted by a fit with all mentioned data (*c*). The fit includes 626 cross section points and has a χ^2 of 789, i.e. a χ^2 per degree of freedom of about 1.26. This is only slightly worse than the fit without the additional data (χ^2 per degree of freedom of 1.20). 49 new points were included and the increase of χ^2 was 96 (increase of χ^2 per degree of freedom of 1.96). This can still be considered reasonable, though it implies a slight tension between the new data and the rest or an underestimation of the uncertainties. As very similar χ^2 values are found for the other jet samples (in both the fit with and without the new data) it is likely that there is a common reason.

Figure 9.5 shows that the extracted PDFs are (as expected) very similar with and without the jet samples. The main differences are in the uncertainties, most importantly in the uncertainty of the gluon PDF, which is shown in Figure 9.6. It is clearly visible that the uncertainty can be reduced even compared to the ZEUS-JETS like fit (which already includes jet data), especially at very high x (above 10^{-1}).

¹²The cross sections in the lowest Q^2 bin of $10 < Q^2 < 16$ GeV² were not reasonably well described by NLO. Details on the problems of extraction of very low Q^2 jet cross sections are discussed in [165]. These cross section points were not included in the fit (including them led to the fit not converging).

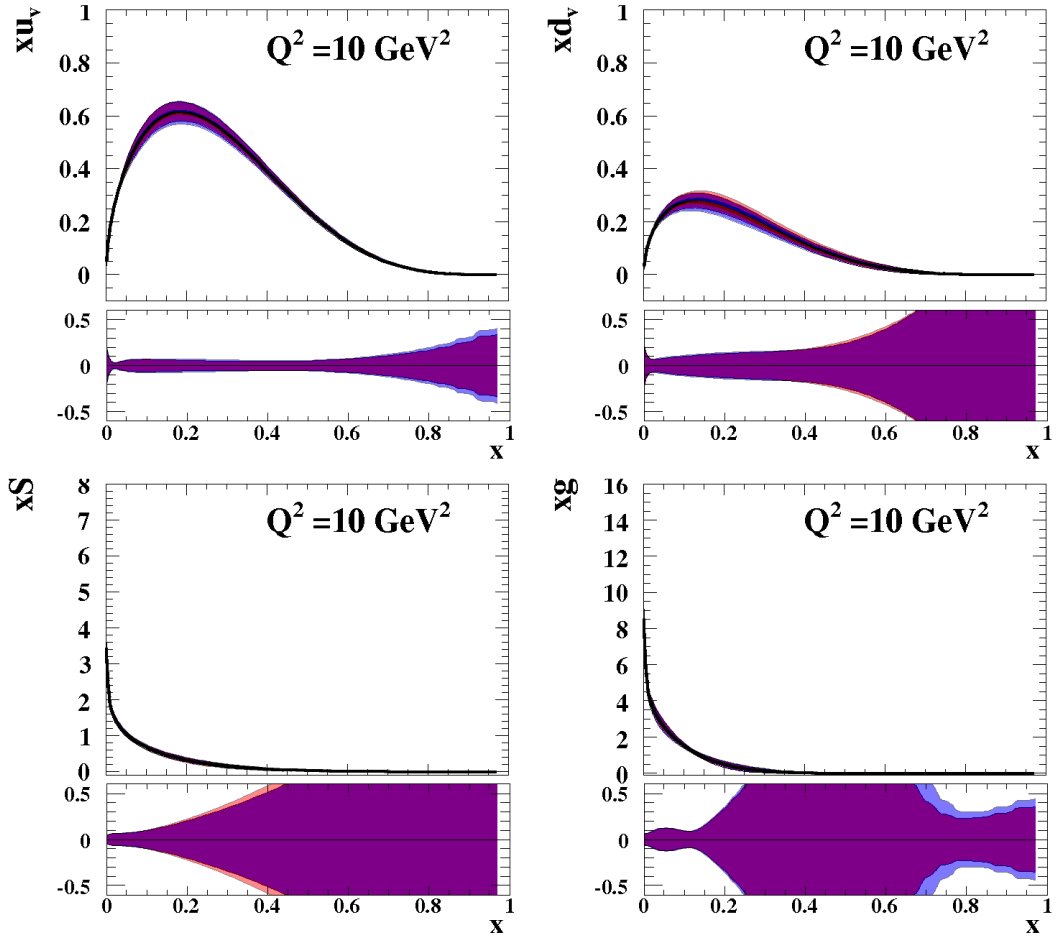


Figure 9.1: Parton densities for the u_v (top left) and d_v (top right) valence quarks, the sea quarks (bottom left) and gluons (bottom right). In addition, the fractional error is shown below each distribution. The PDF fit (blue) without the e^+p NC results from the presented) analysis is overlaid with the same fit including these results (as of [149]) (red band). Thus blue regions in the error plots indicate reduced errors. The figures for each fit were taken from [150] and then combined on this figure for comparison.

ZEUS

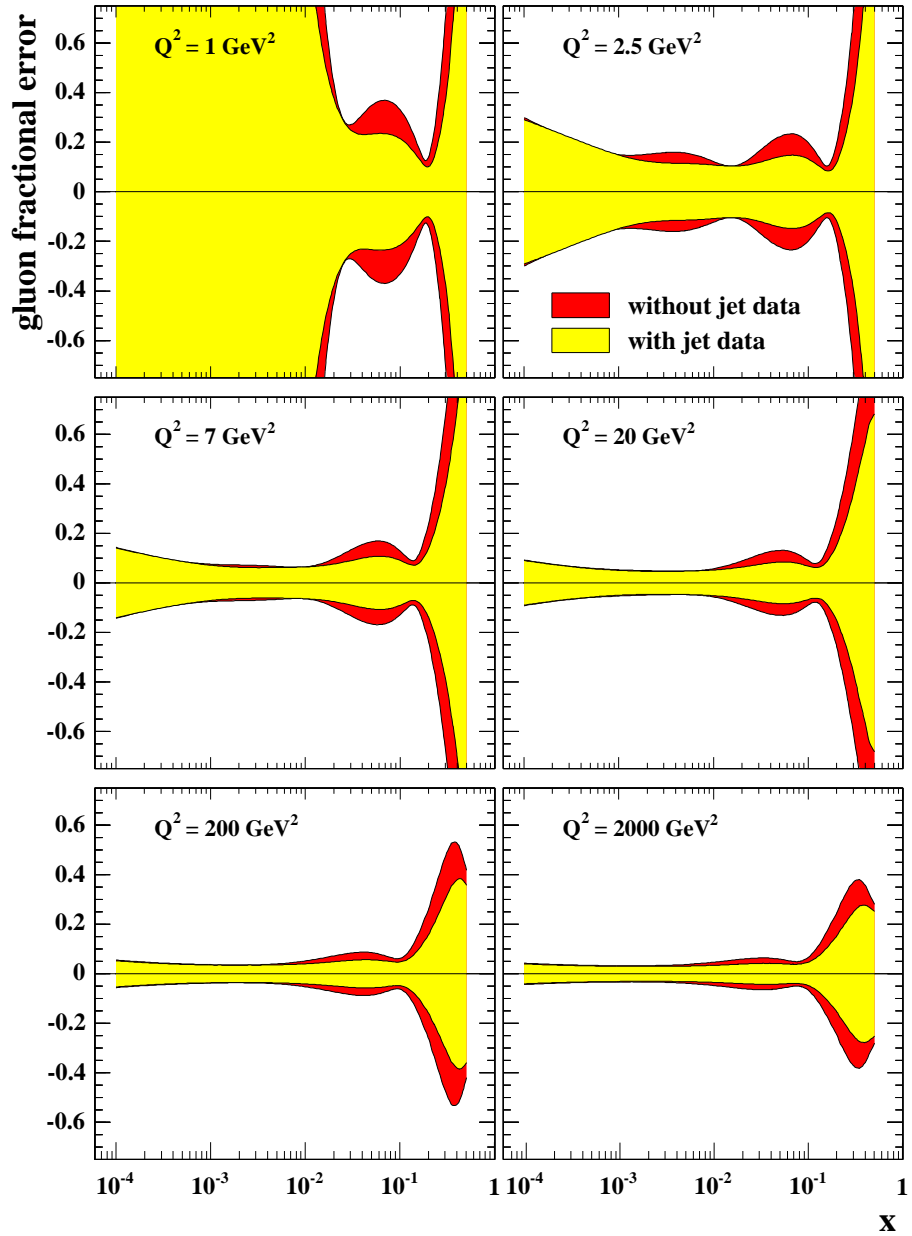


Figure 9.2: The fractional experimental uncertainty on the gluon PDF for a ZEUS-PDF fit using jets (yellow error band) compared to the same fit without the jet data (red error band). From [40, Fig. 8]).

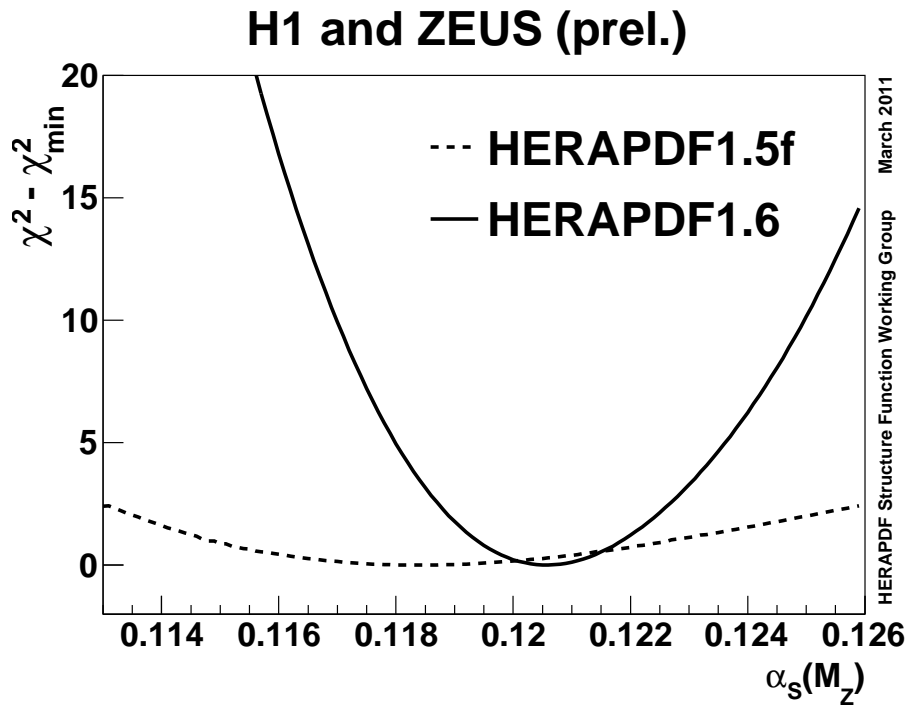


Figure 9.3: $\Delta\chi^2$ distribution as a function of the value of the strong coupling constant α_s for a fit including (HERAPDF 1.6, continuous line) and excluding (HERAPDF 1.5f, hashed line) jet data. From [155].

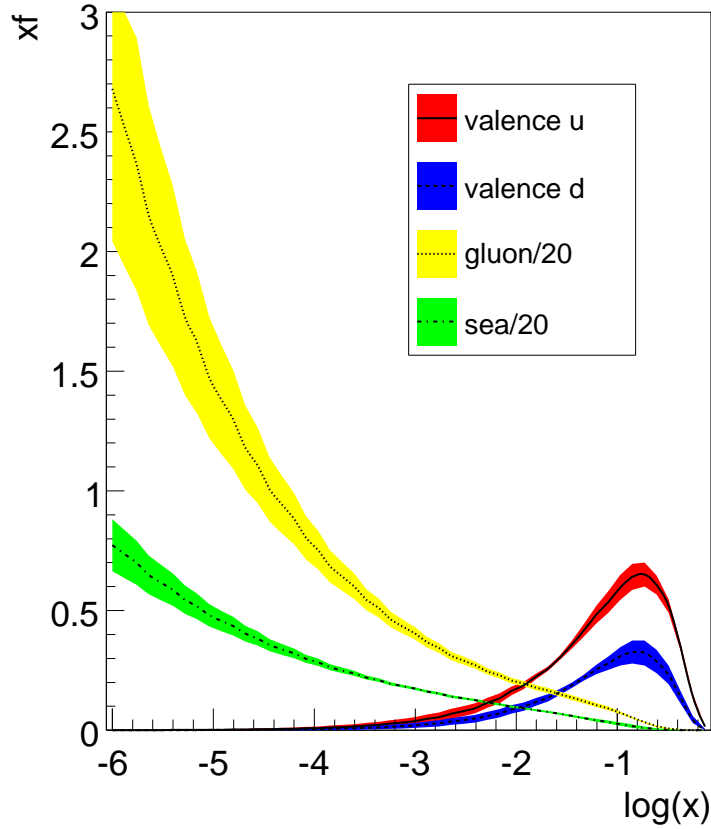


Figure 9.4: Parton density functions as extracted from ZEUS inclusive and jet data (for details refer to Section 9.3.2) at $Q^2 = 10 \text{ GeV}^2$. The valence u_v quark distribution is shown as a continuous line with a red error band, the valence d_v quark distribution is shown as a hashed line with a blue error band, the gluon distribution is shown as a dotted line with a yellow error band and the sea quark distribution as a hashed-dotted line with a green error band. The gluon and sea quark distributions are suppressed by a factor 20 for the plot.

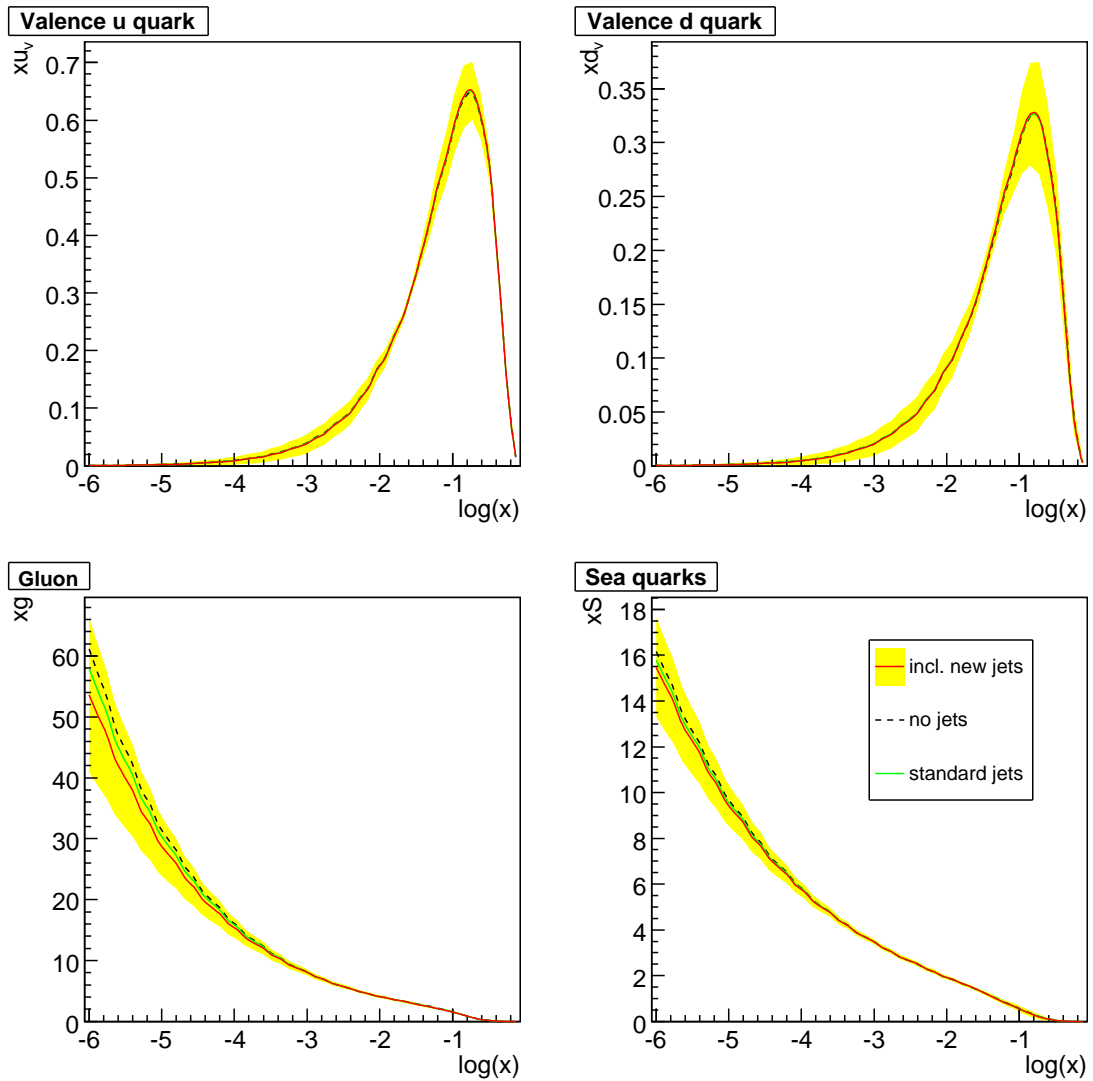


Figure 9.5: Comparison of parton density functions with different amount of jet data: valence u_v (top left), valence d_v (top right), gluon g (bottom left) and sea quark S (bottom right) distributions as extracted from ZEUS inclusive and jet data (for details refer to Section 9.3.2) at $Q^2 = 10 \text{ GeV}^2$. The PDFs with new and old jet data included are shown as a continuous red line with a yellow error band, the PDFs without jet data are shown as hashed black lines, and the PDFs with the jet data of ZEUS-JETS PDF [40] are shown as a continuous green line.

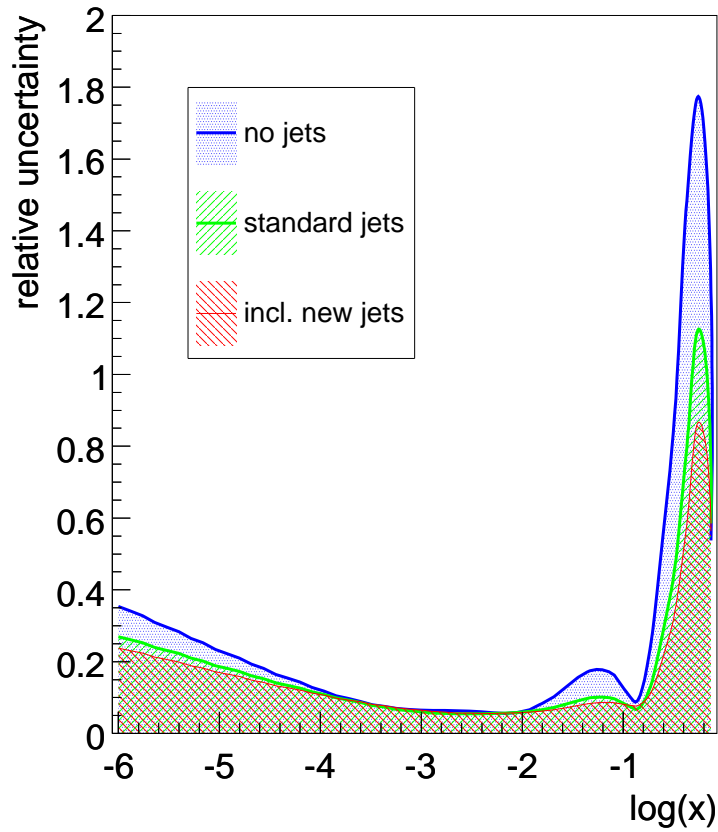


Figure 9.6: The relative uncertainty of the gluon density function as extracted from ZEUS inclusive and jet data (for details refer to Section 9.3.2) at $Q^2 = 10 \text{ GeV}^2$. The relative uncertainty without any jet data is shown as the blue dotted area, the relative uncertainty with the jet data of ZEUS-JETS PDF [40] is shown as the green hashed area and the relative uncertainty with the jet data of [164] in addition is shown as the red hashed area.

9.4. LHC and the Future of PDF Fits

The first results from the LHC have already been published, and within the next years LHC will most probably be the main source of new high energy particle physics results. This does not decrease, but rather increase the importance of results of the presented analysis: With the LHC being a proton-proton collider it is absolutely essential to have as precise as possible proton PDFs. That different PDFs lead to relevantly different cross section predictions for the LHC is e.g. shown in Figure 9.7. This Figure shows predictions of the W -charge asymmetry from different PDF sets and it is clearly visible that they differ considerably.

The uncertainty of cross section predictions at the LHC is often dominated by PDF uncertainties. Several ATLAS and CMS results have already reached a precision level, where these uncertainties are one of the major uncertainty contributions.¹³ This will be the case for even more cross sections in the future. Figure 9.8 shows an ATLAS inclusive jet result with predictions obtained using different PDF sets, where the systematic uncertainty of the measurement and the PDF uncertainty are of a similar size at high transverse momentum.

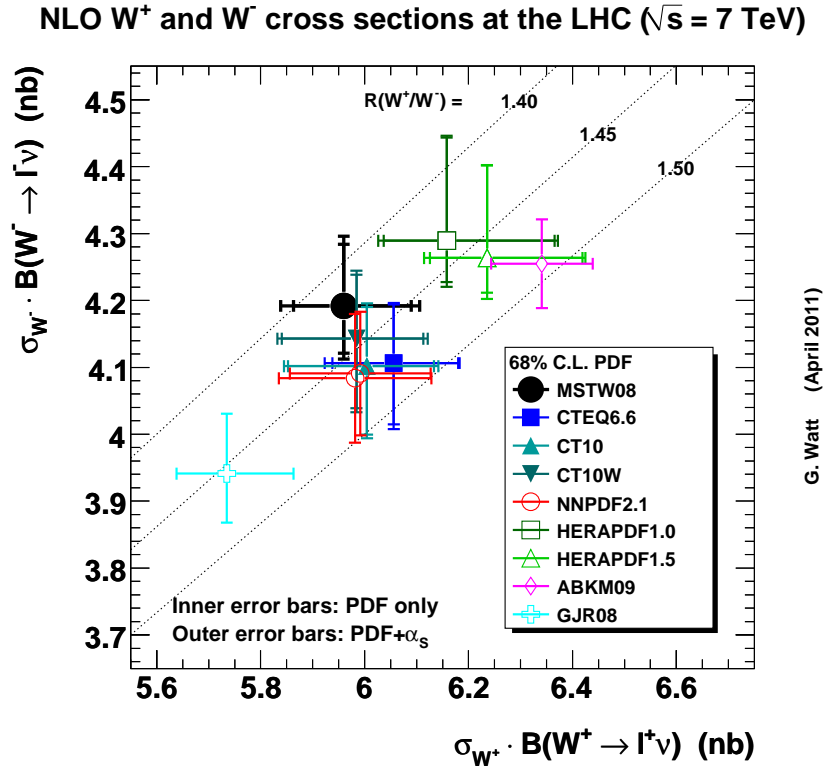


Figure 9.7: Predictions using different PDF sets in NLO for the W^+ total cross section versus the W^- total cross section at $\sqrt{s} = 7$ TeV at the LHC. From [38, Figure 17a].

¹³This is helpful as it points to the potential to constrain the PDFs (see Section 9.4), but can also pose problems to unfolding.

In general it can be stated that HERAPDF 1.5 well describes W and Z results from Tevatron and from LHC as well as HERA data. The description of jet data from Tevatron and LHC is reasonable, even better than predictions from other fitting groups in many cases (see Figure 9.8).

In the next paragraphs a few points will be raised regarding what the analysis described here can contribute to the PDFs and which other sources could lead to better knowledge of the PDFs in the near future.

NC e^+p Data The direct results of this analysis provide the above described (Section 9.2) reduction of uncertainties of the PDFs especially for the high- x gluon and u valence quark. This is of course not only true for the HERAPDF fit. This data will be able to provide valuable precision input for the other major fitting groups as well and will surely be included in their fits as it is one of the most precise samples available.

In addition the polarisation of the lepton beam makes this data predestined for electroweak fits (see Section 2.5.3). Up to now, neither H1 nor ZEUS have published a final fit including polarised HERA-II data and the preliminary ZEUS fit (see Figure 2.13) does not include this NC e^+p data. Improvement due to the results presented here is definitely expected.

Jets in HERAPDF Even though the new HERAPDF preliminary results (HERAPDF 1.6 and HERAPDF 1.7) do already include some jet data, several aspects could be improved. First of all, more jet data could be helpful (as shown above), especially because only four jet data samples [153, 167–169] are included up to now and only [169] includes the high-statistics HERA-II data. Also no results from jets in photoproduction has been included yet.

In addition, the jet data is included in the HERAPDF fit separately for the H1 and the ZEUS data and not combined as in the inclusive case. It would be advantageous to combine the measurements and hopefully reduce systematics through this approach (see discussion for combination of inclusive data in Section 9.1.2). Unfortunately the binning used for jet cross section measurement at H1 and ZEUS has been very different for past publications making it difficult to combine the measurements. [170, 171] Having similar binnings would be advantageous and was suggested [172]. The effort is currently ongoing, e.g. for the analysis of [165].

Future Fits There are several potential candidates for what could be included into HERAPDF fits (and other fits as well) to improve the precision. First of all Tevatron data could be included as it stems from a well-understood experiment in a similar way as HERA data. Thus using only HERA and Tevatron the advantages of the HERAPDF fits of e.g. controlled systematics and their correlations could still remain valid. W and Z data from Tevatron (e.g. Z rapidity and W asymmetry results) could influence the d_v distributions, reducing the uncertainties and most probably leading to a harder high- x d valence quark [173].

Additionally, Tevatron jet data could improve the precision of the PDFs at high x .

Of course LHC data will also be able to contribute to the PDFs eventually. The above mentioned ATLAS results of Figure 9.8 already hint that LHC jet data can be used to

constrain the PDFs in basically the same way as the Tevatron data.¹⁴ In general, the Tevatron and the LHC data can constrain the PDFs in a similar way, but LHC reaches additional kinematic regions. LHCb data may be able to constrain the PDFs at very low x , where the PDF uncertainties are very large.

A possible conclusion to draw is that in addition to the data still to come from HERA, HERAPDF fits could profit from the inclusion of Tevatron data in the near future and LHC data in the middle future.

The proposed successor of HERA, the *LHeC* [174] would improve the knowledge about the PDFs further. This accelerator, where 60 GeV electrons are planned to collide with the 7 TeV protons of the LHC beam, could increase the integrated luminosity reached at HERA by two orders of magnitude and the kinematic range by a factor 20. As a DIS machine it would be the perfect tool for even deeper investigation of the structure of the proton.

¹⁴The fraction of jets induced by qq , qg and gg is different though, so there are differences.

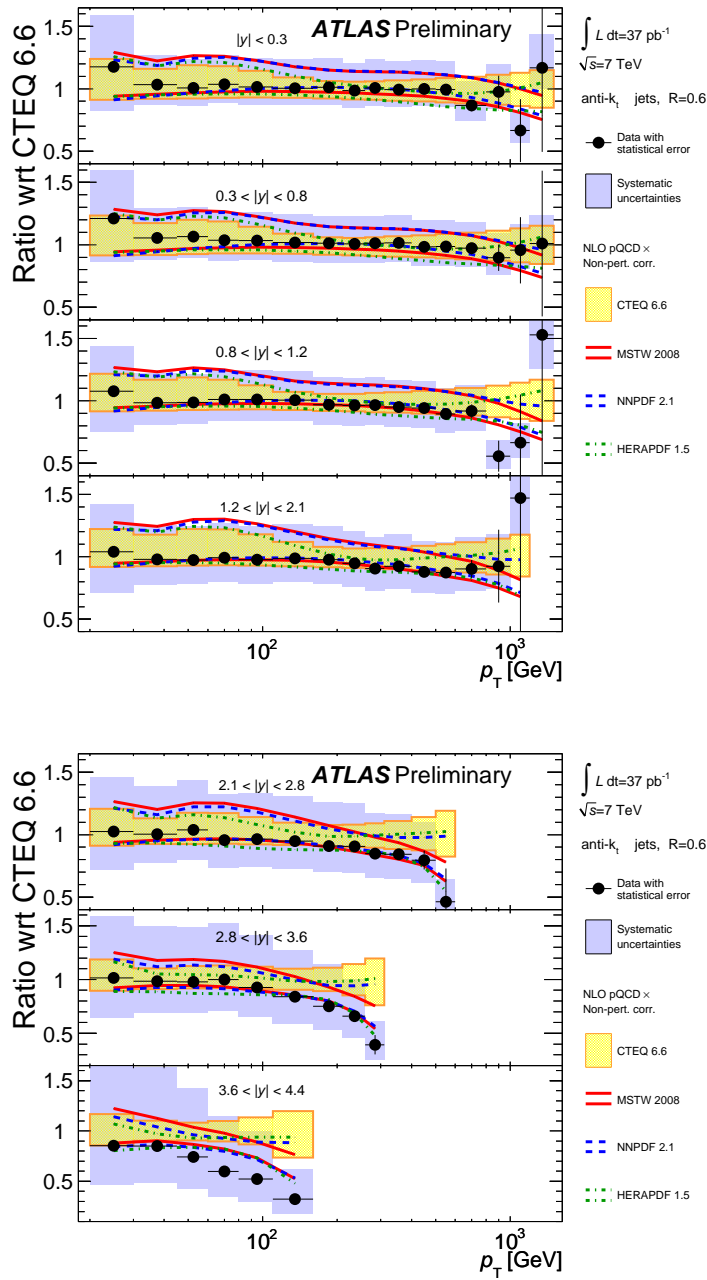


Figure 9.8: ATLAS results (black data points) of inclusive jet double-differential cross sections as a function of jet p_t in different central regions of rapidity comparing different PDF sets (HERAPDF 1.5, CTEQ 6.6, MSTW 2008, NNPDF 2.1). The data points and the error bands are normalized to the theoretical predictions obtained by using the CTEQ6.6 PDF set. From [166, Fig. 14, 15].

10. Studies of Radiation Damage for Silicon Sensors for the XFEL

The European X-ray Free-Electron Laser (*XFEL*) [175] at DESY is planned to start its operations in 2015 [176]. It will generate ultra-short (in the order of 10 fs) X-ray flashes with a wavelength of about 0.1 nm and will reach a very high brilliance.

This imposes grand requirements on the radiation hardness of the detectors for XFEL. The foreseen silicon-pixel sensors will have to tolerate fluences of about $10^{16} \frac{\text{photons}}{\text{cm}^2}$ within three years, where the energy of the photons will be about 12 keV. This corresponds to a radiation dose of the order of 1 GGy at the detector *SiO₂* surface.

The expected radiation-induced effects on the sensors are chiefly surface damages at the *Si – SiO₂* interface, as the energy of the photons is not high enough to cause bulk damage.¹

To be able to estimate how the silicon sensors are affected by these high radiation doses of photons of the described energies a study was started at *HASYLAB* (Hamburger Sychrotronstrahlungs-Labor, see Section 10.2.1): Test structures (gated diodes, see Figure 10.1) were irradiated in three irradiation campaigns and analysed by capacitance-voltage (*CV*) and current-voltage (*IV*) measurements.

After describing the motivation of the study and introducing the test structures (Section 10.1), the set-up and calibration of the test-stand are described (Section 10.2) and results of the first two irradiation campaigns are shown (Section 10.3), in which the author of this thesis was directly involved. Subsequent studies based on these measurements and the measurements of the third irradiation campaign are described in [165, 177].

10.1. The Gated Diodes and Performed Irradiation Campaigns

Gate-controlled (or short gated) diodes² are useful for radiation hardness studies due to the possibility to measure *IV* diode and MOS (Metal Oxide Semiconductor) characteristics with the same structure (see Section 10.3.2 for the MOS and Section 10.3.3 for the diode characteristics). An irradiated diode seen from above is shown in Figure 10.1 and a cross section view is depicted in Figure 10.2.

The diodes are about 285 μm thick *p⁺n* diodes manufactured by *CiS*³ with very low-doped silicon of the order of 10^{12} cm^{-3} . On the *p⁺* side there is a *SiO₂ + Si₃N₄*⁴ layer, on which five aluminum gate rings are placed. The geometry of the diodes was designed

¹Bulk damage is only expected at photon energies above 300 keV.

²Gated diodes were introduced in [178].

³CiS, Institut für Mikrosensorik und Photovoltaik GmbH, Erfurt, Germany

⁴350 nm *SiO₂* and 50 nm *Si₃N₄*

for the ROSE [179] collaboration and is visible in detail in the above mentioned Figures 10.1 and 10.2.

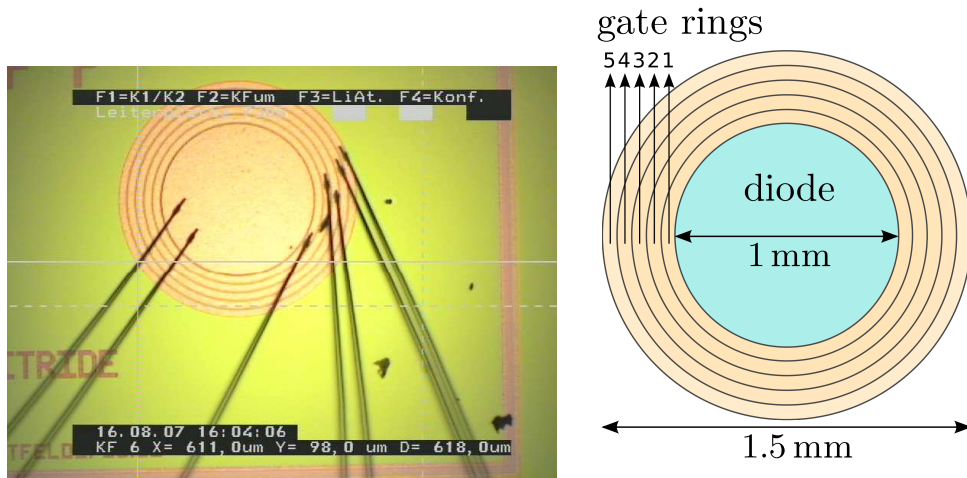


Figure 10.1: Photo (left) and schematic drawing (right) of a utilised gate-controlled diode, seen from top.

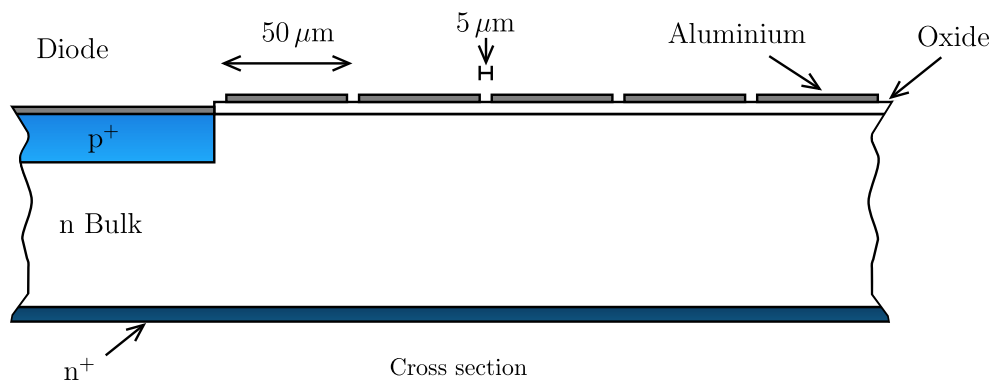


Figure 10.2: Schematics of the cross section of the employed gated diodes, Figure taken from [180].

To investigate the radiation damage caused by photons of about 12 keV, an irradiation stand was set-up at HASYLAB, where synchrotron radiation of appropriate energies is available (see Section 10.2) and the diodes were irradiated in different campaigns. To get reliable results over a broad dose range, two sets of four⁵ and five gated diodes were irradiated in several steps up to 1 MGy (first set) and 1 GGy (second set) respectively.

⁵The bonds of one of the diodes was damaged in between and the diode could not be rebonded. Therefore it was replaced by another diode, which was thus irradiated to 256 kGy in a single step. There is no significant difference due to this replacement expected.

10.2. Irradiation Procedure and Setup

For irradiating the diodes at HASYLAB (see Section 10.2.1) a setup was developed. The gated diodes were glued onto a ceramic substrate and bonded, so that they could be easily handled and measured.

An irradiation table was designed to keep the diodes fixed during the irradiation process (see Figure 10.3). Important features of the irradiation table are:

- Spring-mechanism to keep the ceramics in place, but to make them easily interchangeable
- Possibility to connect the diodes' contact during irradiation to a voltage source to allow e.g. biasing
- Water-cooling applied on the rear side of the ceramic
- Interchangeable collimators with precision alignment
- Chopper to reduce the irradiation rate (up to a factor of 200)

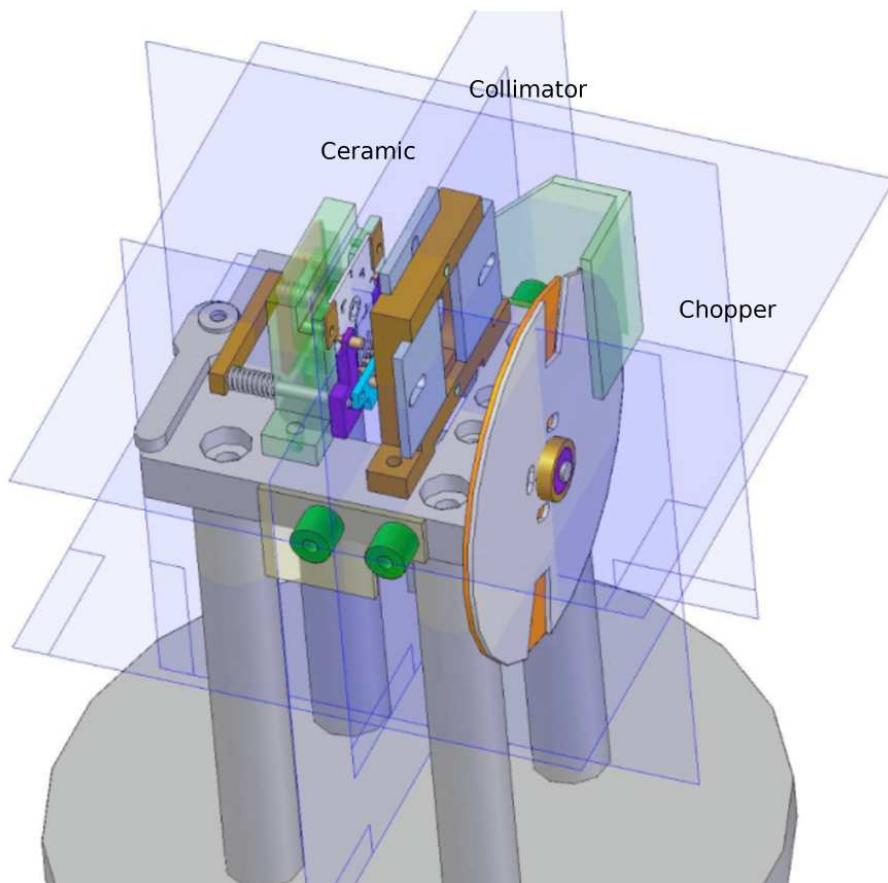


Figure 10.3: 3-D drawing of the irradiation table (see Section 10.2).

The setup can be easily adapted to the usage for other irradiation schemes (with e.g. different test structures) as well.

10.2.1. HASYLAB and Beamlines F3 and F4

At HASYLAB research using accelerator-based light sources is done. For the irradiation described here synchrotron radiation originating from DORIS is used. DORIS was the first storage ring at DESY. Its synchrotron radiation has been used since 1974. Since 1993 the upgraded accelerator DORIS (called DORIS-III after the upgrade) serves nearly⁶ exclusively as a source of synchrotron radiation. DORIS has a circumference of 289 m and stores electrons and positrons with a typical energy of 4.45 GeV. The typical initial beam current is 120 mA. The synchrotron radiation, which is produced in the bendings of the accelerator, is very intense in the X-ray range. There are currently 33 beamlines at DORIS [182] (see Figure 10.4). The gated diodes of this study were irradiated at the beamlines F3 and F4, which provide a white photon beam from a bending magnet. The setup was first used at F3 and then later transferred to F4 for further measurements. The beams will be discussed in more detail in Sections 10.2.2 and 10.2.3.

Other light sources at HASYLAB include PETRA and FLASH. The locations of HASYLAB, PETRA and DORIS are indicated in the schematic view of HERA and its pre-accelerator systems in Figure 3.2.

10.2.2. Spectrum

The spectrum of the synchrotron radiation is important to know in order to determine whether it can be used as an approximation of the radiation at the European XFEL (12 keV photons). The spectrum was calculated at different points of the beam taking into account the material [183] the beam passed through [184–186]. The spectrum at the surface of the diode is depicted in Figure 10.5. The absorbing materials at F3 are a 50 μm Al window, a 250 μm Be window, 20 cm of nitrogen and a 25 μm Kapton window.

The spectrum has a maximum at about 10 keV with a full-width at half-maximum of about 13 keV. As the amount of photons coming from the source changes significantly, mainly due to accelerator conditions, only the energy per photon and not the normalisation from this calculation is used (see Section 10.2.3).

10.2.3. Dose and Beam Profiles

The irradiation dose was measured using a photo diode. The knowledge of the average energy per photon (shown above) together with the amount of energy required to create electron-hole pairs makes it possible to calculate the absolute number of photons.

The relation between the dose D and the current in the photo diode I_{Diode} at this

⁶The OLYMPUS experiment [181] will use DORIS, when it is not used as radiation source.

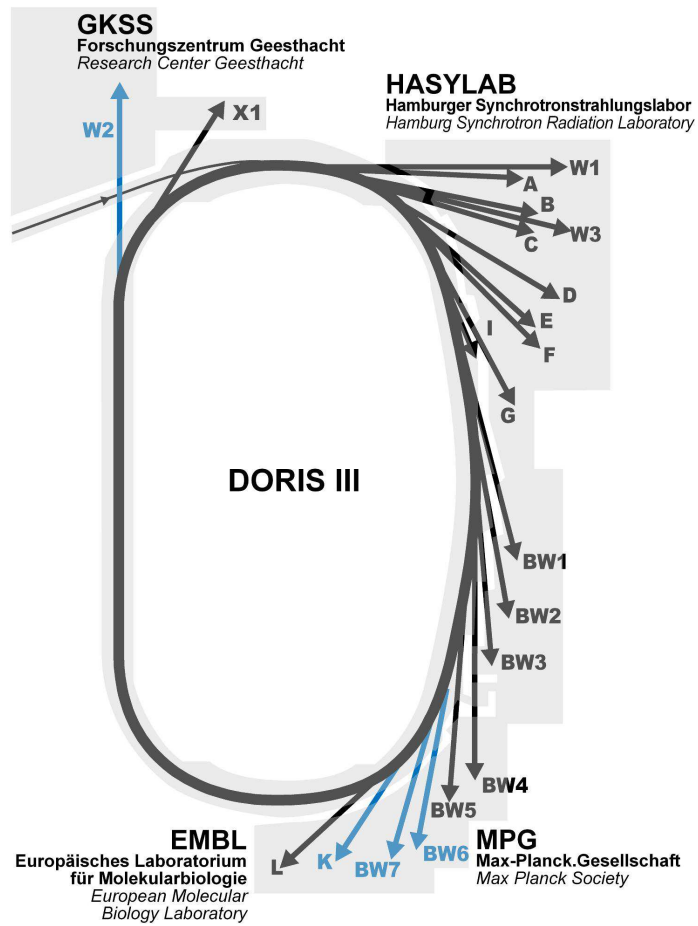


Figure 10.4: DORIS-III and its beamlines (Figure taken from [182]).

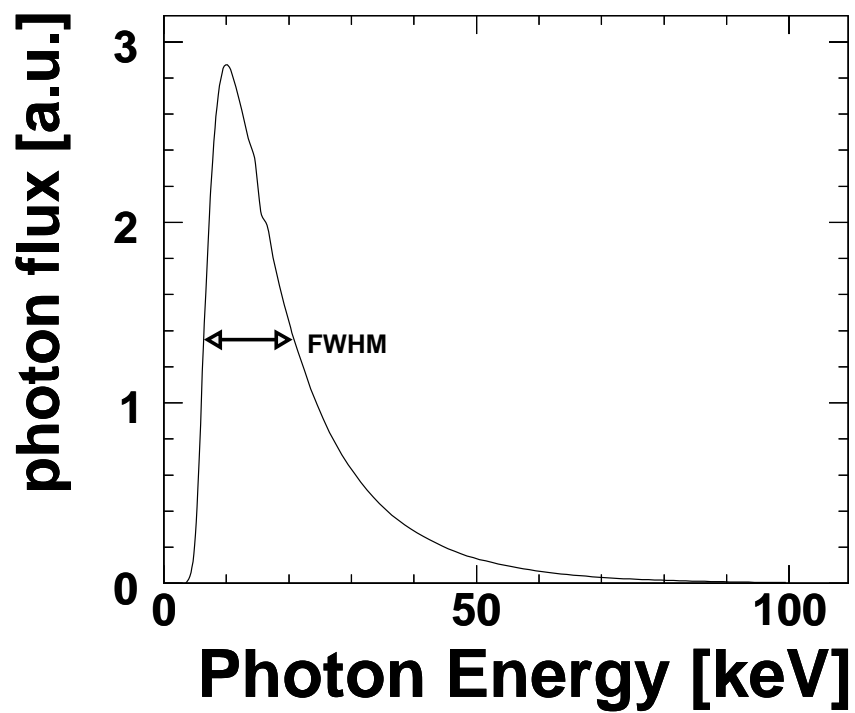


Figure 10.5: Synchrotron radiation spectrum at the location of the surface of the diode in beamline F3. [183,186]

specific setup⁷ was calculated as [184]

$$D(I_{Diode}, t) \approx 0.685 \text{ Gy} \frac{I_{Diode}}{\mu\text{A}} \cdot \frac{t}{s}, \quad (10.1)$$

with the exposure time t .

For most applications the dose rate d is more convenient

$$d(I_{Diode}) = \frac{D}{t} \approx 0.685 \text{ Gy} \frac{I_{Diode}}{\mu\text{A}} \frac{1}{s}. \quad (10.2)$$

As the dose rate and thereby the diode current is directly proportional to the current in the accelerator, the DORIS current I_{DORIS} can be substituted for I_{Diode} . Due to the crucial dependence of the dose rate on the position (see below), the first calculation at each irradiation step was always done after attaining a new measurement of the diode current. Then the proportionality factor,

$$p = \frac{I_{DORIS}}{I_{Diode}}, \quad (10.3)$$

was calculated.

Finally the irradiation time for a specific dose D^{irr} was calculated using

$$t = \frac{D^{irr}[\text{Gy}]}{0.685 \cdot I_{DORIS}^{irr}[\text{mA}]} \cdot p, \quad (10.4)$$

where I_{DORIS}^{irr} refers to the DORIS current at the time of irradiation.⁸

For the dose calculation to be reasonable and the irradiation dose over the area of the gated diode to be reasonably uniform, it is necessary to investigate the spatial profile of the beam, i.e. the dependence of the dose rate (measured was the current of the photo diode) on the position.

For this purpose horizontal and vertical scans were done⁹ while opening one of the collimator slits fully and the other only 0.5 mm. The motor table, on which the irradiation table was mounted, was then moved in the respective plane. The results of such scans are shown in Figure 10.6. The beam profile was found to be - in agreement with theoretical predictions - nearly constant horizontally and nearly Gaussian vertically.^{10,11}

The beam can be considered constant within 20% over an area of 5 mm horizontally and 2 mm vertically. This is sufficient for the gated diodes, which have a diameter of 1.5 mm (see Figure 10.1) as long as the diode is properly centred in the beam. This was assured by remeasuring the beam profiles or testing the beam position with indicator paper regularly.

⁷This formula depends e.g. on the used diode, the beamline, the absorber material.

⁸As the DORIS current slowly changes over time, this needed to be approximated beforehand for the longer irradiation times.

⁹At F4 the beam profile was later measured in two dimensions as well and for even better uniformity the diode was moved through the beam during irradiation, see [165].

¹⁰As there is a collimator within the beamline, the profile is necessarily cut-off at the edges.

¹¹Deviations from the theoretical predictions can be caused e.g. by reflections and misalignments.

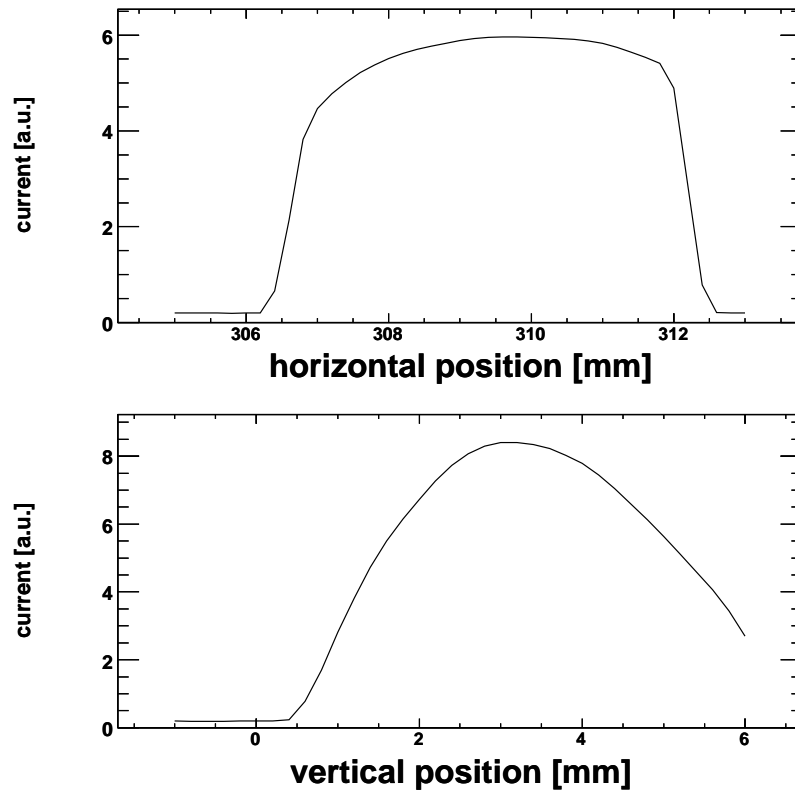


Figure 10.6: Horizontal (top) and vertical (bottom) beam profile at F3 measured with a photo diode.

10.3. Measurement Techniques and Results

The investigated diodes were studied with three different measurement techniques before any irradiation procedure and then again shortly after each irradiation cycle. The MOS capacity characteristics was obtained by means of CV measurements with the aim of obtaining the *flat-band voltage* V_{fb} . IV measurements provided the *surface (generation) current* I_{surf} as well as (after an alternation of the setup) the total diode current.

In [165] the calculation of these quantities based on all three irradiation campaigns is described. Here the measurement method is described and first findings (of the first two irradiation campaigns, in which the author of this thesis was directly involved) are reported.

10.3.1. Measurement Setup in the Laboratory

The IV and CV measurements were performed using a probe station at the detector laboratory of Hamburg University.¹² The ceramic was fixed on the vacuum chuck of the probe station and probe needles were used to access the electrodes of the diode. The measurements were performed in the dark to avoid photo currents.

A Keitley 6517A amperemeter with a built-in voltage source and an Agilent 4284A LCR meter were used for the measurements.¹³ A Keithley 6487 pico amperemeter was utilised as an additional voltage source (see Section 10.3.3).

10.3.2. CV Measurements

The characteristic MOS capacitance curve as a function of the voltage on the second and third gate ring was measured for each diode at each irradiation step. A schematic of this measurement is shown in Figure 10.7. Figure 10.8 illustrates the charge distributions at the $Si - SiO_2$ interface and the depletion layer during measurement: the diode changes from accumulation condition (electrons at the interface) to depletion condition (no charge carriers at the interface) and then to inversion (holes at the interface) with increasingly negative gate voltage V_{gate} .

In accumulation the measured capacitance is given by the oxide capacitance C_{ox} . When the (already negative) gate voltage is decreased and the flat-band voltage V_{fb} ¹⁴ is reached, the diode goes into depletion. The depleted region acts as serial capacitor and thus reduces the total measured capacitance. The depleted region increases (and thus the capacitance decreases) until inversion is reached and the capacitance remains constant again. This behaviour is explained in detail in [178]. It follows that the flat-band voltage (and the oxide capacitance) can be directly extracted from this measurement.

Figure 10.9 shows a CV measurement of an unirradiated diode at two different frequencies. The above described theoretical behaviour with the accumulation, depletion and inversion phase is clearly visible. The extracted values of C_{ox} and V_{fb} are indicated on the plot.

¹²Later on some of the measurements were done within a specially designed box in which the ceramic was fixed and the connections were accessible from outside.

¹³More details about the setup can be found in [187, App. F].

¹⁴The flat-band voltage [188, 189] is the voltage at which the flat-band capacitance, which can be calculated for a specific diode [165, 189], is reached.

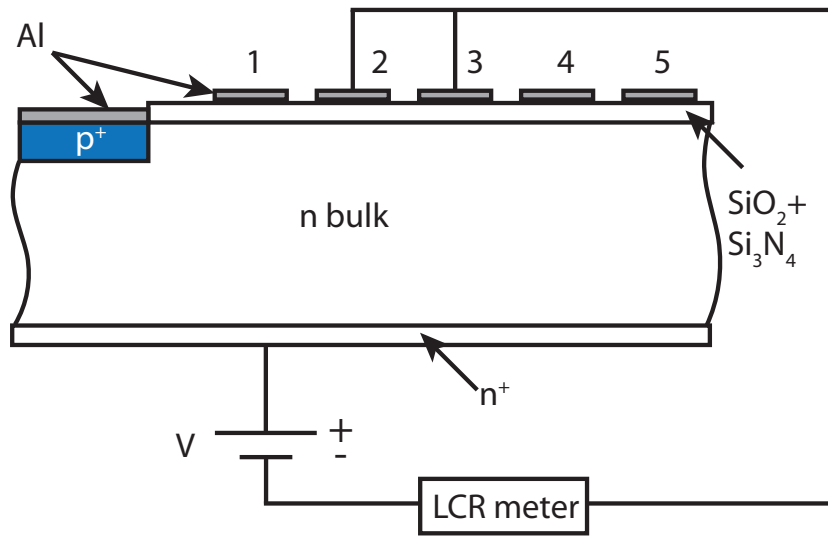


Figure 10.7: Schematic of the CV measurement.

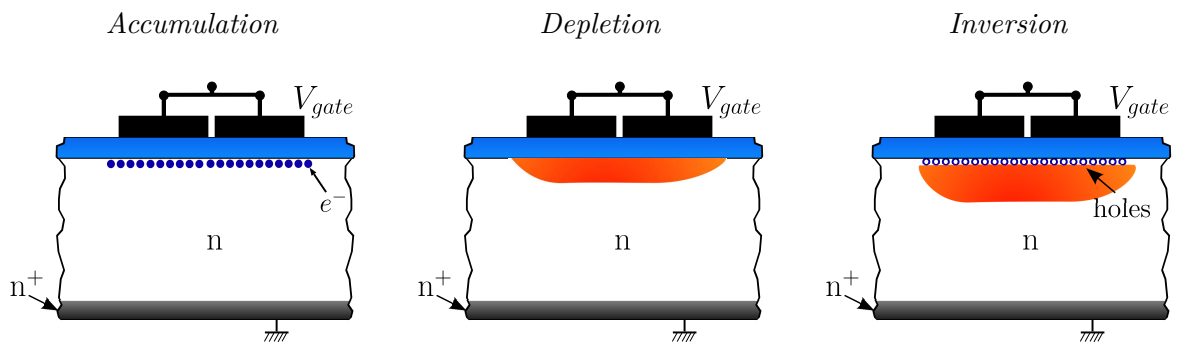


Figure 10.8: Charge distributions under accumulation, depletion, and inversion conditions for CV measurements. The region depleted of charge carriers is indicated in red. Modified from [165, Fig. 10.8], after [189].

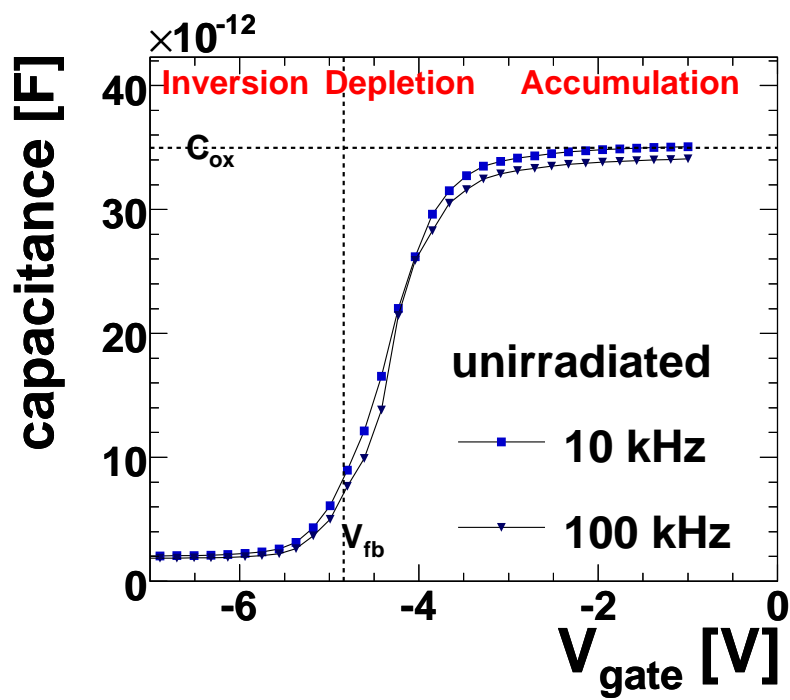


Figure 10.9: CV measurement of unirradiated diode at two different frequencies. The flat-band voltage V_{fb} and oxide capacitance C_{ox} are indicated by the hashed lines.

In Figure 10.10 the 10 kHz curve is shown for different irradiation levels. The measurements show the expected shift of V_{fb} and thus a change of the concentration of surface charges due to the radiation induced fixed oxide charges and charges trapped at the interface states. Interestingly V_{fb} increases only up to doses of 5 MGy irradiation dose and then decreases with the further increasing irradiation dose.¹⁵

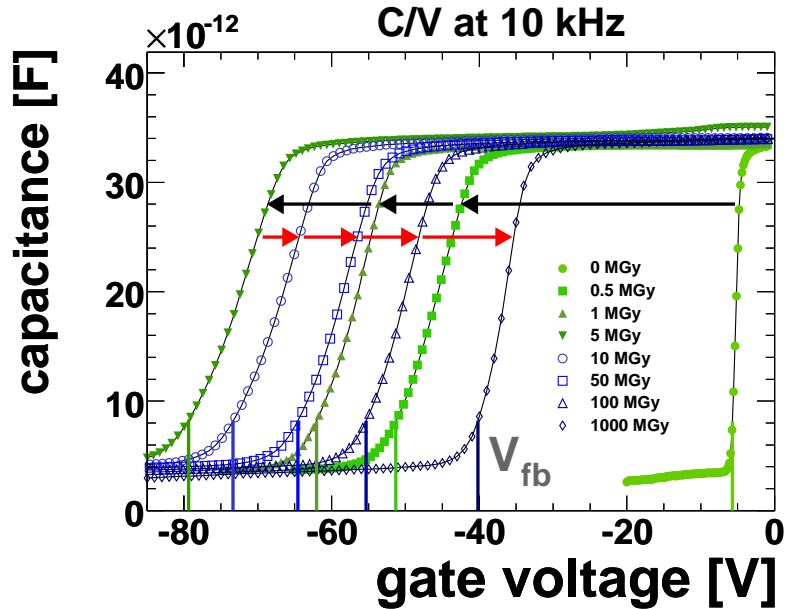


Figure 10.10: Curves of the CV measurements for one of the gated diodes at different irradiation levels. The change of the flat-band voltage (see lines to the x -axis) with irradiation dose is indicated by the arrows.

This behaviour is observed similarly for all measured diodes.¹⁶ A compilation of the measured flat-band voltages as a function of irradiation dose for all measurements is shown in Figure 10.11.

10.3.3. IV Measurements

Two different IV measurements were done for each irradiation step: a measurement directly sensitive to the *surface generation current* I_{surf} and thus suitable for extracting the number of interface states and another measuring the total diode current, both are introduced in the following paragraphs.

Figure 10.12 shows the charge distributions for accumulation, depletion and inversion for the IV measurements (in the measurement of the total diode current, inversion is not reached).

¹⁵It is also visible from this figure, that the transition from accumulation to inversion is much slower for the irradiated capacitor. This is due to the radiation-induced interface traps.

¹⁶Also the third irradiation campaign shown in [165] confirms the results.

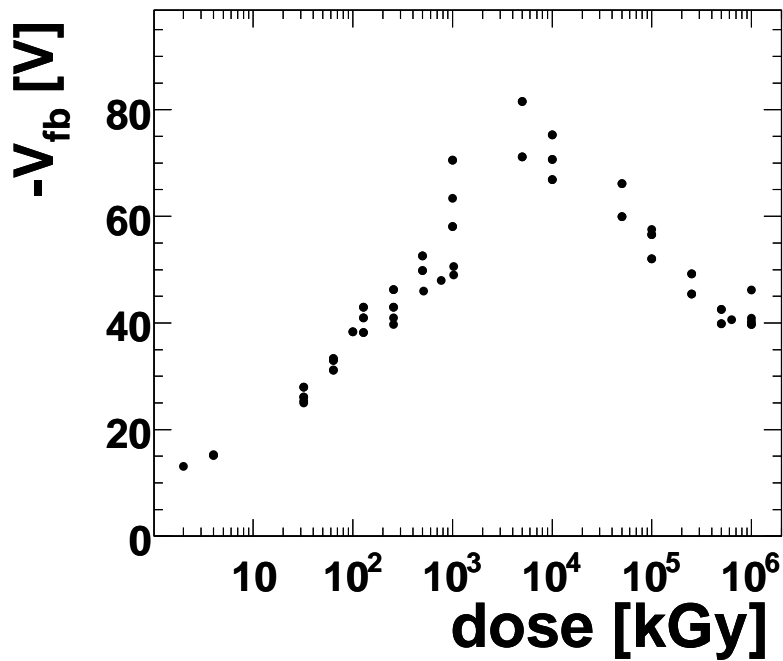


Figure 10.11: Flat-band voltage as a function of irradiation dose. On this plot measurements from all nine diodes are compiled. The values of V_{fb} were extracted from the CV measurement at a frequency of 10 kHz.

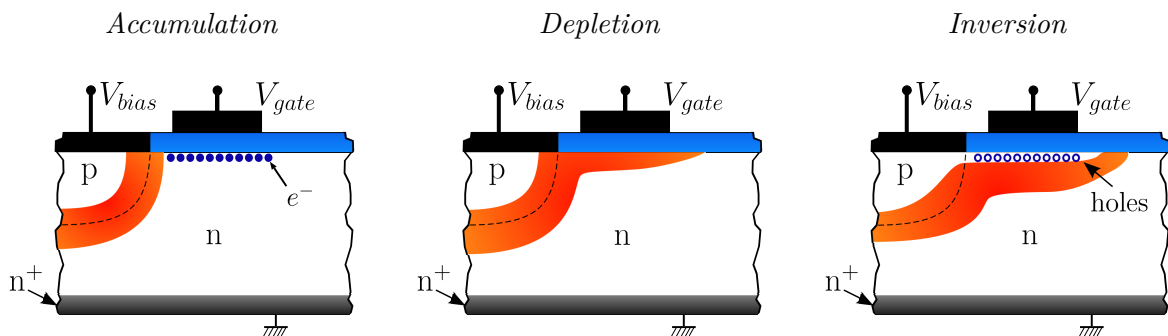


Figure 10.12: Charge distributions under accumulation, depletion, and inversion conditions for IV measurements. The region depleted of charge carriers is indicated in red. Modified from [165, Fig. 10.8], after [189].

10.3.3.a. Surface Generation Current Measurement

When a constant *bias voltage* is applied to the diode and the current through the diode is measured as a function of the voltage applied to the first gate ring (see schematic in Figure 10.13), the three phases of accumulation, depletion and inversion allow a direct measurement of the surface (generation) current. This current, due to the generation of free charge carriers at the $Si - SiO_2$ interface, is also called interface current. It is proportional to the concentration of the interface states at or near to the middle of the band gap.

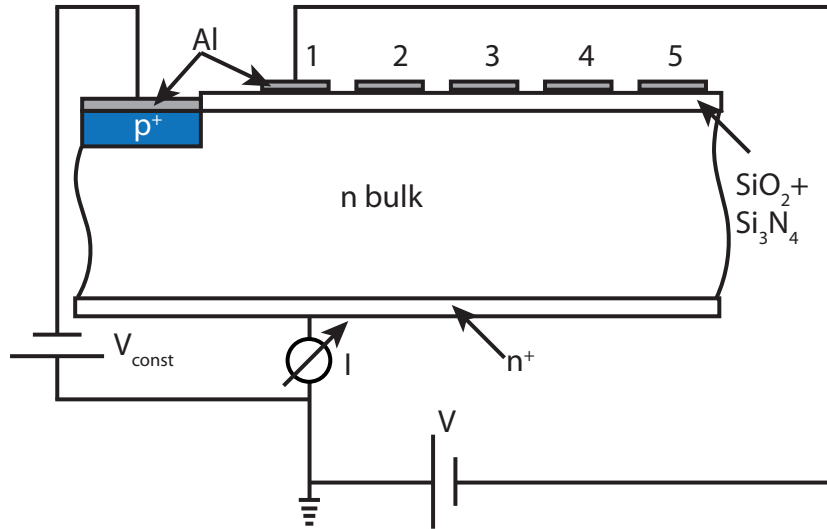


Figure 10.13: Schematic of the surface current IV measurement.

What happens in the three phases is visible from Figure 10.12: In accumulation only the current due to charge carriers in the depleted volume (*volume generation current*) is measured. When depletion is reached under the gate ring, the measured current suddenly rises by the *surface generation current* under the gate area. With increasing voltage the depleted region becomes deeper only (small increase due to more depleted volume under the gate) up to the point when the negative voltage is so high that inversion is reached. At that point the surface is isolated by the layer of holes from the field region and no longer contributes, i.e. only the volume generation current of the increased volume is measured.

An example for the measurement of an unirradiated diode for different bias voltages¹⁷ is shown in Figure 10.14.

Figure 10.15 shows measurements with increasing irradiation up to 256 kGy. The surface current I_{surf} clearly rises. With rising irradiation level (see Figure 10.16) there is a similar behaviour observed as for the CV measurements; the surface current reaches a maximum at about an irradiation dose of 5 MGy and then drops again. This shows a decrease rather than an increase of generation charge carriers at the interface for very high irradiation doses.

¹⁷The different bias voltages should not affect the measured surface current.

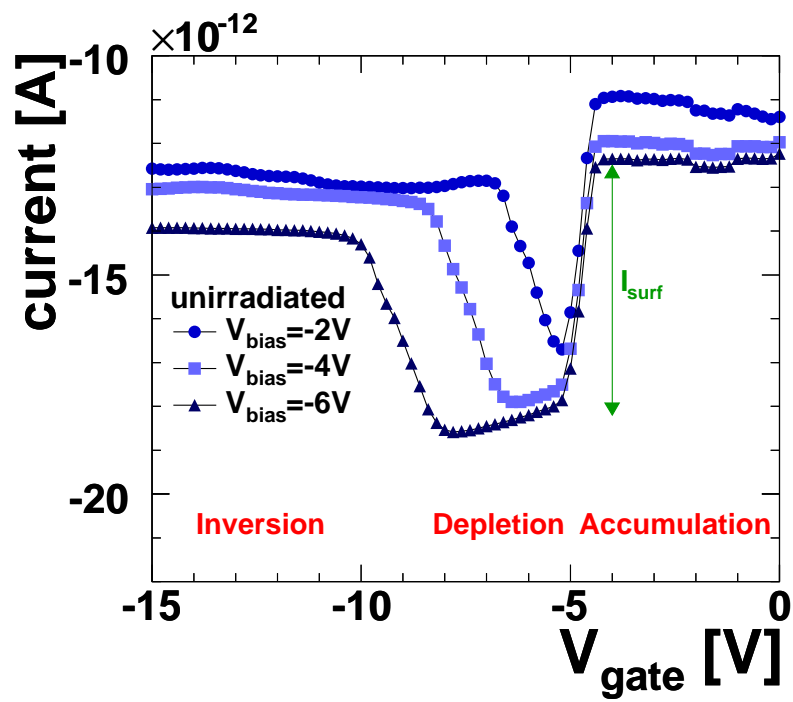


Figure 10.14: Surface current measurement of an unirradiated gated diode for different bias voltages. The surface current is indicated by the green arrow for the $V_{bias} = -6V$ measurement.

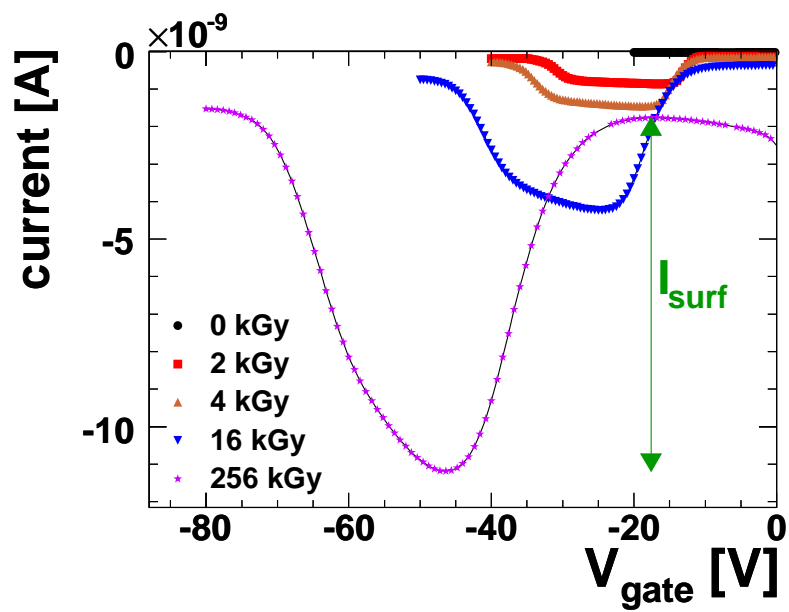


Figure 10.15: Curves of the surface current measurements (schematic see Figure 10.13) for one of the gated diodes at different irradiation levels up to 256 kGy. The measurements shown were performed with a bias voltage of -20 V (the unirradiated with -4 V). The green arrow indicates the surface current for the 256 kGy measurement.

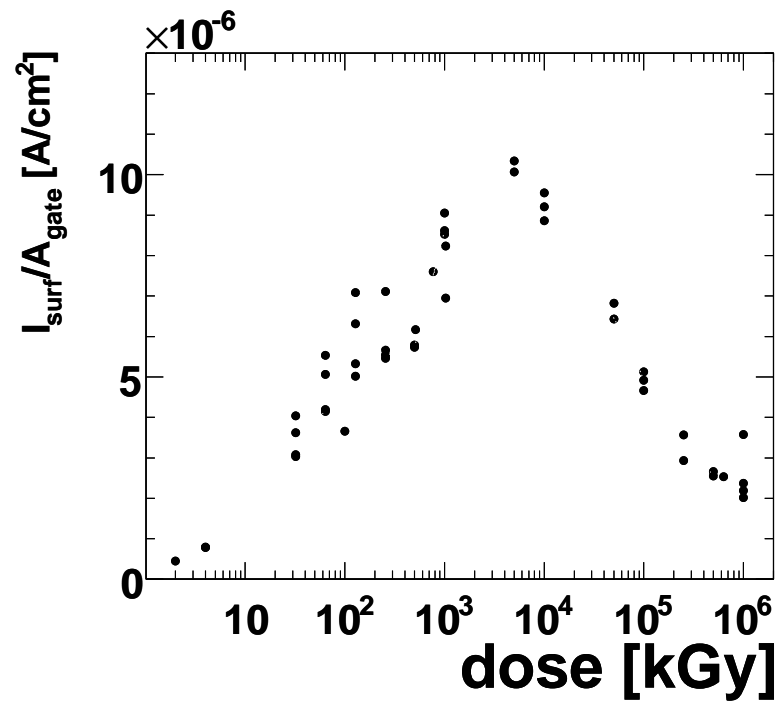


Figure 10.16: Surface current divided by the gate area as a function of irradiation dose. On this plot measurements from all nine diodes are compiled. The values of I_{surf} were extracted from the IV measurements as described in Section 10.3.3.a at a bias voltage of -20 V.

10.3.3.b. Total Diode Current Measurement

The measurement of the total diode current is similar to the standard p^+n diode IV characteristics. It can be achieved by keeping the gate voltage at the same potential as that of the p^+ contact during IV measurement (schematic see Figure 10.17). The measurement is similar to the previously described surface generation measurement, but inversion cannot be reached, because for that $|V_{gate} > V_{bias}|$ would need to be satisfied.¹⁸

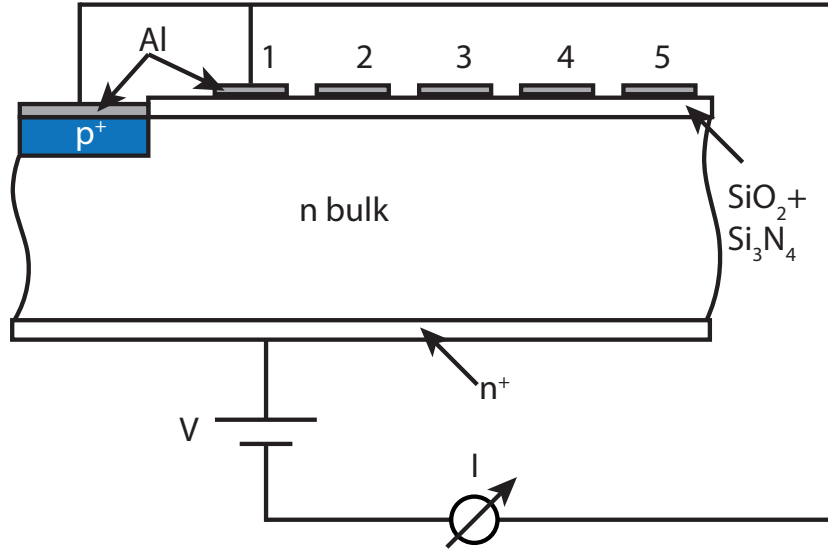


Figure 10.17: Schematic of the total diode current measurement.

Figure 10.18 shows the measurement curves for a diode with irradiation doses up to 256 kGy, which exhibit the expected diode characteristics. The results can also be directly compared to Figure 10.15, showing results of the I_{surf} measurement, demonstrating the close connection. Thus this measurement is a good cross check and illustration of the diode characteristics, but only the measurement described in Section 10.3.3.a was used for the analysis of the surface charges.

10.3.4. Temperature during Irradiation

The results of Sections 10.3.3.a and 10.3.2 indicate a decrease, rather than an increase, of surface charges for doses above 5 MGy. This effect could possibly be explained by temperature-induced annealing, if the temperature of the diodes increased considerable during irradiation. As the dose rate was increased (by making the chopper opening larger and finally removing the chopper) for higher irradiation doses, an increase of the temperature might be considered plausible even though the sample was cooled (see Section 10.2).

To investigate the possibility of such an effect, the temperature of the diode during irradiation with active liquid cooling (set to 20°C) at the back of the ceramic was

¹⁸That the value of V_{gate} at which inversion occurs depends on the voltage of the diode (V_{bias}) is visible in the previously described surface current measurements, see Figure 10.14.

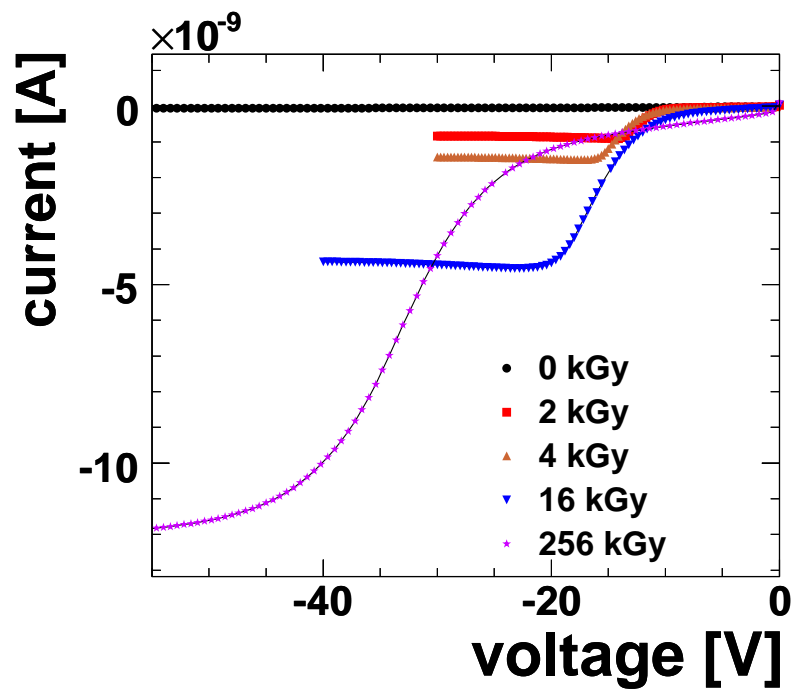


Figure 10.18: Curves of the total diode current IV measurements (schematic see Figure 10.17) for one of the gated diodes at different irradiation levels up to 256 kGy.

measured by attaching a temperature sensor on the silicon (close to, but not on the irradiated area). An example of a temperature measurement is shown in Figure 10.19. The temperature measurements were repeated using different chopper openings for different dose rates.

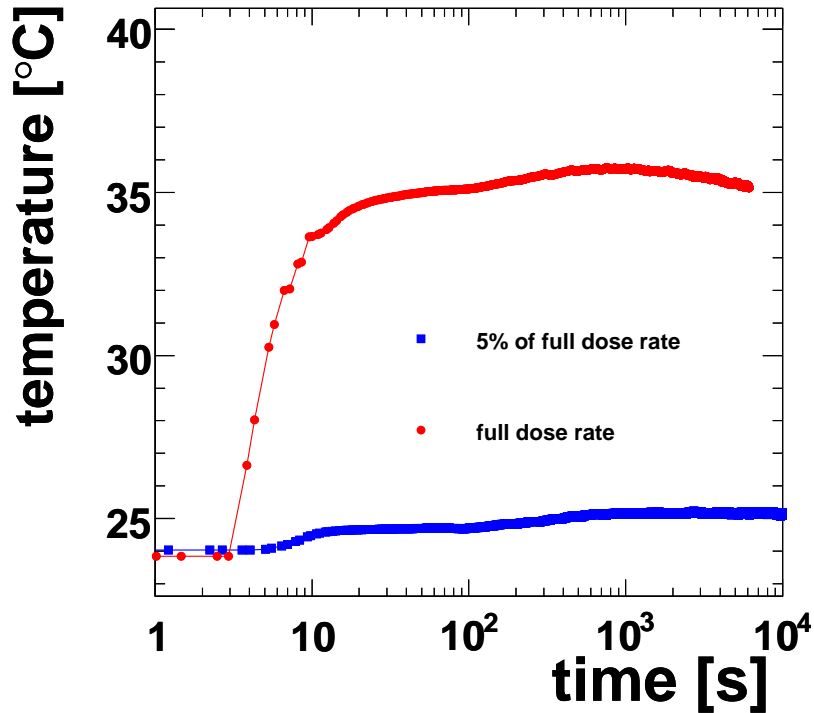


Figure 10.19: The temperature measured by a temperature sensor during irradiation with full dose rate and dose rate reduced to 5%.

The temperature measured before irradiation was about 24°C. There was no significant temperature rise seen at 1% of the full¹⁹ dose rate. At 5% the temperature reached about 25°C and at 10% about 26°C.²⁰ At full dose rate the temperature reached about 36-37°C.²¹

Figure 10.20 shows the measured flat-band voltage for diodes irradiated to the same dose values with different dose rates. It is found that within the reproducibility of the results the flat-band voltage does not depend on the dose rate. It can thus be concluded from the study, that the rise in temperature during high dose rate irradiation is not responsible for the decrease in flat-band voltage at high dose rates.

¹⁹"Full" dose rate refers to the dose rate without reduction through the chopper.

²⁰Switching off the cooling about 28°C were reached. The temperature then drops immediately by about 1°C, when the irradiation is stopped.

²¹A typical annealing temperature would be 80°C.

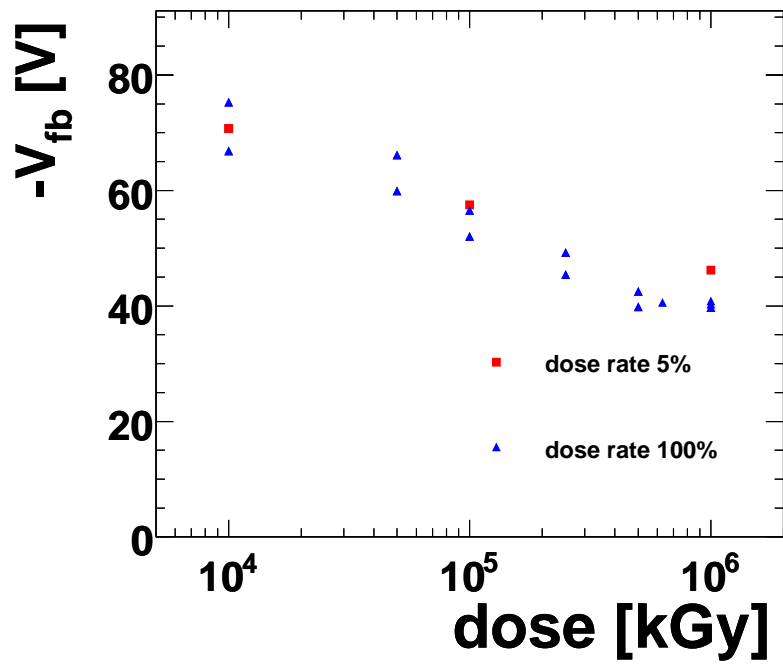


Figure 10.20: Flat-band voltage as a function of irradiation dose for the highest doses with different dose rates. The values of V_{fb} were extracted from the CV measurement at a frequency of 10 kHz. On this plot measurements from four diodes are compiled. The red squares indicate measurements, where the diode was irradiated with the dose rate reduced to 5%, the blue triangles are from measurements after full dose rate irradiation.

10.4. Summary and Outlook

Nine gate-controlled diodes were irradiated at an irradiation stand at HASYLAB with doses from 1 kGy to 1 GGy in several irradiation steps to study the radiation-induced damage on silicon sensors for the European XFEL. *IV* and *CV* measurements were performed before irradiation and after each irradiation step and the surface current I_{surf} and the flatband voltage V_{fb} were extracted from these measurements.

It was found that I_{surf} and $|V_{fb}|$ both strongly increase at low doses, but decrease at high doses (above 5 MeV) in contrast to expectations. No evidence was found that this decrease was caused by temperature-induced annealing.

The study of this not-fully understood effect has afterwards been continued by a third irradiation campaign and extended by further analysis of the results [165,177]. Additional *Thermally Depolarization Relaxation Current* measurements were done and the interface state density as well as the number of interface traps, fixed oxide charges and of border traps were extracted from the measurement data. Though the main results of the analysis presented here were confirmed, it was found that introducing an annealing step makes the results more reproducible and leads to the number of interface states saturating. This could indicate an unstable defect at the interface.

The results indicate that silicon sensors could be suitable for XFEL as the radiation damage saturates. The results of these studies have been included in a sensor simulation program and are used for the optimisation of the design of the AGIPD [190] sensors.

11. Conclusion

NC DIS In this thesis an analysis of Neutral Current Deep Inelastic e^+p Scattering with longitudinally polarised positron beams at a centre-of-mass energy $\sqrt{s} = 318$ GeV has been presented. The analysed data sample was collected with the ZEUS detector in the years 2006 and 2007 during the last running period at full energy at HERA. It corresponds to an integrated luminosity of 135.5 pb^{-1} . A data sample corresponding to 78.8 pb^{-1} was collected with a positive polarisation of the positron beam, while for the remaining 56.7 pb^{-1} the polarisation of the beam was negative. The mean polarisation of the two data sets is 0.32 and -0.36, leading to a mean polarisation of 0.03 for the combined set. This is the largest single e^+p sample collected by the ZEUS detector.

Single-differential cross sections as a function of the virtuality of the exchanged boson, Q^2 , of the event inelasticity, y , and of the Bjorken scaling variable, x , and reduced cross sections (as a function of x and Q^2) were measured in the phase space region $Q^2 > 185 \text{ GeV}^2$, $y < 0.9$ and $y(1-x)^2 > 0.004$.

The cross sections extracted from the complete sample were corrected for the small mean polarisation and quoted for an unpolarised lepton beam.

The single-differential cross sections $\frac{d\sigma}{dQ^2}$, $\frac{d\sigma}{dx}$ and $\frac{d\sigma}{dy}$ were measured and compared with the predictions of the Standard Model. The data description by the theory is good.

The reduced cross sections as a function of x and Q^2 were extracted and compared to the previously published e^-p results [8]. The significant difference at high Q^2 was exploited to measure the structure function $x\tilde{F}_3$, which is sensitive to the valence quarks. In addition $xF_3^{\gamma Z}$ was measured as a function of x at fixed Q^2 by extrapolating the measurements done at different Q^2 values.

The single-differential cross sections and the reduced cross sections were also measured separately for negative and positive polarisation of the lepton beam and were shown to differ significantly at high Q^2 . The $\frac{d\sigma}{dQ^2}$ measurements were used to extract the polarisation asymmetry, measuring directly the parity violation in NC DIS.

The presented measurements of e^+p NC DIS cross sections and of the $x\tilde{F}_3$ structure function exceed the precision of previous ZEUS measurements. The measurement will be used in the HERAPDF fits (and other global fits), in electroweak fits and for searches beyond the Standard Model (Contact Interactions).

The precision of the cross section measurements could be further improved by combining the measurements from H1 and ZEUS, thereby not only reducing the statistical, but also the systematic uncertainty, and (in the unpolarised case) combining measurements of different data-taking periods.

Parton Density Functions The precision of the extracted cross sections has a considerable influence on the better determination of the proton PDFs. The preliminary results of the presented analysis were included in a PDF fit with HERA data. Major reduction of the uncertainties can be seen at high x for the gluon and u -valence distributions.

As the middle- and high- x gluon is not sufficiently constrained by inclusive data, other processes are useful to improve the precision of the PDFs. A study on the impact of including more jet data into PDF fits was presented. It was shown that results from DIS dijets [164], which were put into a fit based on the ZEUS-JETS fit, can further reduce the uncertainty on the gluon distribution at very high x (above 10^{-1}) not only compared to a fit without jet data, but also compared to the ZEUS-JETS fit.

The presented first ZEUS¹ polarised e^+p NC DIS reduced cross sections are especially expected to have a major impact for the electroweak fits, which will be performed at HERA in the near future.

Radiation Damage An irradiation stand was erected at HASYLAB to study the radiation-induced damage by X-rays on silicon sensors for XFEL. Nine gate-controlled diodes were irradiated with doses from 1 kGy to 1 GGy in several irradiation steps. The surface current I_{surf} and the flatband voltage V_{fb} were measured after each irradiation. It was found that both, I_{surf} and V_{fb} , strongly increase at low doses, but decrease at high doses (above 5 MeV). No evidence was found that this decrease was caused by temperature-induced annealing.

This study has been extended further by a third irradiation campaign and further analyses of the results [165,177]. Additional *Thermally Depolarization Relaxation Current* measurements were done and the interface state density as well as the number of interface traps, fixed oxide charges and of border traps were extracted from the data. The main results of the analysis presented here were confirmed, but it was found that introducing an annealing step makes the results more reproducible and leads to the number of interface states saturating.

The results of the studies have been included in a sensor simulation program and are used for the optimisation of the design of the AGIPD [190] sensors.

¹The final publication is expected beginning of 2012. Preliminary results have been made available in Spring 2011 [149].

A. Summary of Selection Cuts

Trigger chain

1. FLT 28, 30, 36, 39, 40, 41, 43, 44, 46, 47
2. SLT EXO1, EXO2, EXO3, DIS7
3. TLT DIS03

Data quality

1. EVTAK
2. MVDTAK
3. STTTAK
4. POLTAK (LPOLTAK for runs with $\mathcal{L}_{LPOL} > \mathcal{L}_{TPOL}$ or TPOLTAK for runs with $\mathcal{L}_{TPOL} > \mathcal{L}_{LPOL}$)

Positron Selection

1. Positron candidate with highest Selection Probability used
2. EM Grand Probability > 0.001
3. e^+ -Energy > 10 GeV
4. Matched track in CTD acceptance $0.3 < \theta < 2.5$
5. Track momentum in CTD Acceptance > 3 GeV
6. DCA(Track,Cluster) < 10 cm in CTD Acceptance
7. Distance to module edge > 1.5 cm in CTD Acceptance
8. Energy not belonging to e^+ in $R < 0.8$ cone < 5 GeV

Geometry cuts

1. Supercrack cut
2. RCAL chimney cut
3. RCAL radius < 175 cm

Background suppression

1. $38 \text{ GeV} < E - p_z < 65 \text{ GeV}$
2. $y_{el} < 0.9$
3. $p_t / \sqrt{E_t} < 4 \text{ GeV}^{0.5}$ and $p_t / E_t < 0.7$
4. Elastic QED Compton rejection
5. $|Z_{vtx}| < 30$ cm and vertex found (according to χ_{vtx}^2)
6. At least one good track ($p_t > 0.2$ GeV, superlayer ≥ 3 , primary vertex fitted)

Phase space and Monte Carlo validation

1. γ_{had} -Projection onto FCAL > 18 cm
2. $y_{JB}(1 - x_{DA})^2 > 0.004$
3. $Q_{DA}^2 > 185 \text{ GeV}^2$

B. FLT Trigger Bits

The FLT bits of the ZEUS Trigger which were used in the NC DIS analysis are summarised on the following pages. For some of the bits, requirements have slightly changed during the running period at about run 60780. *I* refers to runs in the first and *II* to the second part.

Subtriggers used are:

- Isolated electrons
 - FCAL_isoe: isolated electron in FCAL
 - BCAL_isoe: isolated electron in BCAL
 - RCAL_isoe: isolated electron in RCAL
 - FR_isoe: isolated electron in one of three quadrants of RCAL¹
- Energy thresholds
 - RCAL_EMC_E: energy in EMC part of RCAL (except for most inner ring)
 - BCAL_EMC_E: energy in EMC part of BCAL
 - CAL_EMC_E: energy in all EMC parts of CAL (except for inner rings in RCAL and FCAL)
 - CAL_Et: total transverse energy in CAL (except for inner rings in RCAL and FCAL)
 - Cal_allEt20: at least 18 GeV of transverse energy in all of CAL
 - REMCth: energy in EMC part of RCAL in inner ring
- Track vetoes
 - Trkv3: not track class 2 and not track class 8 with 26 or more tracks
 - Trkveto: track class is not 2
 - TRK_q95b: track class of higher than 2
 - Trkv2: track class neither 2 nor 8
- Other Vetoes
 - C5v: veto from C5 counter
 - VWv: veto from Veto Wall
 - SRTD95v2: veto from SRTD
 - S3m_v: veto from S3m

¹Due to high background the quadrant in positive x and negative y direction is excluded.

- S6m_v: veto from S6m
- Fbp: at least 5 GeV in most inner ring of FCAL
- CAL_ev: veto from CAL energy $!(CAL_E) \geq 464$, i.e. one cell

FLT 28

- FCAL_isoe OR (BCAL_isoe AND TRK_q95b)
- Cal_allEt20
- Trkv3
- C5v, VWv, SRTD95v2, S3m_v, S6m_v

FLT 30

- RCAL_isoe
- RCAL_EMC_E of at least 3992 MeV (*I*)/3404 MeV (*II*) or REMCth of at least 15000 MeV
- C5v, VWv, SRTD95v2

FLT 36

- RCAL_isoe
- RCAL_EMC_E of at least 3992 MeV (*I*)/3404 MeV (*II*) or REMCth of at least 5000 MeV
- Trkveto
- C5v, VWv, SRTD95v2, !Fbp, S3m_v, S6m_v

FLT 39

- BCAL_isoe
- BCAL_EMC_E of at least 3404 MeV
- Trkveto, TRK_q95b
- C5v, VWv, SRTD95v2

FLT 40

- CAL_EMC_E of at least 20064 MeV
- Trkv3
- C5v, VWv, SRTD95v2, S3m_v, S6m_v

FLT 41

- CAL_Et of at least 30096 MeV
- Trkveto
- C5v, VWv, SRTD95v2, S3m_v, S6m_v

FLT 43

- CAL_Et of at least 15102 MeV
- Trkveto, TRK_q95b
- C5v, VWv, SRTD95v2, S3m_v, S6m_v

FLT 44

- RCAL_EMC_E of at least 3404 MeV OR BCAL_EMC_E of at least 4776 MeV
- Trkv2, TRK_q95b
- C5v, VWv, SRTD95v2, S3m_v, S6m_v

FLT 46

- FR_isoe
- RCAL_EMC_E of at least 2032 MeV or REMCth of at least 3750 MeV
- Trkveto, TRK_q95b
- C5v, VWv, SRTD95v2

FLT 47

- FR_isoe
- RCAL_EMC_E of at least 2032 MeV or REMCth of at least 3750 MeV
- Trkveto
- C5v, VWv, SRTD95v2, !CAL_Ev

C. Control Distributions

Control distributions of the important variables from the final NC DIS sample are shown here. First, a summary plot for the major variables is shown and then each variable is shown separately including the ratio of Standard Model MC and data.

Major Variable Distributions

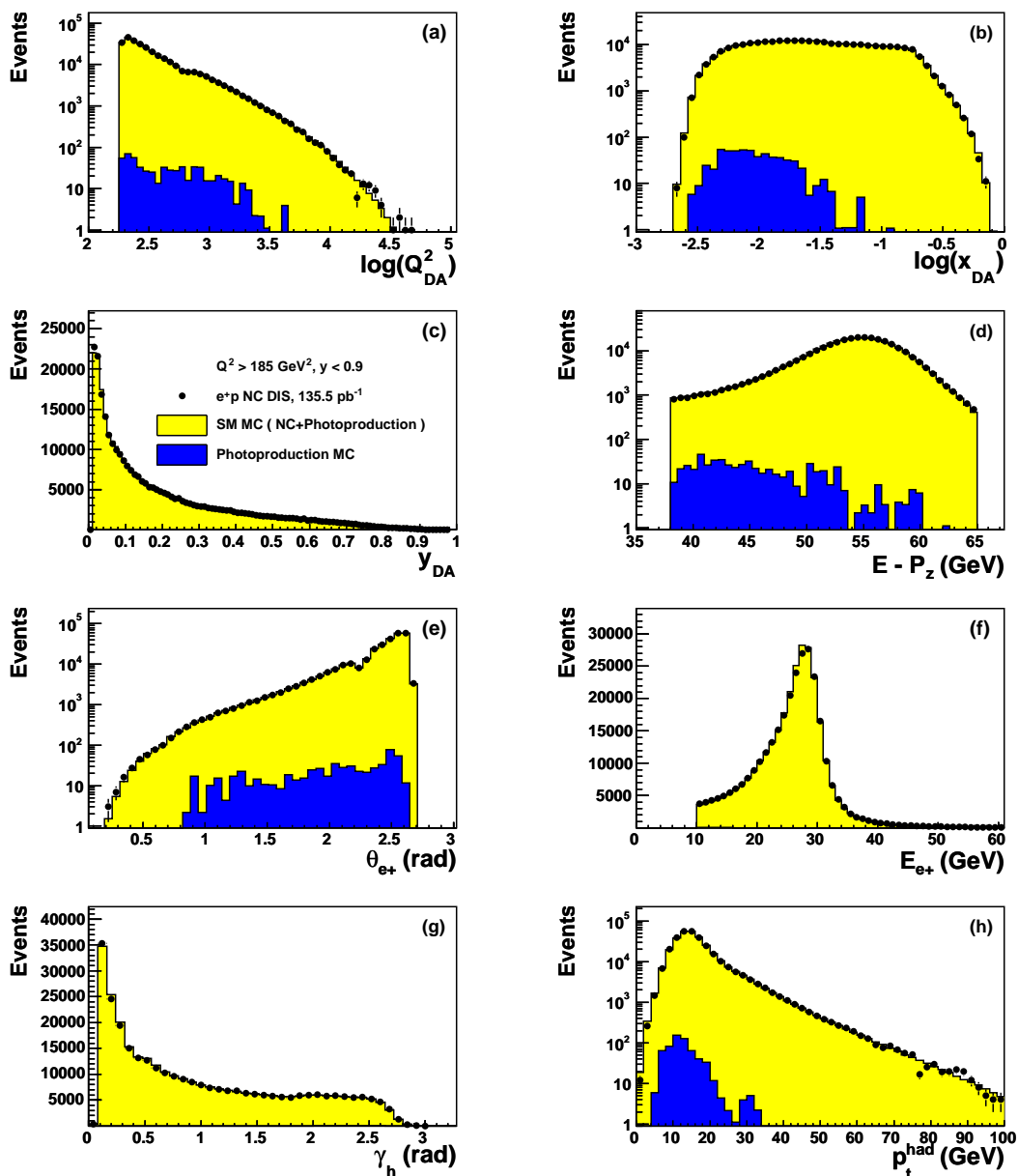


Figure C.1: Distributions of important variables from high Q^2 NC selection. Data is represented by black points, the Standard Model MC (NC DIS and photoproduction) by yellow histograms and the photoproduction background contribution from MC by the blue histograms. a) shows $\log(Q_{DA}^2)$, b) $\log(x_{DA})$, c) y_{DA} , d) $E - p_z$, e) θ of the scattered positron, f) the energy of the scattered positron, g) γ_{had} and h) the hadronic transverse momentum.

Ratio Plots

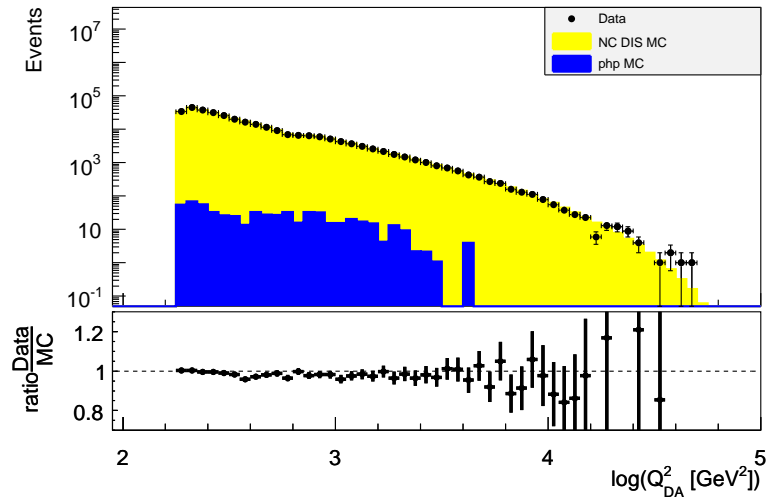


Figure C.2: Distribution of $\log(Q_{DA}^2)$ for data (black points), compared to NC DIS MC (yellow histogram) and photoproduction background MC (blue histogram) after the final selection. In addition the ratio of data and MC is shown in the lower part of the plot.

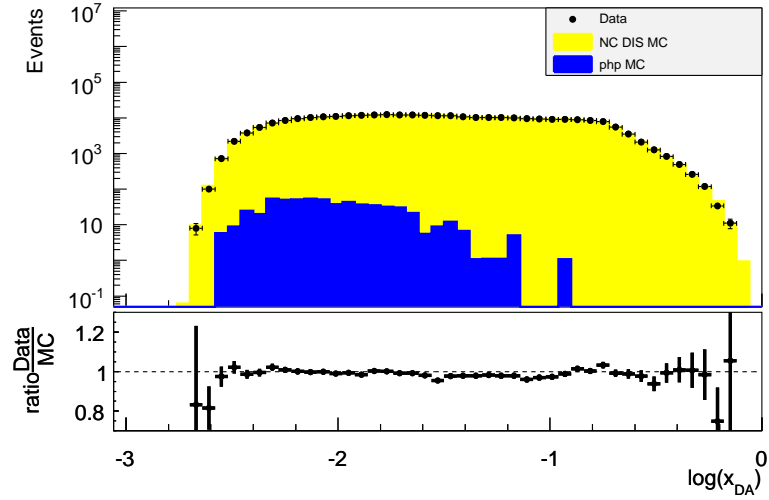


Figure C.3: Distribution of $\log(x_{DA})$ for data (black points), compared to NC DIS MC (yellow histogram) and photoproduction background MC (blue histogram). In addition the ratio of data and MC is shown in the lower part of the plot.

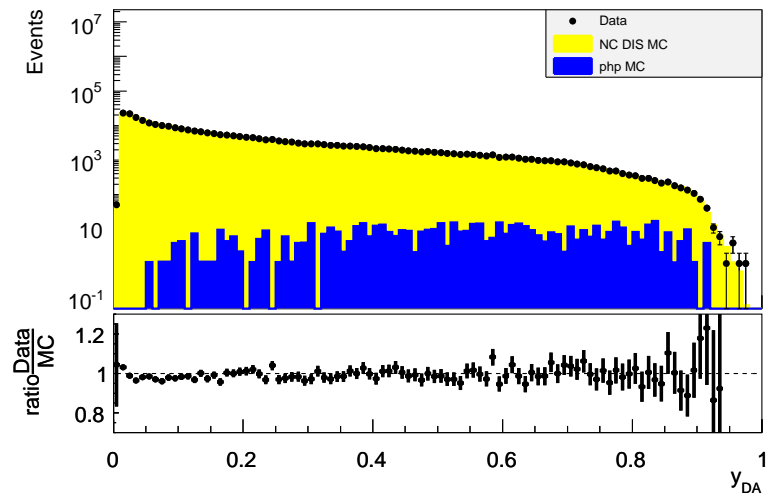


Figure C.4: Distribution of $\log(y_{DA})$ for data (black points), compared to NC DIS MC (yellow histogram) and photoproduction background MC (blue histogram). In addition the ratio of data and MC is shown in the lower part of the plot. Here it is especially important to mention that the Standard Model prediction is reweighted to account for F_L .

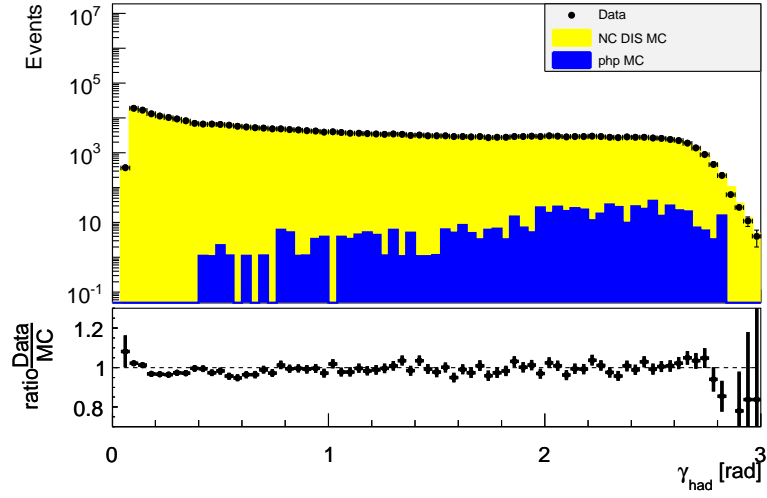


Figure C.5: Distribution of γ_{had} for data (black points), compared to NC DIS MC (yellow histogram) and photoproduction background MC (blue histogram). In addition the ratio of data and MC is shown in the lower part of the plot.

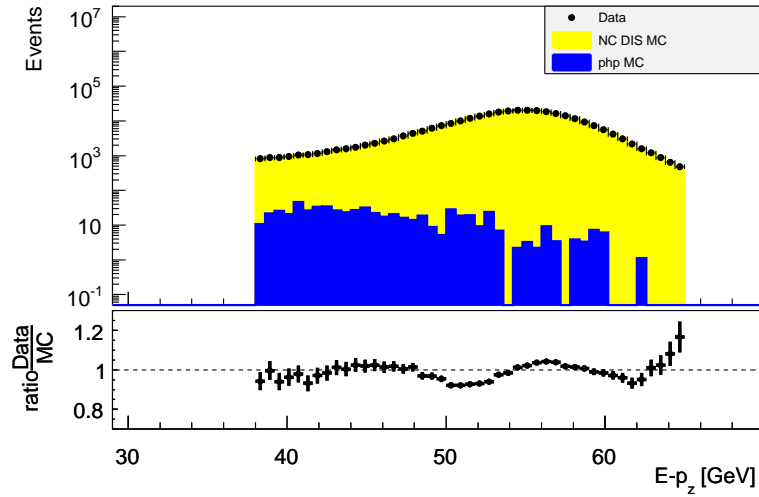


Figure C.6: Distribution of $E - p_z$ for data (black points), compared to NC DIS MC (yellow histogram) and photoproduction background MC (blue histogram). In addition the ratio of data and MC is shown in the lower part of the plot.

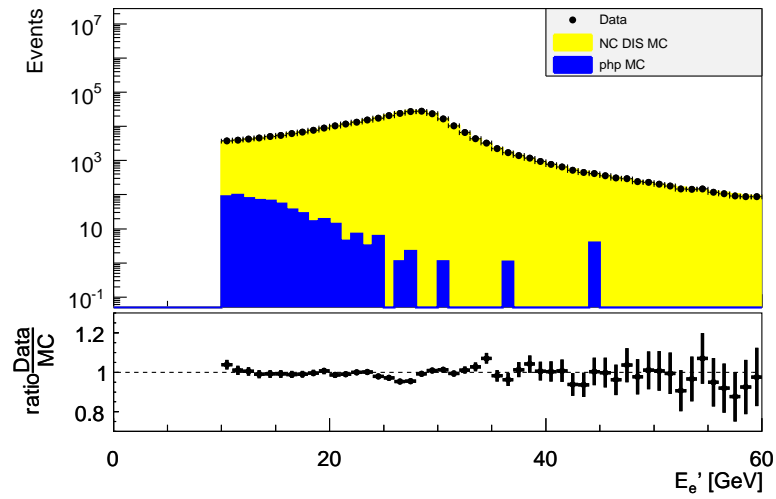


Figure C.7: Distribution of the energy of the scattered positron for data (black points), compared to NC DIS MC (yellow histogram) and photoproduction background MC (blue histogram). In addition the ratio of data and MC is shown in the lower part of the plot.

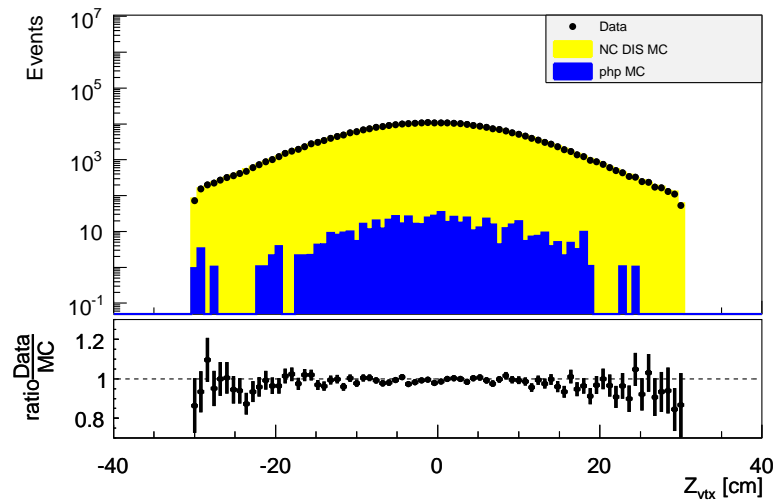


Figure C.8: Distribution of Z_{vtx} for data (black points), compared to NC DIS MC (yellow histogram) and photoproduction background MC (blue histogram). In addition the ratio of data and MC is shown in the lower part of the plot.

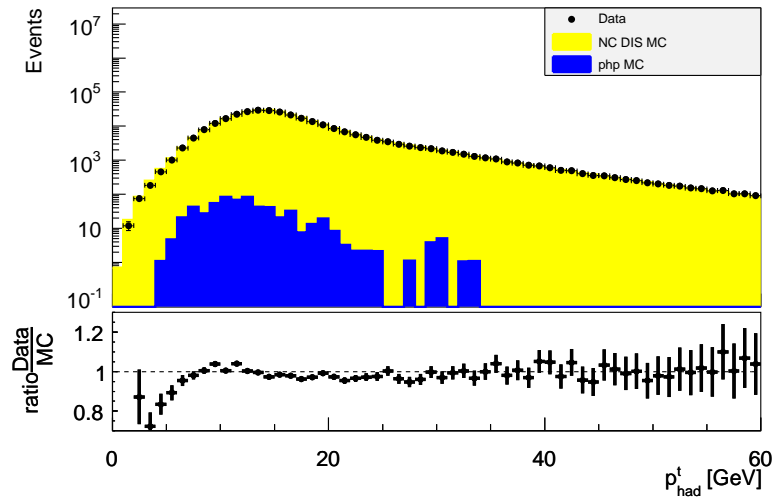


Figure C.9: Distribution of p_t^{had} for data (black points), compared to NC DIS MC (yellow histogram) and photoproduction background MC (blue histogram). In addition the ratio of data and MC is shown in the lower part of the plot.

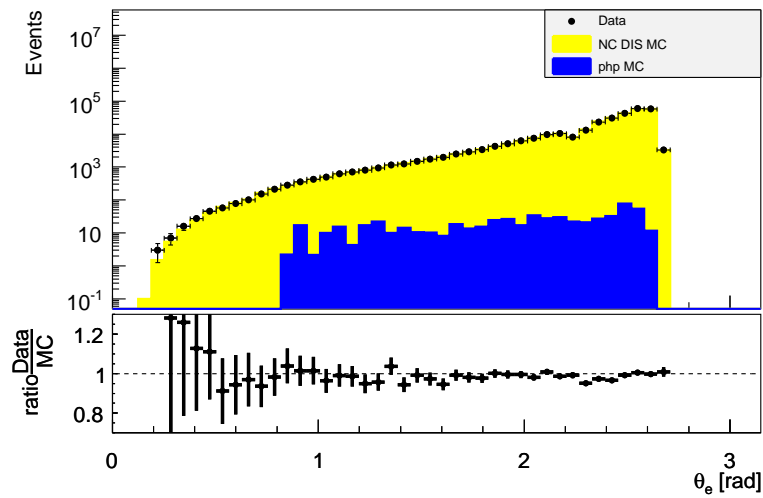


Figure C.10: Distribution of θ of the scattered positron for data (black points), compared to NC DIS MC (yellow histogram) and photoproduction background MC (blue histogram). In addition the ratio of data and MC is shown in the lower part of the plot.

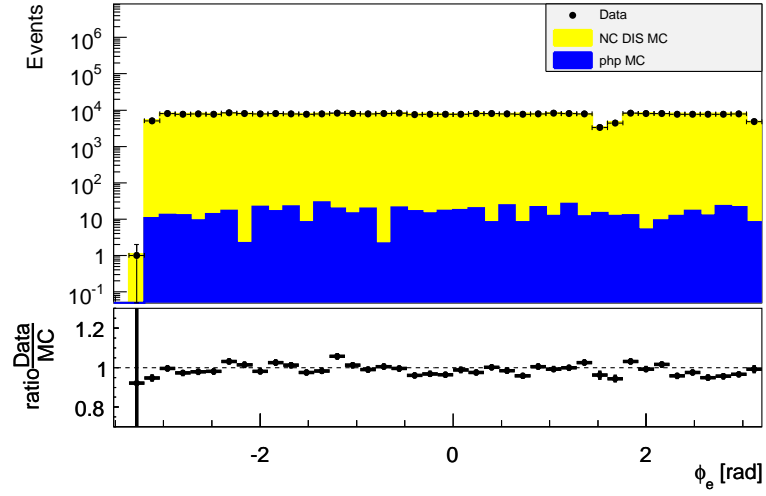


Figure C.11: Distribution of ϕ of the scattered positron for data (black points), compared to NC DIS MC (yellow histogram) and photoproduction background MC (blue histogram). In addition the ratio of data and MC is shown in the lower part of the plot.

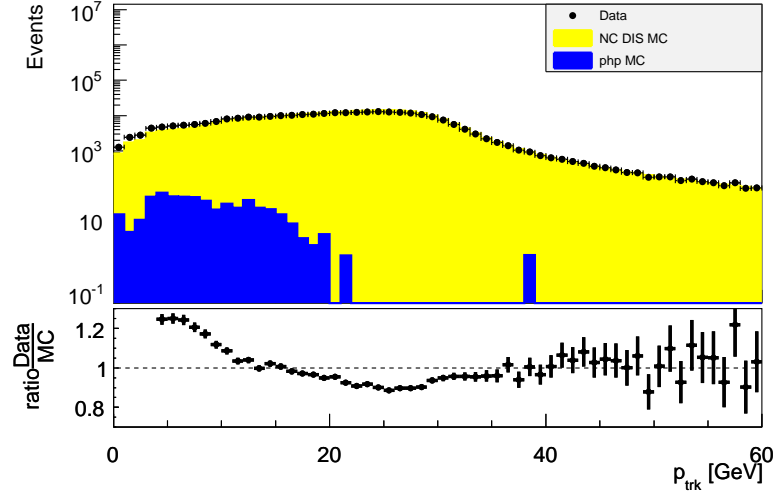


Figure C.12: Distribution of track momentum of the scattered positron for data (black points), compared to NC DIS MC (yellow histogram) and photoproduction background MC (blue histogram). In addition the ratio of data and MC is shown in the lower part of the plot.

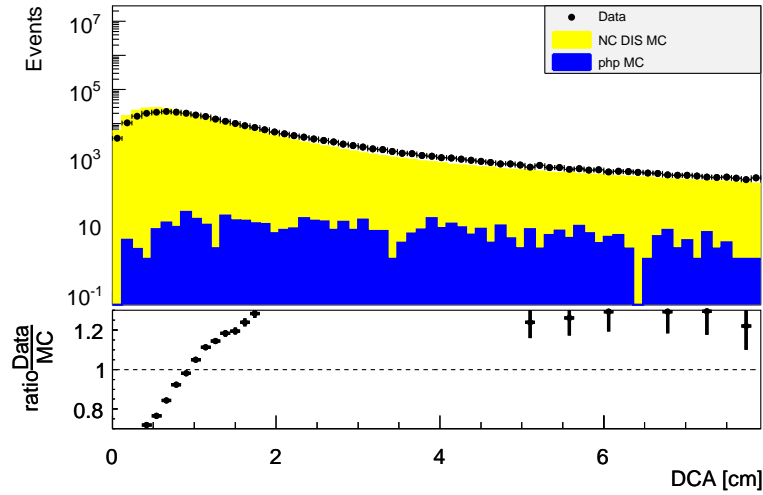


Figure C.13: Distribution of DCA for data (black points), compared to NC DIS MC (yellow histogram) and photoproduction background MC (blue histogram). In addition the ratio of data and MC is shown in the lower part of the plot.

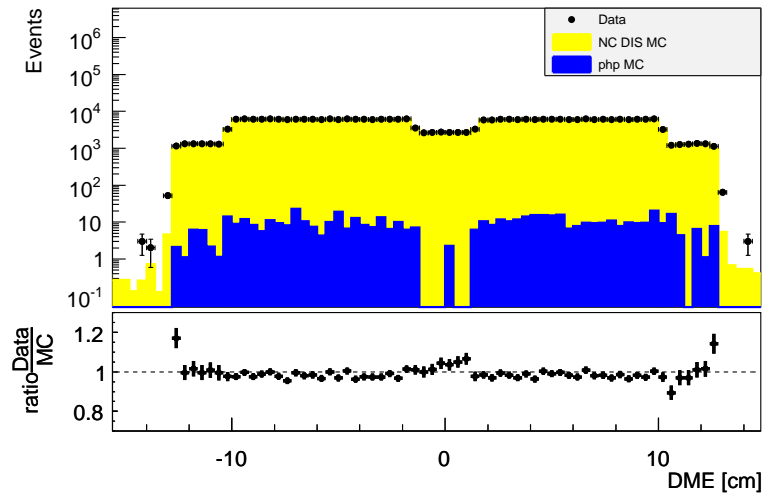


Figure C.14: Distribution of DME for data (black points), compared to NC DIS MC (yellow histogram) and photoproduction background MC (blue histogram). In addition the ratio of data and MC is shown in the lower part of the plot.

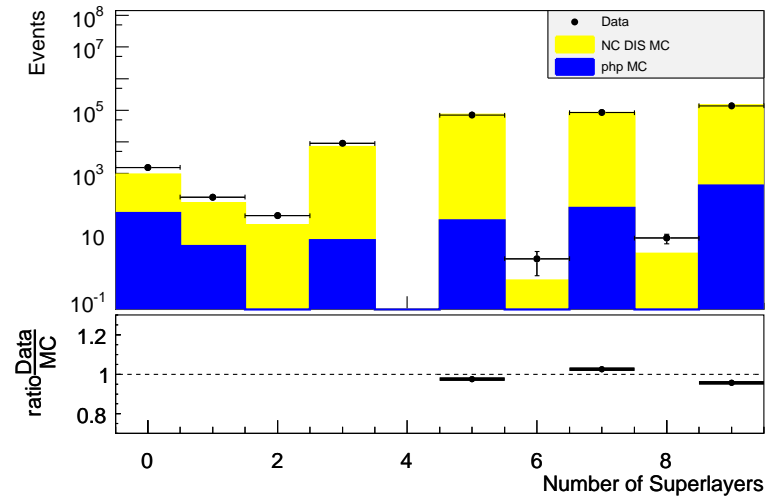


Figure C.15: Distribution of the number of superlayers for data (black points), compared to NC DIS MC (yellow histogram) and photoproduction background MC (blue histogram). In addition the ratio of data and MC is shown in the lower part of the plot.

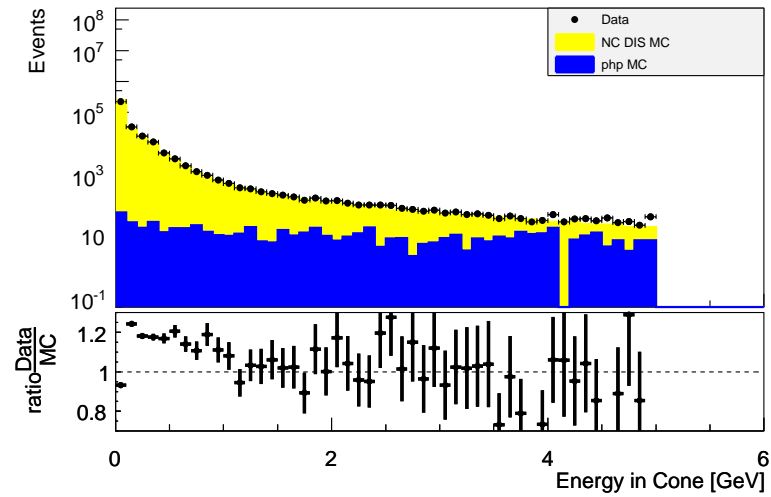


Figure C.16: Distribution of cone energy for data (black points), compared to NC DIS MC (yellow histogram) and photoproduction background MC (blue histogram). In addition the ratio of data and MC is shown in the lower part of the plot.

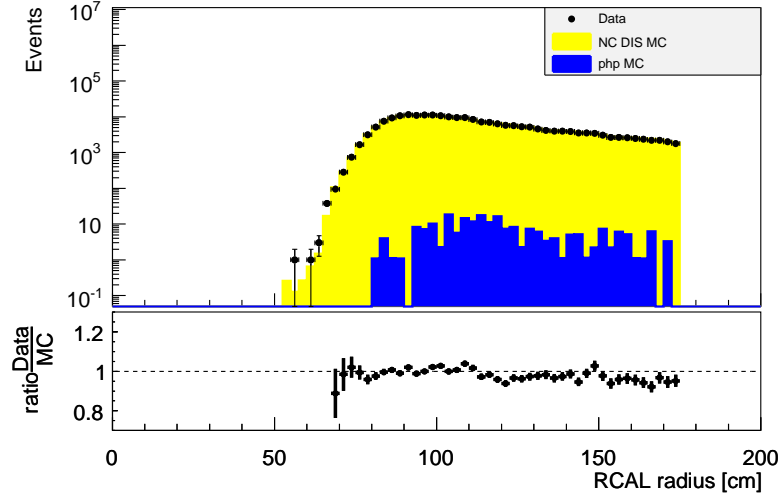


Figure C.17: Distribution of radius of positrons in RCAL for data (black points), compared to NC DIS MC (yellow histogram) and photoproduction background MC (blue histogram). In addition the ratio of data and MC is shown in the lower part of the plot.

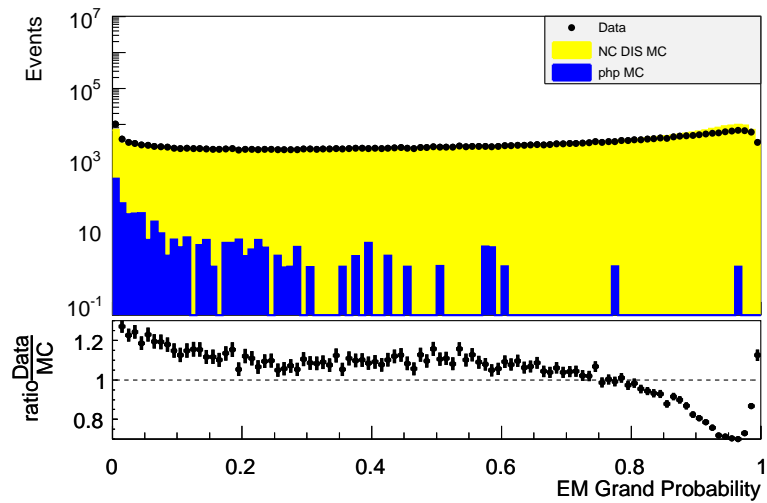


Figure C.18: Distribution of EM Grand Probability for data (black points), compared to NC DIS MC (yellow histogram) and photoproduction background MC (blue histogram). In addition the ratio of data and MC is shown in the lower part of the plot.

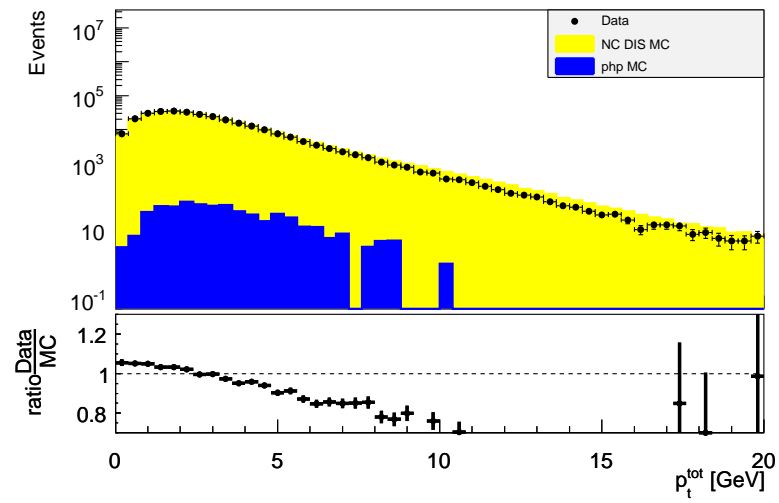


Figure C.19: Distribution of total transverse momentum for data (black points), compared to NC DIS MC (yellow histogram) and photoproduction background MC (blue histogram). In addition the ratio of data and MC is shown in the lower part of the plot.

D. Trigger Rates

The number of events per luminosity (here called rate) of NC DIS events triggered by each of the FLT, SLT and TLT slots used in this analysis are shown in this appendix.¹

FLT

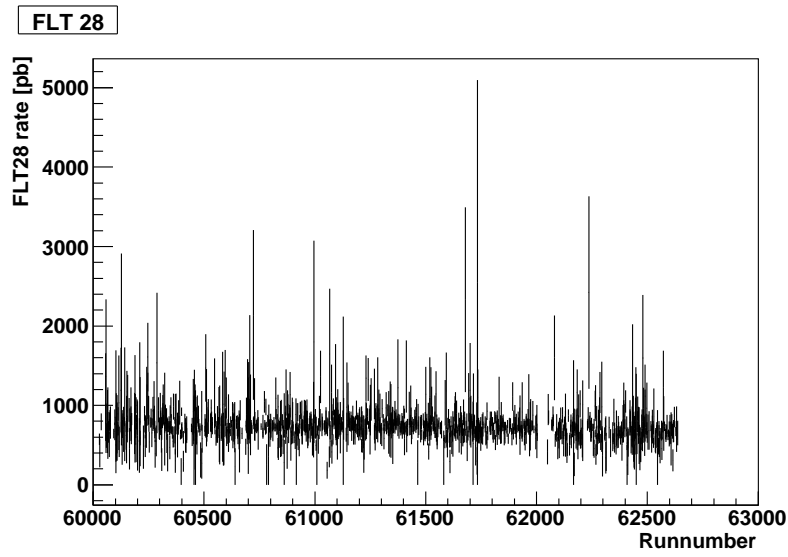


Figure D.1: Rate (Events divided by run luminosity) for NC DIS events triggered by FLT 28.

¹As all events in this analysis must satisfy TLT bit DIS3, its plot includes all events from this analysis.

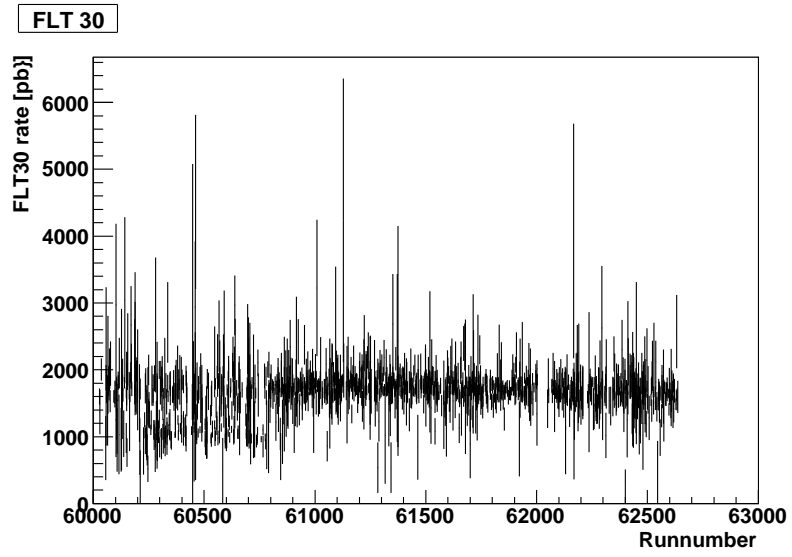


Figure D.2: Rate (Events divided by run luminosity) for NC DIS events triggered by FLT 30.

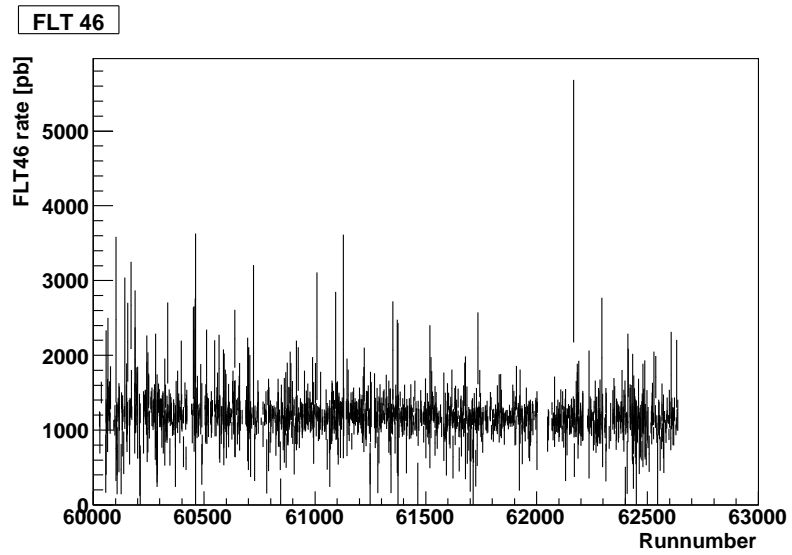


Figure D.3: Rate (Events divided by run luminosity) for NC DIS events triggered by FLT 36.

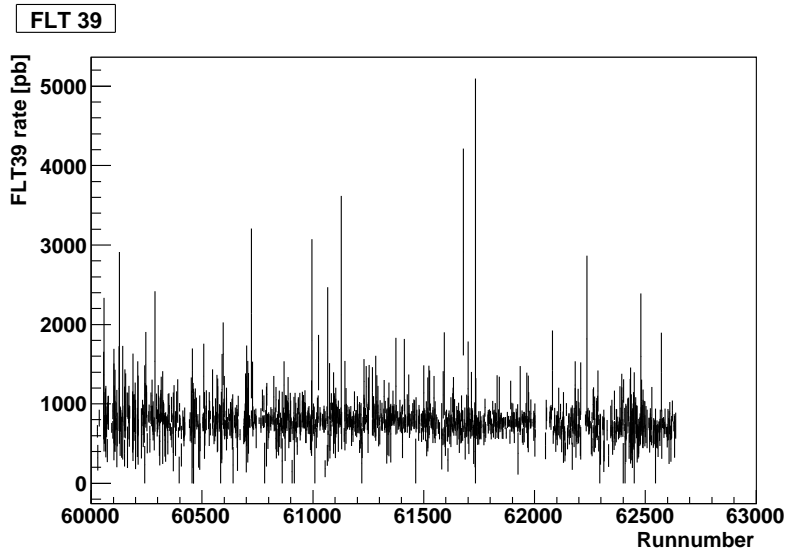


Figure D.4: Rate (Events divided by run luminosity) for NC DIS events triggered by FLT 39.

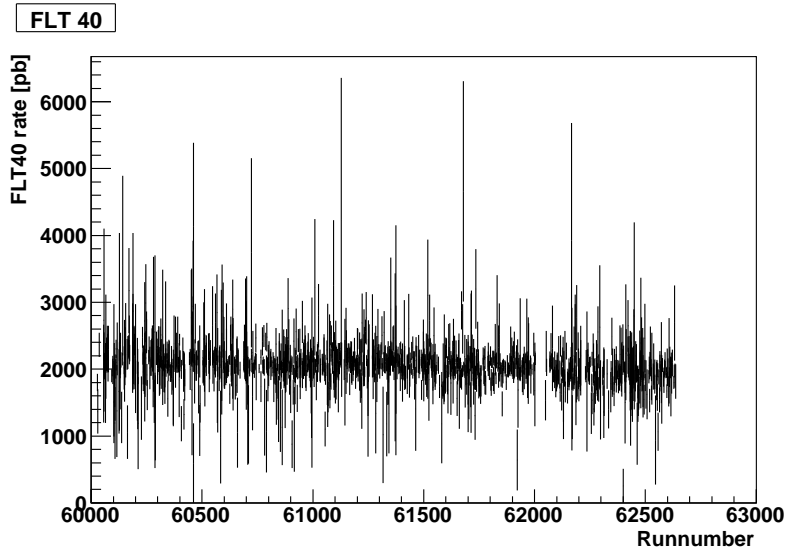


Figure D.5: Rate (Events divided by run luminosity) for NC DIS events triggered by FLT 40.

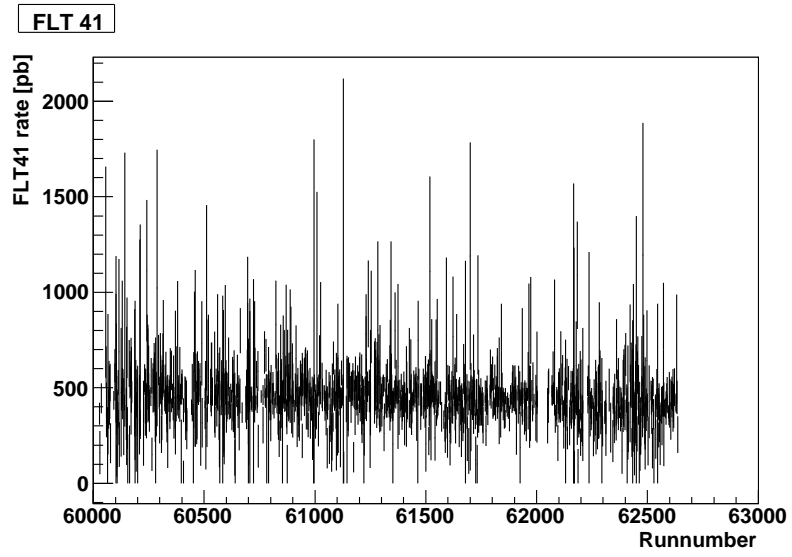


Figure D.6: Rate (Events divided by run luminosity) for NC DIS events triggered by FLT 41.

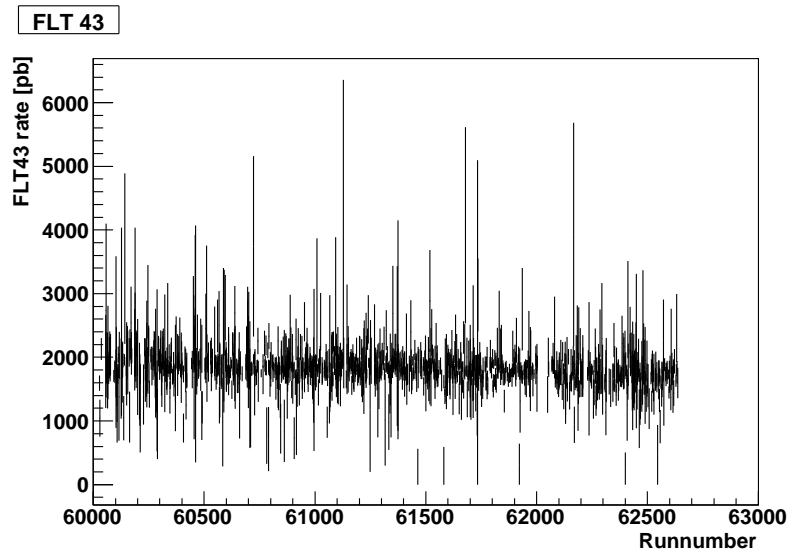


Figure D.7: Rate (Events divided by run luminosity) for NC DIS events triggered by FLT 43.

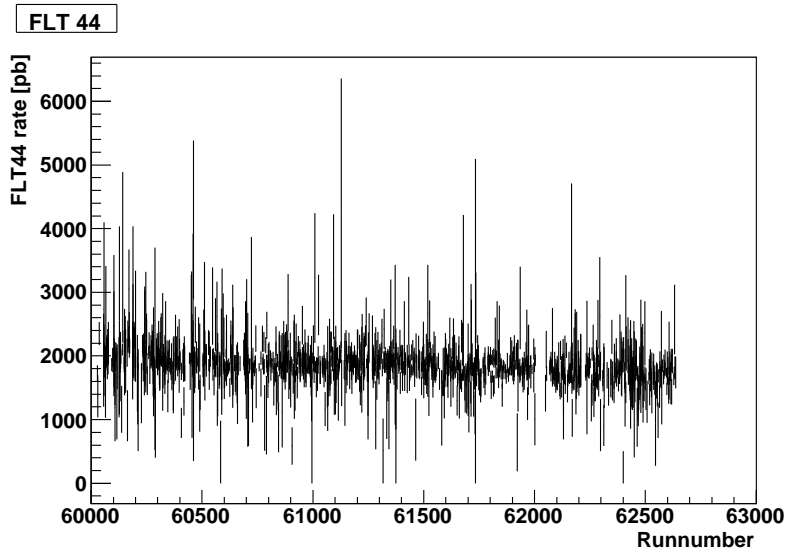


Figure D.8: Rate (Events divided by run luminosity) for NC DIS events triggered by FLT 44.

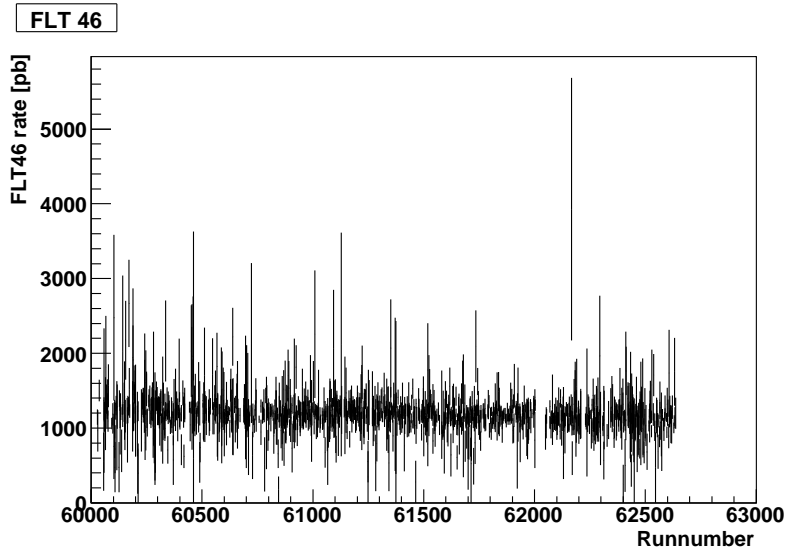


Figure D.9: Rate (Events divided by run luminosity) for NC DIS events triggered by FLT 46.

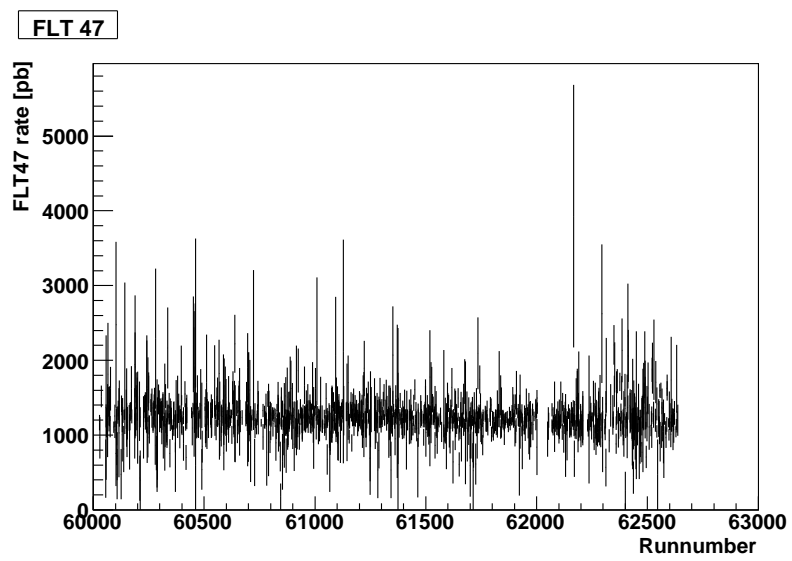


Figure D.10: Rate (Events divided by run luminosity) for NC DIS events triggered by FLT 47.

SLT

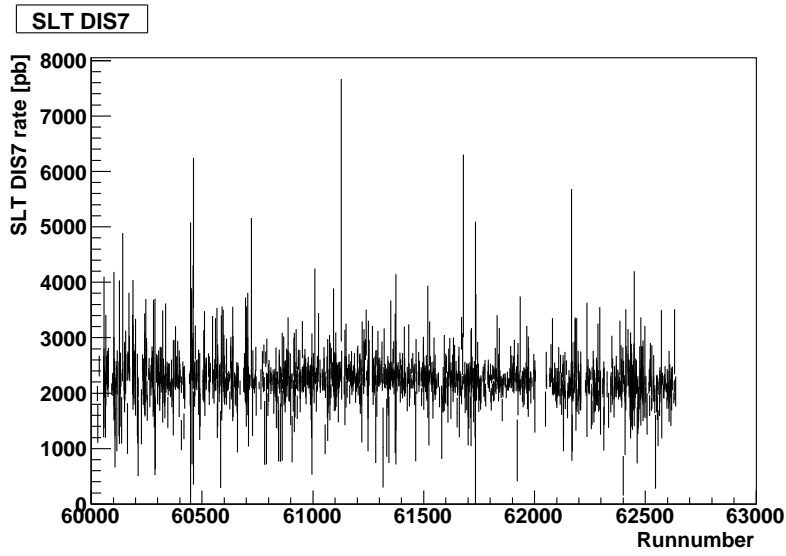


Figure D.11: Rate (Events divided by run luminosity) for NC DIS events triggered by SLT DIS7.

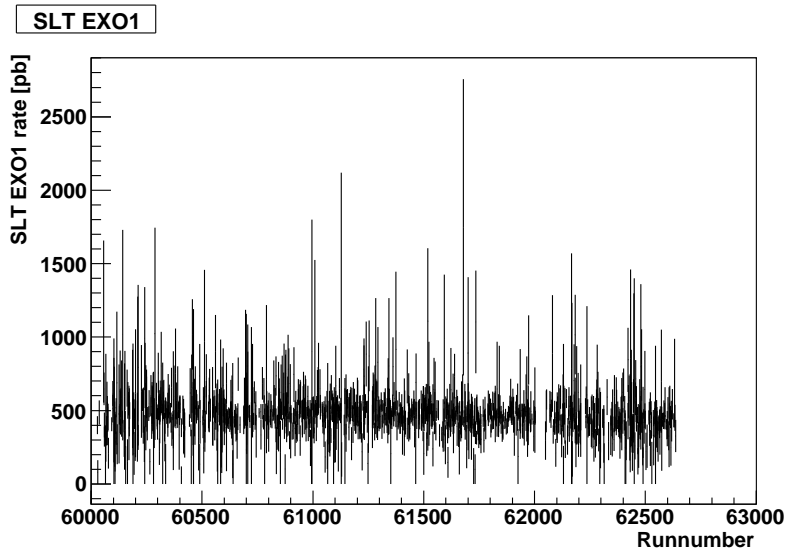


Figure D.12: Rate (Events divided by run luminosity) for NC DIS events triggered by SLT EXO1.

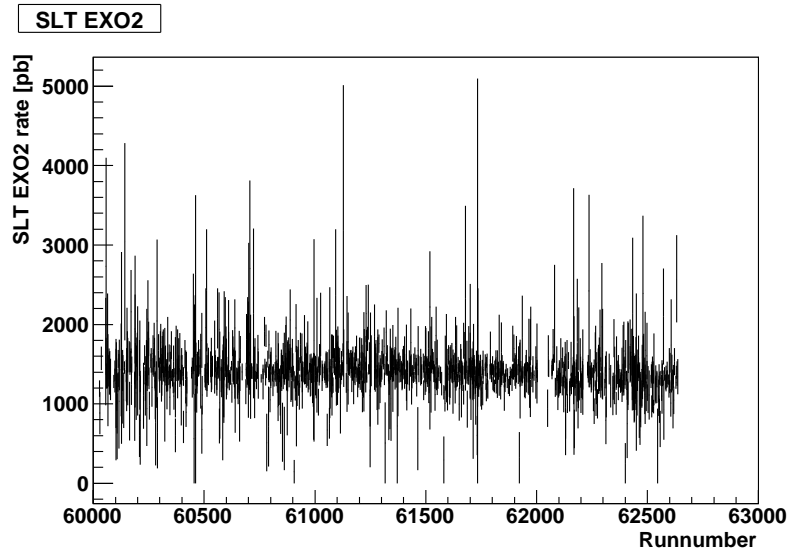


Figure D.13: Rate (Events divided by run luminosity) for NC DIS events triggered by SLT EXO2.

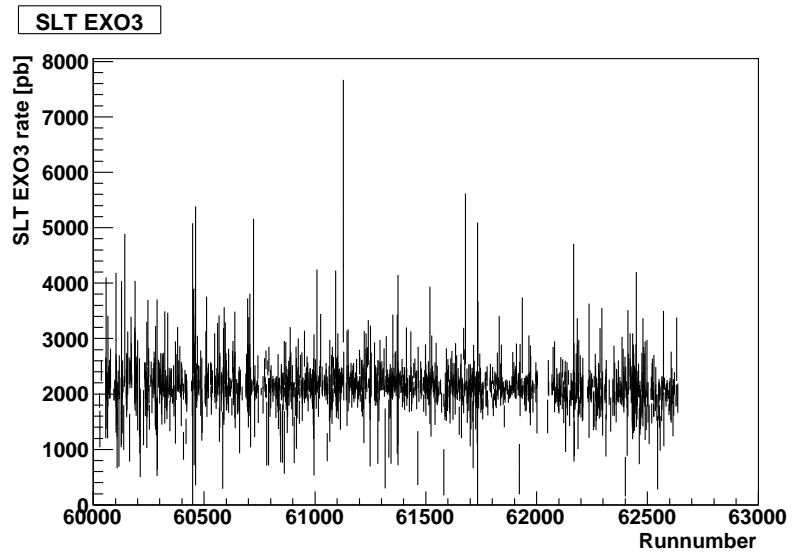


Figure D.14: Rate (Events divided by run luminosity) for NC DIS events triggered by SLT EXO3.

TLT

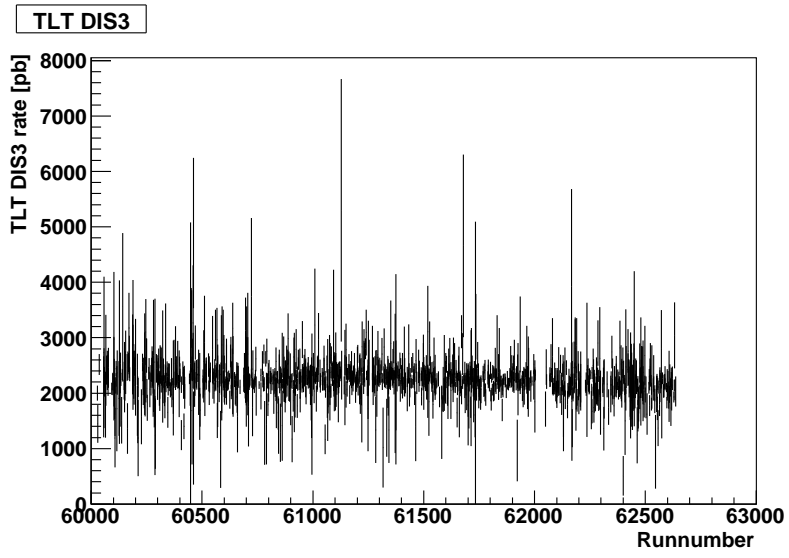


Figure D.15: Rate (Events divided by run luminosity) for NC DIS events triggered by TLT DIS3.

E. Track Matching Efficiency

Here the Track Matching Efficiency is shown as a function of different variables.

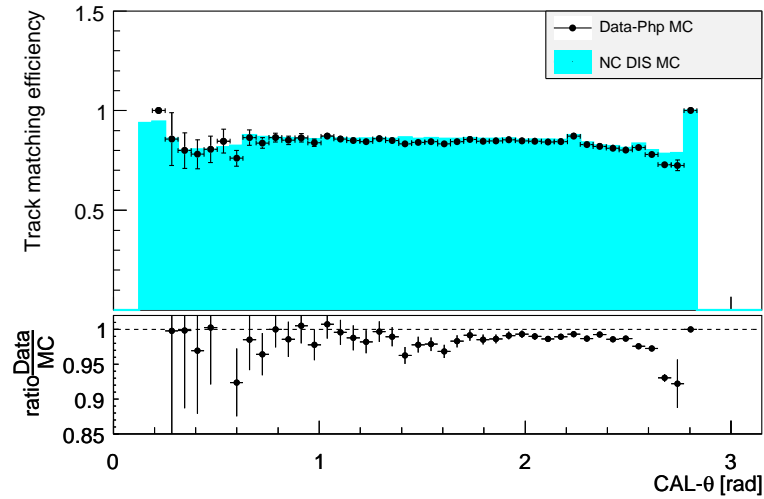


Figure E.1: Track matching efficiency as a function of the angle θ of the scattered positron in the calorimeter with data (black data points, php contribution subtracted from SM prediction) and NC MC (cyan histograms). In addition the ratio of data and MC is shown in the lower part of the plot.

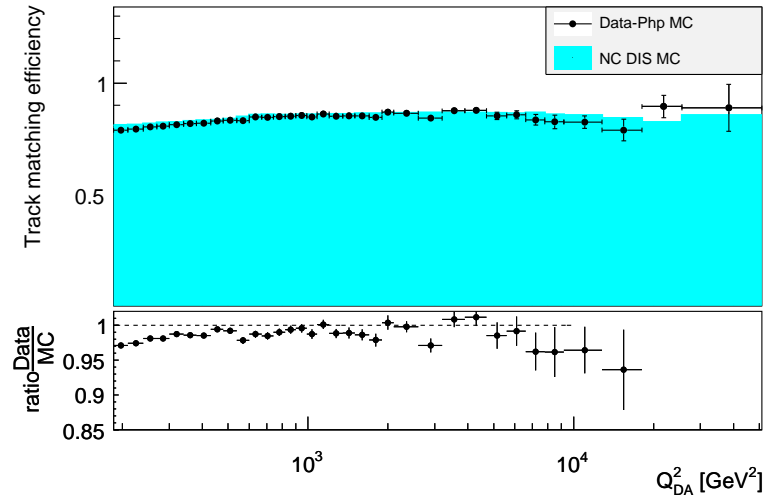


Figure E.2: Track matching efficiency as a function of Q^2 with data (black data points, php contribution subtracted from SM prediction) and NC MC (cyan histograms). In addition the ratio of data and MC is shown in the lower part of the plot.

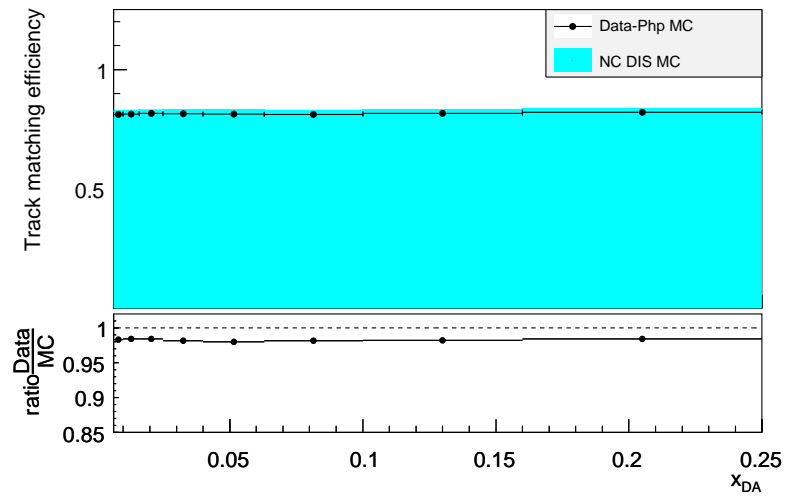


Figure E.3: Track matching efficiency as a function of x with data (black data points, php contribution subtracted from SM prediction) and NC MC (cyan histograms). In addition the ratio of data and MC is shown in the lower part of the plot.

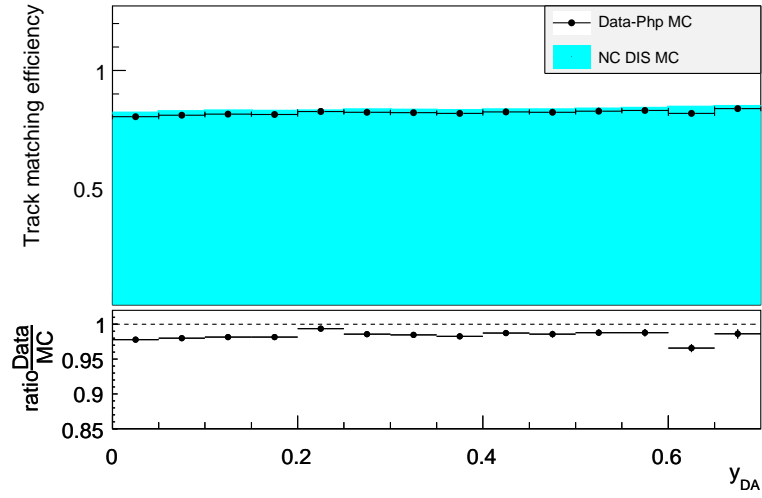


Figure E.4: Track matching efficiency as a function of the angle θ of the scattered positron with data (black data points, php contribution subtracted from SM prediction) and NC MC (cyan histograms). In addition the ratio of data and MC is shown in the lower part of the plot.

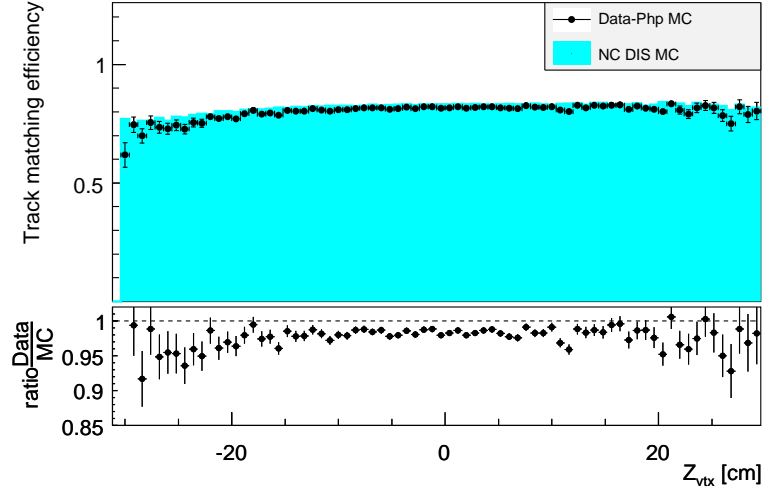


Figure E.5: Track matching efficiency as a function of Z_{vtx} with data (black data points, php contribution subtracted from SM prediction) and NC MC (cyan histograms). In addition the ratio of data and MC is shown in the lower part of the plot.

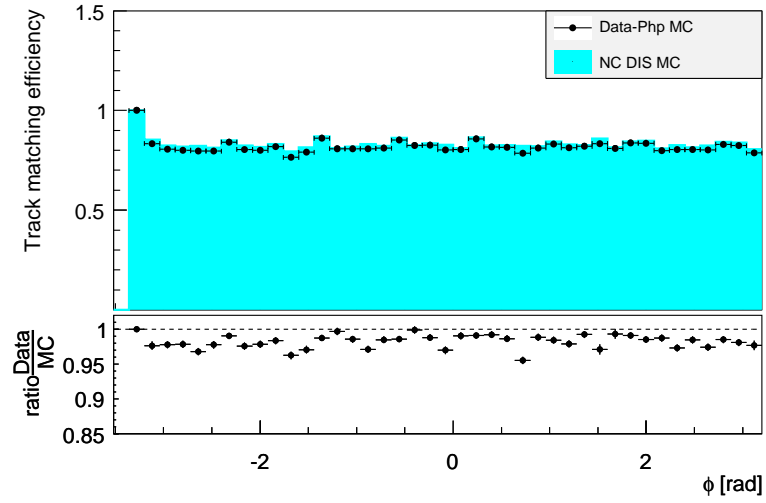


Figure E.6: Track matching efficiency as a function of the angle ϕ of the scattered positron with data (black data points, php contribution subtracted from SM prediction) and NC MC (cyan histograms). In addition the ratio of data and MC is shown in the lower part of the plot.

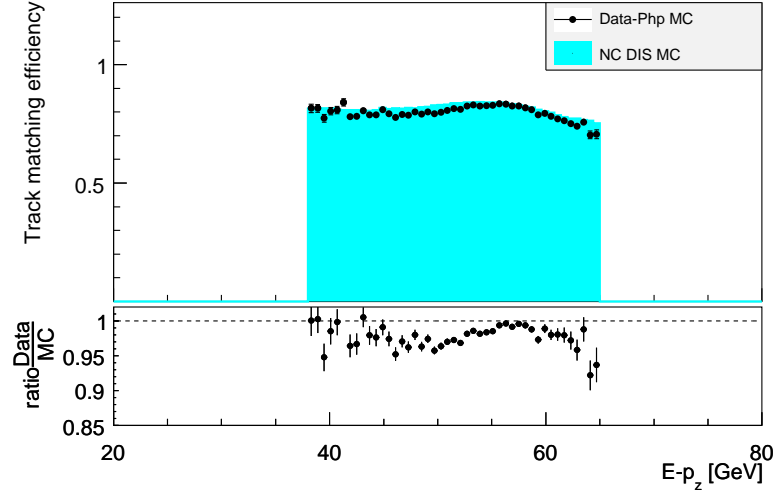


Figure E.7: Track matching efficiency as a function of $E - p_z$ with data (black data points, php contribution subtracted from SM prediction) and NC MC (cyan histograms). In addition the ratio of data and MC is shown in the lower part of the plot.

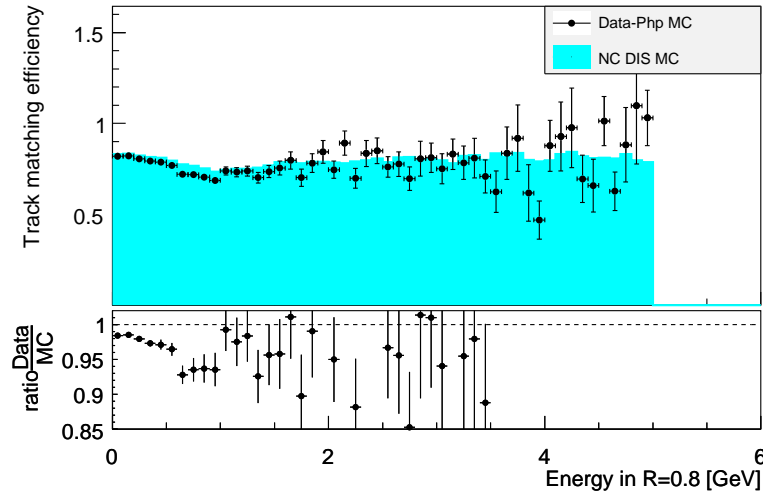


Figure E.8: Track matching efficiency as a function of energy in a 0.8-cone with data (black data points, php contribution subtracted from SM prediction) and NC MC (cyan histograms). In addition the ratio of data and MC is shown in the lower part of the plot.

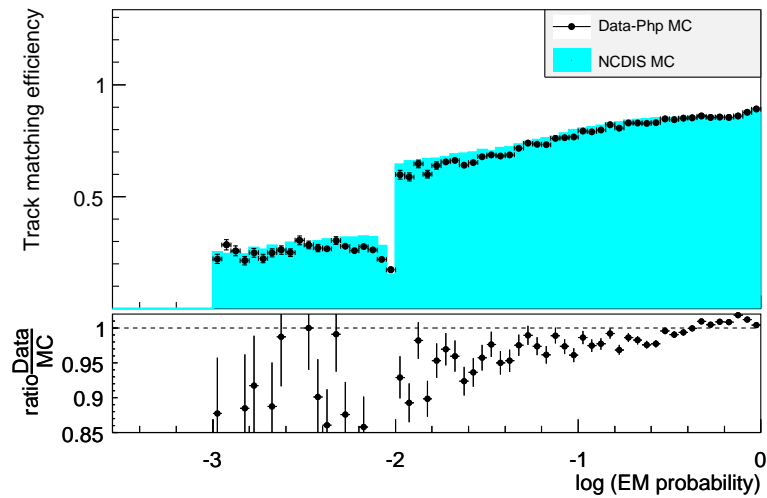


Figure E.9: Track matching efficiency as a function of the logarithm of the Grand Probability from the EM finder¹ of the scattered positron with data (black data points, php contribution subtracted from SM prediction) and NC MC (cyan histograms). In addition the ratio of data and MC is shown in the lower part of the plot.

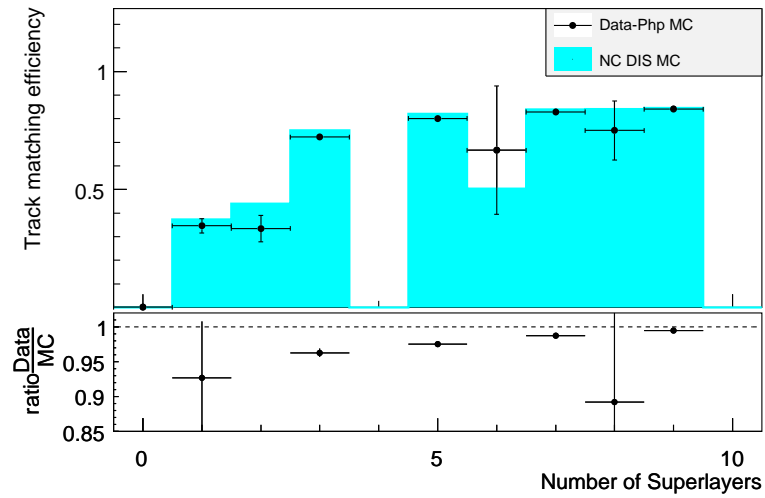


Figure E.10: Track matching efficiency as a function of the superlayers passed by the scattered positron with data (black data points, php contribution subtracted from SM prediction) and NC MC (cyan histograms). In addition the ratio of data and MC is shown in the lower part of the plot.

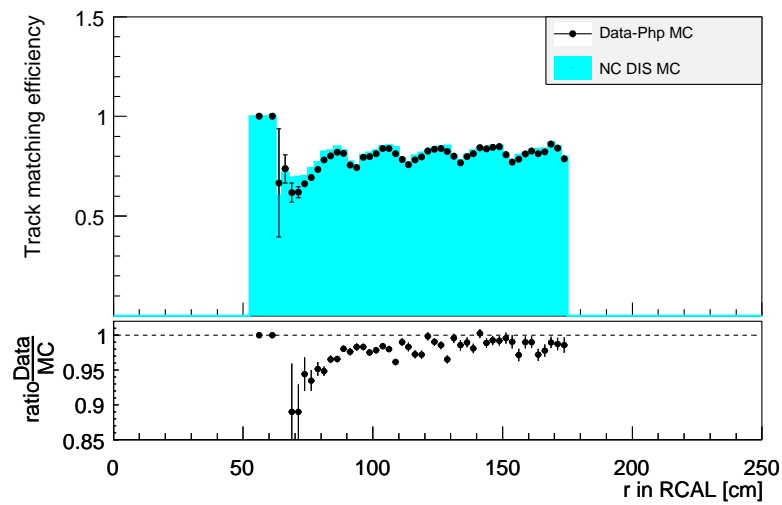


Figure E.11: Track matching efficiency as a function of the RCAL radius of the scattered positron with data (black data points, php contribution subtracted from SM prediction) and NC MC (cyan histograms). In addition the ratio of data and MC is shown in the lower part of the plot.

F. Uncertainties of the Reduced Cross Section

The plots in this appendix show all uncertainty contributions in every bin of the reduced cross section. The plot for $Q^2 = 1500 \text{ GeV}^2$ is found in Chapter 7 as Figure 7.15.

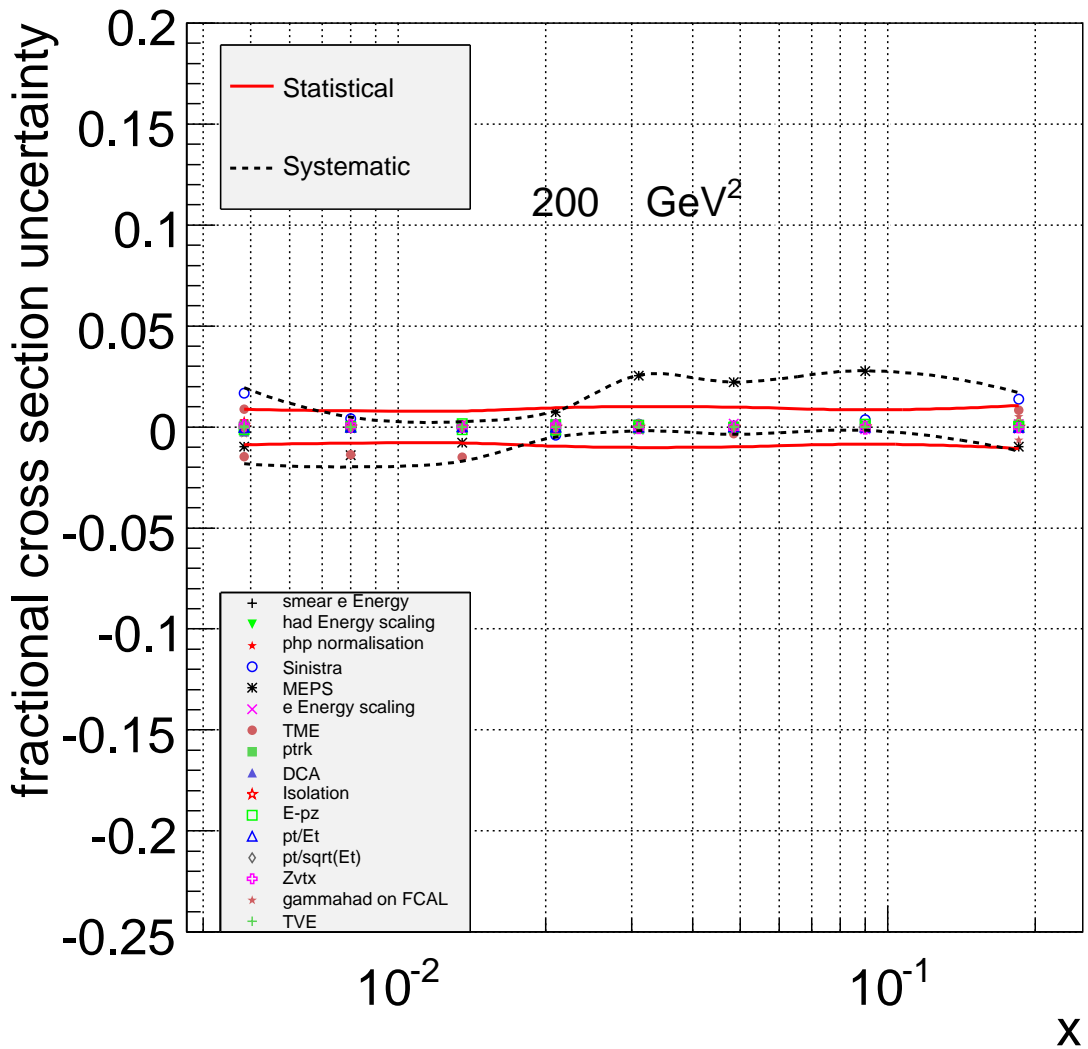


Figure F.1: The fractional systematic and statistical uncertainties of the double-differential cross section $\frac{d\sigma}{dx dQ^2}$ in the bin of $Q^2 = 200 \text{ GeV}^2$. Indicated by the symbols are the individual systematic uncertainties described in Chapter 7. Red lines show the statistical and dashed black lines the quadratic sum of all systematic uncertainties.

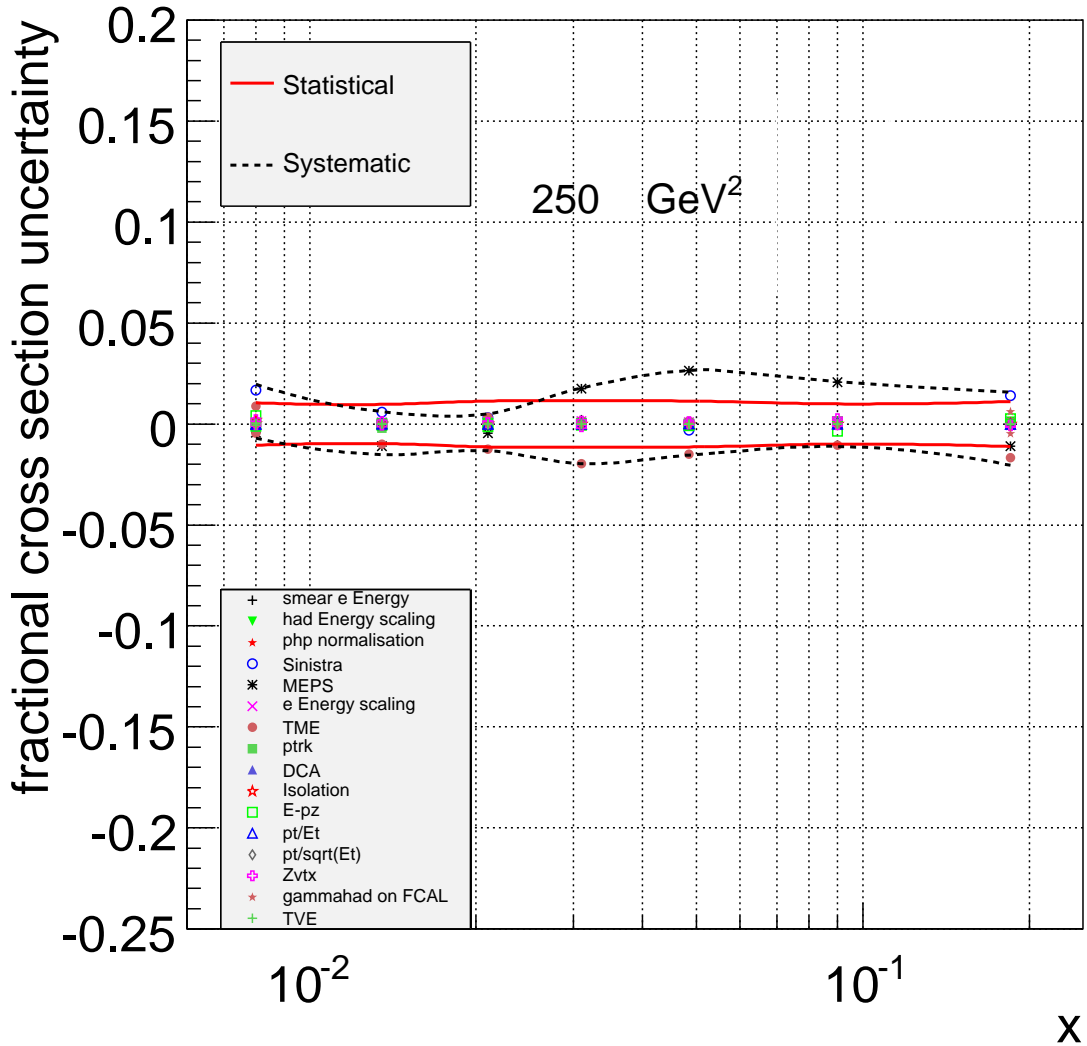


Figure F.2: The fractional systematic and statistical uncertainties of the double-differential cross section $\frac{d\sigma}{dx dQ^2}$ in the bin of $Q^2 = 250 \text{ GeV}^2$. Indicated by the symbols are the individual systematic uncertainties described in Chapter 7. Red lines show the statistical and dashed black lines the quadratic sum of all systematic uncertainties.

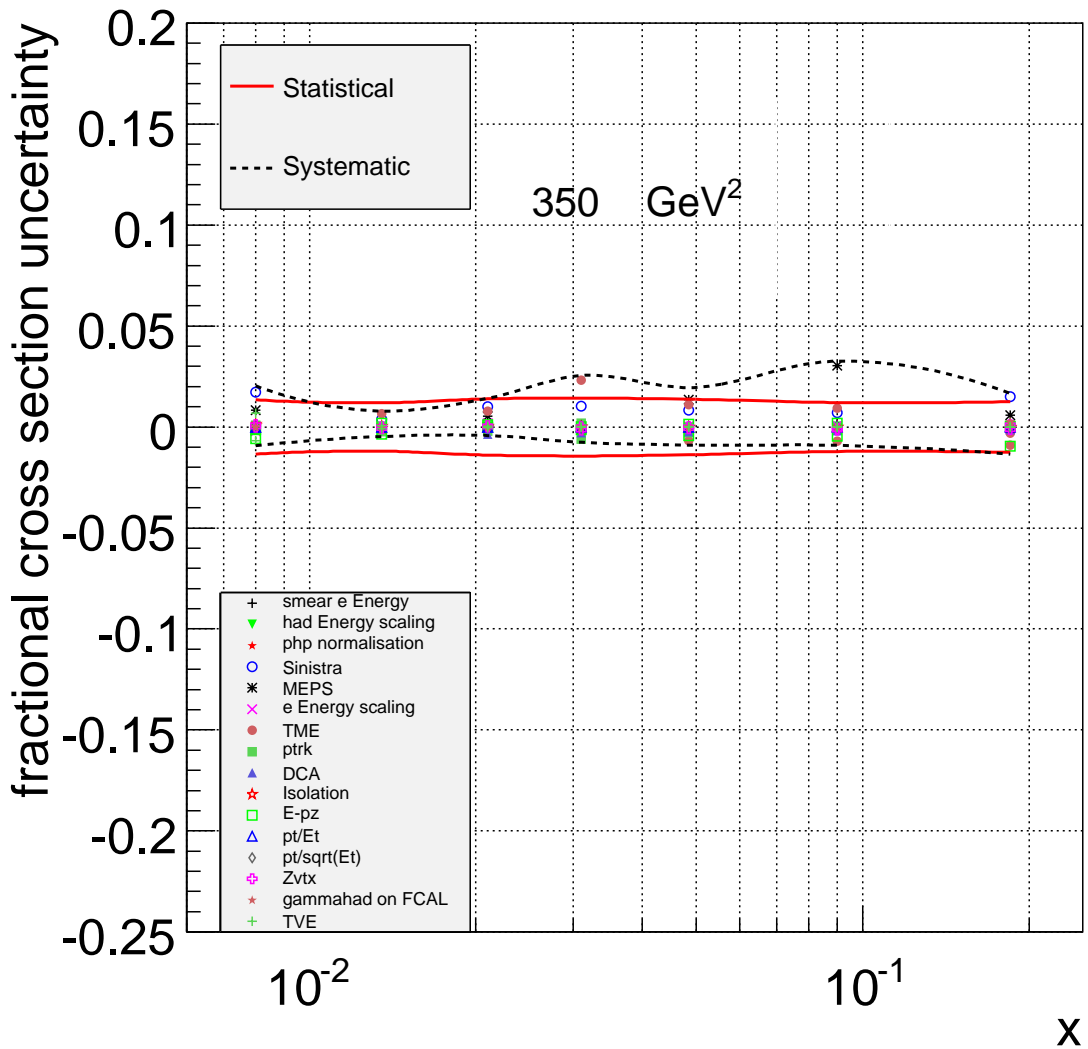


Figure F.3: The fractional systematic and statistical uncertainties of the double-differential cross section $\frac{d\sigma}{dx dQ^2}$ in the bin of $Q^2 = 350 \text{ GeV}^2$. Indicated by the symbols are the individual systematic uncertainties described in Chapter 7. Red lines show the statistical and dashed black lines the quadratic sum of all systematic uncertainties.

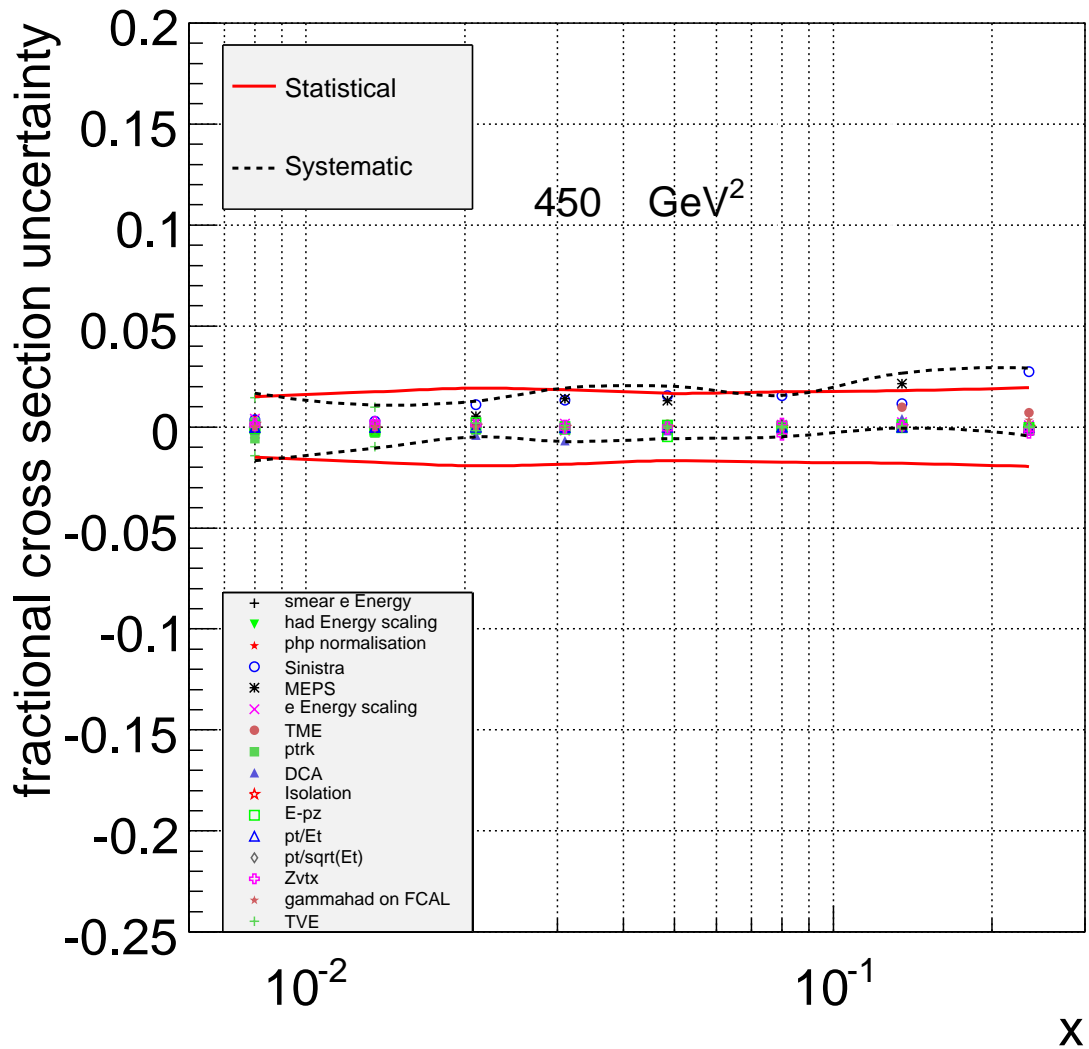


Figure F.4: The fractional systematic and statistical uncertainties of the double-differential cross section $\frac{d\sigma}{dx dQ^2}$ in the bin of $Q^2 = 450 \text{ GeV}^2$. Indicated by the symbols are the individual systematic uncertainties described in Chapter 7. Red lines show the statistical and dashed black lines the quadratic sum of all systematic uncertainties.

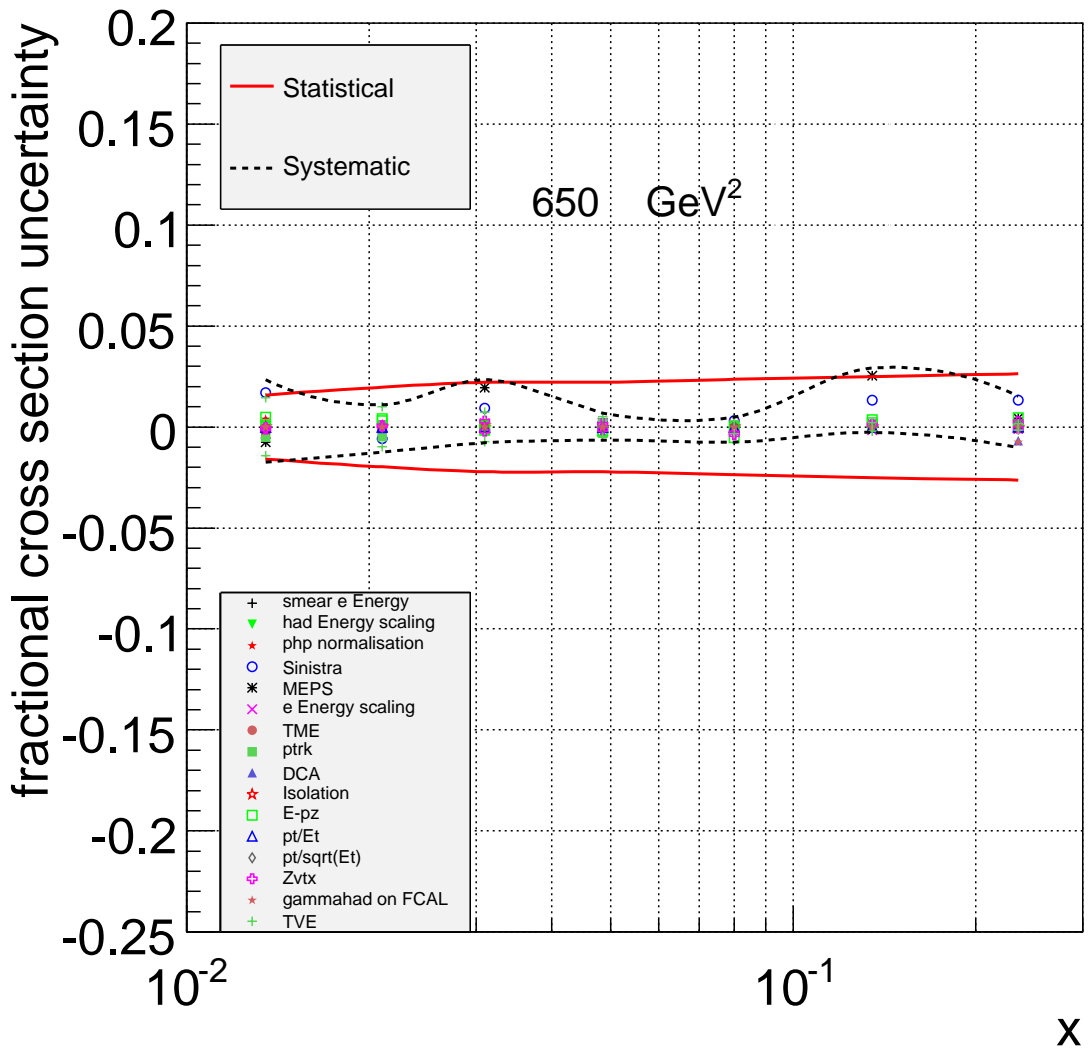


Figure F.5: The fractional systematic and statistical uncertainties of the double-differential cross section $\frac{d\sigma}{dx dQ^2}$ in the bin of $Q^2 = 650 \text{ GeV}^2$. Indicated by the symbols are the individual systematic uncertainties described in Chapter 7. Red lines show the statistical and dashed black lines the quadratic sum of all systematic uncertainties.

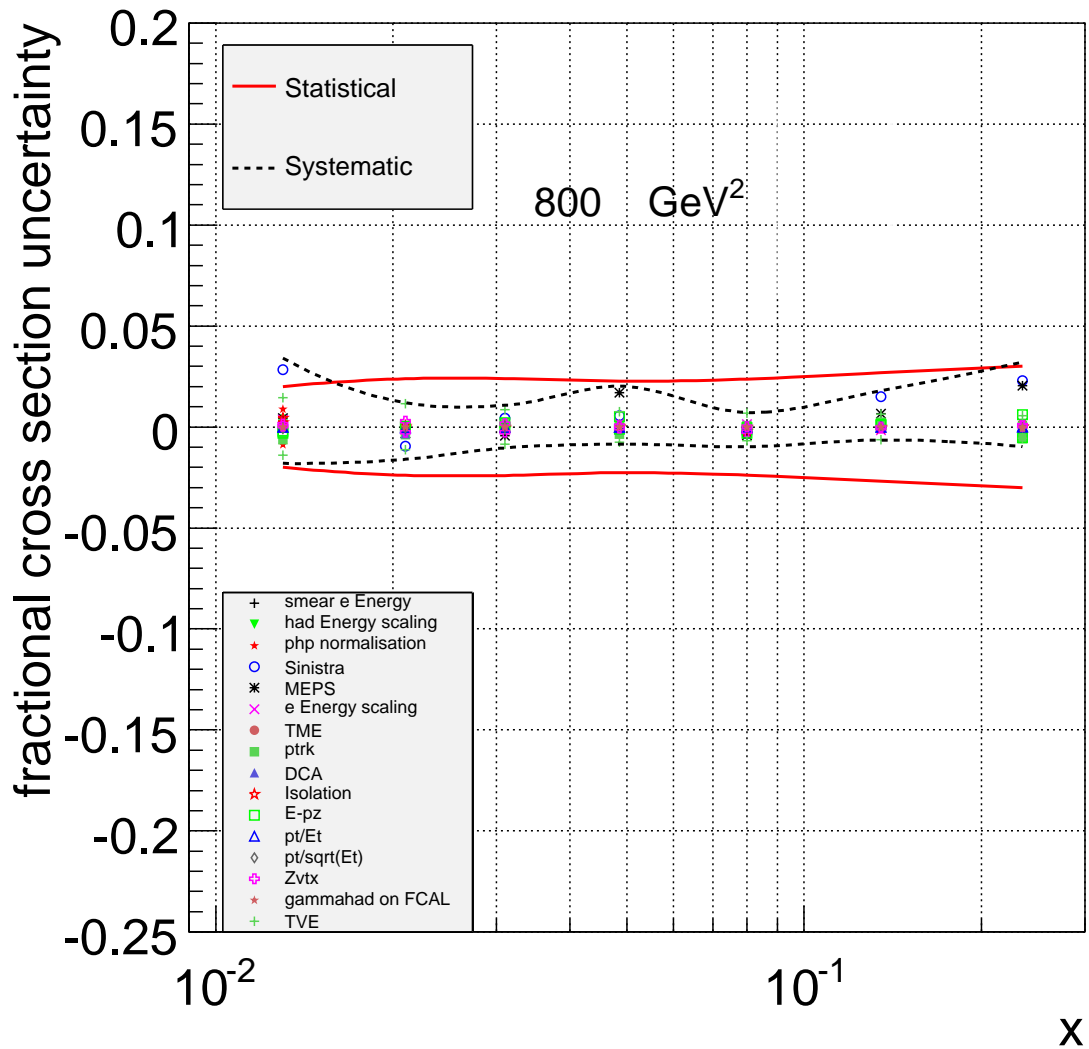


Figure F.6: The fractional systematic and statistical uncertainties of the double-differential cross section $\frac{d\sigma}{dx dQ^2}$ in the bin of $Q^2 = 800 \text{ GeV}^2$. Indicated by the symbols are the individual systematic uncertainties described in Chapter 7. Red lines show the statistical and dashed black lines the quadratic sum of all systematic uncertainties.

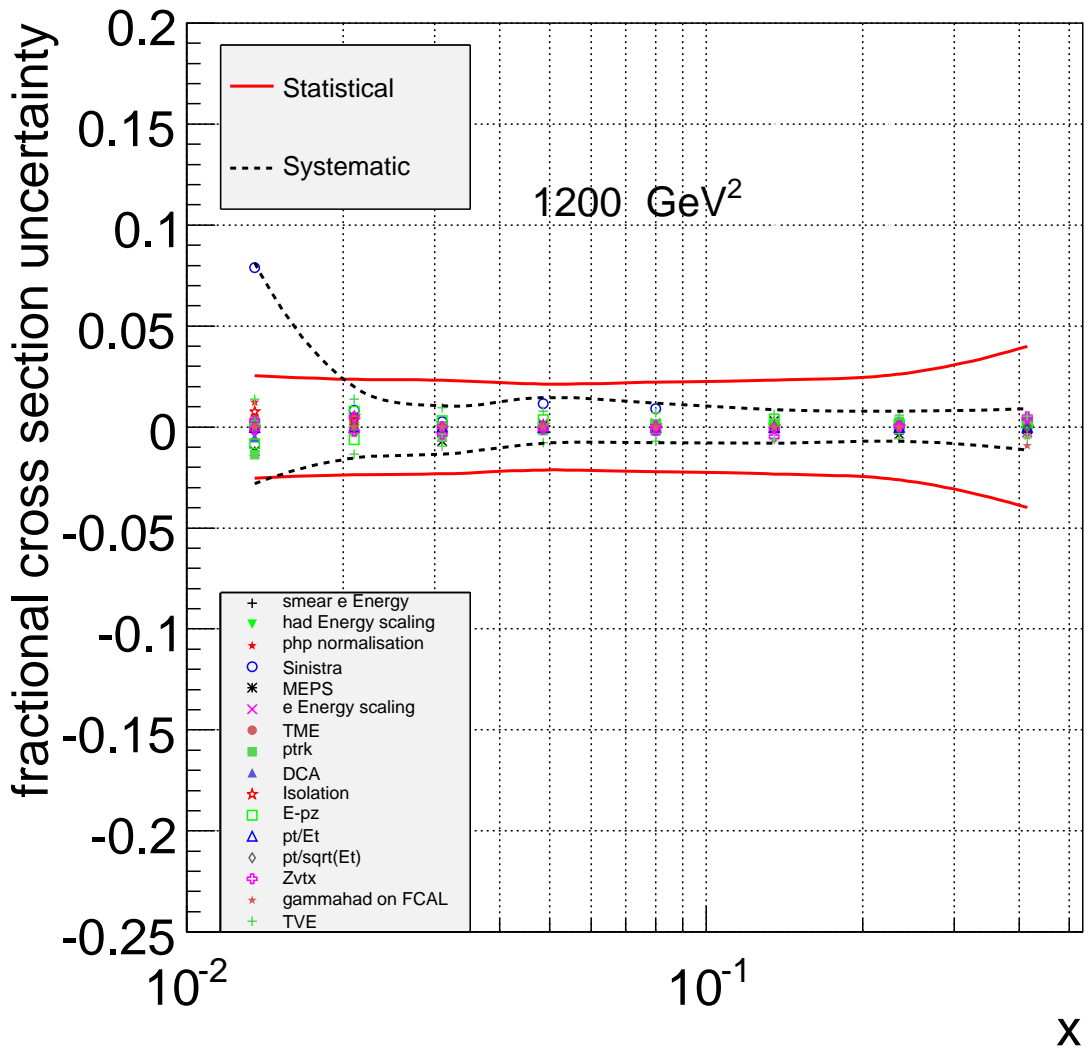


Figure F.7: The fractional systematic and statistical uncertainties of the double-differential cross section $\frac{d\sigma}{dx dQ^2}$ in the bin of $Q^2 = 1200 \text{ GeV}^2$. Indicated by the symbols are the individual systematic uncertainties described in Chapter 7. Red lines show the statistical and dashed black lines the quadratic sum of all systematic uncertainties.

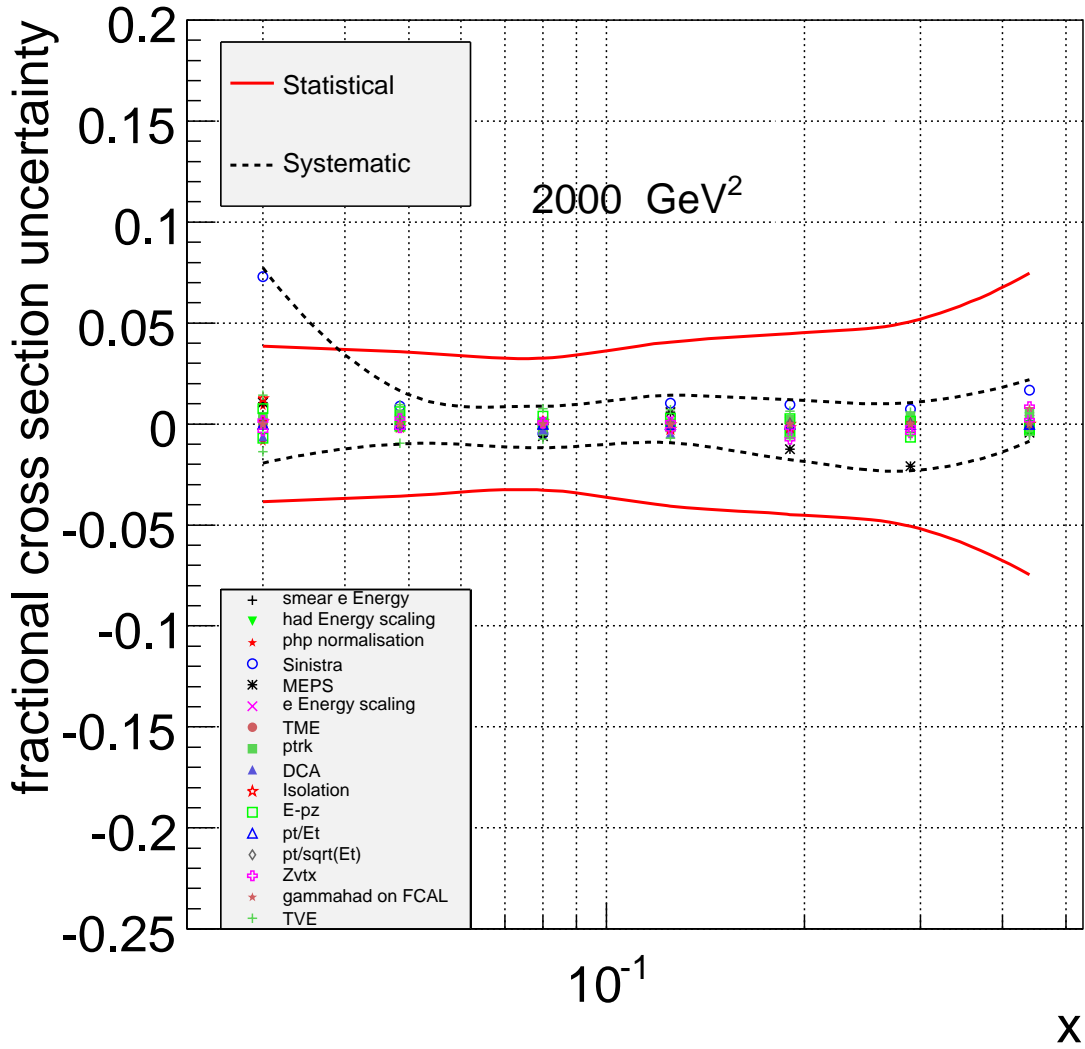


Figure F.8: The fractional systematic and statistical uncertainties of the double-differential cross section $\frac{d\sigma}{dx dQ^2}$ in the bin of $Q^2 = 2000 \text{ GeV}^2$. Indicated by the symbols are the individual systematic uncertainties described in Chapter 7. Red lines show the statistical and dashed black lines the quadratic sum of all systematic uncertainties.

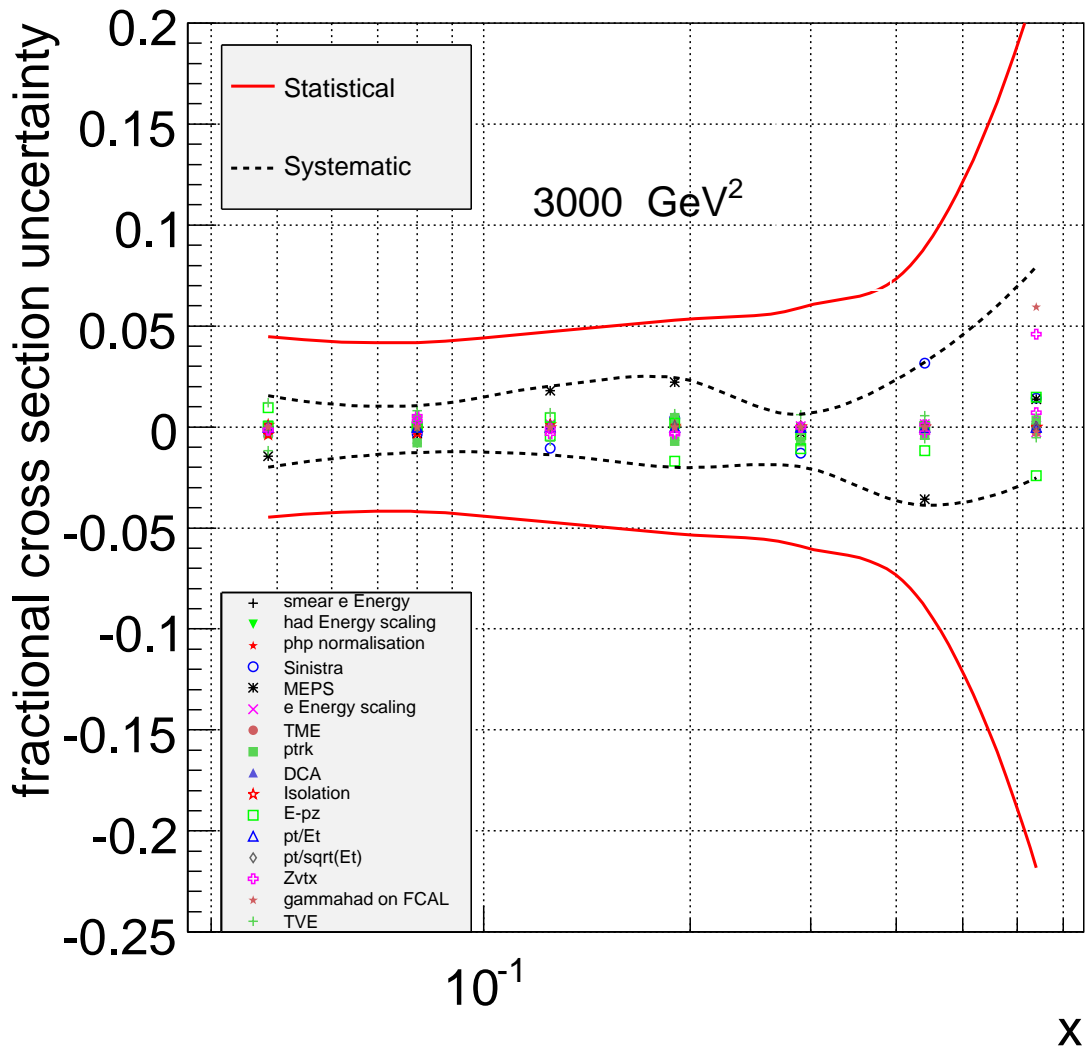


Figure F.9: The fractional systematic and statistical uncertainties of the double-differential cross section $\frac{d\sigma}{dx dQ^2}$ in the bin of $Q^2 = 3000 \text{ GeV}^2$. Indicated by the symbols are the individual systematic uncertainties described in Chapter 7. Red lines show the statistical and dashed black lines the quadratic sum of all systematic uncertainties.

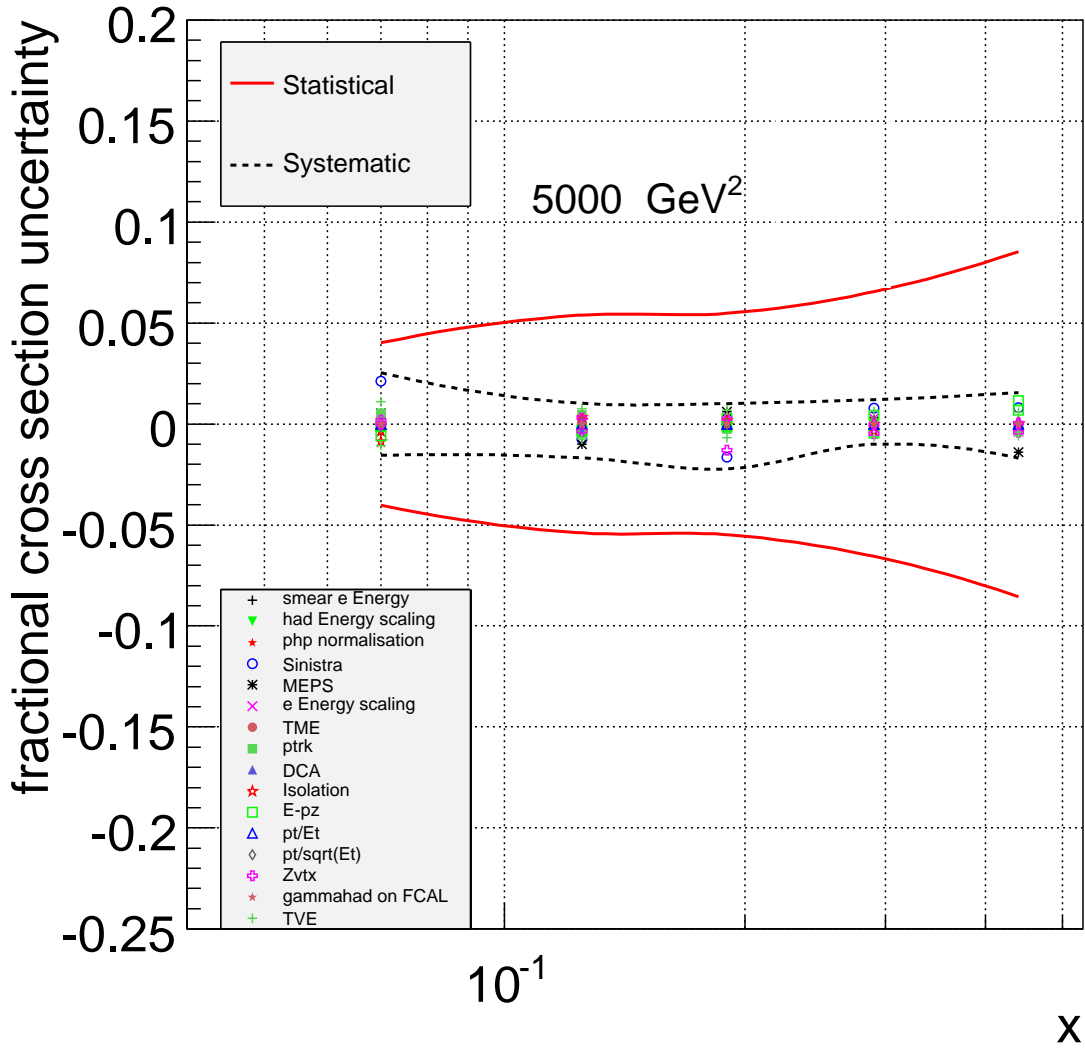


Figure F.10: The fractional systematic and statistical uncertainties of the double-differential cross section $\frac{d\sigma}{dx dQ^2}$ in the bin of $Q^2 = 5000 \text{ GeV}^2$. Indicated by the symbols are the individual systematic uncertainties described in Chapter 7. Red lines show the statistical and dashed black lines the quadratic sum of all systematic uncertainties.

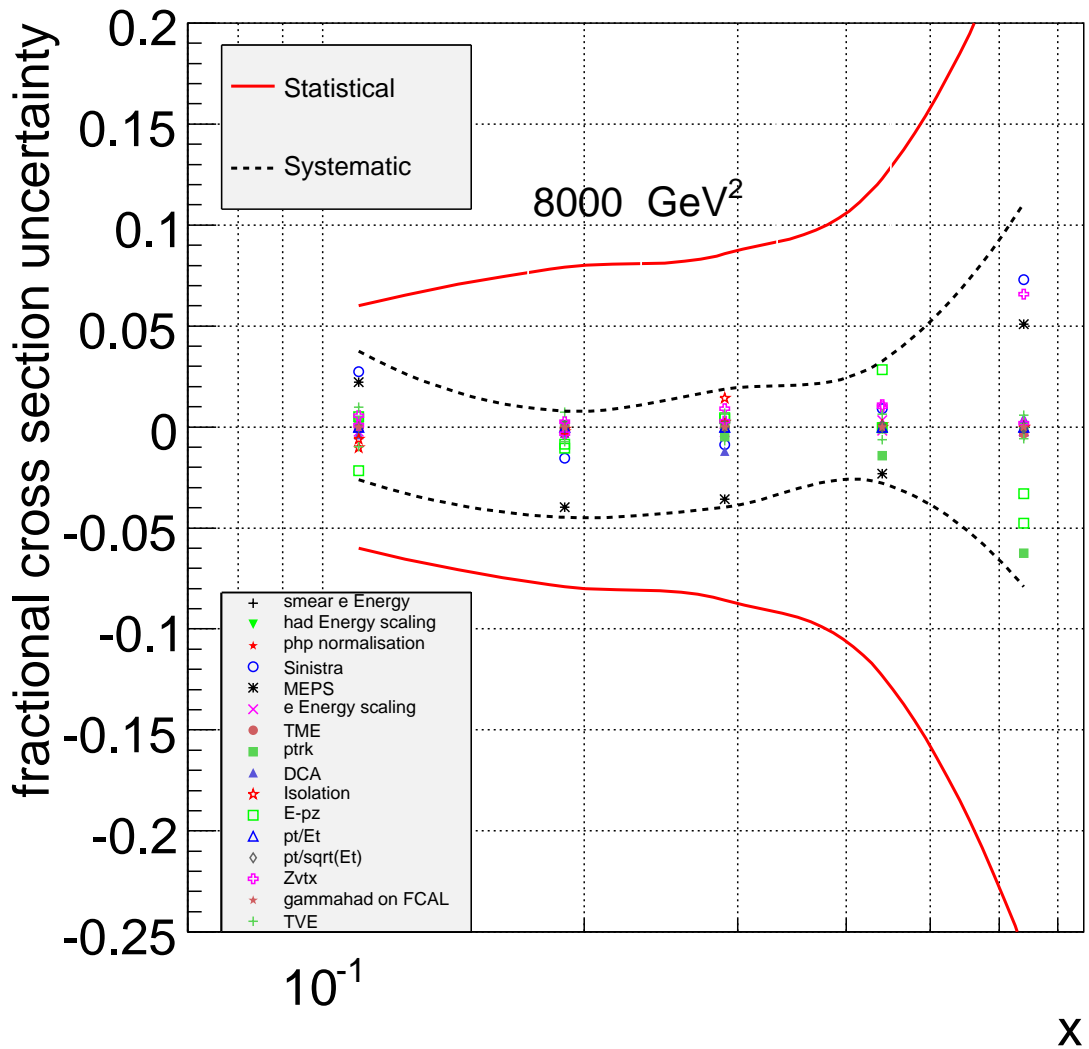


Figure F.11: The fractional systematic and statistical uncertainties of the double-differential cross section $\frac{d\sigma}{dx dQ^2}$ in the bin of $Q^2 = 8000 \text{ GeV}^2$. Indicated by the symbols are the individual systematic uncertainties described in Chapter 7. Red lines show the statistical and dashed black lines the quadratic sum of all systematic uncertainties.

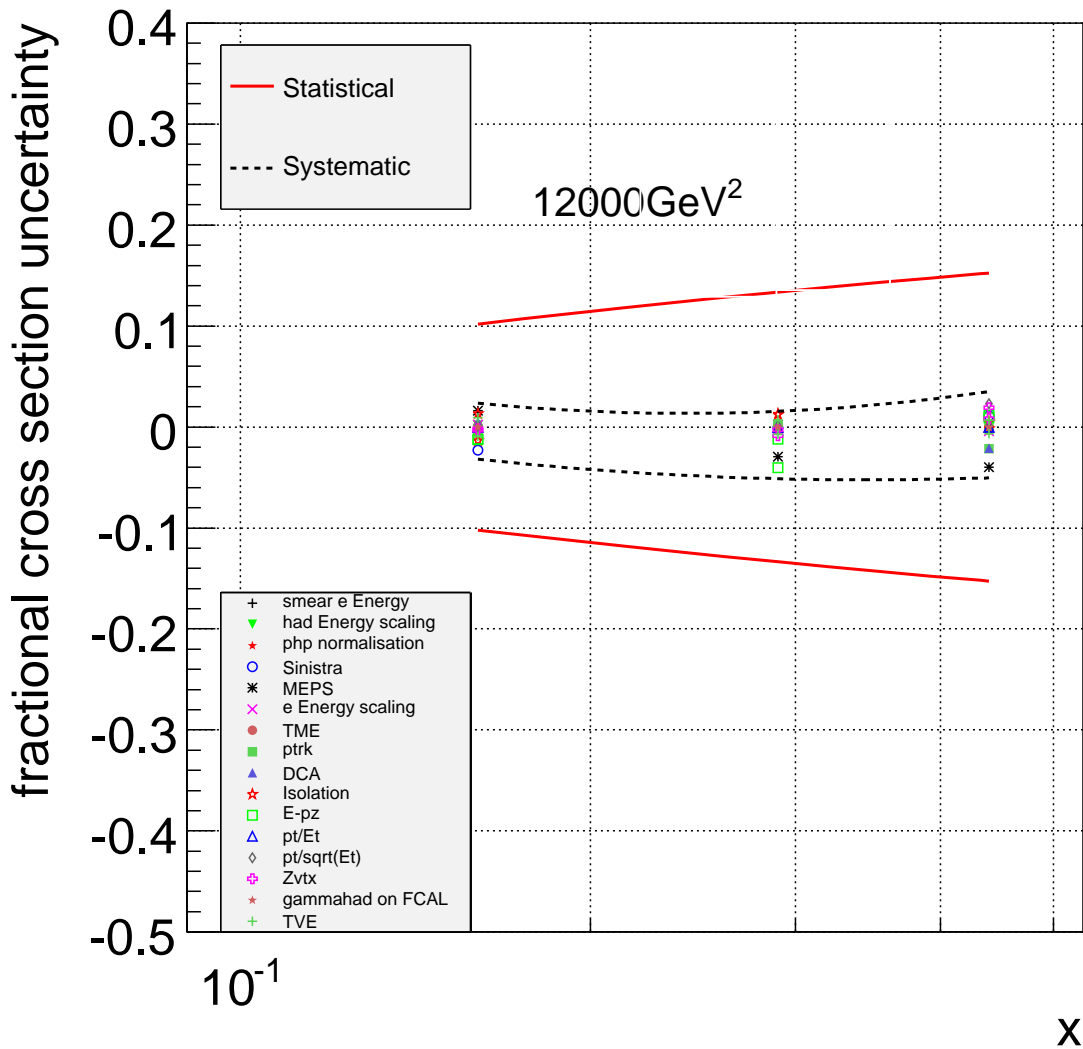
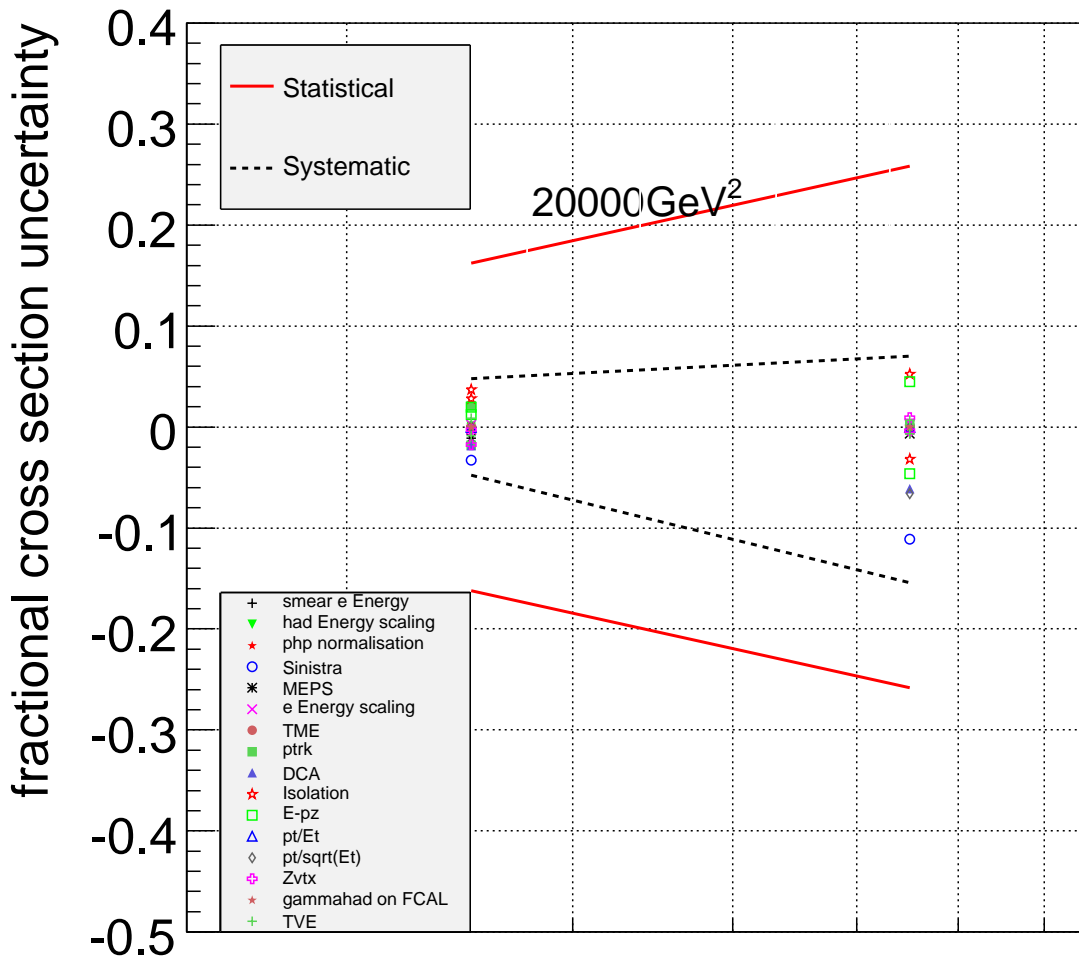
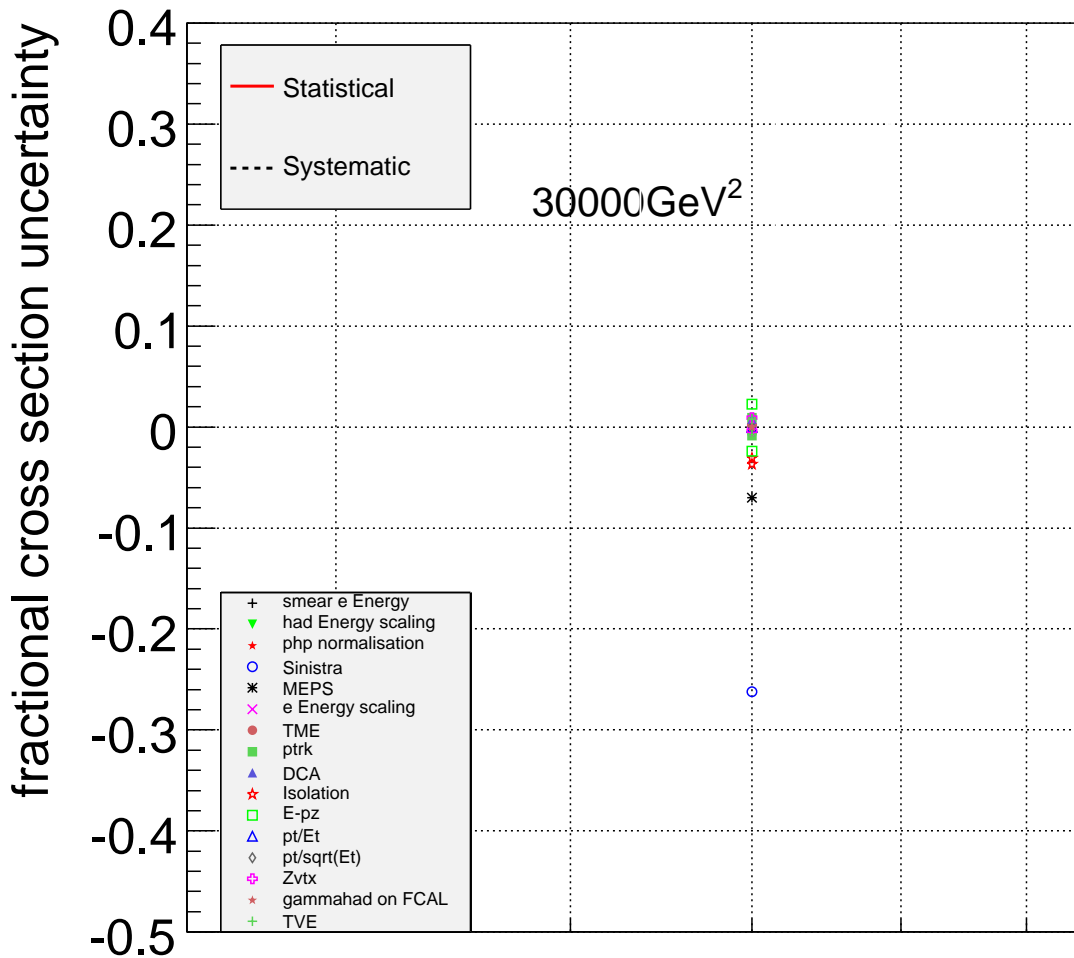


Figure F.12: The fractional systematic and statistical uncertainties of the double-differential cross section $\frac{d\sigma}{dx dQ^2}$ in the bin of $Q^2 = 12000 \text{ GeV}^2$. Indicated by the symbols are the individual systematic uncertainties described in Chapter 7. Red lines show the statistical and dashed black lines the quadratic sum of all systematic uncertainties.



X

Figure F.13: The fractional systematic and statistical uncertainties of the double-differential cross section $\frac{d\sigma}{dx dQ^2}$ in the bin of $Q^2 = 20000 \text{ GeV}^2$. Indicated by the symbols are the individual systematic uncertainties described in Chapter 7. Red lines show the statistical and dashed black lines the quadratic sum of all systematic uncertainties.



X

Figure F.14: The fractional systematic and statistical uncertainties of the double-differential cross section $\frac{d\sigma}{dx dQ^2}$ in the bin of $Q^2 = 30000 \text{ GeV}^2$. Indicated by the symbols are the individual systematic uncertainties described in Chapter 7. Red lines show the statistical and dashed black lines the quadratic sum of all systematic uncertainties.

G. Single Differential Cross Sections and A^+

In this appendix the bins of the single differential cross section measurements are listed and the measured single differential cross sections $\frac{d\sigma}{dQ^2}$, $\frac{d\sigma}{dx}$ and $\frac{d\sigma}{dy}$ are tabulated for zero, positive and negative polarisation. In addition, the measured values and uncertainties of the polarisation asymmetry A^+ are given, which were extracted from these cross sections.

Q_{low}^2 [GeV ²]	Q_{high}^2 [GeV ²]	Q_c^2 [GeV ²]
185	210	195
210	240	220
240	270	255
270	300	285
300	340	320
340	380	360
380	430	400
430	480	450
480	540	510
540	600	570
600	670	630
670	740	700
740	820	780
820	900	860
900	990	940
990	1080	1030
1080	1200	1130
1200	1350	1270
1350	1500	1420
1500	1700	1590
1700	1900	1790
1900	2100	1990
2100	2600	2300
2600	3200	2800
3200	3900	3500
3900	4700	4200
4700	5600	5100
5600	6600	6050
6600	7800	7100
7800	9200	8400
9200	12800	10800
12800	18100	15200
18100	25600	21500
25600	51200	36200

Table G.1: The bins of the measurement of the single differential cross section $\frac{d\sigma}{dQ^2}$. Given are the Q^2 limits and the bin centre Q_c^2 .

x_{low}	x_{high}	x_c
0.0063	0.01	0.00794
0.01	0.016	0.0126
0.016	0.025	0.02
0.025	0.04	0.0316
0.04	0.063	0.0501
0.063	0.1	0.0794
0.1	0.16	0.126
0.16	0.25	0.2

Table G.2: The bins of the measurement of the single differential cross section $\frac{d\sigma}{dx}$ for $Q^2 > 185 \text{ GeV}^2$. Given are the x limits and the bin centre x_c .

x_{low}	x_{high}	x_c
0.04	0.063	0.0501
0.063	0.1	0.0794
0.1	0.16	0.126
0.16	0.25	0.2
0.25	0.4	0.316
0.40	0.75	0.687

Table G.3: The bins of the measurement of the single differential cross section $\frac{d\sigma}{dx}$ for $Q^2 > 3000 \text{ GeV}^2$. Given are the x limits and the bin centre x_c .

y_{low}	y_{high}	y_c
0.00	0.05	0.025
0.05	0.1	0.075
0.1	0.15	0.125
0.15	0.2	0.175
0.2	0.25	0.225
0.25	0.3	0.275
0.3	0.35	0.325
0.35	0.4	0.375
0.4	0.45	0.425
0.45	0.5	0.475
0.5	0.55	0.525
0.55	0.6	0.575
0.6	0.65	0.625
0.65	0.7	0.675
0.7	0.75	0.725

Table G.4: The bins of the measurement of the single differential cross section $\frac{d\sigma}{dy}$ for $Q^2 > 185 \text{ GeV}^2$. Given are the y limits and the bin centre y_c .

y_{low}	y_{high}	y_c
0.05	0.1	0.075
0.1	0.15	0.125
0.15	0.2	0.175
0.2	0.25	0.225
0.25	0.3	0.275
0.3	0.35	0.325
0.35	0.4	0.375
0.4	0.45	0.425
0.45	0.5	0.475
0.5	0.55	0.525
0.55	0.6	0.575
0.6	0.65	0.625
0.65	0.7	0.675
0.7	0.75	0.725
0.75	0.8	0.775
0.8	0.85	0.825
0.85	0.9	0.875

Table G.5: The bins of the measurement of the single differential cross section $\frac{d\sigma}{dy}$ for $Q^2 > 3000 \text{ GeV}^2$. Given are the y limits and the bin centre y_c .

Q_c^2 [GeV ²]	$\frac{d\sigma}{dQ^2}$ [pb/GeV ²]	stat	syst	δ_1	δ_2	δ_3	δ_4	δ_5	δ_6
195	$1.90 \cdot 10^1$	± 0.5	$+0.8$ -0.6	$+0.2$ -0.1	+0.6	+0.1	$+0.2$ -0.5	+0.0 -0.0	$+0.2$ -0.1
220	$1.43 \cdot 10^1$	± 0.5	$+0.8$ -0.7	$+0.2$ -0.1	+0.4	+0.5	$+0.2$ -0.6	+0.0 -0.0	$+0.0$ -0.1
255	$1.00 \cdot 10^1$	± 0.6	$+1.0$ -1.5	$+0.2$ -0.1	+0.6	+0.7	$+0.1$ -1.4	+0.0 -0.0	$+0.1$ -0.0
285	7.78	± 0.7	$+0.7$ -1.1	$+0.2$ -0.2	+0.6	-0.2	$+0.3$ -1.0	+0.1 -0.1	$+0.0$ -0.1
320	5.78	± 0.7	$+1.3$ -0.9	$+0.2$ -0.2	+1.1	+0.4	$+0.4$ -0.7	+0.1 -0.1	$+0.1$ -0.4
360	4.33	± 0.8	$+1.6$ -0.5	$+0.2$ -0.1	+0.7	+1.1	$+1.0$ -0.1	+0.2 -0.2	$+0.0$ -0.2
400	3.33	± 0.8	$+1.8$ -0.4	$+0.2$ -0.2	+1.3	+0.7	$+0.8$ -0.1	+0.3 -0.3	$+0.0$ -0.0
450	2.55	± 1.0	$+2.1$ -0.6	$+0.2$ -0.3	+1.9	+0.7	$+0.1$ -0.0	+0.4 -0.4	$+0.0$ -0.0
510	1.89	± 1.0	$+1.0$ -0.7	$+0.3$ -0.2	+0.7	-0.1	$+0.1$ -0.0	+0.5 -0.5	$+0.0$ -0.2
570	1.39	± 1.2	$+2.0$ -0.9	$+0.4$ -0.3	+1.7	+0.3	$+0.1$ -0.0	+0.7 -0.7	$+0.4$ -0.0
630	1.14	± 1.3	$+1.2$ -1.0	$+0.3$ -0.2	+0.5	+0.2	$+0.0$ -0.0	+0.9 -0.9	$+0.2$ -0.0
700	$8.67 \cdot 10^{-1}$	± 1.4	$+1.9$ -1.2	$+0.2$ -0.2	+1.6	+0.2	$+0.0$ -0.0	+1.0 -0.9	$+0.0$ -0.3
780	$6.65 \cdot 10^{-1}$	± 1.4	$+1.2$ -1.1	$+0.3$ -0.1	+0.6	+0.4	$+0.1$ -0.0	+0.9 -0.9	$+0.1$ -0.1
860	$5.07 \cdot 10^{-1}$	± 1.5	$+1.8$ -1.0	$+0.2$ -0.0	+1.4	-0.1	$+0.1$ -0.0	+0.9 -0.9	$+0.1$ -0.0
940	$4.17 \cdot 10^{-1}$	± 1.6	$+1.2$ -1.3	$+0.1$ -0.3	+0.8	-0.8	$+0.0$ -0.0	+0.9 -0.9	$+0.1$ -0.1
1030	$3.20 \cdot 10^{-1}$	± 1.8	$+2.4$ -1.3	$+0.2$ -0.2	+2.2	-0.6	$+0.0$ -0.1	+0.9 -0.9	$+0.2$ -0.4
1130	$2.55 \cdot 10^{-1}$	± 1.7	$+1.7$ -1.0	$+0.1$ -0.1	+1.0	+0.9	$+0.1$ -0.0	+0.9 -0.9	$+0.3$ -0.0
1270	$1.96 \cdot 10^{-1}$	± 1.8	$+2.6$ -1.0	$+0.2$ -0.1	+2.3	-0.4	$+0.0$ -0.0	+0.9 -0.9	$+0.4$ -0.1
1420	$1.42 \cdot 10^{-1}$	± 2.1	$+2.0$ -1.0	$+0.3$ -0.1	+1.6	-0.0	$+0.1$ -0.0	+0.9 -0.9	$+0.4$ -0.5
1590	$1.08 \cdot 10^{-1}$	± 2.0	$+2.5$ -1.0	$+0.2$ -0.1	+2.3	+0.3	$+0.0$ -0.1	+0.9 -0.9	$+0.0$ -0.1
1790	$7.83 \cdot 10^{-2}$	± 2.4	$+2.2$ -1.1	$+0.2$ -0.0	+1.9	+0.4	$+0.2$ -0.0	+0.9 -0.9	$+0.0$ -0.3
1990	$5.86 \cdot 10^{-2}$	± 2.7	$+2.4$ -1.4	$+0.3$ -0.1	+2.1	-1.0	$+0.1$ -0.0	+0.9 -0.9	$+0.3$ -0.0
2300	$4.02 \cdot 10^{-2}$	± 2.1	$+1.4$ -1.0	$+0.1$ -0.1	+1.1	-0.0	$+0.0$ -0.0	+0.9 -0.9	$+0.3$ -0.1
2800	$2.33 \cdot 10^{-2}$	± 2.6	$+1.3$ -1.0	$+0.1$ -0.1	+0.7	+0.4	$+0.1$ -0.0	+0.9 -0.8	$+0.0$ -0.0
3500	$1.32 \cdot 10^{-2}$	± 3.1	$+1.1$ -1.1	$+0.0$ -0.3	+0.7	-0.2	$+0.0$ -0.1	+0.8 -0.8	$+0.0$ -0.5
4200	$7.75 \cdot 10^{-3}$	± 3.8	$+1.5$ -1.2	$+0.2$ -0.1	+1.2	-0.8	$+0.1$ -0.0	+0.8 -0.8	$+0.0$ -0.2
5100	$4.15 \cdot 10^{-3}$	± 4.8	$+1.1$ -1.4	$+0.2$ -0.1	-0.3	+0.6	$+0.1$ -0.0	+0.8 -0.8	$+0.2$ -0.4
6050	$2.70 \cdot 10^{-3}$	± 5.6	$+1.2$ -2.9	$+0.1$ -0.2	-0.9	-2.2	$+0.0$ -0.1	+0.8 -0.8	$+0.0$ -0.1
7100	$1.46 \cdot 10^{-3}$	± 7.0	$+3.6$ -2.8	$+0.1$ -0.3	+2.2	+1.8	$+0.0$ -0.1	+0.8 -0.8	$+1.6$ -2.4
8400	$9.33 \cdot 10^{-4}$	± 8.2	$+3.2$ -2.9	$+0.2$ -0.1	+2.9	-2.1	$+0.1$ -0.0	+0.8 -0.8	$+0.0$ -1.2
10800	$3.43 \cdot 10^{-4}$	± 8.3	$+2.3$ -3.0	$+0.3$ -0.2	+1.0	-0.9	$+0.0$ -0.0	+0.8 -0.8	$+0.1$ -2.5
15200	$9.03 \cdot 10^{-5}$	± 13.4	$+3.7$ -10.4	$+0.1$ -0.3	-9.5	-0.9	$+0.0$ -0.1	+0.8 -0.8	$+2.0$ -0.1
21500	$3.74 \cdot 10^{-5}$	± 17.2	$+7.5$ -7.6	$+0.3$ -0.3	-6.7	-1.9	$+0.0$ -0.1	+0.8 -0.8	$+2.2$ -1.8
36200	$1.68 \cdot 10^{-6}$	± 35.4	$+3.0$ -17.5	$+0.3$ -0.3	-15.1	-6.8	$+0.3$ -0.0	+0.8 -0.8	$+2.4$ -2.7

Table G.6: The measured single differential cross section $\frac{d\sigma}{dQ^2}$ ($y < 0.9$, $y(1-x)^2 > 0.004$) for the reaction $e^+p \rightarrow e^+X$ ($\mathcal{L} = 135.5 \text{ pb}^{-1}$, $P_e = 0$). The bin centre, Q_c^2 , the cross section corrected to the electroweak Born level and the statistical and the systematic uncertainty (in %) are given. In addition the contributions of the variation of the electron energy scale (δ_1), the variation of the electron identification (δ_2), the variation of the parton shower model (δ_3), the variation of the track requirement region (δ_4), the variation of the Track Veto Efficiency correction (δ_5) and the variation of the $E-p_z$ cut (δ_6) to the systematic uncertainty are shown. All uncertainties are given in %.

x_c	$\frac{d\sigma}{dx}$ [pb/GeV ²]	stat	syst	δ_1	δ_2	δ_3	δ_4	δ_5	δ_6
0.00794	$8.70 \cdot 10^4$	± 0.6	$+1.1$ -1.1	$+0.2$ -0.2	+0.9	-0.6	$+0.3$ -0.8	$+0.4$ -0.4	$+0.0$ -0.0
0.01260	$5.83 \cdot 10^4$	± 0.5	$+1.0$ -1.1	$+0.1$ -0.0	+0.9	-0.6	$+0.2$ -0.8	$+0.4$ -0.4	$+0.0$ -0.1
0.02000	$3.62 \cdot 10^4$	± 0.5	$+0.7$ -0.6	$+0.2$ -0.0	+0.5	+0.2	$+0.2$ -0.5	$+0.3$ -0.3	$+0.2$ -0.1
0.03160	$2.10 \cdot 10^4$	± 0.5	$+1.7$ -0.6	$+0.1$ -0.1	+0.6	+1.5	$+0.4$ -0.5	$+0.2$ -0.2	$+0.0$ -0.0
0.05010	$1.23 \cdot 10^4$	± 0.6	$+1.7$ -0.6	$+0.1$ -0.1	+0.5	+1.6	$+0.3$ -0.5	$+0.2$ -0.2	$+0.0$ -0.0
0.07940	$6.89 \cdot 10^3$	± 0.6	$+1.6$ -0.4	$+0.1$ -0.1	+0.4	+1.5	$+0.1$ -0.3	$+0.2$ -0.2	$+0.0$ -0.2
0.12600	$3.89 \cdot 10^3$	± 0.6	$+1.5$ -0.4	$+0.2$ -0.1	+0.6	+1.4	$+0.1$ -0.3	$+0.1$ -0.1	$+0.1$ -0.2
0.20000	$2.04 \cdot 10^3$	± 0.8	$+1.9$ -1.4	$+0.1$ -0.1	+1.6	-0.8	$+0.0$ -0.5	$+0.2$ -0.2	$+0.2$ -0.1

Table G.7: The measured single differential cross section $\frac{d\sigma}{dx}$ ($Q^2 > 185$ GeV², $y < 0.9$, $y(1-x)^2 > 0.004$) for the reaction $e^+p \rightarrow e^+X$ ($\mathcal{L} = 135.5$ pb⁻¹, $P_e = 0$). The bin centre, x_c , the cross section corrected to the electroweak Born level and the statistical and the systematic uncertainty (in %) are given. In addition the contributions of the variation of the electron energy scale (δ_1), the variation of the electron identification (δ_2), the variation of the parton shower model (δ_3), the variation of the track requirement region (δ_4), the variation of the Track Veto Efficiency correction (δ_5) and the variation of the $E - p_z$ cut (δ_6) to the systematic uncertainty are shown. All uncertainties are given in %.

x_c	$\frac{d\sigma}{dx}$ [pb/GeV ²]	stat	syst	δ_1	δ_2	δ_3	δ_4	δ_5	δ_6
0.05010	$1.72 \cdot 10^2$	± 4.8	$+1.6$ -1.7	$+0.0$ -0.3	-0.2	+0.8	$+0.1$ -0.1	$+1.3$ -1.3	$+0.0$ -0.6
0.07940	$1.60 \cdot 10^2$	± 3.8	$+2.2$ -1.1	$+0.1$ -0.1	+1.9	+0.3	$+0.0$ -0.0	$+1.0$ -0.9	$+0.0$ -0.1
0.12600	$1.18 \cdot 10^2$	± 3.4	$+0.9$ -1.6	$+0.2$ -0.1	-1.2	+0.0	$+0.0$ -0.0	$+0.8$ -0.8	$+0.0$ -0.6
0.20000	$6.71 \cdot 10^1$	± 3.7	$+0.8$ -1.5	$+0.1$ -0.1	-0.4	-0.2	$+0.0$ -0.0	$+0.7$ -0.7	$+0.0$ -0.8
0.31600	$3.26 \cdot 10^1$	± 4.2	$+1.1$ -1.3	$+0.2$ -0.2	+0.4	-1.1	$+0.0$ -0.0	$+0.6$ -0.6	$+0.0$ -0.0
0.68700	1.20	± 6.5	$+2.1$ -2.2	$+0.1$ -0.3	+1.2	-1.5	$+0.0$ -0.1	$+0.6$ -0.6	$+1.2$ -0.0

Table G.8: The measured single differential cross section $\frac{d\sigma}{dx}$ ($Q^2 > 3000$ GeV², $y < 0.9$, $y(1-x)^2 > 0.004$) for the reaction $e^+p \rightarrow e^+X$ ($\mathcal{L} = 135.5$ pb⁻¹, $P_e = 0$). The bin centre, x_c , the cross section corrected to the electroweak Born level and the statistical and the systematic uncertainty (in %) are given. In addition the contributions of the variation of the electron energy scale (δ_1), the variation of the electron identification (δ_2), the variation of the parton shower model (δ_3), the variation of the track requirement region (δ_4), the variation of the Track Veto Efficiency correction (δ_5) and the variation of the $E - p_z$ cut (δ_6) to the systematic uncertainty are shown. All uncertainties are given in %.

y_c	$\frac{d\sigma}{dy}$ [pb/GeV ²]	stat	syst	δ_1	δ_2	δ_3	δ_4	δ_5	δ_6
0.02500	$1.63 \cdot 10^4$	± 0.4	$+1.5$ -0.5	$+0.1$ -0.1	+0.8	+1.2	$+0.1$ -0.4	$+0.0$ -0.0	$+0.1$ -0.1
0.07500	$8.09 \cdot 10^3$	± 0.5	$+1.8$ -0.6	$+0.1$ -0.1	+0.3	+1.7	$+0.3$ -0.5	$+0.1$ -0.1	$+0.0$ -0.1
0.12500	$5.64 \cdot 10^3$	± 0.6	$+0.6$ -0.7	$+0.1$ -0.0	+0.3	+0.1	$+0.4$ -0.7	$+0.1$ -0.1	$+0.1$ -0.2
0.17500	$4.37 \cdot 10^3$	± 0.7	$+0.5$ -1.2	$+0.1$ -0.1	+0.4	-0.4	$+0.1$ -1.1	$+0.2$ -0.2	$+0.0$ -0.0
0.22500	$3.61 \cdot 10^3$	± 0.7	$+0.5$ -1.1	$+0.1$ -0.0	+0.3	-0.9	$+0.0$ -0.6	$+0.2$ -0.2	$+0.1$ -0.1
0.27500	$2.93 \cdot 10^3$	± 0.8	$+0.9$ -1.0	$+0.1$ -0.0	+0.9	-0.5	$+0.2$ -0.9	$+0.2$ -0.2	$+0.1$ -0.0
0.32500	$2.53 \cdot 10^3$	± 0.9	$+1.2$ -0.9	$+0.0$ -0.0	+1.0	-0.0	$+0.2$ -0.8	$+0.3$ -0.3	$+0.3$ -0.1
0.37500	$2.24 \cdot 10^3$	± 1.0	$+0.7$ -1.4	$+0.1$ -0.1	+0.2	-0.5	$+0.5$ -1.1	$+0.4$ -0.4	$+0.1$ -0.2
0.42500	$1.98 \cdot 10^3$	± 1.0	$+1.3$ -0.9	$+0.0$ -0.0	+0.8	-0.6	$+0.7$ -0.2	$+0.5$ -0.5	$+0.0$ -0.0
0.47500	$1.73 \cdot 10^3$	± 1.1	$+2.2$ -1.0	$+0.1$ -0.0	+1.9	-0.3	$+0.7$ -0.0	$+0.7$ -0.7	$+0.0$ -0.4
0.52500	$1.54 \cdot 10^3$	± 1.2	$+2.0$ -1.0	$+0.2$ -0.0	+1.6	-0.1	$+0.7$ -0.0	$+0.8$ -0.8	$+0.4$ -0.1
0.57500	$1.42 \cdot 10^3$	± 1.3	$+2.4$ -1.4	$+0.3$ -0.2	+2.0	-0.7	$+0.2$ -0.0	$+0.9$ -0.9	$+0.0$ -0.5
0.62500	$1.28 \cdot 10^3$	± 1.4	$+3.9$ -1.9	$+0.6$ -0.7	+3.6	-1.1	$+0.0$ -0.1	$+1.1$ -1.1	$+0.4$ -0.0
0.67500	$1.20 \cdot 10^3$	± 1.5	$+2.5$ -2.8	$+1.1$ -1.2	+1.8	-1.9	$+0.0$ -0.0	$+1.2$ -1.2	$+0.0$ -0.4
0.72500	$1.12 \cdot 10^3$	± 1.8	$+5.9$ -2.9	$+2.2$ -2.0	+5.3	-1.2	$+0.0$ -0.0	$+1.3$ -1.2	$+0.3$ -0.0

Table G.9: The measured single differential cross section $\frac{d\sigma}{dy}$ ($Q^2 > 185$ GeV², $y(1-x)^2 > 0.004$) for the reaction $e^+p \rightarrow e^+X$ ($\mathcal{L} = 135.5$ pb⁻¹, $P_e = 0$). The bin centre, y_c , the cross section corrected to the electroweak Born level and the statistical and the systematic uncertainty (in %) are given. In addition the contributions of the variation of the electron energy scale (δ_1), the variation of the electron identification (δ_2), the variation of the parton shower model (δ_3), the variation of the track requirement region (δ_4), the variation of the Track Veto Efficiency correction (δ_5) and the variation of the $E - p_z$ cut (δ_6) to the systematic uncertainty are shown. All uncertainties are given in %.

y_c	$\frac{d\sigma}{dy}$	stat	syst	δ_1	δ_2	δ_3	δ_4	δ_5	δ_6
0.07500	$3.28 \cdot 10^1$	± 7.6	$+1.5$ -1.7	$+0.0$ -0.4	+1.3	-1.4	$+0.0$ -0.2	$+0.6$ -0.6	$+0.3$ -0.0
0.12500	$5.53 \cdot 10^1$	± 5.6	$+1.1$ -0.7	$+0.1$ -0.2	+0.9	+0.1	$+0.0$ -0.0	$+0.6$ -0.6	$+0.0$ -0.2
0.17500	$5.87 \cdot 10^1$	± 5.3	$+1.4$ -1.5	$+0.2$ -0.1	+0.6	-0.5	$+0.1$ -0.0	$+0.7$ -0.7	$+0.9$ -0.8
0.22500	$5.66 \cdot 10^1$	± 5.4	$+1.0$ -1.6	$+0.1$ -0.2	-0.7	-0.8	$+0.0$ -0.1	$+0.7$ -0.7	$+0.4$ -0.5
0.27500	$4.97 \cdot 10^1$	± 5.7	$+0.8$ -1.5	$+0.1$ -0.1	-0.8	-0.3	$+0.0$ -0.0	$+0.7$ -0.7	$+0.0$ -0.8
0.32500	$5.10 \cdot 10^1$	± 5.6	$+1.1$ -1.3	$+0.2$ -0.0	-0.4	-0.3	$+0.0$ -0.0	$+0.7$ -0.7	$+0.8$ -0.4
0.37500	$3.72 \cdot 10^1$	± 6.6	$+1.2$ -2.3	$+0.1$ -0.1	+0.6	-1.8	$+0.1$ -0.0	$+0.8$ -0.7	$+0.0$ -0.9
0.42500	$3.42 \cdot 10^1$	± 6.9	$+1.2$ -2.7	$+0.2$ -0.1	-2.3	-0.4	$+0.0$ -0.0	$+0.8$ -0.8	$+0.0$ -0.6
0.47500	$3.58 \cdot 10^1$	± 6.8	$+1.0$ -3.1	$+0.1$ -0.1	-2.4	-1.6	$+0.0$ -0.0	$+0.8$ -0.8	$+0.3$ -0.1
0.52500	$2.85 \cdot 10^1$	± 7.7	$+0.9$ -3.2	$+0.1$ -0.0	-1.6	-2.0	$+0.0$ -0.0	$+0.9$ -0.9	$+0.0$ -1.5
0.57500	$2.91 \cdot 10^1$	± 7.6	$+1.9$ -1.3	$+0.0$ -0.2	+7.7	+0.6	$+0.0$ -0.2	$+0.9$ -0.9	$+0.0$ -0.7
0.62500	$2.42 \cdot 10^1$	± 8.8	$+7.8$ -1.7	$+0.1$ -0.0	+6.2	+3.4	$+0.0$ -0.0	$+1.0$ -1.0	$+0.8$ -0.0
0.67500	$2.28 \cdot 10^1$	± 8.7	$+2.2$ -5.4	$+0.0$ -0.0	-5.0	+1.8	$+0.1$ -0.0	$+1.1$ -1.1	$+0.4$ -1.7
0.72500	$2.35 \cdot 10^1$	± 8.7	$+2.4$ -3.9	$+0.0$ -0.0	-1.2	+2.0	$+0.1$ -0.0	$+1.2$ -1.2	$+0.0$ -2.8
0.77500	$2.12 \cdot 10^1$	± 9.2	$+1.7$ -4.0	$+0.1$ -0.1	-2.6	+0.5	$+0.1$ -0.0	$+1.4$ -1.3	$+0.0$ -2.5
0.82500	$1.89 \cdot 10^1$	± 9.9	$+6.7$ -3.1	$+0.0$ -1.2	+5.8	+1.2	$+0.1$ -1.0	$+1.4$ -1.4	$+1.6$ -0.5
0.87500	$1.94 \cdot 10^1$	± 10.8	$+6.4$ -7.9	$+1.6$ -1.2	+5.4	+1.6	$+0.8$ -0.0	$+1.4$ -1.4	$+0.4$ -2.3

Table G.10: The measured single differential cross section $\frac{d\sigma}{dy}$ ($Q^2 > 3000 \text{ GeV}^2$, $y(1-x)^2 > 0.004$) for the reaction $e^+p \rightarrow e^+X$ ($\mathcal{L} = 135.5 \text{ pb}^{-1}$, $P_e = 0$). The bin centre, y_c , the cross section corrected to the electroweak Born level and the statistical and the systematic uncertainty (in %) are given. In addition the contributions of the variation of the electron energy scale (δ_1), the variation of the electron identification (δ_2), the variation of the parton shower model (δ_3), the variation of the track requirement region (δ_4), the variation of the Track Veto Efficiency correction (δ_5) and the variation of the $E - p_z$ cut (δ_6) to the systematic uncertainty are shown. All uncertainties are given in %.

Q_c^2 [GeV ²]	$\frac{d\sigma}{dQ^2}$ [pb/GeV ²]	stat	syst	δ_1	δ_2	δ_3	δ_4	δ_5	δ_6
195	$1.91 \cdot 10^1$	± 0.6	+0.7 -0.6	+0.2 -0.1	+0.6	+0.1	+0.2 -0.5	+0.0 -0.0	+0.3 -0.1
220	$1.43 \cdot 10^1$	± 0.6	+0.9 -0.7	+0.2 -0.1	+0.5	+0.5	+0.3 -0.6	+0.0 -0.0	+0.0 -0.0
255	$1.01 \cdot 10^1$	± 0.7	+1.1 -1.6	+0.2 -0.1	+0.7	+0.7	+0.0 -1.6	+0.0 -0.0	+0.2 -0.0
285	7.90	± 0.8	+0.4 -1.2	+0.2 -0.2	+0.3	-0.2	+0.1 -1.2	+0.1 -0.1	+0.0 -0.1
320	5.86	± 0.9	+1.4 -1.1	+0.2 -0.2	+1.2	+0.3	+0.6 -0.9	+0.1 -0.1	+0.0 -0.4
360	4.40	± 1.0	+1.6 -0.5	+0.2 -0.1	+0.8	+1.1	+0.8 -0.1	+0.2 -0.2	+0.0 -0.3
400	3.41	± 1.1	+1.5 -0.4	+0.2 -0.2	+1.1	+0.7	+0.7 -0.1	+0.2 -0.2	+0.1 -0.0
450	2.60	± 1.2	+1.9 -0.5	+0.2 -0.3	+1.6	+0.7	+0.0 -0.0	+0.3 -0.3	+0.3 -0.1
510	1.93	± 1.3	+1.4 -0.6	+0.3 -0.2	+1.3	-0.2	+0.1 -0.0	+0.4 -0.4	+0.0 -0.3
570	1.42	± 1.6	+1.6 -0.8	+0.4 -0.3	+1.3	+0.3	+0.1 -0.0	+0.6 -0.6	+0.2 -0.0
630	1.16	± 1.7	+1.0 -0.9	+0.3 -0.2	+0.4	+0.2	+0.0 -0.0	+0.7 -0.7	+0.3 -0.0
700	$8.88 \cdot 10^{-1}$	± 1.8	+1.3 -1.1	+0.2 -0.2	+1.0	+0.2	+0.0 -0.0	+0.7 -0.7	+0.0 -0.6
780	$6.78 \cdot 10^{-1}$	± 1.7	+1.0 -0.9	+0.2 -0.1	+0.3	+0.4	+0.1 -0.0	+0.7 -0.7	+0.0 -0.2
860	$5.22 \cdot 10^{-1}$	± 1.9	+1.9 -0.8	+0.2 -0.1	+1.6	-0.1	+0.1 -0.0	+0.7 -0.7	+0.2 -0.0
940	$4.31 \cdot 10^{-1}$	± 2.0	+0.9 -1.1	+0.1 -0.3	+0.3	-0.8	+0.0 -0.1	+0.7 -0.7	+0.5 -0.2
1030	$3.37 \cdot 10^{-1}$	± 2.3	+2.1 -1.2	+0.1 -0.2	+2.0	-0.6	+0.0 -0.1	+0.7 -0.7	+0.1 -0.5
1130	$2.61 \cdot 10^{-1}$	± 2.2	+1.4 -0.8	+0.1 -0.1	+0.7	+0.9	+0.1 -0.0	+0.7 -0.7	+0.1 -0.3
1270	$2.01 \cdot 10^{-1}$	± 2.2	+2.8 -0.9	+0.2 -0.0	+2.7	-0.4	+0.0 -0.0	+0.7 -0.7	+0.3 -0.1
1420	$1.42 \cdot 10^{-1}$	± 2.7	+1.8 -0.9	+0.3 -0.1	+1.4	-0.0	+0.1 -0.0	+0.7 -0.7	+0.4 -0.4
1590	$1.15 \cdot 10^{-1}$	± 2.5	+2.5 -0.8	+0.2 -0.1	+2.3	+0.3	+0.0 -0.1	+0.7 -0.7	+0.1 -0.0
1790	$8.07 \cdot 10^{-2}$	± 3.0	+2.4 -1.1	+0.2 -0.0	+2.1	+0.4	+0.2 -0.0	+0.7 -0.7	+0.1 -0.5
1990	$6.09 \cdot 10^{-2}$	± 3.5	+1.9 -1.3	+0.3 -0.0	+1.6	-0.9	+0.1 -0.0	+0.7 -0.7	+0.0 -0.0
2300	$4.15 \cdot 10^{-2}$	± 2.7	+1.7 -0.9	+0.1 -0.1	+1.5	-0.0	+0.0 -0.0	+0.7 -0.7	+0.3 -0.2
2800	$2.37 \cdot 10^{-2}$	± 3.3	+1.2 -0.8	+0.1 -0.1	+0.6	+0.5	+0.1 -0.0	+0.7 -0.7	+0.4 -0.1
3500	$1.41 \cdot 10^{-2}$	± 3.9	+2.1 -1.1	+0.0 -0.3	+1.9	-0.2	+0.0 -0.1	+0.7 -0.7	+0.0 -0.7
4200	$8.78 \cdot 10^{-3}$	± 4.7	+1.1 -1.3	+0.2 -0.1	+0.8	-0.8	+0.1 -0.0	+0.7 -0.7	+0.0 -0.7
5100	$4.52 \cdot 10^{-3}$	± 6.0	+1.1 -1.0	+0.2 -0.1	+0.2	+0.6	+0.1 -0.0	+0.6 -0.6	+0.0 -0.5
6050	$2.94 \cdot 10^{-3}$	± 7.1	+1.4 -2.5	+0.1 -0.2	-0.5	-2.2	+0.0 -0.1	+0.6 -0.6	+0.5 -0.0
7100	$1.48 \cdot 10^{-3}$	± 9.1	+4.5 -4.9	+0.1 -0.3	+3.4	+1.8	+0.0 -0.1	+0.6 -0.6	+2.0 -4.3
8400	$1.01 \cdot 10^{-3}$	± 10.3	+2.0 -3.7	+0.2 -0.1	+1.6	-2.1	+0.1 -0.0	+0.6 -0.6	+0.0 -1.2
10800	$3.97 \cdot 10^{-4}$	± 10.1	+3.3 -3.9	+0.3 -0.2	+0.9	-0.9	+0.0 -0.0	+0.6 -0.6	+0.0 -3.5
15200	$1.12 \cdot 10^{-4}$	± 15.8	+2.7 -8.3	+0.1 -0.3	-7.9	-0.9	+0.0 -0.1	+0.6 -0.6	+1.7 -0.0
21500	$2.67 \cdot 10^{-5}$	± 26.7	+12.7 -9.3	+0.3 -0.3	+3.5	-1.9	+0.0 -0.1	+0.6 -0.6	+2.2 -1.8
36200	$1.82 \cdot 10^{-6}$	± 44.7	+3.0 -44.4	+0.3 -0.3	-41.8	-6.7	+0.3 -0.0	+0.6 -0.6	+2.4 -2.6

Table G.11: The measured single differential cross section $\frac{d\sigma}{dQ^2}$ ($y < 0.9$, $y(1-x)^2 > 0.004$) for the reaction $e^+p \rightarrow e^+X$ ($\mathcal{L} = 135.5 \text{ pb}^{-1}$, $P_e = +0.32$). The bin centre, Q_c^2 , the cross section corrected to the electroweak Born level and the statistical and the systematic uncertainty (in %) are given. In addition the contributions of the variation of the electron energy scale (δ_1), the variation of the electron identification (δ_2), the variation of the parton shower model (δ_3), the variation of the track requirement region (δ_4), the variation of the Track Veto Efficiency correction (δ_5) and the variation of the $E-p_z$ cut (δ_6) to the systematic uncertainty are shown. All uncertainties are given in %.

x_c	$\frac{d\sigma}{dx}$ [pb/GeV ²]	stat	syst	δ_1	δ_2	δ_3	δ_4	δ_5	δ_6
0.00794	$8.79 \cdot 10^4$	± 0.7	$^{+0.8}_{-0.9}$	$^{+0.2}_{-0.2}$	+0.6	-0.6	$^{+0.1}_{-0.5}$	$^{+0.3}_{-0.3}$	$^{+0.0}_{-0.0}$
0.01260	$5.87 \cdot 10^4$	± 0.7	$^{+0.9}_{-1.1}$	$^{+0.1}_{-0.0}$	+0.8	-0.6	$^{+0.1}_{-0.8}$	$^{+0.3}_{-0.3}$	$^{+0.1}_{-0.1}$
0.02000	$3.69 \cdot 10^4$	± 0.7	$^{+0.7}_{-0.7}$	$^{+0.2}_{-0.0}$	+0.5	+0.2	$^{+0.1}_{-0.6}$	$^{+0.2}_{-0.2}$	$^{+0.2}_{-0.1}$
0.03160	$2.12 \cdot 10^4$	± 0.7	$^{+1.7}_{-0.7}$	$^{+0.1}_{-0.1}$	+0.7	+1.5	$^{+0.4}_{-0.6}$	$^{+0.2}_{-0.2}$	$^{+0.1}_{-0.0}$
0.05010	$1.25 \cdot 10^4$	± 0.7	$^{+1.7}_{-0.6}$	$^{+0.1}_{-0.1}$	+0.3	+1.6	$^{+0.4}_{-0.6}$	$^{+0.2}_{-0.2}$	$^{+0.1}_{-0.1}$
0.07940	$6.97 \cdot 10^3$	± 0.8	$^{+1.6}_{-0.4}$	$^{+0.1}_{-0.1}$	+0.4	+1.5	$^{+0.1}_{-0.4}$	$^{+0.1}_{-0.1}$	$^{+0.0}_{-0.1}$
0.12600	$3.97 \cdot 10^3$	± 0.8	$^{+1.6}_{-0.5}$	$^{+0.2}_{-0.1}$	+0.8	+1.4	$^{+0.1}_{-0.4}$	$^{+0.1}_{-0.1}$	$^{+0.1}_{-0.2}$
0.20000	$2.09 \cdot 10^3$	± 1.0	$^{+2.1}_{-1.1}$	$^{+0.1}_{-0.1}$	+1.8	-0.8	$^{+0.0}_{-0.5}$	$^{+0.1}_{-0.1}$	$^{+0.2}_{-0.1}$

Table G.12: The measured single differential cross section $\frac{d\sigma}{dx}$ ($Q^2 > 185$ GeV², $y < 0.9$, $y(1-x)^2 > 0.004$) for the reaction $e^+p \rightarrow e^+X$ ($\mathcal{L} = 135.5$ pb⁻¹, $P_e = +0.32$). The bin centre, x_c , the cross section corrected to the electroweak Born level and the statistical and the systematic uncertainty (in %) are given. In addition the contributions of the variation of the electron energy scale (δ_1), the variation of the electron identification (δ_2), the variation of the parton shower model (δ_3), the variation of the track requirement region (δ_4), the variation of the Track Veto Efficiency correction (δ_5) and the variation of the $E - p_z$ cut (δ_6) to the systematic uncertainty are shown. All uncertainties are given in %.

x_c	$\frac{d\sigma}{dx}$ [pb/GeV ²]	stat	syst	δ_1	δ_2	δ_3	δ_4	δ_5	δ_6
0.05010	$1.82 \cdot 10^2$	± 6.1	$^{+1.9}_{-1.5}$	$^{+0.0}_{-0.3}$	+1.1	+0.8	$^{+0.1}_{-0.0}$	$^{+1.0}_{-1.0}$	$^{+0.0}_{-0.7}$
0.07940	$1.69 \cdot 10^2$	± 4.9	$^{+1.9}_{-1.0}$	$^{+0.1}_{-0.1}$	+1.7	+0.3	$^{+0.0}_{-0.0}$	$^{+0.7}_{-0.7}$	$^{+0.0}_{-0.1}$
0.12600	$1.28 \cdot 10^2$	± 4.3	$^{+0.7}_{-1.2}$	$^{+0.2}_{-0.1}$	+0.2	-0.0	$^{+0.0}_{-0.0}$	$^{+0.6}_{-0.6}$	$^{+0.0}_{-1.0}$
0.20000	$7.45 \cdot 10^1$	± 4.6	$^{+0.8}_{-1.9}$	$^{+0.1}_{-0.1}$	-1.3	-0.2	$^{+0.0}_{-0.0}$	$^{+0.6}_{-0.6}$	$^{+0.0}_{-1.0}$
0.31600	$3.45 \cdot 10^1$	± 5.4	$^{+2.4}_{-1.4}$	$^{+0.2}_{-0.2}$	+2.1	-1.1	$^{+0.0}_{-0.0}$	$^{+0.5}_{-0.5}$	$^{+0.0}_{-0.5}$
0.68700	1.30	± 8.1	$^{+1.6}_{-2.4}$	$^{+0.1}_{-0.3}$	-0.5	-1.5	$^{+0.0}_{-0.1}$	$^{+0.5}_{-0.5}$	$^{+1.2}_{-0.0}$

Table G.13: The measured single differential cross section $\frac{d\sigma}{dx}$ ($Q^2 > 3000$ GeV², $y < 0.9$, $y(1-x)^2 > 0.004$) for the reaction $e^+p \rightarrow e^+X$ ($\mathcal{L} = 135.5$ pb⁻¹, $P_e = +0.32$). The bin centre, x_c , the cross section corrected to the electroweak Born level and the statistical and the systematic uncertainty (in %) are given. In addition the contributions of the variation of the electron energy scale (δ_1), the variation of the electron identification (δ_2), the variation of the parton shower model (δ_3), the variation of the track requirement region (δ_4), the variation of the Track Veto Efficiency correction (δ_5) and the variation of the $E - p_z$ cut (δ_6) to the systematic uncertainty are shown. All uncertainties are given in %.

y_c	$\frac{d\sigma}{dy}$ [pb/GeV ²]	stat	syst	δ_1	δ_2	δ_3	δ_4	δ_5	δ_6
0.02500	$1.65 \cdot 10^4$	± 0.5	$+1.6$ -0.6	$+0.1$ -0.1	+0.8	+1.2	$+0.0$ -0.5	$+0.0$ -0.0	$+0.1$ -0.1
0.07500	$8.18 \cdot 10^3$	± 0.6	$+1.8$ -0.7	$+0.1$ -0.1	+0.3	+1.7	$+0.3$ -0.6	$+0.1$ -0.1	$+0.0$ -0.2
0.12500	$5.73 \cdot 10^3$	± 0.7	$+0.6$ -0.8	$+0.1$ -0.0	+0.2	+0.1	$+0.4$ -0.8	$+0.1$ -0.1	$+0.1$ -0.2
0.17500	$4.40 \cdot 10^3$	± 0.8	$+0.4$ -1.1	$+0.1$ -0.1	+0.3	-0.4	$+0.1$ -0.9	$+0.1$ -0.1	$+0.0$ -0.1
0.22500	$3.66 \cdot 10^3$	± 0.9	$+0.4$ -1.1	$+0.1$ -0.0	+0.3	-0.9	$+0.0$ -0.6	$+0.1$ -0.1	$+0.2$ -0.1
0.27500	$2.95 \cdot 10^3$	± 1.1	$+0.7$ -0.7	$+0.1$ -0.0	+0.7	-0.5	$+0.1$ -0.4	$+0.2$ -0.2	$+0.1$ -0.0
0.32500	$2.58 \cdot 10^3$	± 1.1	$+1.2$ -0.8	$+0.0$ -0.0	+1.0	-0.0	$+0.0$ -0.7	$+0.2$ -0.2	$+0.4$ -0.2
0.37500	$2.25 \cdot 10^3$	± 1.2	$+1.1$ -1.3	$+0.1$ -0.1	+0.6	-0.6	$+0.9$ -1.0	$+0.3$ -0.3	$+0.0$ -0.1
0.42500	$2.00 \cdot 10^3$	± 1.3	$+1.0$ -0.9	$+0.0$ -0.0	+0.8	-0.6	$+0.4$ -0.5	$+0.4$ -0.4	$+0.1$ -0.0
0.47500	$1.76 \cdot 10^3$	± 1.4	$+2.0$ -1.1	$+0.1$ -0.0	+1.9	-0.3	$+0.1$ -0.0	$+0.5$ -0.5	$+0.0$ -0.6
0.52500	$1.56 \cdot 10^3$	± 1.6	$+1.8$ -0.8	$+0.2$ -0.0	+1.3	-0.1	$+0.8$ -0.0	$+0.7$ -0.7	$+0.4$ -0.0
0.57500	$1.45 \cdot 10^3$	± 1.6	$+2.1$ -1.2	$+0.3$ -0.2	+1.8	-0.7	$+0.3$ -0.0	$+0.8$ -0.8	$+0.0$ -0.5
0.62500	$1.31 \cdot 10^3$	± 1.8	$+2.7$ -1.8	$+0.6$ -0.7	+2.4	-1.1	$+0.0$ -0.1	$+0.9$ -0.8	$+0.4$ -0.0
0.67500	$1.22 \cdot 10^3$	± 2.0	$+3.2$ -2.7	$+1.1$ -1.2	+2.7	-1.9	$+0.0$ -0.0	$+0.9$ -0.9	$+0.0$ -0.4
0.72500	$1.12 \cdot 10^3$	± 2.3	$+6.7$ -2.8	$+2.1$ -2.0	+6.2	-1.2	$+0.0$ -0.0	$+0.9$ -0.9	$+0.5$ -0.7

Table G.14: The measured single differential cross section $\frac{d\sigma}{dy}$ ($Q^2 > 185$ GeV², $y(1-x)^2 > 0.004$) for the reaction $e^+p \rightarrow e^+X$ ($\mathcal{L} = 135.5$ pb⁻¹, $P_e = +0.32$). The bin centre, y_c , the cross section corrected to the electroweak Born level and the statistical and the systematic uncertainty (in %) are given. In addition the contributions of the variation of the electron energy scale (δ_1), the variation of the electron identification (δ_2), the variation of the parton shower model (δ_3), the variation of the track requirement region (δ_4), the variation of the Track Veto Efficiency correction (δ_5) and the variation of the $E - p_z$ cut (δ_6) to the systematic uncertainty are shown. All uncertainties are given in %.

y_c	$\frac{d\sigma}{dy}$ [pb/GeV ²]	stat	syst	δ_1	δ_2	δ_3	δ_4	δ_5	δ_6
0.07500	$3.50 \cdot 10^1$	± 9.6	+1.1 -1.8	+0.0 -0.4	+0.7	-1.5	+0.0 -0.2	+0.5 -0.5	+0.5 -0.2
0.12500	$5.86 \cdot 10^1$	± 7.1	+1.6 -1.0	+0.1 -0.2	+1.4	+0.1	+0.0 -0.0	+0.5 -0.5	+0.0 -0.9
0.17500	$6.34 \cdot 10^1$	± 6.7	+0.8 -1.9	+0.2 -0.1	-0.5	-0.4	+0.1 -0.0	+0.6 -0.5	+0.3 -0.6
0.22500	$6.36 \cdot 10^1$	± 6.7	+1.3 -1.4	+0.1 -0.2	+1.1	-0.8	+0.0 -0.1	+0.6 -0.6	+0.1 -0.6
0.27500	$5.60 \cdot 10^1$	± 7.0	+0.6 -1.8	+0.1 -0.1	-1.3	-0.3	+0.0 -0.0	+0.6 -0.6	+0.0 -0.8
0.32500	$5.66 \cdot 10^1$	± 7.0	+1.0 -1.3	+0.2 -0.0	-0.2	-0.3	+0.0 -0.0	+0.6 -0.6	+0.6 -0.5
0.37500	$3.89 \cdot 10^1$	± 8.5	+2.0 -2.1	+0.1 -0.1	+1.6	-1.8	+0.1 -0.0	+0.6 -0.6	+0.0 -0.8
0.42500	$3.58 \cdot 10^1$	± 8.8	+1.4 -1.5	+0.2 -0.1	-0.7	-0.3	+0.0 -0.0	+0.6 -0.6	+0.0 -1.0
0.47500	$3.59 \cdot 10^1$	± 8.8	+1.9 -2.3	+0.1 -0.1	+1.7	-1.6	+0.0 -0.0	+0.6 -0.6	+0.4 -0.3
0.52500	$2.93 \cdot 10^1$	± 9.9	+1.1 -4.7	+0.1 -0.0	-3.3	-2.0	+0.0 -0.0	+0.6 -0.6	+0.0 -2.5
0.57500	$3.16 \cdot 10^1$	± 9.5	+6.3 -1.0	+0.0 -0.2	+6.1	+0.7	+0.0 -0.2	+0.7 -0.7	+0.7 -0.3
0.62500	$2.57 \cdot 10^1$	± 10.9	+7.4 -1.6	+0.1 -0.0	+5.5	+3.4	+0.0 -0.0	+0.8 -0.8	+1.0 -0.5
0.67500	$2.69 \cdot 10^1$	± 10.5	+2.5 -6.9	+0.0 -0.0	-6.6	+1.8	+0.1 -0.0	+0.9 -0.8	+1.1 -1.2
0.72500	$2.39 \cdot 10^1$	± 11.3	+2.4 -5.8	+0.0 -0.0	+0.3	+2.0	+0.1 -0.0	+1.0 -0.9	+0.0 -5.3
0.77500	$2.19 \cdot 10^1$	± 11.9	+1.6 -5.3	+0.1 -0.1	-4.3	+0.5	+0.1 -0.0	+1.1 -1.1	+0.0 -2.5
0.82500	$2.17 \cdot 10^1$	± 12.1	+6.5 -3.6	+0.0 -1.1	+4.5	+1.2	+0.1 -0.9	+1.2 -1.1	+0.6 -0.0
0.87500	$2.01 \cdot 10^1$	± 13.9	+10.7 -9.7	+1.6 -1.2	+10.2	+1.7	+0.8 -0.0	+1.1 -1.1	+0.0 -2.3

Table G.15: The measured single differential cross section $\frac{d\sigma}{dy}$ ($Q^2 > 3000$ GeV², $y(1-x)^2 > 0.004$) for the reaction $e^+p \rightarrow e^+X$ ($\mathcal{L} = 135.5$ pb⁻¹, $P_e = +0.32$). The bin centre, y_c , the cross section corrected to the electroweak Born level and the statistical and the systematic uncertainty (in %) are given. In addition the contributions of the variation of the electron energy scale (δ_1), the variation of the electron identification (δ_2), the variation of the parton shower model (δ_3), the variation of the track requirement region (δ_4), the variation of the Track Veto Efficiency correction (δ_5) and the variation of the $E - p_z$ cut (δ_6) to the systematic uncertainty are shown. All uncertainties are given in %.

Q_c^2 [GeV ²]	$\frac{d\sigma}{dQ^2}$ [pb/GeV ²]	stat	syst	δ_1	δ_2	δ_3	δ_4	δ_5	δ_6
195	$1.90 \cdot 10^1$	± 0.7	$+0.8$ -0.7	$+0.2$ -0.1	$+0.7$	$+0.1$	$+0.2$ -0.6	$+0.0$ -0.0	$+0.1$ -0.0
220	$1.43 \cdot 10^1$	± 0.7	$+0.7$ -0.7	$+0.2$ -0.1	$+0.3$	$+0.5$	$+0.1$ -0.6	$+0.0$ -0.0	$+0.0$ -0.1
255	9.94	± 0.9	$+0.9$ -1.3	$+0.2$ -0.1	$+0.4$	$+0.7$	$+0.2$ -1.2	$+0.1$ -0.1	$+0.1$ -0.1
285	7.64	± 1.0	$+1.2$ -0.9	$+0.2$ -0.2	$+1.0$	-0.2	$+0.7$ -0.8	$+0.1$ -0.1	$+0.0$ -0.2
320	5.68	± 1.0	$+1.1$ -0.8	$+0.2$ -0.2	$+1.0$	$+0.4$	$+0.2$ -0.5	$+0.2$ -0.2	$+0.1$ -0.4
360	4.26	± 1.2	$+1.8$ -0.7	$+0.2$ -0.1	$+0.6$	$+1.1$	$+1.2$ -0.1	$+0.3$ -0.3	$+0.0$ -0.4
400	3.23	± 1.3	$+2.2$ -0.6	$+0.2$ -0.2	$+1.7$	$+0.7$	$+1.1$ -0.1	$+0.4$ -0.4	$+0.0$ -0.2
450	2.49	± 1.5	$+2.5$ -0.9	$+0.2$ -0.3	$+2.2$	$+0.7$	$+0.4$ -0.0	$+0.5$ -0.5	$+0.2$ -0.5
510	1.85	± 1.6	$+0.8$ -0.8	$+0.3$ -0.2	-0.2	-0.1	$+0.1$ -0.0	$+0.7$ -0.7	$+0.0$ -0.1
570	1.34	± 1.9	$+2.6$ -1.2	$+0.4$ -0.3	$+2.2$	$+0.3$	$+0.0$ -0.0	$+0.9$ -0.9	$+0.7$ -0.0
630	1.11	± 2.0	$+1.5$ -1.3	$+0.3$ -0.2	$+0.8$	$+0.2$	$+0.0$ -0.0	$+1.2$ -1.2	$+0.4$ -0.0
700	$8.43 \cdot 10^{-1}$	± 2.1	$+2.8$ -1.4	$+0.2$ -0.2	$+2.5$	$+0.2$	$+0.0$ -0.0	$+1.2$ -1.2	$+0.1$ -0.0
780	$6.50 \cdot 10^{-1}$	± 2.1	$+1.7$ -1.4	$+0.3$ -0.1	$+0.9$	$+0.4$	$+0.1$ -0.0	$+1.2$ -1.2	$+0.5$ -0.0
860	$4.89 \cdot 10^{-1}$	± 2.4	$+1.8$ -1.2	$+0.2$ -0.0	$+1.1$	-0.1	$+0.1$ -0.0	$+1.2$ -1.1	$+0.3$ -0.0
940	$4.00 \cdot 10^{-1}$	± 2.4	$+1.9$ -1.6	$+0.1$ -0.3	$+1.4$	-0.8	$+0.0$ -0.0	$+1.2$ -1.1	$+0.0$ -0.4
1030	$2.99 \cdot 10^{-1}$	± 2.8	$+2.9$ -1.5	$+0.2$ -0.2	$+2.6$	-0.6	$+0.0$ -0.1	$+1.1$ -1.1	$+0.4$ -0.2
1130	$2.47 \cdot 10^{-1}$	± 2.7	$+2.2$ -1.2	$+0.1$ -0.1	$+1.4$	$+0.9$	$+0.1$ -0.0	$+1.2$ -1.1	$+0.7$ -0.0
1270	$1.90 \cdot 10^{-1}$	± 2.7	$+2.3$ -1.3	$+0.2$ -0.1	$+1.8$	-0.3	$+0.0$ -0.0	$+1.1$ -1.1	$+0.5$ -0.0
1420	$1.43 \cdot 10^{-1}$	± 3.1	$+2.3$ -1.3	$+0.3$ -0.1	$+1.9$	$+0.0$	$+0.1$ -0.0	$+1.1$ -1.1	$+0.3$ -0.5
1590	$1.00 \cdot 10^{-1}$	± 3.2	$+2.6$ -1.3	$+0.2$ -0.1	$+2.3$	$+0.3$	$+0.0$ -0.1	$+1.1$ -1.1	$+0.0$ -0.2
1790	$7.58 \cdot 10^{-2}$	± 3.7	$+2.1$ -1.2	$+0.2$ -0.0	$+1.6$	$+0.4$	$+0.2$ -0.0	$+1.1$ -1.1	$+0.1$ -0.2
1990	$5.60 \cdot 10^{-2}$	± 4.3	$+3.3$ -1.6	$+0.3$ -0.1	$+2.9$	-1.0	$+0.1$ -0.0	$+1.1$ -1.1	$+0.7$ -0.0
2300	$3.89 \cdot 10^{-2}$	± 3.3	$+1.3$ -1.2	$+0.1$ -0.1	$+0.5$	-0.1	$+0.0$ -0.0	$+1.1$ -1.1	$+0.3$ -0.0
2800	$2.31 \cdot 10^{-2}$	± 4.0	$+1.6$ -1.5	$+0.1$ -0.1	$+0.9$	$+0.4$	$+0.1$ -0.0	$+1.1$ -1.1	$+0.2$ -0.6
3500	$1.20 \cdot 10^{-2}$	± 5.0	$+1.4$ -1.9	$+0.0$ -0.3	-1.4	-0.2	$+0.0$ -0.1	$+1.1$ -1.1	$+0.1$ -0.3
4200	$6.42 \cdot 10^{-3}$	± 6.5	$+2.8$ -1.7	$+0.2$ -0.1	$+2.0$	-0.8	$+0.1$ -0.0	$+1.1$ -1.1	$+1.3$ -0.0
5100	$3.71 \cdot 10^{-3}$	± 7.8	$+2.0$ -3.3	$+0.2$ -0.1	-1.1	$+0.6$	$+0.1$ -0.0	$+1.1$ -1.0	$+1.3$ -0.2
6050	$2.43 \cdot 10^{-3}$	± 9.2	$+1.4$ -4.0	$+0.1$ -0.2	-1.4	-2.2	$+0.0$ -0.1	$+1.1$ -1.0	$+0.0$ -1.1
7100	$1.47 \cdot 10^{-3}$	± 10.8	$+3.1$ -1.3	$+0.1$ -0.3	$+0.4$	$+1.7$	$+0.0$ -0.1	$+1.1$ -1.0	$+1.1$ -0.0
8400	$8.53 \cdot 10^{-4}$	± 13.3	$+5.7$ -3.4	$+0.2$ -0.1	$+5.1$	-2.2	$+0.1$ -0.0	$+1.1$ -1.0	$+0.0$ -1.9
10800	$2.75 \cdot 10^{-4}$	± 14.4	$+3.0$ -2.5	$+0.3$ -0.2	$+1.2$	-0.9	$+0.0$ -0.0	$+1.0$ -1.0	$+0.7$ -0.4
15200	$6.30 \cdot 10^{-5}$	± 25.0	$+8.8$ -18.5	$+0.1$ -0.3	-13.5	-0.9	$+0.0$ -0.1	$+1.0$ -1.0	$+4.7$ -4.6
21500	$5.37 \cdot 10^{-5}$	± 22.4	$+8.1$ -14.8	$+0.3$ -0.3	-13.9	-2.0	$+0.0$ -0.1	$+1.0$ -1.0	$+2.2$ -1.8
36200	$1.52 \cdot 10^{-6}$	± 57.7	$+30.8$ -8.1	$+0.3$ -0.3	$+29.5$	-6.8	$+0.3$ -0.0	$+1.0$ -1.0	$+2.4$ -2.7

Table G.16: The measured single differential cross section $\frac{d\sigma}{dQ^2}$ ($y < 0.9$, $y(1-x)^2 > 0.004$) for the reaction $e^+p \rightarrow e^+X$ ($\mathcal{L} = 135.5 \text{ pb}^{-1}$, $P_e = -0.36$). The bin centre, Q_c^2 , the cross section corrected to the electroweak Born level and the statistical and the systematic uncertainty (in %) are given. In addition the contributions of the variation of the electron energy scale (δ_1), the variation of the electron identification (δ_2), the variation of the parton shower model (δ_3), the variation of the track requirement region (δ_4), the variation of the Track Veto Efficiency correction (δ_5) and the variation of the $E-p_z$ cut (δ_6) to the systematic uncertainty are shown. All uncertainties are given in %.

x_c	$\frac{d\sigma}{dx}$ [pb/GeV ²]	stat	syst	δ_1	δ_2	δ_3	δ_4	δ_5	δ_6
0.00794	$8.60 \cdot 10^4$	± 0.9	$+1.5$ -1.5	$+0.2$ -0.2	+1.3	-0.6	$+0.4$ -1.2	$+0.5$ -0.5	$+0.0$ -0.0
0.01260	$5.79 \cdot 10^4$	± 0.8	$+1.1$ -1.2	$+0.1$ -0.0	+0.9	-0.6	$+0.2$ -0.9	$+0.4$ -0.4	$+0.0$ -0.1
0.02000	$3.53 \cdot 10^4$	± 0.8	$+0.8$ -0.5	$+0.2$ -0.0	+0.5	+0.2	$+0.3$ -0.3	$+0.4$ -0.3	$+0.1$ -0.1
0.03160	$2.07 \cdot 10^4$	± 0.8	$+1.7$ -0.5	$+0.1$ -0.1	+0.4	+1.5	$+0.3$ -0.3	$+0.3$ -0.3	$+0.0$ -0.1
0.05010	$1.21 \cdot 10^4$	± 0.9	$+1.8$ -0.6	$+0.1$ -0.1	+0.7	+1.6	$+0.2$ -0.5	$+0.3$ -0.3	$+0.1$ -0.0
0.07940	$6.84 \cdot 10^3$	± 0.9	$+1.6$ -0.5	$+0.1$ -0.1	+0.3	+1.5	$+0.1$ -0.2	$+0.2$ -0.2	$+0.0$ -0.3
0.12600	$3.79 \cdot 10^3$	± 0.9	$+1.5$ -0.3	$+0.2$ -0.1	+0.4	+1.4	$+0.1$ -0.2	$+0.2$ -0.2	$+0.0$ -0.1
0.20000	$1.97 \cdot 10^3$	± 1.2	$+1.5$ -1.9	$+0.1$ -0.1	+1.3	-0.8	$+0.2$ -0.4	$+0.2$ -0.2	$+0.1$ -0.1

Table G.17: The measured single differential cross section $\frac{d\sigma}{dx}$ ($Q^2 > 185$ GeV², $y < 0.9$, $y(1-x)^2 > 0.004$) for the reaction $e^+p \rightarrow e^+X$ ($\mathcal{L} = 135.5$ pb⁻¹, $P_e = -0.36$). The bin centre, x_c , the cross section corrected to the electroweak Born level and the statistical and the systematic uncertainty (in %) are given. In addition the contributions of the variation of the electron energy scale (δ_1), the variation of the electron identification (δ_2), the variation of the parton shower model (δ_3), the variation of the track requirement region (δ_4), the variation of the Track Veto Efficiency correction (δ_5) and the variation of the $E - p_z$ cut (δ_6) to the systematic uncertainty are shown. All uncertainties are given in %.

x_c	$\frac{d\sigma}{dx}$ [pb/GeV ²]	stat	syst	δ_1	δ_2	δ_3	δ_4	δ_5	δ_6
0.05010	$1.62 \cdot 10^2$	± 7.7	$^{+2.0}_{-3.4}$	$^{+0.0}_{-0.4}$	-2.2	+0.8	$^{+0.1}_{-0.1}$	$^{+1.6}_{-1.6}$	$^{+0.8}_{-0.6}$
0.07940	$1.50 \cdot 10^2$	± 6.1	$^{+2.9}_{-1.5}$	$^{+0.1}_{-0.1}$	+2.3	+0.3	$^{+0.0}_{-0.0}$	$^{+1.3}_{-1.2}$	$^{+0.0}_{-0.2}$
0.12600	$1.05 \cdot 10^2$	± 5.6	$^{+1.2}_{-3.9}$	$^{+0.2}_{-0.1}$	-3.5	+0.0	$^{+0.0}_{-0.0}$	$^{+1.0}_{-1.0}$	$^{+0.0}_{-0.4}$
0.20000	$5.79 \cdot 10^1$	± 6.2	$^{+1.6}_{-1.7}$	$^{+0.1}_{-0.1}$	+1.3	-0.2	$^{+0.0}_{-0.0}$	$^{+0.9}_{-0.9}$	$^{+0.2}_{-0.4}$
0.31600	$3.04 \cdot 10^1$	± 6.8	$^{+1.4}_{-2.9}$	$^{+0.2}_{-0.2}$	-2.5	-1.1	$^{+0.0}_{-0.0}$	$^{+0.8}_{-0.8}$	$^{+0.8}_{-0.0}$
0.68700	1.09	± 10.7	$^{+4.7}_{-2.2}$	$^{+0.1}_{-0.3}$	+4.3	-1.4	$^{+0.0}_{-0.1}$	$^{+0.7}_{-0.7}$	$^{+1.3}_{-0.7}$

Table G.18: The measured single differential cross section $\frac{d\sigma}{dx}$ ($Q^2 > 3000$ GeV², $y < 0.9$, $y(1-x)^2 > 0.004$) for the reaction $e^+p \rightarrow e^+X$ ($\mathcal{L} = 135.5$ pb⁻¹, $P_e = -0.36$). The bin centre, x_c , the cross section corrected to the electroweak Born level and the statistical and the systematic uncertainty (in %) are given. In addition the contributions of the variation of the electron energy scale (δ_1), the variation of the electron identification (δ_2), the variation of the parton shower model (δ_3), the variation of the track requirement region (δ_4), the variation of the Track Veto Efficiency correction (δ_5) and the variation of the $E - p_z$ cut (δ_6) to the systematic uncertainty are shown. All uncertainties are given in %.

y_c	$\frac{d\sigma}{dy}$ [pb/GeV ²]	stat	syst	δ_1	δ_2	δ_3	δ_4	δ_5	δ_6
0.02500	$1.60 \cdot 10^4$	± 0.6	+1.4 -0.4	+0.1 -0.1	+0.7	+1.2	+0.1 -0.2	+0.0 -0.0	+0.0 -0.2
0.07500	$7.97 \cdot 10^3$	± 0.7	+1.8 -0.5	+0.1 -0.1	+0.3	+1.7	+0.2 -0.4	+0.1 -0.1	+0.0 -0.0
0.12500	$5.51 \cdot 10^3$	± 0.8	+0.6 -0.6	+0.1 -0.0	+0.3	+0.1	+0.4 -0.5	+0.2 -0.2	+0.0 -0.1
0.17500	$4.34 \cdot 10^3$	± 1.0	+0.7 -1.4	+0.1 -0.1	+0.6	-0.4	+0.2 -1.2	+0.2 -0.2	+0.1 -0.2
0.22500	$3.55 \cdot 10^3$	± 1.1	+0.6 -1.1	+0.1 -0.0	+0.4	-0.9	+0.2 -0.5	+0.3 -0.3	+0.1 -0.1
0.27500	$2.89 \cdot 10^3$	± 1.2	+1.2 -1.7	+0.1 -0.0	+1.1	-0.5	+0.3 -1.6	+0.3 -0.3	+0.2 -0.1
0.32500	$2.47 \cdot 10^3$	± 1.4	+1.3 -1.2	+0.0 -0.0	+1.1	-0.0	+0.5 -1.0	+0.4 -0.4	+0.1 -0.1
0.37500	$2.24 \cdot 10^3$	± 1.4	+0.6 -1.6	+0.1 -0.1	-0.3	-0.5	+0.0 -1.3	+0.5 -0.5	+0.2 -0.3
0.42500	$1.94 \cdot 10^3$	± 1.6	+1.7 -1.1	+0.0 -0.1	+0.9	-0.6	+1.2 -0.0	+0.6 -0.6	+0.0 -0.0
0.47500	$1.68 \cdot 10^3$	± 1.7	+2.7 -1.0	+0.1 -0.0	+1.9	-0.2	+1.6 -0.0	+0.8 -0.8	+0.1 -0.3
0.52500	$1.51 \cdot 10^3$	± 1.8	+2.4 -1.1	+0.2 -0.0	+1.9	-0.1	+0.6 -0.0	+1.0 -1.0	+0.4 -0.3
0.57500	$1.37 \cdot 10^3$	± 2.0	+2.7 -1.6	+0.3 -0.2	+2.4	-0.7	+0.0 -0.0	+1.2 -1.1	+0.0 -0.5
0.62500	$1.25 \cdot 10^3$	± 2.1	+5.6 -2.2	+0.6 -0.7	+5.4	-1.1	+0.0 -0.0	+1.4 -1.3	+0.5 -0.0
0.67500	$1.17 \cdot 10^3$	± 2.4	+2.0 -3.1	+1.1 -1.2	+0.4	-1.9	+0.0 -0.0	+1.5 -1.5	+0.0 -0.3
0.72500	$1.11 \cdot 10^3$	± 2.7	+5.0 -3.2	+2.2 -2.0	+4.0	-1.2	+0.0 -0.1	+1.6 -1.6	+1.1 -0.0

Table G.19: The measured single differential cross section $\frac{d\sigma}{dy}$ ($Q^2 > 185$ GeV², $y(1-x)^2 > 0.004$) for the reaction $e^+p \rightarrow e^+X$ ($\mathcal{L} = 135.5$ pb⁻¹, $P_e = -0.36$). The bin centre, y_c , the cross section corrected to the electroweak Born level and the statistical and the systematic uncertainty (in %) are given. In addition the contributions of the variation of the electron energy scale (δ_1), the variation of the electron identification (δ_2), the variation of the parton shower model (δ_3), the variation of the track requirement region (δ_4), the variation of the Track Veto Efficiency correction (δ_5) and the variation of the $E - p_z$ cut (δ_6) to the systematic uncertainty are shown. All uncertainties are given in %.

y_c	$\frac{d\sigma}{dy}$ [pb/GeV ²]	stat	syst	δ_1	δ_2	δ_3	δ_4	δ_5	δ_6
0.07500	$3.04 \cdot 10^1$	± 12.3	$+2.8$ -1.9	$+0.0$ -0.4	+2.2	-1.4	$+0.0$ -0.2	$+0.7$ -0.7	$+1.0$ -0.1
0.12500	$5.16 \cdot 10^1$	± 9.0	$+1.4$ -1.5	$+0.1$ -0.2	+0.0	+0.1	$+0.0$ -0.0	$+0.8$ -0.8	$+1.2$ -0.3
0.17500	$5.29 \cdot 10^1$	± 8.7	$+3.3$ -1.8	$+0.2$ -0.1	+2.4	-0.5	$+0.1$ -0.0	$+0.8$ -0.8	$+2.0$ -1.1
0.22500	$4.77 \cdot 10^1$	± 9.2	$+1.9$ -4.3	$+0.1$ -0.2	-4.0	-0.8	$+0.0$ -0.1	$+0.9$ -0.9	$+1.0$ -0.2
0.27500	$4.17 \cdot 10^1$	± 9.6	$+1.5$ -1.4	$+0.1$ -0.1	+0.3	-0.2	$+0.0$ -0.0	$+0.9$ -0.9	$+0.0$ -0.7
0.32500	$4.42 \cdot 10^1$	± 9.4	$+1.6$ -1.5	$+0.2$ -0.0	-0.7	-0.2	$+0.0$ -0.0	$+1.0$ -0.9	$+1.1$ -0.1
0.37500	$3.55 \cdot 10^1$	± 10.5	$+1.7$ -3.4	$+0.1$ -0.1	-0.9	-1.8	$+0.1$ -0.0	$+1.0$ -1.0	$+0.0$ -0.9
0.42500	$3.26 \cdot 10^1$	± 10.9	$+1.3$ -5.4	$+0.2$ -0.1	-4.8	-0.4	$+0.0$ -0.0	$+1.1$ -1.0	$+0.1$ -0.1
0.47500	$3.61 \cdot 10^1$	± 10.4	$+1.8$ -8.4	$+0.1$ -0.1	-8.1	-1.6	$+0.0$ -0.0	$+1.1$ -1.1	$+0.2$ -0.0
0.52500	$2.80 \cdot 10^1$	± 12.0	$+1.7$ -2.9	$+0.1$ -0.0	+1.0	-2.0	$+0.0$ -0.0	$+1.2$ -1.2	$+0.2$ -0.0
0.57500	$2.61 \cdot 10^1$	± 12.3	$+10.6$ -2.1	$+0.0$ -0.2	+10.4	+0.4	$+0.0$ -0.2	$+1.3$ -1.2	$+0.0$ -1.4
0.62500	$2.25 \cdot 10^1$	± 13.6	$+8.9$ -2.5	$+0.1$ -0.0	+7.3	+3.5	$+0.0$ -0.0	$+1.4$ -1.4	$+1.8$ -0.0
0.67500	$1.76 \cdot 10^1$	± 15.3	$+2.3$ -4.7	$+0.0$ -0.0	-1.3	+1.8	$+0.1$ -0.0	$+1.5$ -1.4	$+0.0$ -2.6
0.72500	$2.32 \cdot 10^1$	± 13.5	$+2.7$ -4.5	$+0.0$ -0.0	-3.3	+2.0	$+0.1$ -0.0	$+1.6$ -1.5	$+0.7$ -0.0
0.77500	$2.07 \cdot 10^1$	± 14.5	$+2.0$ -3.5	$+0.1$ -0.1	-0.0	+0.5	$+0.1$ -0.0	$+1.7$ -1.7	$+0.0$ -2.5
0.82500	$1.54 \cdot 10^1$	± 16.9	$+10.0$ -4.9	$+0.0$ -1.5	+8.6	+1.3	$+0.1$ -1.3	$+1.8$ -1.7	$+3.4$ -1.4
0.87500	$1.89 \cdot 10^1$	± 16.9	$+4.9$ -6.2	$+1.6$ -1.3	-1.4	+1.6	$+0.8$ -0.0	$+1.7$ -1.7	$+2.2$ -2.3

Table G.20: The measured single differential cross section $\frac{d\sigma}{dy}$ ($Q^2 > 3000$ GeV², $y(1-x)^2 > 0.004$) for the reaction $e^+p \rightarrow e^+X$ ($\mathcal{L} = 135.5$ pb⁻¹, $P_e = -0.36$). The bin centre, y_c , the cross section corrected to the electroweak Born level and the statistical and the systematic uncertainty (in %) are given. In addition the contributions of the variation of the electron energy scale (δ_1), the variation of the electron identification (δ_2), the variation of the parton shower model (δ_3), the variation of the track requirement region (δ_4), the variation of the Track Veto Efficiency correction (δ_5) and the variation of the $E - p_z$ cut (δ_6) to the systematic uncertainty are shown. All uncertainties are given in %.

Q_c^2 [GeV ²]	A^+	stat
195	0.01	±0.01
220	0.00	±0.01
255	0.03	±0.02
285	0.05	±0.02
320	0.05	±0.02
360	0.05	±0.02
400	0.08	±0.02
450	0.07	±0.03
510	0.06	±0.03
570	0.09	±0.04
630	0.07	±0.04
700	0.08	±0.04
780	0.06	±0.04
860	0.09	±0.04
940	0.11	±0.05
1030	0.17	±0.05
1130	0.08	±0.05
1270	0.09	±0.05
1420	-0.01	±0.06
1590	0.20	±0.06
1790	0.09	±0.07
1990	0.12	±0.08
2300	0.10	±0.06
2800	0.04	±0.08
3500	0.24	±0.09
4200	0.46	±0.11
5100	0.29	±0.14
6050	0.28	±0.17
7100	0.01	±0.21
8400	0.24	±0.24
10800	0.54	±0.25
15200	0.82	±0.41
21500	-0.99	±0.54
36200	0.26	±1.06

Table G.21: The polarisation asymmetry, A^+ , measured with positron beams of positive and negative polarisation. The bin centre Q_c^2 , the asymmetry, A^+ , and its statistical uncertainty (in absolute value) are given.

H. Reduced Cross Section, $x\tilde{F}_3$ and $xF_3^{\gamma Z}$

In this appendix the bins of the reduced cross section measurement are listed and the measured reduced cross section $\tilde{\sigma}$ is tabulated for zero, positive and negative polarisation. In addition, the measured values and uncertainties of the structure function $x\tilde{F}_3$ and the interference term $xF_3^{\gamma Z}$ are given, which were extracted from these results and the published e^-p results [8].

Table H.1: The bins of the reduced cross section measurement. Given are the Q^2 and x limits as well as the bin centres Q_c^2 and x_c .

Q_{low}^2 [GeV ²]	Q_{high}^2 [GeV ²]	Q_c^2 [GeV ²]	x_{low}	x_{high}	x_c
185	240	200	0.0037	0.006	0.005
			0.006	0.01	0.008
			0.01	0.017	0.013
			0.017	0.025	0.021
			0.025	0.037	0.032
			0.037	0.06	0.05
			0.06	0.12	0.08
			0.12	0.25	0.18
240	310	250	0.006	0.01	0.008
			0.01	0.017	0.013
			0.017	0.025	0.021
			0.025	0.037	0.032
			0.037	0.06	0.05
			0.06	0.12	0.08
			0.12	0.25	0.18
310	410	350	0.006	0.01	0.008
			0.01	0.017	0.013
			0.017	0.025	0.021
			0.025	0.037	0.032
			0.037	0.06	0.05
			0.06	0.12	0.08
			0.12	0.25	0.18
Bins for Reduced Cross Sections			Continued on next page		

Table H.1 – continued from previous page

Q_{low}^2 [GeV ²]	Q_{high}^2 [GeV ²]	Q_c^2 [GeV ²]	x_{low}	x_{high}	x_c
410	530	450	0.006	0.01	0.008
			0.01	0.017	0.013
			0.017	0.025	0.021
			0.025	0.037	0.032
			0.037	0.06	0.05
			0.06	0.1	0.08
			0.1	0.17	0.13
			0.17	0.3	0.25
530	710	650	0.01	0.017	0.013
			0.017	0.025	0.021
			0.025	0.037	0.032
			0.037	0.06	0.05
			0.06	0.1	0.08
			0.1	0.17	0.13
			0.17	0.3	0.25
			710	900	800
0.017	0.025	0.021			
0.025	0.037	0.032			
0.037	0.06	0.05			
0.06	0.1	0.08			
0.1	0.17	0.13			
0.17	0.3	0.25			
900	1300	1200			
			0.017	0.025	0.021
			0.025	0.037	0.032
			0.037	0.06	0.05
			0.06	0.1	0.08
			0.1	0.17	0.13
			0.17	0.3	0.25
			0.3	0.53	0.4
1300	1800	1500	0.017	0.025	0.021
			0.025	0.037	0.032
			0.037	0.06	0.05
			0.06	0.1	0.08
			0.1	0.15	0.13
			0.15	0.23	0.18
			0.23	0.35	0.25
			0.35	0.53	0.4
Bins for Reduced Cross Sections			Continued on next page		

Table H.1 – continued from previous page

Q_{low}^2 [GeV ²]	Q_{high}^2 [GeV ²]	Q_c^2 [GeV ²]	x_{low}	x_{high}	x_c
1800	2500	2000	0.023	0.037	0.032
			0.037	0.06	0.05
			0.06	0.1	0.08
			0.1	0.15	0.13
			0.15	0.23	0.18
			0.23	0.35	0.25
			0.35	0.53	0.4
2500	3500	3000	0.037	0.06	0.05
			0.06	0.1	0.08
			0.1	0.15	0.13
			0.15	0.23	0.18
			0.23	0.35	0.25
			0.35	0.53	0.4
			0.53	0.75	0.65
3500	5600	5000	0.04	0.1	0.08
			0.1	0.15	0.13
			0.15	0.23	0.18
			0.23	0.35	0.25
			0.35	0.53	0.4
5600	9000	8000	0.07	0.15	0.13
			0.15	0.23	0.18
			0.23	0.35	0.25
			0.35	0.53	0.4
			0.53	0.75	0.65
9000	15000	12000	0.09	0.23	0.18
			0.23	0.35	0.25
			0.35	0.53	0.4
15000	25000	20000	0.15	0.35	0.25
			0.35	0.75	0.4
25000	50000	30000	0.25	0.75	0.4

Table H.1: Bins for Reduced Cross Sections

Table H.2: The measured reduced cross section $\tilde{\sigma}$ for the reaction $e^+p \rightarrow e^+X$ ($\mathcal{L} = 135.5 \text{ pb}^{-1}$, $P_e = 0$). The bin centres, Q_c^2 and x_c , the cross section corrected to the electroweak Born level and the statistical and the systematic uncertainty (in %) are given. In addition the contributions of the variation of the electron energy scale (δ_1), the variation of the electron identification (δ_2), the variation of the parton shower model (δ_3), the variation of the track requirement region (δ_4), the variation of the Track Veto Efficiency correction (δ_5) and the variation of the $E - p_z$ cut (δ_6) to the systematic uncertainty are shown. All uncertainties are given in %.

Q_c^2 [GeV ²]	x_c	$\tilde{\sigma}$	stat.	syst.	δ_1	δ_2	δ_3	δ_4	δ_5	δ_6
200	0.005	1.11	± 0.9	+1.9 -1.8	+0.1 -0.1	+1.7	-1.0	+0.9 -1.5	+0.0 -0.0	+0.0 -0.1
200	0.008	$9.44 \cdot 10^{-1}$	± 0.8	+0.5 -2.0	+0.0 -0.0	+0.4	-1.4	+0.2 -1.4	+0.0 -0.0	+0.0 -0.0
200	0.013	$8.00 \cdot 10^{-1}$	± 0.8	+0.3 -1.7	+0.1 -0.0	+0.0	-0.8	+0.1 -1.5	+0.0 -0.0	+0.2 -0.1
200	0.021	$6.79 \cdot 10^{-1}$	± 1.0	+0.8 -0.5	+0.2 -0.0	-0.4	+0.7	+0.1 -0.2	+0.0 -0.0	+0.1 -0.2
200	0.032	$5.64 \cdot 10^{-1}$	± 1.0	+2.6 -0.2	+0.1 -0.1	+0.1	+2.5	+0.2 -0.0	+0.0 -0.0	+0.1 -0.1
200	0.050	$5.11 \cdot 10^{-1}$	± 1.0	+2.2 -0.4	+0.2 -0.1	+0.1	+2.2	+0.1 -0.3	+0.0 -0.0	+0.0 -0.0
200	0.080	$4.33 \cdot 10^{-1}$	± 0.8	+2.8 -0.2	+0.1 -0.1	+0.4	+2.8	+0.1 -0.0	+0.0 -0.0	+0.1 -0.0
200	0.180	$3.46 \cdot 10^{-1}$	± 1.1	+1.7 -1.2	+0.1 -0.1	+1.4	-1.0	+0.8 -0.0	+0.0 -0.0	+0.0 -0.0
250	0.008	$9.28 \cdot 10^{-1}$	± 1.0	+2.0 -0.7	+0.0 -0.1	+1.7	-0.4	+0.9 -0.4	+0.0 -0.0	+0.4 -0.1
250	0.013	$8.20 \cdot 10^{-1}$	± 1.0	+0.6 -1.5	+0.1 -0.0	+0.6	-1.1	+0.0 -1.0	+0.0 -0.0	+0.0 -0.1
250	0.021	$6.92 \cdot 10^{-1}$	± 1.1	+0.5 -1.3	+0.1 -0.0	+0.3	-0.4	+0.3 -1.2	+0.0 -0.0	+0.0 -0.1
250	0.032	$5.85 \cdot 10^{-1}$	± 1.2	+1.8 -2.0	+0.1 -0.1	+0.0	+1.8	+0.2 -2.0	+0.0 -0.0	+0.0 -0.1
250	0.050	$5.12 \cdot 10^{-1}$	± 1.1	+2.7 -1.5	+0.1 -0.1	-0.3	+2.6	+0.1 -1.5	+0.0 -0.0	+0.0 -0.1
250	0.080	$4.34 \cdot 10^{-1}$	± 1.0	+2.1 -1.1	+0.1 -0.1	+0.0	+2.1	+0.0 -1.0	+0.0 -0.0	+0.1 -0.4
250	0.180	$3.37 \cdot 10^{-1}$	± 1.1	+1.6 -2.0	+0.1 -0.1	+1.4	-1.1	+0.1 -1.7	+0.0 -0.0	+0.3 -0.0
350	0.008	$9.48 \cdot 10^{-1}$	± 1.3	+2.0 -0.9	+0.0 -0.2	+1.7	+0.8	+0.0 -0.0	+0.7 -0.7	+0.0 -0.6
350	0.013	$8.08 \cdot 10^{-1}$	± 1.2	+0.8 -0.5	+0.0 -0.0	+0.4	-0.1	+0.7 -0.1	+0.1 -0.1	+0.2 -0.4
350	0.021	$6.72 \cdot 10^{-1}$	± 1.4	+1.4 -0.4	+0.2 -0.0	+1.0	+0.5	+0.8 -0.0	+0.0 -0.0	+0.1 -0.0
350	0.032	$5.76 \cdot 10^{-1}$	± 1.4	+2.5 -0.8	+0.0 -0.1	+1.0	-0.1	+2.3 -0.2	+0.0 -0.0	+0.0 -0.1
350	0.050	$5.05 \cdot 10^{-1}$	± 1.4	+2.0 -0.9	+0.0 -0.0	+0.8	+1.4	+1.1 -0.7	+0.0 -0.0	+0.1 -0.4
350	0.080	$4.17 \cdot 10^{-1}$	± 1.2	+3.3 -0.9	+0.1 -0.1	+0.7	+3.0	+0.9 -0.7	+0.0 -0.0	+0.2 -0.5
350	0.180	$3.24 \cdot 10^{-1}$	± 1.3	+1.7 -1.3	+0.1 -0.1	+1.5	+0.6	+0.0 -0.9	+0.0 -0.0	+0.0 -1.0

Reduced Cross Sections for 0 Polarisation

Continued on next page

Table H.2 – continued from previous page

Q_c^2 [GeV ²]	x_c	$\tilde{\sigma}$	stat.	syst.	δ_1	δ_2	δ_3	δ_4	δ_5	δ_6
450	0.008	1.02	±1.5	+1.7 -1.7	+0.4 -0.3	+0.4	-0.0	+0.0 -0.0	+1.4 -1.4	+0.1 -0.1
450	0.013	$8.16 \cdot 10^{-1}$	±1.7	+1.1 -1.0	+0.1 -0.0	+0.3	-0.0	+0.1 -0.0	+1.0 -1.0	+0.0 -0.2
450	0.021	$7.06 \cdot 10^{-1}$	±1.9	+1.3 -0.5	+0.2 -0.1	+1.1	+0.5	+0.1 -0.0	+0.2 -0.2	+0.2 -0.1
450	0.032	$5.80 \cdot 10^{-1}$	±1.8	+1.9 -0.7	+0.2 -0.2	+1.3	+1.4	+0.0 -0.1	+0.1 -0.1	+0.0 -0.1
450	0.050	$5.11 \cdot 10^{-1}$	±1.7	+2.0 -0.6	+0.1 -0.1	+1.6	+1.3	+0.2 -0.0	+0.1 -0.1	+0.1 -0.5
450	0.080	$4.25 \cdot 10^{-1}$	±1.7	+1.6 -0.5	+0.1 -0.1	+1.5	+0.0	+0.1 -0.0	+0.0 -0.0	+0.0 -0.1
450	0.130	$3.64 \cdot 10^{-1}$	±1.8	+2.7 -0.1	+0.2 -0.0	+1.2	+2.1	+1.0 -0.0	+0.0 -0.0	+0.1 -0.0
450	0.250	$2.58 \cdot 10^{-1}$	±2.0	+2.9 -0.4	+0.1 -0.0	+2.7	+0.0	+0.7 -0.1	+0.0 -0.0	+0.0 -0.1
650	0.013	$8.66 \cdot 10^{-1}$	±1.6	+2.3 -1.7	+0.1 -0.0	+1.7	-0.8	+0.0 -0.0	+1.5 -1.4	+0.5 -0.0
650	0.021	$7.34 \cdot 10^{-1}$	±2.0	+1.1 -1.2	+0.1 -0.0	-0.6	+0.0	+0.0 -0.0	+1.0 -1.0	+0.4 -0.0
650	0.032	$6.08 \cdot 10^{-1}$	±2.2	+2.3 -0.8	+0.2 -0.0	+0.9	+2.0	+0.1 -0.0	+0.7 -0.7	+0.1 -0.2
650	0.050	$5.11 \cdot 10^{-1}$	±2.2	+0.7 -0.6	+0.2 -0.1	+0.2	+0.2	+0.1 -0.0	+0.5 -0.5	+0.0 -0.2
650	0.080	$4.32 \cdot 10^{-1}$	±2.4	+0.5 -0.7	+0.1 -0.1	+0.3	+0.1	+0.1 -0.0	+0.3 -0.3	+0.0 -0.5
650	0.130	$3.34 \cdot 10^{-1}$	±2.5	+2.9 -0.3	+0.2 -0.1	+1.3	+2.5	+0.0 -0.0	+0.2 -0.2	+0.4 -0.0
650	0.250	$2.38 \cdot 10^{-1}$	±2.6	+1.5 -1.0	+0.2 -0.1	+1.3	+0.4	+0.1 -0.0	+0.2 -0.2	+0.5 -0.0
800	0.013	$8.33 \cdot 10^{-1}$	±2.0	+3.4 -1.8	+0.4 -0.0	+2.8	+0.4	+0.1 -0.0	+1.4 -1.4	+0.0 -0.3
800	0.021	$7.41 \cdot 10^{-1}$	±2.4	+1.2 -1.6	+0.1 -0.0	-0.9	-0.3	+0.0 -0.0	+1.1 -1.1	+0.0 -0.0
800	0.032	$6.10 \cdot 10^{-1}$	±2.4	+1.1 -1.0	+0.0 -0.1	+0.4	-0.4	+0.0 -0.0	+0.9 -0.9	+0.2 -0.0
800	0.050	$5.13 \cdot 10^{-1}$	±2.3	+2.0 -0.8	+0.2 -0.1	+0.6	+1.7	+0.0 -0.0	+0.8 -0.7	+0.5 -0.1
800	0.080	$4.54 \cdot 10^{-1}$	±2.4	+0.7 -1.0	+0.1 -0.1	-0.3	-0.4	+0.0 -0.0	+0.7 -0.7	+0.0 -0.3
800	0.130	$3.45 \cdot 10^{-1}$	±2.7	+1.8 -0.6	+0.1 -0.1	+1.5	+0.7	+0.0 -0.0	+0.6 -0.6	+0.1 -0.0
800	0.250	$2.42 \cdot 10^{-1}$	±3.0	+3.2 -1.0	+0.2 -0.1	+2.3	+2.1	+0.1 -0.0	+0.6 -0.6	+0.6 -0.5
1200	0.014	$8.19 \cdot 10^{-1}$	±2.5	+8.1 -2.8	+0.2 -0.5	+7.9	-1.2	+0.1 -0.0	+1.4 -1.3	+0.1 -0.8
1200	0.021	$7.39 \cdot 10^{-1}$	±2.4	+2.0 -1.5	+0.1 -0.0	+0.8	+0.3	+0.0 -0.1	+1.4 -1.3	+0.8 -0.6
1200	0.032	$6.25 \cdot 10^{-1}$	±2.3	+1.0 -1.4	+0.1 -0.2	+0.3	-0.7	+0.0 -0.1	+1.0 -0.9	+0.3 -0.1
1200	0.050	$5.12 \cdot 10^{-1}$	±2.1	+1.5 -0.8	+0.2 -0.1	+1.2	+0.0	+0.0 -0.0	+0.8 -0.8	+0.4 -0.1
1200	0.080	$4.23 \cdot 10^{-1}$	±2.2	+1.2 -0.8	+0.2 -0.2	+0.9	+0.1	+0.0 -0.0	+0.7 -0.7	+0.1 -0.1
1200	0.130	$3.52 \cdot 10^{-1}$	±2.3	+0.9 -0.8	+0.1 -0.1	+0.1	+0.3	+0.0 -0.0	+0.6 -0.6	+0.4 -0.0
1200	0.250	$2.47 \cdot 10^{-1}$	±2.6	+0.8 -0.7	+0.2 -0.1	+0.1	-0.3	+0.0 -0.0	+0.6 -0.6	+0.1 -0.0
1200	0.400	$1.30 \cdot 10^{-1}$	±4.0	+0.9 -1.1	+0.0 -0.2	+0.4	-0.1	+0.0 -0.2	+0.5 -0.5	+0.2 -0.0
1500	0.021	$7.26 \cdot 10^{-1}$	±3.4	+8.9 -1.9	+0.2 -0.0	+8.6	+1.3	+0.1 -0.0	+1.4 -1.4	+0.0 -0.4
1500	0.032	$5.82 \cdot 10^{-1}$	±3.3	+4.4 -1.2	+0.0 -0.1	+4.1	+0.3	+0.1 -0.0	+1.2 -1.1	+0.4 -0.1
1500	0.050	$5.32 \cdot 10^{-1}$	±2.8	+1.0 -1.7	+0.1 -0.1	-0.7	-1.2	+0.0 -0.0	+0.8 -0.8	+0.3 -0.0
1500	0.080	$4.47 \cdot 10^{-1}$	±2.8	+0.9 -1.0	+0.2 -0.2	+0.2	+0.4	+0.0 -0.0	+0.7 -0.7	+0.1 -0.3
1500	0.130	$3.72 \cdot 10^{-1}$	±3.3	+0.8 -1.1	+0.2 -0.2	+0.1	-0.5	+0.0 -0.1	+0.7 -0.7	+0.0 -0.7
1500	0.180	$3.05 \cdot 10^{-1}$	±3.6	+1.1 -0.8	+0.1 -0.2	+0.5	+0.3	+0.0 -0.1	+0.6 -0.6	+0.5 -0.2
1500	0.250	$2.42 \cdot 10^{-1}$	±4.3	+1.7 -0.7	+0.3 -0.1	+0.5	+1.0	+0.1 -0.0	+0.6 -0.6	+0.8 -0.3
1500	0.400	$1.19 \cdot 10^{-1}$	±6.3	+1.7 -3.1	+0.1 -0.3	-1.1	-2.2	+0.0 -0.2	+0.5 -0.5	+0.5 -0.0

Reduced Cross Sections for 0 Polarisation

Continued on next page

Table H.2 – continued from previous page

Q_c^2 [GeV ²]	x_c	$\tilde{\sigma}$	stat.	syst.	δ_1	δ_2	δ_3	δ_4	δ_5	δ_6
2000	0.032	$5.92 \cdot 10^{-1}$	± 3.9	$^{+7.7}_{-1.9}$	$^{+0.1}_{-0.0}$	+7.3	+1.1	$^{+0.0}_{-0.0}$	$^{+1.4}_{-1.4}$	$^{+0.8}_{-0.7}$
2000	0.050	$4.93 \cdot 10^{-1}$	± 3.6	$^{+1.7}_{-1.0}$	$^{+0.3}_{-0.0}$	+0.9	+0.2	$^{+0.2}_{-0.0}$	$^{+1.0}_{-0.9}$	$^{+0.6}_{-0.1}$
2000	0.080	$4.74 \cdot 10^{-1}$	± 3.3	$^{+0.9}_{-1.2}$	$^{+0.1}_{-0.1}$	-0.5	-0.6	$^{+0.0}_{-0.0}$	$^{+0.8}_{-0.7}$	$^{+0.4}_{-0.0}$
2000	0.130	$3.53 \cdot 10^{-1}$	± 4.1	$^{+1.4}_{-0.9}$	$^{+0.2}_{-0.1}$	+1.0	+0.6	$^{+0.0}_{-0.0}$	$^{+0.7}_{-0.7}$	$^{+0.3}_{-0.1}$
2000	0.180	$2.72 \cdot 10^{-1}$	± 4.5	$^{+1.2}_{-1.8}$	$^{+0.1}_{-0.1}$	+0.9	-1.3	$^{+0.0}_{-0.1}$	$^{+0.6}_{-0.6}$	$^{+0.3}_{-0.4}$
2000	0.250	$2.48 \cdot 10^{-1}$	± 5.1	$^{+1.1}_{-2.3}$	$^{+0.2}_{-0.1}$	+0.7	-2.1	$^{+0.0}_{-0.0}$	$^{+0.6}_{-0.6}$	$^{+0.1}_{-0.7}$
2000	0.400	$1.19 \cdot 10^{-1}$	± 7.5	$^{+2.2}_{-0.9}$	$^{+0.2}_{-0.2}$	+1.7	-0.4	$^{+0.0}_{-0.1}$	$^{+0.6}_{-0.5}$	$^{+0.0}_{-0.3}$
3000	0.050	$5.05 \cdot 10^{-1}$	± 4.5	$^{+1.5}_{-2.0}$	$^{+0.0}_{-0.3}$	-0.1	-1.4	$^{+0.0}_{-0.0}$	$^{+1.2}_{-1.2}$	$^{+1.0}_{-0.0}$
3000	0.080	$4.28 \cdot 10^{-1}$	± 4.2	$^{+1.1}_{-1.3}$	$^{+0.1}_{-0.1}$	-0.4	-0.3	$^{+0.0}_{-0.0}$	$^{+0.8}_{-0.8}$	$^{+0.0}_{-0.0}$
3000	0.130	$3.65 \cdot 10^{-1}$	± 4.7	$^{+2.0}_{-1.4}$	$^{+0.1}_{-0.1}$	-1.0	+1.8	$^{+0.0}_{-0.0}$	$^{+0.7}_{-0.7}$	$^{+0.5}_{-0.4}$
3000	0.180	$2.73 \cdot 10^{-1}$	± 5.3	$^{+2.4}_{-2.0}$	$^{+0.2}_{-0.1}$	+0.4	+2.2	$^{+0.1}_{-0.0}$	$^{+0.7}_{-0.7}$	$^{+0.2}_{-1.7}$
3000	0.250	$2.46 \cdot 10^{-1}$	± 5.9	$^{+0.6}_{-2.0}$	$^{+0.0}_{-0.2}$	-1.3	-0.3	$^{+0.0}_{-0.1}$	$^{+0.6}_{-0.6}$	$^{+0.0}_{-1.1}$
3000	0.400	$1.22 \cdot 10^{-1}$	± 8.9	$^{+3.2}_{-3.9}$	$^{+0.1}_{-0.4}$	+3.2	-3.6	$^{+0.1}_{-0.1}$	$^{+0.6}_{-0.6}$	$^{+0.0}_{-1.2}$
3000	0.650	$1.45 \cdot 10^{-2}$	± 21.8	$^{+7.9}_{-2.5}$	$^{+0.1}_{-0.2}$	+1.4	+1.4	$^{+0.0}_{-0.3}$	$^{+0.5}_{-0.5}$	$^{+1.5}_{-2.4}$
5000	0.080	$4.04 \cdot 10^{-1}$	± 4.0	$^{+2.6}_{-1.6}$	$^{+0.2}_{-0.1}$	+2.1	+0.5	$^{+0.1}_{-0.0}$	$^{+1.1}_{-1.1}$	$^{+0.0}_{-0.6}$
5000	0.130	$3.28 \cdot 10^{-1}$	± 5.4	$^{+1.0}_{-1.7}$	$^{+0.2}_{-0.1}$	-0.8	-1.0	$^{+0.1}_{-0.0}$	$^{+0.8}_{-0.7}$	$^{+0.0}_{-0.4}$
5000	0.180	$2.84 \cdot 10^{-1}$	± 5.5	$^{+1.0}_{-2.2}$	$^{+0.0}_{-0.1}$	-1.6	+0.6	$^{+0.0}_{-0.1}$	$^{+0.7}_{-0.7}$	$^{+0.3}_{-0.1}$
5000	0.250	$2.15 \cdot 10^{-1}$	± 6.6	$^{+1.2}_{-1.0}$	$^{+0.3}_{-0.1}$	+0.8	+0.1	$^{+0.1}_{-0.0}$	$^{+0.6}_{-0.6}$	$^{+0.4}_{-0.5}$
5000	0.400	$1.36 \cdot 10^{-1}$	± 8.5	$^{+1.5}_{-1.7}$	$^{+0.0}_{-0.4}$	+0.8	-1.4	$^{+0.0}_{-0.3}$	$^{+0.6}_{-0.6}$	$^{+1.1}_{-0.0}$
8000	0.130	$3.11 \cdot 10^{-1}$	± 6.0	$^{+3.7}_{-2.6}$	$^{+0.1}_{-0.2}$	+2.7	+2.2	$^{+0.0}_{-0.0}$	$^{+1.0}_{-1.0}$	$^{+0.5}_{-2.2}$
8000	0.180	$2.43 \cdot 10^{-1}$	± 7.9	$^{+0.8}_{-4.5}$	$^{+0.1}_{-0.1}$	-1.5	-4.0	$^{+0.0}_{-0.0}$	$^{+0.7}_{-0.7}$	$^{+0.0}_{-1.0}$
8000	0.250	$2.19 \cdot 10^{-1}$	± 8.6	$^{+1.9}_{-4.0}$	$^{+0.1}_{-0.2}$	-0.9	-3.6	$^{+0.0}_{-0.0}$	$^{+0.7}_{-0.7}$	$^{+0.5}_{-0.0}$
8000	0.400	$1.04 \cdot 10^{-1}$	± 12.3	$^{+3.3}_{-2.8}$	$^{+0.3}_{-0.2}$	+0.9	-2.3	$^{+0.0}_{-0.0}$	$^{+0.6}_{-0.6}$	$^{+2.8}_{-0.0}$
8000	0.650	$1.63 \cdot 10^{-2}$	± 25.8	$^{+11.1}_{-7.9}$	$^{+0.0}_{-0.2}$	+7.3	+5.1	$^{+0.0}_{-0.3}$	$^{+0.6}_{-0.6}$	$^{+0.0}_{-4.8}$
12000	0.180	$1.92 \cdot 10^{-1}$	± 10.2	$^{+2.4}_{-3.2}$	$^{+0.2}_{-0.2}$	-2.3	+1.6	$^{+0.1}_{-0.0}$	$^{+0.9}_{-0.9}$	$^{+0.0}_{-1.3}$
12000	0.250	$1.54 \cdot 10^{-1}$	± 13.4	$^{+1.5}_{-5.1}$	$^{+0.2}_{-0.1}$	-0.1	-2.9	$^{+0.1}_{-0.1}$	$^{+0.7}_{-0.7}$	$^{+0.0}_{-4.0}$
12000	0.400	$1.14 \cdot 10^{-1}$	± 15.2	$^{+3.5}_{-5.0}$	$^{+0.0}_{-0.4}$	+1.1	-4.0	$^{+0.0}_{-0.3}$	$^{+0.7}_{-0.7}$	$^{+1.2}_{-0.0}$
20000	0.250	$1.54 \cdot 10^{-1}$	± 16.2	$^{+4.8}_{-4.8}$	$^{+0.2}_{-0.3}$	-3.3	-1.1	$^{+0.0}_{-0.0}$	$^{+0.9}_{-0.8}$	$^{+2.0}_{-0.0}$
20000	0.400	$6.40 \cdot 10^{-2}$	± 25.8	$^{+7.0}_{-15.4}$	$^{+0.2}_{-0.2}$	-11.1	-0.7	$^{+0.1}_{-0.0}$	$^{+0.7}_{-0.7}$	$^{+4.5}_{-4.6}$
30000	0.400	$6.18 \cdot 10^{-2}$	± 33.3	$^{+2.9}_{-27.5}$	$^{+0.4}_{-0.2}$	-26.2	-7.0	$^{+0.3}_{-0.0}$	$^{+0.8}_{-0.8}$	$^{+2.2}_{-2.4}$

Table H.2: Reduced Cross Sections for 0 Polarisation

Table H.3: The measured reduced cross section $\tilde{\sigma}$ for the reaction $e^+p \rightarrow e^+X$ ($\mathcal{L} = 135.5 \text{ pb}^{-1}$, $P_e = +0.32$). The bin centres, Q_c^2 and x_c , the cross section corrected to the electroweak Born level and the statistical and the systematic uncertainty (in %) are given. In addition the contributions of the variation of the electron energy scale (δ_1), the variation of the electron identification (δ_2), the variation of the parton shower model (δ_3), the variation of the track requirement region (δ_4), the variation of the Track Veto Efficiency correction (δ_5) and the variation of the $E - p_z$ cut (δ_6) to the systematic uncertainty are shown. All uncertainties are given in %.

Q_c^2 [GeV ²]	x_c	$\tilde{\sigma}$	stat.	syst.	δ_1	δ_2	δ_3	δ_4	δ_5	δ_6
200	0.005	1.12	± 1.1	+1.8 -1.8	+0.1 -0.1	+1.7	-1.0	+0.7 -1.5	+0.0 -0.0	+0.0 -0.2
200	0.008	$9.44 \cdot 10^{-1}$	± 1.0	+0.5 -1.7	+0.0 -0.0	+0.3	-1.4	+0.3 -0.9	+0.0 -0.0	+0.0 -0.0
200	0.013	$7.97 \cdot 10^{-1}$	± 1.0	+0.3 -1.6	+0.1 -0.0	-0.1	-0.8	+0.1 -1.4	+0.0 -0.0	+0.2 -0.2
200	0.021	$6.81 \cdot 10^{-1}$	± 1.2	+0.8 -0.6	+0.2 -0.0	-0.3	+0.7	+0.0 -0.5	+0.0 -0.0	+0.2 -0.2
200	0.032	$5.62 \cdot 10^{-1}$	± 1.3	+2.6 -0.3	+0.1 -0.1	+0.3	+2.5	+0.2 -0.0	+0.0 -0.0	+0.1 -0.0
200	0.050	$5.13 \cdot 10^{-1}$	± 1.3	+2.2 -0.5	+0.2 -0.1	-0.2	+2.2	+0.1 -0.4	+0.0 -0.0	+0.1 -0.0
200	0.080	$4.34 \cdot 10^{-1}$	± 1.1	+2.9 -0.2	+0.1 -0.1	+0.6	+2.8	+0.1 -0.0	+0.0 -0.0	+0.2 -0.0
200	0.180	$3.46 \cdot 10^{-1}$	± 1.4	+2.0 -1.1	+0.1 -0.1	+1.5	-1.0	+0.7 -0.0	+0.0 -0.0	+0.2 -0.0
250	0.008	$9.39 \cdot 10^{-1}$	± 1.4	+1.6 -0.7	+0.0 -0.1	+1.5	-0.4	+0.4 -0.4	+0.0 -0.0	+0.3 -0.0
250	0.013	$8.22 \cdot 10^{-1}$	± 1.3	+0.7 -1.5	+0.1 -0.0	+0.7	-1.1	+0.0 -1.0	+0.0 -0.0	+0.1 -0.0
250	0.021	$7.11 \cdot 10^{-1}$	± 1.5	+0.3 -1.7	+0.1 -0.0	-0.1	-0.4	+0.1 -1.6	+0.0 -0.0	+0.0 -0.1
250	0.032	$6.06 \cdot 10^{-1}$	± 1.5	+1.8 -2.2	+0.1 -0.1	+0.3	+1.7	+0.3 -2.2	+0.0 -0.0	+0.1 -0.1
250	0.050	$5.12 \cdot 10^{-1}$	± 1.5	+2.7 -1.4	+0.1 -0.1	-0.4	+2.6	+0.2 -1.3	+0.0 -0.0	+0.1 -0.0
250	0.080	$4.36 \cdot 10^{-1}$	± 1.3	+2.1 -1.2	+0.1 -0.1	+0.1	+2.1	+0.0 -1.1	+0.0 -0.0	+0.1 -0.1
250	0.180	$3.40 \cdot 10^{-1}$	± 1.5	+1.9 -2.3	+0.1 -0.1	+1.7	-1.1	+0.1 -2.0	+0.0 -0.0	+0.3 -0.1
350	0.008	$9.64 \cdot 10^{-1}$	± 1.7	+1.6 -0.9	+0.0 -0.2	+1.2	+0.8	+0.0 -0.0	+0.5 -0.5	+0.0 -0.6
350	0.013	$8.17 \cdot 10^{-1}$	± 1.6	+0.9 -0.5	+0.0 -0.0	+0.8	-0.1	+0.5 -0.1	+0.1 -0.1	+0.1 -0.2
350	0.021	$6.88 \cdot 10^{-1}$	± 1.8	+1.5 -0.4	+0.2 -0.0	+0.9	+0.5	+1.0 -0.0	+0.0 -0.0	+0.1 -0.2
350	0.032	$5.77 \cdot 10^{-1}$	± 1.9	+2.8 -0.7	+0.0 -0.1	+0.9	-0.1	+2.6 -0.2	+0.0 -0.0	+0.2 -0.0
350	0.050	$5.19 \cdot 10^{-1}$	± 1.8	+1.9 -1.2	+0.0 -0.0	+0.9	+1.4	+0.9 -0.8	+0.0 -0.0	+0.1 -0.7
350	0.080	$4.25 \cdot 10^{-1}$	± 1.6	+3.3 -1.2	+0.1 -0.1	+0.6	+3.0	+1.1 -1.1	+0.0 -0.0	+0.4 -0.4
350	0.180	$3.35 \cdot 10^{-1}$	± 1.6	+1.9 -1.5	+0.1 -0.1	+1.8	+0.6	+0.0 -1.1	+0.0 -0.0	+0.1 -1.0
450	0.008	1.04	± 1.9	+1.4 -1.4	+0.4 -0.3	+0.4	-0.0	+0.0 -0.0	+1.2 -1.1	+0.1 -0.3
450	0.013	$8.28 \cdot 10^{-1}$	± 2.3	+1.2 -0.8	+0.1 -0.0	+0.8	-0.1	+0.1 -0.0	+0.8 -0.8	+0.3 -0.1
450	0.021	$7.15 \cdot 10^{-1}$	± 2.5	+1.6 -0.5	+0.2 -0.1	+1.3	+0.5	+0.1 -0.0	+0.1 -0.1	+0.6 -0.0
450	0.032	$5.96 \cdot 10^{-1}$	± 2.4	+1.9 -0.8	+0.2 -0.2	+1.2	+1.4	+0.1 -0.1	+0.1 -0.1	+0.2 -0.0
450	0.050	$5.04 \cdot 10^{-1}$	± 2.2	+1.8 -0.9	+0.1 -0.1	+1.2	+1.3	+0.1 -0.0	+0.0 -0.0	+0.0 -0.7
450	0.080	$4.33 \cdot 10^{-1}$	± 2.3	+2.0 -0.7	+0.1 -0.1	+1.9	+0.0	+0.1 -0.7	+0.0 -0.0	+0.2 -0.0
450	0.130	$3.82 \cdot 10^{-1}$	± 2.3	+2.4 -0.1	+0.2 -0.0	+0.9	+2.1	+0.4 -0.0	+0.0 -0.0	+0.2 -0.1
450	0.250	$2.65 \cdot 10^{-1}$	± 2.5	+2.3 -0.4	+0.1 -0.0	+2.3	+0.0	+0.4 -0.2	+0.0 -0.0	+0.0 -0.1

Reduced Cross Sections for Positive Polarisation

Continued on next page

Table H.3 – continued from previous page

Q_c^2 [GeV ²]	x_c	$\tilde{\sigma}$	stat.	syst.	δ_1	δ_2	δ_3	δ_4	δ_5	δ_6	
650	0.013	$9.00 \cdot 10^{-1}$	± 2.0	$+1.7$ -1.5	$+0.1$ -0.0	+1.1	-0.8	$+0.0$ -0.0	$+1.2$ -1.1	$+0.2$ -0.0	
650	0.021	$7.63 \cdot 10^{-1}$	± 2.5	$+0.8$ -1.0	$+0.1$ -0.0	-0.4	+0.0	$+0.0$ -0.0	$+0.7$ -0.7	$+0.3$ -0.0	
650	0.032	$6.26 \cdot 10^{-1}$	± 2.9	$+2.2$ -0.8	$+0.2$ -0.0	+0.7	+1.9	$+0.1$ -0.0	$+0.5$ -0.5	$+0.2$ -0.2	
650	0.050	$5.20 \cdot 10^{-1}$	± 2.9	$+0.6$ -0.9	$+0.2$ -0.1	+0.3	+0.2	$+0.1$ -0.0	$+0.4$ -0.4	$+0.0$ -0.8	
650	0.080	$4.39 \cdot 10^{-1}$	± 3.1	$+0.8$ -0.9	$+0.1$ -0.1	+0.7	+0.0	$+0.1$ -0.0	$+0.3$ -0.3	$+0.0$ -0.8	
650	0.130	$3.19 \cdot 10^{-1}$	± 3.4	$+3.3$ -0.3	$+0.2$ -0.2	+1.9	+2.6	$+0.0$ -0.0	$+0.2$ -0.2	$+0.2$ -0.1	
650	0.250	$2.44 \cdot 10^{-1}$	± 3.4	$+1.9$ -1.3	$+0.2$ -0.1	+1.7	+0.4	$+0.1$ -0.0	$+0.1$ -0.1	$+0.5$ -0.4	
800	0.013	$8.68 \cdot 10^{-1}$	± 2.6	$+2.8$ -1.8	$+0.3$ -0.0	+2.2	+0.4	$+0.1$ -0.0	$+1.2$ -1.1	$+0.0$ -0.6	
800	0.021	$7.47 \cdot 10^{-1}$	± 3.1	$+1.0$ -1.2	$+0.1$ -0.0	-0.6	-0.3	$+0.0$ -0.0	$+0.9$ -0.9	$+0.1$ -0.1	
800	0.032	$6.06 \cdot 10^{-1}$	± 3.2	$+0.8$ -0.9	$+0.0$ -0.1	+0.0	-0.5	$+0.0$ -0.0	$+0.6$ -0.6	$+0.0$ -0.1	
800	0.050	$5.32 \cdot 10^{-1}$	± 2.9	$+1.9$ -0.6	$+0.2$ -0.1	-0.1	+1.7	$+0.0$ -0.0	$+0.6$ -0.6	$+0.4$ -0.1	
800	0.080	$4.55 \cdot 10^{-1}$	± 3.1	$+0.8$ -1.3	$+0.1$ -0.1	-1.0	-0.4	$+0.0$ -0.0	$+0.6$ -0.6	$+0.0$ -0.4	
800	0.130	$3.63 \cdot 10^{-1}$	± 3.4	$+2.1$ -0.6	$+0.1$ -0.1	+1.9	+0.7	$+0.0$ -0.0	$+0.5$ -0.5	$+0.1$ -0.0	
800	0.250	$2.42 \cdot 10^{-1}$	± 3.9	$+3.4$ -1.0	$+0.2$ -0.1	+2.4	+2.1	$+0.1$ -0.0	$+0.5$ -0.5	$+1.0$ -0.7	
1200	0.014	$8.57 \cdot 10^{-1}$	± 3.2	$+7.0$ -2.7	$+0.2$ -0.5	+6.8	-1.2	$+0.1$ -0.0	$+1.1$ -1.1	$+0.0$ -1.2	
1200	0.021	$7.60 \cdot 10^{-1}$	± 3.0	$+1.6$ -1.3	$+0.0$ -0.0	+0.7	+0.3	$+0.0$ -0.1	$+1.1$ -1.1	$+0.6$ -0.5	
1200	0.032	$6.41 \cdot 10^{-1}$	± 3.0	$+0.8$ -1.3	$+0.1$ -0.2	-0.1	-0.7	$+0.0$ -0.1	$+0.7$ -0.7	$+0.4$ -0.4	
1200	0.050	$5.30 \cdot 10^{-1}$	± 2.7	$+1.5$ -0.6	$+0.2$ -0.1	+1.2	+0.0	$+0.0$ -0.0	$+0.6$ -0.6	$+0.6$ -0.1	
1200	0.080	$4.37 \cdot 10^{-1}$	± 2.9	$+1.0$ -0.7	$+0.2$ -0.2	+0.8	+0.1	$+0.0$ -0.0	$+0.6$ -0.6	$+0.0$ -0.1	
1200	0.130	$3.65 \cdot 10^{-1}$	± 3.0	$+1.1$ -0.8	$+0.1$ -0.1	+0.6	+0.3	$+0.0$ -0.0	$+0.5$ -0.5	$+0.5$ -0.0	
1200	0.250	$2.60 \cdot 10^{-1}$	± 3.3	$+0.8$ -0.7	$+0.2$ -0.1	-0.1	-0.4	$+0.0$ -0.0	$+0.5$ -0.5	$+0.2$ -0.0	
1200	0.400	$1.33 \cdot 10^{-1}$	± 5.2	$+1.3$ -0.9	$+0.0$ -0.2	+0.8	-0.1	$+0.0$ -0.2	$+0.4$ -0.4	$+0.2$ -0.3	
1500	0.021	$7.48 \cdot 10^{-1}$	± 4.3	$+8.9$ -1.7	$+0.2$ -0.0	+8.7	+1.3	$+0.1$ -0.0	$+1.2$ -1.1	$+0.0$ -0.1	
1500	0.032	$5.84 \cdot 10^{-1}$	± 4.2	$+6.8$ -0.9	$+0.0$ -0.1	+6.7	+0.3	$+0.1$ -0.0	$+0.9$ -0.9	$+0.6$ -0.0	
1500	0.050	$5.62 \cdot 10^{-1}$	± 3.5	$+0.9$ -1.9	$+0.1$ -0.1	-1.2	-1.2	$+0.0$ -0.0	$+0.6$ -0.6	$+0.4$ -0.1	
1500	0.080	$4.58 \cdot 10^{-1}$	± 3.6	$+1.0$ -0.9	$+0.2$ -0.2	+0.6	+0.4	$+0.0$ -0.0	$+0.6$ -0.6	$+0.2$ -0.3	
1500	0.130	$3.87 \cdot 10^{-1}$	± 4.3	$+0.7$ -1.4	$+0.2$ -0.2	-0.5	-0.5	$+0.0$ -0.1	$+0.6$ -0.6	$+0.0$ -1.1	
1500	0.180	$3.29 \cdot 10^{-1}$	± 4.5	$+1.0$ -0.8	$+0.1$ -0.2	+0.5	+0.3	$+0.0$ -0.1	$+0.5$ -0.5	$+0.5$ -0.4	
1500	0.250	$2.49 \cdot 10^{-1}$	± 5.6	$+1.8$ -0.7	$+0.3$ -0.1	+0.2	+1.0	$+0.1$ -0.0	$+0.5$ -0.5	$+1.0$ -0.0	
1500	0.400	$1.15 \cdot 10^{-1}$	± 8.4	$+1.5$ -3.5	$+0.1$ -0.3	-2.2	-2.2	$+0.0$ -0.2	$+0.4$ -0.4	$+0.6$ -0.6	
Reduced Cross Sections for Positive Polarisation							Continued on next page				

Table H.3 – continued from previous page

Q_c^2 [GeV ²]	x_c	$\tilde{\sigma}$	stat.	syst.	δ_1	δ_2	δ_3	δ_4	δ_5	δ_6
2000	0.032	$5.83 \cdot 10^{-1}$	± 5.1	$+10.7$ -1.7	$+0.1$ -0.0	+10.3	+1.1	$+0.0$ -0.0	$+1.1$ -1.1	$+0.9$ -0.4
2000	0.050	$5.20 \cdot 10^{-1}$	± 4.6	$+1.3$ -2.1	$+0.3$ -0.0	-1.9	+0.2	$+0.2$ -0.0	$+0.7$ -0.7	$+0.9$ -0.2
2000	0.080	$5.03 \cdot 10^{-1}$	± 4.1	$+0.7$ -1.0	$+0.1$ -0.1	-0.1	-0.6	$+0.0$ -0.0	$+0.6$ -0.6	$+0.3$ -0.4
2000	0.130	$3.56 \cdot 10^{-1}$	± 5.3	$+1.0$ -1.3	$+0.2$ -0.1	-0.0	+0.6	$+0.0$ -0.0	$+0.6$ -0.6	$+0.3$ -0.0
2000	0.180	$2.75 \cdot 10^{-1}$	± 5.8	$+0.6$ -2.2	$+0.1$ -0.1	+0.1	-1.2	$+0.0$ -0.1	$+0.5$ -0.5	$+0.0$ -0.4
2000	0.250	$2.55 \cdot 10^{-1}$	± 6.5	$+1.0$ -2.6	$+0.2$ -0.1	+0.7	-2.0	$+0.0$ -0.0	$+0.5$ -0.5	$+0.0$ -1.4
2000	0.400	$1.20 \cdot 10^{-1}$	± 9.7	$+5.5$ -0.9	$+0.2$ -0.2	+5.3	-0.4	$+0.0$ -0.1	$+0.5$ -0.5	$+0.0$ -0.5
3000	0.050	$5.02 \cdot 10^{-1}$	± 5.9	$+1.7$ -2.1	$+0.0$ -0.3	+0.2	-1.4	$+0.0$ -0.0	$+0.9$ -0.9	$+1.2$ -0.5
3000	0.080	$4.32 \cdot 10^{-1}$	± 5.5	$+1.9$ -1.1	$+0.1$ -0.1	+1.7	-0.3	$+0.0$ -0.0	$+0.6$ -0.6	$+0.3$ -0.0
3000	0.130	$3.80 \cdot 10^{-1}$	± 6.1	$+2.0$ -1.5	$+0.1$ -0.1	-0.7	+1.8	$+0.0$ -0.0	$+0.6$ -0.6	$+0.0$ -1.1
3000	0.180	$2.96 \cdot 10^{-1}$	± 6.7	$+2.4$ -1.1	$+0.2$ -0.1	+0.4	+2.3	$+0.1$ -0.0	$+0.6$ -0.6	$+0.0$ -0.7
3000	0.250	$2.67 \cdot 10^{-1}$	± 7.4	$+0.6$ -1.4	$+0.0$ -0.2	+0.3	-0.3	$+0.0$ -0.1	$+0.5$ -0.5	$+0.0$ -1.2
3000	0.400	$1.15 \cdot 10^{-1}$	± 12.0	$+2.3$ -4.1	$+0.1$ -0.4	+2.2	-3.6	$+0.1$ -0.1	$+0.5$ -0.5	$+0.0$ -1.3
3000	0.650	$1.53 \cdot 10^{-2}$	± 27.7	$+9.8$ -2.5	$+0.1$ -0.3	+1.4	+1.5	$+0.0$ -0.3	$+0.4$ -0.4	$+1.5$ -2.4
5000	0.080	$4.49 \cdot 10^{-1}$	± 5.0	$+2.4$ -1.1	$+0.2$ -0.1	+1.9	+0.5	$+0.1$ -0.0	$+0.8$ -0.8	$+0.0$ -0.4
5000	0.130	$3.70 \cdot 10^{-1}$	± 6.7	$+1.3$ -1.7	$+0.2$ -0.1	+1.0	-1.1	$+0.1$ -0.0	$+0.6$ -0.6	$+0.0$ -0.9
5000	0.180	$3.24 \cdot 10^{-1}$	± 6.7	$+0.9$ -2.1	$+0.0$ -0.1	-1.8	+0.7	$+0.0$ -0.1	$+0.6$ -0.6	$+0.0$ -0.3
5000	0.250	$2.35 \cdot 10^{-1}$	± 8.2	$+1.0$ -2.0	$+0.3$ -0.1	+0.5	+0.1	$+0.1$ -0.0	$+0.5$ -0.5	$+0.5$ -1.5
5000	0.400	$1.50 \cdot 10^{-1}$	± 10.7	$+1.6$ -1.7	$+0.0$ -0.4	+0.8	-1.4	$+0.0$ -0.3	$+0.5$ -0.5	$+1.1$ -0.0
8000	0.130	$3.38 \cdot 10^{-1}$	± 7.6	$+3.4$ -3.9	$+0.1$ -0.2	+2.2	+2.2	$+0.0$ -0.0	$+0.7$ -0.7	$+1.0$ -3.4
8000	0.180	$2.32 \cdot 10^{-1}$	± 10.7	$+1.6$ -4.1	$+0.1$ -0.1	+1.0	-3.9	$+0.0$ -0.1	$+0.6$ -0.6	$+0.0$ -1.0
8000	0.250	$2.47 \cdot 10^{-1}$	± 10.6	$+1.5$ -4.4	$+0.1$ -0.2	-0.9	-3.6	$+0.0$ -0.0	$+0.6$ -0.6	$+0.1$ -0.0
8000	0.400	$1.11 \cdot 10^{-1}$	± 15.6	$+5.1$ -3.3	$+0.3$ -0.2	+3.4	-2.3	$+0.0$ -0.0	$+0.5$ -0.5	$+3.2$ -0.0
8000	0.650	$1.86 \cdot 10^{-2}$	± 31.6	$+11.3$ -10.2	$+0.0$ -0.2	+0.6	+5.0	$+0.0$ -0.3	$+0.5$ -0.5	$+2.0$ -3.3
12000	0.180	$2.16 \cdot 10^{-1}$	± 12.7	$+3.5$ -6.3	$+0.2$ -0.2	-5.1	+1.6	$+0.1$ -0.0	$+0.7$ -0.7	$+0.0$ -1.4
12000	0.250	$1.91 \cdot 10^{-1}$	± 15.8	$+2.1$ -7.0	$+0.2$ -0.1	+0.3	-2.9	$+0.1$ -0.1	$+0.6$ -0.6	$+0.0$ -6.2
12000	0.400	$1.51 \cdot 10^{-1}$	± 17.4	$+2.0$ -5.9	$+0.0$ -0.4	+1.1	-4.0	$+0.0$ -0.3	$+0.6$ -0.5	$+1.2$ -1.4
20000	0.250	$1.35 \cdot 10^{-1}$	± 22.9	$+10.2$ -2.0	$+0.2$ -0.2	+5.9	-1.1	$+0.0$ -0.0	$+0.6$ -0.6	$+2.0$ -1.4
20000	0.400	$5.89 \cdot 10^{-2}$	± 35.4	$+10.4$ -9.3	$+0.2$ -0.2	+1.6	-0.6	$+0.1$ -0.0	$+0.6$ -0.6	$+10.2$ -0.0
30000	0.400	$5.97 \cdot 10^{-2}$	± 44.7	$+2.9$ -68.3	$+0.4$ -0.2	-66.6	-7.0	$+0.3$ -0.0	$+0.6$ -0.6	$+2.2$ -2.4

Table H.3: Reduced Cross Sections for Positive Polarisation

Table H.4: The measured reduced cross section $\tilde{\sigma}$ for the reaction $e^+p \rightarrow e^+X$ ($\mathcal{L} = 135.5 \text{ pb}^{-1}$, $P_e = -0.36$). The bin centres, Q_c^2 and x_c , the cross section corrected to the electroweak Born level and the statistical and the systematic uncertainty (in %) are given. In addition the contributions of the variation of the electron energy scale (δ_1), the variation of the electron identification (δ_2), the variation of the parton shower model (δ_3), the variation of the track requirement region (δ_4), the variation of the Track Veto Efficiency correction (δ_5) and the variation of the $E - p_z$ cut (δ_6) to the systematic uncertainty are shown. All uncertainties are given in %.

Q_c^2 [GeV ²]	x_c	$\tilde{\sigma}$	stat.	syst.	δ_1	δ_2	δ_3	δ_4	δ_5	δ_6
200	0.005	1.09	± 1.4	$^{+2.1}_{-1.8}$	$^{+0.1}_{-0.1}$	+1.7	-1.0	$^{+1.2}_{-1.4}$	$^{+0.0}_{-0.0}$	$^{+0.0}_{-0.1}$
200	0.008	$9.46 \cdot 10^{-1}$	± 1.2	$^{+0.7}_{-2.5}$	$^{+0.0}_{-0.0}$	+0.6	-1.4	$^{+0.0}_{-2.0}$	$^{+0.0}_{-0.0}$	$^{+0.0}_{-0.0}$
200	0.013	$8.06 \cdot 10^{-1}$	± 1.2	$^{+0.3}_{-1.8}$	$^{+0.1}_{-0.0}$	+0.2	-0.8	$^{+0.1}_{-1.6}$	$^{+0.0}_{-0.0}$	$^{+0.0}_{-0.0}$
200	0.021	$6.77 \cdot 10^{-1}$	± 1.5	$^{+0.8}_{-0.6}$	$^{+0.2}_{-0.0}$	-0.5	+0.7	$^{+0.2}_{-0.0}$	$^{+0.0}_{-0.0}$	$^{+0.1}_{-0.1}$
200	0.032	$5.69 \cdot 10^{-1}$	± 1.6	$^{+2.6}_{-0.3}$	$^{+0.1}_{-0.1}$	-0.2	+2.6	$^{+0.1}_{-0.0}$	$^{+0.0}_{-0.0}$	$^{+0.1}_{-0.1}$
200	0.050	$5.09 \cdot 10^{-1}$	± 1.5	$^{+2.2}_{-0.3}$	$^{+0.2}_{-0.1}$	+0.4	+2.2	$^{+0.0}_{-0.2}$	$^{+0.0}_{-0.0}$	$^{+0.0}_{-0.2}$
200	0.080	$4.32 \cdot 10^{-1}$	± 1.3	$^{+2.7}_{-0.2}$	$^{+0.1}_{-0.1}$	-0.0	+2.7	$^{+0.1}_{-0.0}$	$^{+0.0}_{-0.0}$	$^{+0.0}_{-0.1}$
200	0.180	$3.46 \cdot 10^{-1}$	± 1.7	$^{+1.6}_{-1.5}$	$^{+0.1}_{-0.1}$	+1.2	-1.0	$^{+1.1}_{-0.0}$	$^{+0.0}_{-0.0}$	$^{+0.0}_{-0.2}$
250	0.008	$9.15 \cdot 10^{-1}$	± 1.6	$^{+2.6}_{-0.9}$	$^{+0.0}_{-0.1}$	+1.9	-0.5	$^{+1.6}_{-0.6}$	$^{+0.1}_{-0.1}$	$^{+0.5}_{-0.3}$
250	0.013	$8.20 \cdot 10^{-1}$	± 1.5	$^{+0.5}_{-1.5}$	$^{+0.1}_{-0.0}$	+0.4	-1.1	$^{+0.2}_{-1.0}$	$^{+0.0}_{-0.0}$	$^{+0.0}_{-0.2}$
250	0.021	$6.66 \cdot 10^{-1}$	± 1.8	$^{+1.1}_{-0.8}$	$^{+0.1}_{-0.0}$	+0.9	-0.5	$^{+0.7}_{-0.7}$	$^{+0.0}_{-0.0}$	$^{+0.0}_{-0.2}$
250	0.032	$5.57 \cdot 10^{-1}$	± 1.8	$^{+1.8}_{-1.7}$	$^{+0.1}_{-0.1}$	-0.4	+1.8	$^{+0.0}_{-1.6}$	$^{+0.0}_{-0.0}$	$^{+0.3}_{-0.2}$
250	0.050	$5.13 \cdot 10^{-1}$	± 1.8	$^{+2.7}_{-1.7}$	$^{+0.1}_{-0.1}$	-0.1	+2.7	$^{+0.0}_{-1.7}$	$^{+0.0}_{-0.0}$	$^{+0.0}_{-0.2}$
250	0.080	$4.32 \cdot 10^{-1}$	± 1.5	$^{+2.1}_{-1.2}$	$^{+0.1}_{-0.1}$	-0.0	+2.1	$^{+0.0}_{-0.9}$	$^{+0.0}_{-0.0}$	$^{+0.1}_{-0.8}$
250	0.180	$3.35 \cdot 10^{-1}$	± 1.7	$^{+1.2}_{-2.0}$	$^{+0.1}_{-0.1}$	+1.1	-1.1	$^{+0.1}_{-1.2}$	$^{+0.0}_{-0.0}$	$^{+0.3}_{-0.0}$
350	0.008	$9.29 \cdot 10^{-1}$	± 2.1	$^{+2.8}_{-1.1}$	$^{+0.0}_{-0.2}$	+2.5	+0.9	$^{+0.1}_{-0.0}$	$^{+0.8}_{-0.8}$	$^{+0.0}_{-0.6}$
350	0.013	$7.99 \cdot 10^{-1}$	± 1.9	$^{+1.0}_{-0.7}$	$^{+0.0}_{-0.0}$	-0.2	-0.0	$^{+0.9}_{-0.0}$	$^{+0.1}_{-0.1}$	$^{+0.3}_{-0.6}$
350	0.021	$6.52 \cdot 10^{-1}$	± 2.2	$^{+1.4}_{-0.5}$	$^{+0.2}_{-0.0}$	+1.1	+0.5	$^{+0.5}_{-0.0}$	$^{+0.0}_{-0.0}$	$^{+0.2}_{-0.0}$
350	0.032	$5.76 \cdot 10^{-1}$	± 2.2	$^{+2.3}_{-1.0}$	$^{+0.0}_{-0.1}$	+1.2	-0.1	$^{+2.0}_{-0.1}$	$^{+0.0}_{-0.0}$	$^{+0.0}_{-0.6}$
350	0.050	$4.87 \cdot 10^{-1}$	± 2.2	$^{+2.1}_{-0.7}$	$^{+0.0}_{-0.0}$	+0.7	+1.3	$^{+1.5}_{-0.4}$	$^{+0.0}_{-0.0}$	$^{+0.2}_{-0.0}$
350	0.080	$4.07 \cdot 10^{-1}$	± 1.9	$^{+3.3}_{-0.6}$	$^{+0.1}_{-0.1}$	+0.9	+3.0	$^{+0.7}_{-0.2}$	$^{+0.0}_{-0.0}$	$^{+0.0}_{-0.5}$
350	0.180	$3.10 \cdot 10^{-1}$	± 2.0	$^{+1.4}_{-1.2}$	$^{+0.1}_{-0.1}$	+1.1	+0.6	$^{+0.0}_{-0.7}$	$^{+0.0}_{-0.0}$	$^{+0.0}_{-0.9}$

Reduced Cross Sections for Negative Polarisation

Continued on next page

Table H.4 – continued from previous page

Q_c^2 [GeV ²]	x_c	$\tilde{\sigma}$	stat.	syst.	δ_1	δ_2	δ_3	δ_4	δ_5	δ_6
450	0.008	$9.96 \cdot 10^{-1}$	± 2.4	+2.0 -2.1	+0.4 -0.3	+0.3	-0.0	+0.0 -0.0	+1.8 -1.7	+0.2 -0.0
450	0.013	$8.03 \cdot 10^{-1}$	± 2.7	+1.3 -1.7	+0.1 -0.0	-0.5	-0.0	+0.1 -0.0	+1.2 -1.2	+0.0 -0.7
450	0.021	$6.96 \cdot 10^{-1}$	± 3.0	+1.0 -0.6	+0.2 -0.1	+0.8	+0.5	+0.1 -0.0	+0.3 -0.3	+0.0 -0.4
450	0.032	$5.60 \cdot 10^{-1}$	± 2.9	+2.1 -1.0	+0.2 -0.2	+1.5	+1.4	+0.0 -0.0	+0.1 -0.1	+0.0 -0.3
450	0.050	$5.22 \cdot 10^{-1}$	± 2.6	+2.4 -0.3	+0.1 -0.1	+2.0	+1.3	+0.3 -0.1	+0.1 -0.1	+0.3 -0.2
450	0.080	$4.15 \cdot 10^{-1}$	± 2.7	+1.6 -1.0	+0.1 -0.1	+1.0	-0.0	+1.2 -0.0	+0.1 -0.1	+0.1 -0.4
450	0.130	$3.41 \cdot 10^{-1}$	± 2.9	+3.3 -0.2	+0.2 -0.0	+1.5	+2.1	+1.9 -0.0	+0.0 -0.0	+0.1 -0.0
450	0.250	$2.49 \cdot 10^{-1}$	± 3.1	+4.2 -0.6	+0.1 -0.0	+3.4	-0.0	+1.3 -0.1	+0.0 -0.0	+0.0 -0.2
650	0.013	$8.22 \cdot 10^{-1}$	± 2.5	+3.3 -2.0	+0.1 -0.0	+2.6	-0.7	+0.0 -0.0	+1.8 -1.7	+0.9 -0.1
650	0.021	$6.97 \cdot 10^{-1}$	± 3.1	+1.5 -1.7	+0.1 -0.0	-0.9	-0.0	+0.0 -0.0	+1.4 -1.3	+0.6 -0.0
650	0.032	$5.86 \cdot 10^{-1}$	± 3.5	+2.6 -1.0	+0.2 -0.0	+1.3	+2.0	+0.1 -0.0	+1.0 -1.0	+0.0 -0.1
650	0.050	$5.02 \cdot 10^{-1}$	± 3.5	+1.0 -1.0	+0.2 -0.1	+0.1	+0.2	+0.1 -0.0	+0.7 -0.7	+0.5 -0.2
650	0.080	$4.24 \cdot 10^{-1}$	± 3.7	+0.5 -1.3	+0.1 -0.1	-0.3	+0.1	+0.1 -0.0	+0.4 -0.4	+0.0 -0.1
650	0.130	$3.57 \cdot 10^{-1}$	± 3.8	+2.8 -0.4	+0.2 -0.1	+0.5	+2.5	+0.0 -0.0	+0.3 -0.3	+0.9 -0.0
650	0.250	$2.30 \cdot 10^{-1}$	± 4.2	+1.2 -0.8	+0.2 -0.1	+0.8	+0.4	+0.1 -0.0	+0.2 -0.2	+0.8 -0.0
800	0.013	$7.88 \cdot 10^{-1}$	± 3.2	+4.4 -2.0	+0.4 -0.0	+3.8	+0.5	+0.1 -0.0	+1.8 -1.7	+0.2 -0.0
800	0.021	$7.36 \cdot 10^{-1}$	± 3.7	+1.6 -2.4	+0.1 -0.0	-1.5	-0.3	+0.0 -0.0	+1.5 -1.5	+0.1 -0.1
800	0.032	$6.20 \cdot 10^{-1}$	± 3.7	+1.7 -1.3	+0.0 -0.1	+0.9	-0.4	+0.0 -0.0	+1.2 -1.2	+0.7 -0.0
800	0.050	$4.89 \cdot 10^{-1}$	± 3.6	+2.6 -1.4	+0.2 -0.1	+1.5	+1.7	+0.0 -0.0	+1.0 -1.0	+0.7 -0.1
800	0.080	$4.56 \cdot 10^{-1}$	± 3.7	+1.1 -1.1	+0.1 -0.1	+0.6	-0.4	+0.0 -0.0	+0.9 -0.8	+0.1 -0.2
800	0.130	$3.21 \cdot 10^{-1}$	± 4.3	+1.4 -0.9	+0.1 -0.2	+0.9	+0.6	+0.0 -0.0	+0.8 -0.8	+0.3 -0.0
800	0.250	$2.43 \cdot 10^{-1}$	± 4.6	+3.1 -1.1	+0.2 -0.1	+2.1	+2.0	+0.1 -0.0	+0.7 -0.7	+0.1 -0.3
1200	0.014	$7.72 \cdot 10^{-1}$	± 4.1	+9.9 -3.1	+0.2 -0.5	+9.6	-1.2	+0.1 -0.0	+1.7 -1.7	+0.7 -0.2
1200	0.021	$7.14 \cdot 10^{-1}$	± 3.7	+2.5 -1.9	+0.1 -0.0	+1.0	+0.3	+0.0 -0.1	+1.7 -1.7	+1.1 -0.7
1200	0.032	$6.07 \cdot 10^{-1}$	± 3.7	+1.6 -1.6	+0.1 -0.2	+0.8	-0.7	+0.0 -0.1	+1.3 -1.3	+0.4 -0.0
1200	0.050	$4.90 \cdot 10^{-1}$	± 3.4	+1.5 -1.2	+0.2 -0.1	+1.0	+0.1	+0.0 -0.0	+1.1 -1.0	+0.1 -0.1
1200	0.080	$4.06 \cdot 10^{-1}$	± 3.5	+1.5 -1.0	+0.2 -0.2	+1.0	+0.1	+0.0 -0.0	+0.9 -0.9	+0.4 -0.1
1200	0.130	$3.36 \cdot 10^{-1}$	± 3.7	+0.9 -1.1	+0.1 -0.1	-0.6	+0.4	+0.0 -0.0	+0.8 -0.8	+0.3 -0.1
1200	0.250	$2.31 \cdot 10^{-1}$	± 4.2	+1.0 -0.8	+0.2 -0.1	+0.4	-0.3	+0.0 -0.0	+0.7 -0.7	+0.3 -0.0
1200	0.400	$1.26 \cdot 10^{-1}$	± 6.3	+1.3 -2.4	+0.0 -0.3	-0.4	-0.1	+0.0 -0.2	+0.7 -0.7	+1.0 -0.0
1500	0.021	$7.00 \cdot 10^{-1}$	± 5.3	+8.9 -2.8	+0.2 -0.0	+8.6	+1.3	+0.1 -0.0	+1.8 -1.7	+0.0 -0.8
1500	0.032	$5.85 \cdot 10^{-1}$	± 5.0	+1.9 -1.8	+0.0 -0.1	+0.5	+0.4	+0.1 -0.0	+1.5 -1.5	+0.1 -0.6
1500	0.050	$4.94 \cdot 10^{-1}$	± 4.5	+1.4 -1.7	+0.1 -0.1	+0.0	-1.2	+0.0 -0.0	+1.2 -1.1	+0.4 -0.0
1500	0.080	$4.34 \cdot 10^{-1}$	± 4.4	+1.1 -1.3	+0.2 -0.2	-0.3	+0.4	+0.0 -0.0	+1.0 -0.9	+0.0 -0.3
1500	0.130	$3.55 \cdot 10^{-1}$	± 5.3	+1.5 -1.3	+0.2 -0.2	+0.9	-0.5	+0.0 -0.1	+0.8 -0.8	+0.6 -0.5
1500	0.180	$2.74 \cdot 10^{-1}$	± 5.9	+1.4 -0.9	+0.1 -0.2	+0.4	+0.3	+0.0 -0.1	+0.8 -0.8	+0.5 -0.0
1500	0.250	$2.35 \cdot 10^{-1}$	± 6.9	+2.0 -1.3	+0.3 -0.1	+1.0	+1.0	+0.1 -0.0	+0.7 -0.7	+0.4 -1.1
1500	0.400	$1.26 \cdot 10^{-1}$	± 9.6	+2.7 -3.4	+0.1 -0.3	+0.4	-2.3	+0.0 -0.2	+0.7 -0.7	+1.6 -0.0

Reduced Cross Sections for Negative Polarisation

Continued on next page

Table H.4 – continued from previous page

Q_c^2 [GeV ²]	x_c	$\tilde{\sigma}$	stat.	syst.	δ_1	δ_2	δ_3	δ_4	δ_5	δ_6
2000	0.032	$6.11 \cdot 10^{-1}$	± 5.9	+4.1 -2.4	+0.1 -0.0	+3.3	+1.0	+0.0 -0.0	+1.8 -1.7	+0.6 -1.1
2000	0.050	$4.61 \cdot 10^{-1}$	± 5.8	+5.6 -1.4	+0.4 -0.0	+5.4	+0.2	+0.2 -0.0	+1.3 -1.3	+0.1 -0.0
2000	0.080	$4.39 \cdot 10^{-1}$	± 5.3	+1.3 -1.7	+0.1 -0.1	-1.1	-0.6	+0.0 -0.0	+1.0 -1.0	+0.7 -0.0
2000	0.130	$3.51 \cdot 10^{-1}$	± 6.3	+2.9 -1.1	+0.2 -0.1	+2.6	+0.6	+0.0 -0.0	+0.9 -0.9	+0.3 -0.5
2000	0.180	$2.72 \cdot 10^{-1}$	± 7.0	+2.5 -1.6	+0.1 -0.1	+2.1	-1.3	+0.0 -0.1	+0.8 -0.8	+1.0 -0.5
2000	0.250	$2.41 \cdot 10^{-1}$	± 8.0	+1.6 -2.4	+0.2 -0.1	+0.7	-2.1	+0.0 -0.0	+0.7 -0.7	+1.0 -0.0
2000	0.400	$1.18 \cdot 10^{-1}$	± 11.7	+1.4 -3.6	+0.2 -0.2	-3.5	-0.4	+0.0 -0.1	+0.7 -0.7	+0.0 -0.0
3000	0.050	$5.16 \cdot 10^{-1}$	± 6.9	+1.8 -2.3	+0.0 -0.3	-0.4	-1.4	+0.0 -0.0	+1.5 -1.5	+0.8 -0.0
3000	0.080	$4.28 \cdot 10^{-1}$	± 6.5	+1.4 -3.6	+0.1 -0.1	-3.3	-0.4	+0.0 -0.0	+1.1 -1.1	+0.0 -0.5
3000	0.130	$3.50 \cdot 10^{-1}$	± 7.5	+2.3 -1.9	+0.1 -0.1	-1.5	+1.8	+0.0 -0.0	+0.9 -0.9	+1.1 -0.0
3000	0.180	$2.45 \cdot 10^{-1}$	± 8.7	+2.6 -3.8	+0.2 -0.0	+0.4	+2.2	+0.1 -0.0	+0.8 -0.8	+1.0 -3.5
3000	0.250	$2.20 \cdot 10^{-1}$	± 9.8	+1.5 -4.5	+0.0 -0.2	-4.0	-0.3	+0.0 -0.1	+0.8 -0.7	+1.1 -1.1
3000	0.400	$1.34 \cdot 10^{-1}$	± 13.2	+4.8 -4.2	+0.1 -0.4	+4.3	-3.6	+0.1 -0.1	+0.7 -0.7	+1.6 -2.0
3000	0.650	$1.35 \cdot 10^{-2}$	± 35.4	+6.7 -2.5	+0.1 -0.2	+1.4	+1.2	+0.0 -0.2	+0.7 -0.7	+1.5 -2.4
5000	0.080	$3.50 \cdot 10^{-1}$	± 6.7	+3.0 -2.8	+0.2 -0.1	+2.5	+0.5	+0.1 -0.0	+1.4 -1.4	+0.2 -0.9
5000	0.130	$2.75 \cdot 10^{-1}$	± 9.1	+1.7 -4.4	+0.2 -0.1	-4.1	-0.9	+0.1 -0.0	+1.0 -1.0	+0.7 -0.0
5000	0.180	$2.33 \cdot 10^{-1}$	± 9.4	+1.4 -2.7	+0.0 -0.1	-1.4	+0.5	+0.0 -0.1	+0.9 -0.9	+0.8 -0.0
5000	0.250	$1.90 \cdot 10^{-1}$	± 10.8	+2.2 -1.4	+0.3 -0.1	+1.2	+0.2	+0.2 -0.0	+0.8 -0.8	+1.3 -0.0
5000	0.400	$1.19 \cdot 10^{-1}$	± 14.3	+1.7 -2.3	+0.0 -0.4	+0.8	-1.4	+0.0 -0.3	+0.7 -0.7	+1.2 -0.0
8000	0.130	$2.80 \cdot 10^{-1}$	± 9.8	+4.6 -2.3	+0.1 -0.2	+3.6	+2.2	+0.0 -0.0	+1.3 -1.3	+0.0 -0.3
8000	0.180	$2.65 \cdot 10^{-1}$	± 11.8	+1.0 -6.7	+0.1 -0.1	-4.6	-4.0	+0.0 -0.1	+1.0 -0.9	+0.0 -1.7
8000	0.250	$1.83 \cdot 10^{-1}$	± 14.6	+3.1 -3.8	+0.1 -0.2	-0.8	-3.6	+0.0 -0.0	+0.8 -0.8	+1.2 -0.0
8000	0.400	$9.67 \cdot 10^{-2}$	± 20.0	+2.6 -4.9	+0.4 -0.2	-3.3	-2.4	+0.0 -0.0	+0.8 -0.8	+2.3 -2.5
8000	0.650	$1.33 \cdot 10^{-2}$	± 44.7	+21.3 -18.4	+0.0 -0.2	+20.7	+5.1	+0.0 -0.3	+0.7 -0.7	+0.0 -18.4
12000	0.180	$1.64 \cdot 10^{-1}$	± 17.1	+4.3 -3.6	+0.2 -0.2	+2.9	+1.7	+0.1 -0.0	+1.2 -1.2	+0.0 -1.2
12000	0.250	$1.07 \cdot 10^{-1}$	± 25.0	+2.3 -3.6	+0.2 -0.1	-1.0	-3.0	+0.0 -0.1	+0.9 -0.9	+1.4 -1.2
12000	0.400	$6.53 \cdot 10^{-2}$	± 31.6	+16.3 -4.1	+0.1 -0.4	+1.2	-4.0	+0.0 -0.3	+0.8 -0.8	+8.5 -0.0
20000	0.250	$1.85 \cdot 10^{-1}$	± 22.9	+9.0 -15.0	+0.2 -0.3	-12.5	-1.2	+0.0 -0.0	+1.2 -1.1	+3.8 -0.0
20000	0.400	$7.32 \cdot 10^{-2}$	± 37.8	+12.8 -36.1	+0.3 -0.2	-27.5	-0.7	+0.1 -0.0	+0.9 -0.9	+0.0 -12.4
30000	0.400	$6.69 \cdot 10^{-2}$	± 50.0	+25.8 -8.2	+0.4 -0.2	+24.3	-7.1	+0.3 -0.0	+1.1 -1.0	+2.3 -2.4

Table H.4: Reduced Cross Sections for Negative Polarisation

Q_c^2 [GeV ²]	x_c	$x\tilde{F}_3$	stat.	syst.
1500	0.021	0.02	± 0.02	$+0.02$ -0.03
1500	0.032	0.04	± 0.02	$+0.00$ -0.01
1500	0.050	-0.01	± 0.03	$+0.01$ -0.00
1500	0.080	0.08	± 0.04	$+0.01$ -0.01
1500	0.130	0.02	± 0.07	$+0.04$ -0.04
1500	0.180	0.04	± 0.09	$+0.04$ -0.03
1500	0.250	0.18	± 0.12	$+0.04$ -0.04
1500	0.400	0.12	± 0.14	$+0.20$ -0.11
2000	0.032	0.03	± 0.02	$+0.02$ -0.02
2000	0.050	0.08	± 0.03	$+0.00$ -0.00
2000	0.080	-0.03	± 0.04	$+0.02$ -0.02
2000	0.130	0.07	± 0.06	$+0.00$ -0.00
2000	0.180	0.16	± 0.07	$+0.00$ -0.03
2000	0.250	-0.01	± 0.10	$+0.00$ -0.00
2000	0.400	0.01	± 0.12	$+0.02$ -0.05
3000	0.050	0.05	± 0.02	$+0.01$ -0.00
3000	0.080	0.09	± 0.03	$+0.00$ -0.00
3000	0.130	0.03	± 0.05	$+0.00$ -0.00
3000	0.180	0.13	± 0.06	$+0.00$ -0.00
3000	0.250	0.16	± 0.08	$+0.12$ -0.12
3000	0.400	0.08	± 0.10	$+0.02$ -0.02
3000	0.650	0.03	± 0.04	$+0.02$ -0.02
5000	0.080	0.08	± 0.02	$+0.01$ -0.00
5000	0.130	0.15	± 0.03	$+0.00$ -0.00
5000	0.180	0.09	± 0.03	$+0.00$ -0.00
5000	0.250	0.07	± 0.05	$+0.00$ -0.00
5000	0.400	0.02	± 0.06	$+0.05$ -0.05
8000	0.130	0.17	± 0.02	$+0.00$ -0.01
8000	0.180	0.18	± 0.03	$+0.02$ -0.02
8000	0.250	0.12	± 0.04	$+0.02$ -0.02
8000	0.400	0.02	± 0.04	$+0.02$ -0.02
8000	0.650	0.01	± 0.02	$+0.00$ -0.00
12000	0.180	0.17	± 0.02	$+0.00$ -0.02
12000	0.250	0.18	± 0.03	$+0.01$ -0.01
12000	0.400	0.06	± 0.04	$+0.01$ -0.00
20000	0.250	0.17	± 0.03	$+0.03$ -0.02
20000	0.400	0.10	± 0.03	$+0.01$ -0.01
30000	0.400	0.10	± 0.03	$+0.02$ -0.02

Table H.5: The structure function $x\tilde{F}_3$. The bin centres, Q_c^2 and x_c , $x\tilde{F}_3$ and the statistical and the systematic uncertainty (in absolute values) are given.

x_c	$xF_3^{\gamma Z}$	stat.	syst.
0.021	0.26	± 0.06	$^{+0.19}_{-0.16}$
0.032	0.19	± 0.05	$^{+0.12}_{-0.12}$
0.050	0.35	± 0.04	$^{+0.08}_{-0.08}$
0.080	0.33	± 0.03	$^{+0.05}_{-0.04}$
0.130	0.51	± 0.03	$^{+0.04}_{-0.05}$
0.180	0.46	± 0.02	$^{+0.04}_{-0.05}$
0.250	0.39	± 0.02	$^{+0.04}_{-0.05}$
0.400	0.21	± 0.02	$^{+0.04}_{-0.04}$

Table H.6: The interference structure function $xF_3^{\gamma Z}$ evaluated at $Q^2 = 1500 \text{ GeV}^2$. The bin centre x_c , $xF_3^{\gamma Z}$ and the statistical and the systematic uncertainty (in absolute values) are given.

Bibliography

- [1] H. Diels, Die Fragmente der Vorsokratiker, Vol. 2, Weidmannsche Verlagsbuchhandlung, 1952, edited by Walther Kranz.
- [2] B. K. Matilal, Nyāya-Vaiśeṣika, in: J. Gonda (Ed.), A history of Indian literature, Vol. 6/2, 1977, pp. 53–126.
- [3] J. Perrin, Brownian movement and molecular reality, Taylor and Francis, London, United Kingdom, 1910, translated from Ann. Chim. Phys. 18 (8me Serie), 5–114 (1909).
- [4] E. Rutherford, The scattering of alpha and beta particles by matter and the structure of the atom, Phil.Mag. 21 (1911) 669–688.
- [5] E. Rutherford, Collision of Alpha Particles with Light Atoms I. Hydrogen, Phil.Mag. 37 (1919) 537–561.
- [6] F. Abe, et al., Evidence for top quark production in $\bar{p}p$ collisions at $\sqrt{s} = 1.8$ TeV, Phys.Rev. D50 (1994) 2966–3026.
doi:10.1103/PhysRevD.50.2966.
- [7] K. Kodama, et al., Observation of tau neutrino interactions, Phys.Lett. B504 (2001) 218–224.
arXiv:hep-ex/0012035, doi:10.1016/S0370-2693(01)00307-0.
URL http://www.fnal.gov/pub/presspass/press_releases/donut.html
- [8] S. Chekanov, et al., Measurement of high- Q^2 neutral current deep inelastic e^-p scattering cross sections with a longitudinally polarised electron beam at HERA, Eur. Phys. J. C62 (2009) 625–658.
arXiv:0901.2385, doi:10.1140/epjc/s10052-009-1055-6.
- [9] S. L. Glashow, Partial Symmetries of Weak Interactions, Nucl. Phys. 22 (1961) 579–588.
doi:10.1016/0029-5582(61)90469-2.
- [10] S. Weinberg, A Model of Leptons, Phys. Rev. Lett. 19 (1967) 1264–1266.
doi:10.1103/PhysRevLett.19.1264.
- [11] D. H. Perkins, Introduction to high energy physics, Cambridge Univ. Press, Cambridge, UK, 2000.
- [12] E. Lohrmann, Hochenergiephysik, Teubner, Stuttgart, Germany, 2005.
- [13] M. Breidenbach, et al., Observed Behavior of Highly Inelastic electron-Proton Scattering, Phys. Rev. Lett. 23 (1969) 935–939.
doi:10.1103/PhysRevLett.23.935.
- [14] E. D. Bloom, et al., High-Energy Inelastic $e p$ Scattering at 6-Degrees and 10-Degrees, Phys. Rev. Lett. 23 (1969) 930–934.

- doi:10.1103/PhysRevLett.23.930.
- [15] J. D. Bjorken, Asymptotic Sum Rules at Infinite Momentum, *Phys. Rev.* 179 (1969) 1547–1553.
doi:10.1103/PhysRev.179.1547.
- [16] R. P. Feynman, Very high-energy collisions of hadrons, *Phys. Rev. Lett.* 23 (1969) 1415–1417.
doi:10.1103/PhysRevLett.23.1415.
- [17] M. Gell-Mann, A schematic model of baryons and mesons, *Phys.Lett.* 8 (1964) 214–215.
doi:10.1016/S0031-9163(64)92001-3.
- [18] G. Zweig, An $su(3)$ model for strong interaction symmetry and its breaking. 2, Ph.D. thesis, CERN, CERN-TH-412 (1964).
- [19] T. Eichten, et al., Measurement of the neutrino - nucleon anti-neutrino - nucleon total cross-sections, *Phys. Lett.* B46 (1973) 274–280.
doi:10.1016/0370-2693(73)90702-8.
- [20] H. Fritzsch, M. Gell-Mann, H. Leutwyler, Advantages of the color octet gluon picture, *Phys. Lett.* B47 (1973) 365–368.
- [21] K. Nakamura, et al., Review of particle physics, *J. Phys.* G37 (2010) 075021.
doi:10.1088/0954-3899/37/7A/075021.
- [22] R. Brandelik, et al., Evidence for Planar Events in $e^+ e^-$ Annihilation at High-Energies, *Phys. Lett.* B86 (1979) 243.
doi:10.1016/0370-2693(79)90830-X.
- [23] C. Berger, et al., Evidence for Gluon Bremsstrahlung in $e^+ e^-$ Annihilations at High-Energies, *Phys. Lett.* B86 (1979) 418.
doi:10.1016/0370-2693(79)90869-4.
- [24] D. P. Barber, et al., Discovery of Three Jet Events and a Test of Quantum Chromodynamics at PETRA Energies, *Phys. Rev. Lett.* 43 (1979) 830.
doi:10.1103/PhysRevLett.43.830.
- [25] W. Bartel, et al., Search for narrow resonances in $e^+ e^-$ annihilation at c.m. energies between 29.90-GeV and 31.46-GeV, *Phys. Lett.* B91 (1980) 152.
doi:10.1016/0370-2693(80)90682-6.
- [26] G. 't Hooft, M. Veltman, Regularization and renormalization of gauge fields, *Nucl.Phys.* B44 (1972) 189–213.
doi:10.1016/0550-3213(72)90279-9.
- [27] R. Devenish, A. Cooper-Sarkar, Deep inelastic scattering, Oxford Univ. Press, Oxford, UK, 2004.
- [28] J. Blumlein, Λ_{QCD} and $\alpha_s(M_Z^2)$ from DIS Structure Functions, in: G. Grindhammer, K. Sachs (Eds.), Proceedings to the 15th International Workshop on Deep-Inelastic Scattering and Related Subjects (DIS 2007), April 16-20, 2007 Munich, Germany, Vol. 1 of Progress in High Energy Physics, SciWiPub, 2007, pp. 1099–1101.
arXiv:0706.2430, doi:10.3360/dis.2007.212.

- [29] G. Altarelli, Partons in Quantum Chromodynamics, Phys. Rept. 81 (1982) 1.
doi:10.1016/0370-1573(82)90127-2.
- [30] F. D. Aaron, et al., Combined Measurement and QCD Analysis of the Inclusive ep Scattering Cross Sections at HERA, JHEP 01 (2010) 109.
arXiv:0911.0884, doi:10.1007/JHEP01(2010)109.
- [31] A. Aktas, et al., A determination of electroweak parameters at HERA, Phys. Lett. B632 (2006) 35–42.
arXiv:hep-ex/0507080, doi:10.1016/j.physletb.2005.10.035.
- [32] H. Abramowicz, et al., HERA Combined Results, h1ZEUS combined webpage, last visited 09.09.2011.
URL https://www.desy.de/h1zeus/combined_results/
- [33] H. Abramowicz, et al., Combined Measurement of the longitudinal structure function at HERA , H1-prelim-10-043, ZEUS-prel-10-001 (2010).
- [34] H. Abramowicz, et al., QCD NLO analysis of inclusive data (HERAPDF 1.5) , H1prelim-10-142, ZEUS-prel-10-018 (2010).
- [35] H.-L. Lai, et al., New parton distributions for collider physics, Phys. Rev. D82 (2010) 074024.
arXiv:1007.2241, doi:10.1103/PhysRevD.82.074024.
- [36] J. Pumplin, et al., New generation of parton distributions with uncertainties from global QCD analysis, JHEP 07 (2002) 012.
arXiv:hep-ph/0201195.
- [37] A. D. Martin, W. J. Stirling, R. S. Thorne, G. Watt, Parton distributions for the LHC, Eur. Phys. J. C63 (2009) 189–285.
arXiv:0901.0002, doi:10.1140/epjc/s10052-009-1072-5.
- [38] G. Watt, Parton distribution function dependence of benchmark Standard Model total cross sections at the 7 TeV LHC, Ph.D. thesis, CERN, CERN-PH-TH/2011-149 (2011).
arXiv:1106.5788.
- [39] R. D. Ball, et al., A first unbiased global NLO determination of parton distributions and their uncertainties, Nucl. Phys. B838 (2010) 136–206.
arXiv:1002.4407, doi:10.1016/j.nuclphysb.2010.05.008.
- [40] S. Chekanov, et al., An NLO QCD analysis of inclusive cross-section and jet-production data from the ZEUS experiment, Eur. Phys. J. C42 (2005) 1–16.
arXiv:hep-ph/0503274, doi:10.1140/epjc/s2005-02293-x.
- [41] E. Lobodzinska, private communication (2011).
- [42] H. Abramowicz, et al., QCD NLO analysis of inclusive, charm and jet data (HERAPDF 1.7) , ZEUS-prel-11-010, H1prelim-11-143 (2011).
- [43] S. Chekanov, et al., ZEUS-POL combined EW+QCD Fits , ZEUS-prel-07-027 (2007).
- [44] Z.-Q. Zhang, Combined electroweak and QCD fits including NC and CC data with polarised electron beam at HERA-2, PoS DIS2010 (2010) 056.

- [45] F. Januschek, Multi-lepton production at HERA, Diploma thesis at University of Hamburg (2007).
- [46] U. Holm, et al., The ZEUS Detector, Status Report (unpublished), DESY (1993). URL www-zeus.desy.de/bluebook/bluebook.html
- [47] Technical Design Report, Status Report (unpublished), DESY-PRC (1995).
- [48] K. Ackerstaff, et al., The HERMES Spectrometer, Nucl. Instrum. Meth. A417 (1998) 230–265.
[arXiv:hep-ex/9806008](https://arxiv.org/abs/hep-ex/9806008).
- [49] G. H. Hoffstaetter, The luminosity upgrade of HERA, ICFA Beam Dyn. Newslett. 24 (2001) 8–18.
- [50] M. G. Minty, HERA Performance Upgrade: Achievements and Plans for the Future, presented at the 9th European Particle Accelerator Conference (EPAC 2004), Lucerne, Switzerland, 5-9 Jul 2004.
- [51] B. Foster, ZEUS at HERA II (2001).
[arXiv:hep-ex/0107066](https://arxiv.org/abs/hep-ex/0107066).
- [52] A. A. Sokolov, I. M. Ternov, On Polarization and spin effects in the theory of synchrotron radiation, Sov. Phys. Dokl. 8 (1964) 1203–1205.
- [53] C. Helebrant, In search of new phenomena using polarization: HERA and ILC, Ph.D. thesis, Hamburg University, DESY-THESIS-2009-049 (2009).
- [54] D. P. Barber, et al., The First achievement of longitudinal spin polarization in a high-energy electron storage ring, Phys. Lett. B343 (1995) 436–443.
[doi:10.1016/0370-2693\(94\)01465-0](https://doi.org/10.1016/0370-2693(94)01465-0).
- [55] M. e. a. Beckmann, The longitudinal polarimeter at HERA, Nucl. Instrum. Meth. A479 (2002) 334–348.
[arXiv:physics/0009047](https://arxiv.org/abs/physics/0009047), [doi:10.1016/S0168-9002\(01\)00901-9](https://doi.org/10.1016/S0168-9002(01)00901-9).
- [56] J. Bohme, Precision measurement with the transverse polarimeter at HERA?II, Eur. Phys. J. C33 (2004) s1067–s1069.
[doi:10.1140/epjcd/s2004-03-1845-9](https://doi.org/10.1140/epjcd/s2004-03-1845-9).
- [57] A. Airapetian et al., Using the HERA Polarization Measurements. Recommendations for the Summer 2007 Conferences, DESY note POL2000-2007-001 (July 2007).
- [58] J. Andruszkow et al., First Measurement of HERA Luminosity by ZEUS Lumi Monitor, ZEUS internal note 92-024 (1992).
- [59] ZEUS Luminosity Group, Luminosity Measurement in the ZEUS Experiment, ZEUS internal note 01-004 (2001).
- [60] M. Helbich, Y. Ning, S. Paganis, Z. Ren, W. e. a. Schmidke, The spectrometer system for measuring ZEUS luminosity at HERA, Nucl.Instrum.Meth. A565 (2006) 572–588.
[arXiv:physics/0512153](https://arxiv.org/abs/physics/0512153), [doi:10.1016/j.nima.2006.06.049](https://doi.org/10.1016/j.nima.2006.06.049).
- [61] L. Adamczyk et al., Luminosity Measurement in the ZEUS Experiment, ZEUS internal note 01-004 (2001).

- [62] J. Chwastowski, J. Figiel, A. Kotarba, K. Olkiewicz, L. Suszycki, Aerogel cherenkov detectors for the luminosity measurement at HERA, Nucl.Instrum.Meth. A504 (2003) 222–227.
doi:10.1016/S0168-9002(03)00794-0.
- [63] V. Drugakov, Luminosity Measurement, ZEUS internal talk during collaboration week (February 2010).
URL https://www-zeus.desy.de/zems/ZEUS_ONLY/display.php?p_active=11649
- [64] C. Coldewey, The ZEUS microvertex detector, Nucl. Instrum. Meth. A447 (2000) 44–54.
- [65] B. Foster, et al., The Design and Construction of the ZEUS Central Tracking Detector, Nucl. Instrum. Meth. A338 (1994) 254–283.
- [66] R. Hall-Wilton, N. McCubbin, P. Nylander, M. Sutton and M. Wing, The CTD Tracking Resolution, ZEUS internal note 99-024 (1999).
- [67] H. Bethe, Bremsformel für Elektronen relativistischer Geschwindigkeit, Zeitschrift für Physik 76 (1932) 293–299.
- [68] M. Derrick, et al., Design and Construction of the ZEUS Barrel Calorimeter, Nucl. Instrum. Meth. A309 (1991) 77–100.
- [69] A. Andresen, et al., Construction and Beam Test of the ZEUS Forward and Rear Calorimeter, Nucl. Instrum. Meth. A309 (1991) 101–142.
- [70] A. Bernstein, et al., Beam Tests of the ZEUS Barrel Calorimeter, Nucl. Instrum. Meth. A336 (1993) 23–52.
- [71] S. Silverstein, et al., The ZEUS Calorimeter First Level Trigger, Nucl. Instrum. Meth. A360 (1995) 322–324.
- [72] H. Uijterwaal, The Global Second Level Trigger for ZEUS, Ph.D. thesis, University of Amsterdam (1992).
- [73] ADAMO: User guide, CERN (1993).
- [74] D. C. Bailey, et al., The ZEUS Third Level Trigger Hardware Architecture, presented at International Conference on Open Bus Systems 92, Zurich, Switzerland, 13-15 Oct 1992.
- [75] H. Spiesberger, DJANGO.
URL <http://wwwthep.physik.uni-mainz.de/~hspiesb/djangoh/djangoh.html>
- [76] H. L. Lai, et al., Global QCD Analysis of Parton Structure of the Nucleon: CTEQ5 Parton Distributions, Eur. Phys. J. C12 (2000) 375–392.
- [77] A. Kwiatkowski, H. Spiesberger, H. J. Mohring, Heracles: An event generator for e p interactions at hera energies including radiative processes: Version 1.0, Comp. Phys. Commun. 69 (1992) 155–172.
doi:10.1016/0010-4655(92)90136-M.
- [78] U. Pettersson, Ariadne: a Monte Carlo for QCD cascades in the color dipole fomulation, IU-TP-88-5.

- [79] G. Gustafson, U. Pettersson, Dipole Formulation of QCD Cascades, Nucl.Phys. B306 (1988) 746.
doi:10.1016/0550-3213(88)90441-5.
- [80] G. Ingelman, A. Edin, J. Rathsman, LEPTO 6.5 - A Monte Carlo Generator for Deep Inelastic Lepton-Nucleon Scattering, Comput. Phys. Commun. 101 (1997) 108–134.
arXiv:hep-ph/9605286, doi:10.1016/S0010-4655(96)00157-9.
- [81] T. Sjostrand, M. Bengtsson, The Lund Monte Carlo for Jet Fragmentation and $e^+ e^-$ Physics. Jetset Version 6.3: An Update, Comput. Phys. Commun. 43 (1987) 367.
doi:10.1016/0010-4655(87)90054-3.
- [82] J. R. Morais Silva Gonzalo, Measurement of the High- Q^2 Neutral Current Deep Inelastic Scattering Cross Sections with the ZEUS Detector at HERA, Ph.D. thesis, Imperial College London, DESY-THESIS-2003-009 (2003).
- [83] M. Derrick, et al., Observation of events with a large rapidity gap in deep inelastic scattering at HERA, Phys. Lett. B315 (1993) 481–493.
doi:10.1016/0370-2693(93)91645-4.
- [84] S. U. Noor, Measurement of neutral current electron-proton cross sections with longitudinally polarised electrons using the ZEUS detector, Ph.D. thesis, York University, Toronto, ISBN-9780494390443 (2007).
- [85] Y. Ri, Measurement of e^-p Neutral-Current Deep Inelastic Scattering Cross Sections with Longitudinally Polarized Electron Beams at $\sqrt{s}=318$ GeV, Ph.D. thesis, Tokyo Metropolitan University, thesis at DESY (2009).
- [86] M. Wlasenko, Measurement of the Neutral Current Deep Inelastic $e^+ p$ Scattering Cross Sections with Longitudinally Polarized Positrons with ZEUS, Ph.D. thesis, University of Bonn, BONN-IR-2009-05 (2009).
- [87] G. Marchesini, et al., HERWIG version 5.9: A Monte Carlo event generator (1996).
arXiv:hep-ph/9607393.
- [88] H. L. Lai, et al., Improved parton distributions from global analysis of recent deep inelastic scattering and inclusive jet data, Phys. Rev. D55 (1997) 1280–1296.
arXiv:hep-ph/9606399, doi:10.1103/PhysRevD.55.1280.
- [89] U. Holm, et al., The ZEUS Detector, Status Report (unpublished), DESY, chapter 17 (1993).
URL www-zeus.desy.de/bluebook/bluebook.html
- [90] St. Schlenstedt, Running Offline Software on IBM/MVS: ZDIS, MOZART, ZGANNA, ZEPHYR, EAZE, ZEUS internal note 91-079.
- [91] C. Catterall, Understanding MOZART.
URL http://www-zeus.desy.de/lectures/mozart_lecture.ppt
- [92] R. Brun, R. Hagelberg, M. Hansroul, J. C. Lassalle, GEANT: simulation program for particle physics experiments. User guide and reference manual, CERN-DD-78-2-REV.

- [93] Els de Wolf, ZGANA.
URL www.nikhef.nl/pub/experiments/zeus/zgana/
- [94] ZEUS MC Team, Funnel - The ZEUS Monte Carlo Production Facility, last visited 04.10.2011 (September 2010).
URL <http://www-zeus.desy.de/components/funnel/>
- [95] R. Walsh, The Orange Homepage, ZEUS internal webpage.
URL http://www-zeus.desy.de/ZEUS_ONLY/analysis/orange/
- [96] B. Straub, Introduction to ORANGE.
URL http://www-zeus.desy.de/lectures/orange_lecture.ps.gz
- [97] T. P. Stewart, Measurement of High- Q^2 Neutral Current cross-sections with longitudinally polarised positrons with the ZEUS Detector, Ph.D. thesis, University of Toronto, in preparation (2011).
- [98] R. Brun, F. Rademakers, ROOT: An object oriented data analysis framework, Nucl.Instrum.Meth. A389 (1997) 81–86.
doi:10.1016/S0168-9002(97)00048-X.
- [99] W. Dorth, LAZE, Logical Access to ZEUS Events, ZEUS internal note 91-069.
- [100] Zevis Team, ZeVis - Zeus Event Visualization.
URL <http://www-zeus.desy.de-zevis/>
- [101] A. Spiridonov, Mathematical Framework for Fast and Rigorous Track Fit for the ZEUS Detector, ZEUS internal note 08-003 (2008).
- [102] E. Maddoz, A Kalman filter track fit for the ZEUS microvertex detector, ZEUS internal note 03-008 (2003).
- [103] B. Straub, The EM Electron Finder, Zeus internal webpage.
URL http://www-zeus.desy.de/~straub/ZEUS_ONLY/doc/em.ps
- [104] Halina Abramowicz and Allen Caldwell and Ralph Sinkus, Neural Network Based Electron Identification in the ZEUS Calorimeter, Nucl. Instrum. Meth. A365 (1995) 508–517.
- [105] A. Lopez-Duran Viani and S. Schlenstedt, Electron finder efficiencies and impurities. A comparison between SINISTRA95, EM and EMNET, ZEUS internal note 99-077 (1999).
- [106] J. Grosse-Knetter, Corrections for the hadronic final state, ZEUS internal note 98-031 (1998).
- [107] S. Bentvelsen, J. Engelen, P. Kooijman, Reconstruction of (x, Q^{*2}) and extraction of structure functions in neutral current scattering at HERA, in: W. Buchmuller, G. Ingelman (Eds.), Physics at HERA. Proceedings, Workshop, Vol. 1/3, 1992, pp. 23 – 42.
- [108] H. Chaves, R. Seifert, G. Zech, Kinematic fitting of neutral current events, in: W. Buchmuller, G. Ingelman (Eds.), Physics at HERA. Proceedings, Workshop, Vol. 1/3, 1992, pp. 57 – 70.
- [109] R. Aggarwal, Kinematic Fitting, ZEUS internal talk at Collaboration Meeting (October 2010).

- URL https://www-zeus.desy.de/zems/ZEUS_ONLY/display.php?p_active=12038
- [110] R. Aggarwal, Measurement of high- x Neutral current ep cross sections and extraction of xF_3 structure function using ZEUS detector at HERA, Ph.D. thesis, Panjab University, in preparation (2012).
- [111] A. Caldwell, D. Kollar, K. Kroninger, BAT: The Bayesian Analysis Toolkit, *Comput.Phys.Commun.* 180 (2009) 2197–2209.
arXiv:0808.2552, doi:10.1016/j.cpc.2009.06.026.
- [112] J. Edmonds, J. Grosse-Knetter, A. Quadt, Neutral Current Cross Sections at High Q^2 , ZEUS internal note 99-016 (1999).
- [113] K. Nagano, HECTOR interfaced to BASES, Zeus internal webpage, last visited 15.07.2011 (June 2005).
URL http://www-zeus.desy.de/~nagano/ZEUS_ONLY/nc0304/hector.html
- [114] B. Reisert, private communication (2010).
- [115] J. Ferrando, private communication (2010).
- [116] A. Arbuzov, D. Y. Bardin, J. Blumlein, L. Kalinovskaya, T. Riemann, HECTOR 1.00 - A program for the calculation of QED, QCD and electroweak corrections to ep and in deep inelastic neutral and charged current scattering, *Comput. Phys. Commun.* 94 (1996) 128–184.
arXiv:hep-ph/9511434, doi:10.1016/0010-4655(96)00005-7.
- [117] P. Plucinski, ZEUS Run Coordinators Report - Week 05.02 - 11.02 2007, Zeus internal talk, last visited 24.08.2011 (February 2007).
URL https://www-zeus.desy.de/zems/ZEUS_ONLY/display.php?p_active=8537
- [118] W. Schmidke, private communication (2010).
- [119] K. Olkiewicz, private communication (2010).
- [120] V. Drugakov, Revision to 2006/07 e^+ luminosity measurement, ZEUS internal talk at collaboration week (February 2011).
URL https://www-zeus.desy.de/zems/ZEUS_ONLY/display.php?p_active=12221
- [121] V. Drugakov, private communication (2010).
- [122] Y. Yamazaki, GFLT status report: mis-configuration for the Risoe2ir slots, ZEUS internal talk at collaboration week (October 2006).
URL https://www-zeus.desy.de/zems/ZEUS_ONLY/display.php?p_active=7837
- [123] Y. Yamazaki, CTD FLT classes and track veto: how to check, Zeus internal webpage (April 2003).
URL <http://www-zeus.desy.de/components/gflt/yycontents/trkv.html>

- [124] K. Oliver, J. Ferrando, R. Devenish, A Minimum Bias Z Vertex Distribution for 2005-2007 eP Interactions at ZEUS, ZEUS internal note 07-008 (2007).
- [125] T. Stewart, private communication (2011).
- [126] R. Aggarwal, RCAL Electron Energy Scale Calibration for GR data, Talk at ZEUS Analysis Forum (2009).
- [127] H.-J. Grabosch, A. Meyer, S. Schlenstedt, X_0 Determination and Electron Energy Correction with the Presampler, ZEUS internal note 98-045 (1998).
- [128] A. Caldwell, W. Liu, B. Straub, BCAL Electron Studies; PART I: MC and Test Beam Energy Studies, ZEUS internal note 98-002 (1998).
- [129] I. Singh, Neutral Current Deep Inelastic e^-p Scattering with high x at HERA, Ph.D. thesis, Panjab University, in preparation (2011).
- [130] F. Januschek, NC DIS in 06/07 e^+p data - Status report, ZEUS internal talk at analysis form (June 2011).
URL https://www-zeus.desy.de/zems/ZEUS_ONLY/display.php?p_active=12524
- [131] ZEUS Offline Team, zesLite, last visited 24.05.2011 (March 2007).
URL <http://www-zeus.desy.de/zes/index.html>
- [132] M. Moritz, Measurement of the High- Q^2 Neutral Current DIS Cross Section at HERA, Ph.D. thesis, University of Hamburg, dESY-THESIS-2002-009 (2002).
- [133] G. A. Schuler, H. Spiesberger, DJANGO: The interface for the event generators HERACLES and LEPTO, in: W. Buchmuller, G. Ingelman (Eds.), Physics at HERA. Proceedings, Workshop, Vol. 3/3, 1992, pp. 1419 – 1432.
- [134] K. Oliver, Measurement of High Q^2 Charged-Current Deep-Inelastic Scattering With Polarised Positron Beams Using the ZEUS Detector at HERA, Ph.D. thesis, University of Oxford (2011).
- [135] S. Chekanov, et al., A ZEUS next-to-leading-order QCD analysis of data on deep inelastic scattering, Phys.Rev. D67 (2003) 012007.
arXiv:hep-ex/0208023, doi:10.1103/PhysRevD.67.012007.
- [136] C. Adloff, et al., Measurement and QCD analysis of neutral and charged current cross sections at HERA, Eur. Phys. J. C30 (2003) 1–32.
arXiv:hep-ex/0304003, doi:10.1140/epjc/s2003-01257-6.
- [137] C. Adloff, et al., Deep inelastic inclusive e p scattering at low x and a determination of $\alpha(s)$, Eur.Phys.J. C21 (2001) 33–61.
arXiv:hep-ex/0012053, doi:10.1007/s100520100720.
- [138] J. Breitweg, et al., ZEUS results on the measurement and phenomenology of $F(2)$ at low x and low Q^{*2} , Eur.Phys.J. C7 (1999) 609–630.
arXiv:hep-ex/9809005, doi:10.1007/s100529901084.
- [139] S. Chekanov, et al., Measurement of the neutral current cross-section and $F(2)$ structure function for deep inelastic e + p scattering at HERA, Eur.Phys.J. C21 (2001) 443–471.
arXiv:hep-ex/0105090, doi:10.1007/s100520100749.

- [140] J. Breitweg, et al., Measurement of high Q^{*2} charged current $e^+ p$ deep inelastic scattering cross-sections at HERA, *Eur.Phys.J. C12* (2000) 411–428.
arXiv:hep-ex/9907010, doi:10.1007/s100529900280.
- [141] S. Chekanov, et al., Measurement of high Q^{*2} charged current cross-sections in $e^- p$ deep inelastic scattering at HERA, *Phys.Lett. B539* (2002) 197–217.
arXiv:hep-ex/0205091, doi:10.1016/S0370-2693(02)02093-2.
- [142] S. Chekanov, et al., Measurement of high Q^{*2} $e^- p$ neutral current cross-sections at HERA and the extraction of $xF(3)$, *Eur.Phys.J. C28* (2003) 175–201.
arXiv:hep-ex/0208040.
- [143] R. Thorne, R. Roberts, An ordered analysis of heavy flavor production in deep inelastic scattering, *Phys.Rev. D57* (1998) 6871–6898.
arXiv:hep-ph/9709442, doi:10.1103/PhysRevD.57.6871.
- [144] D. Bourilkov, R. C. Group, M. R. Whalley, LHAPDF: PDF use from the Tevatron to the LHC (2006).
arXiv:hep-ph/0605240.
- [145] A. Glazov, Averaging of DIS cross section data, *AIP Conf.Proc. 792* (2005) 237–240.
doi:10.1063/1.2122026.
- [146] R. Thorne, A Variable-flavor number scheme for NNLO, *Phys.Rev. D73* (2006) 054019.
arXiv:hep-ph/0601245, doi:10.1103/PhysRevD.73.054019.
- [147] V. Radescu, Combination and QCD analysis of the HERA inclusive cross sections, *PoS ICHEP2010* (2010) 168.
- [148] H. Abramowicz, et al., QCD NNLO analysis of inclusive data (HERAPDF 1.5) , H1prelim-11-042, ZEUS-prel-11-002 (2011).
- [149] H. Abramowicz, et al., Measurement of high- q^2 neutral current deep inelastic e^+p scattering cross sections with a longitudinally polarised positron beam at HERA, ZEUS-prel-11-003.
- [150] A. Cooper-Sarkar, private communication (2011).
- [151] S. Chekanov, et al., High Q^{*2} neutral current cross-sections in $e^+ p$ deep inelastic scattering at $s^{*(1/2)} = 318$ -GeV, *Phys.Rev. D70* (2004) 052001.
arXiv:hep-ex/0401003, doi:10.1103/PhysRevD.70.052001.
- [152] S. Chekanov, et al., Measurement of high Q^{*2} charged current cross-sections in $e^+ p$ deep inelastic scattering at HERA, *Eur.Phys.J. C32* (2003) 1–16.
arXiv:hep-ex/0307043, doi:10.1140/epjc/s2003-01363-5.
- [153] S. Chekanov, et al., Inclusive jet cross-sections in the Breit frame in neutral current deep inelastic scattering at HERA and determination of $\alpha(s)$, *Phys.Lett. B547* (2002) 164–180.
arXiv:hep-ex/0208037, doi:10.1016/S0370-2693(02)02763-6.
- [154] S. Chekanov, et al., Dijet photoproduction at HERA and the structure of the photon, *Eur.Phys.J. C23* (2002) 615–631.
arXiv:hep-ex/0112029, doi:10.1007/s100520200936.

- [155] H. Abramowicz, et al., QCD analysis with determination of α_s based on HERA inclusive and jet data - HERAPDF1.6 , H1prelim-11-034, ZEUS-prel-11-001 (2011).
- [156] T. Schörner-Sadenius, Jet Physics in Electron-Proton Scattering, University of Hamburg, Habil., 2009.
- [157] M. Wobisch, Measurement and QCD analysis of jet cross-sections in deep inelastic positron proton collisions at $s^{*}(1/2) = 300\text{-GeV}$, Ph.D. thesis, Rheinisch-Westfälische Technische Hochschule Aachen, DESY-THESIS-2000-049 (2000).
- [158] S. Catani, M. Seymour, A general algorithm for calculating jet cross-sections in NLO QCD, Nucl.Phys. B485 (1997) 291–419.
arXiv:hep-ph/9605323, doi:10.1016/S0550-3213(96)00589-5.
- [159] S. Catani, M. Seymour, QCD jet calculations in DIS based on the subtraction method and dipole formalism (1996).
arXiv:hep-ph/9609237.
- [160] Thomas Schörner-Sadenius, private communication (2008).
- [161] B. Opitz, Studies towards an improved determination of the gluon density in the proton using jet measurements at HERA, diploma thesis at University of Hamburg (2008).
- [162] T. Kluge, K. Rabbertz, M. Wobisch, FastNLO: Fast pQCD calculations for PDF fits (2006).
arXiv:hep-ph/0609285.
- [163] T. Carli, D. Clements, A. Cooper-Sarkar, C. Gwenlan, G. P. Salam, et al., A posteriori inclusion of parton density functions in NLO QCD final-state calculations at hadron colliders: The APPLGRID Project, Eur.Phys.J. C66 (2010) 503–524.
arXiv:0911.2985, doi:10.1140/epjc/s10052-010-1255-0.
- [164] S. Chekanov, et al., Dijet production in neutral current deep inelastic scattering at HERA, Eur.Phys.J. C23 (2002) 13–27.
arXiv:hep-ex/0109029, doi:10.1007/s100520100845.
- [165] H. Perrey, Jets at low Q^2 at HERA and radiation damage studies for silicon sensors for the XFEL, Ph.D. thesis, University of Hamburg, DESY-THESIS-2011-021 (2011).
- [166] G. Aad, et al., Measurement of inclusive jet and dijet cross sections in proton-proton collision data at 7 TeV centre-of-mass energy using the ATLAS detector, aTLAS-CONF-2011-047 (2011).
- [167] S. Chekanov, et al., Inclusive-jet and dijet cross-sections in deep inelastic scattering at HERA, Nucl.Phys. B765 (2007) 1–30.
arXiv:hep-ex/0608048, doi:10.1016/j.nuclphysb.2006.09.018.
- [168] F. Aaron, et al., Jet Production in ep Collisions at Low Q^{*2} and Determination of $\alpha(s)$, Eur.Phys.J. C67 (2010) 1–24.
arXiv:0911.5678, doi:10.1140/epjc/s10052-010-1282-x.

- [169] F. Aaron, et al., Jet Production in ep Collisions at High Q^{*2} and Determination of $\alpha(s)$, *Eur.Phys.J. C* 65 (2010) 363–383.
arXiv:0904.3870, doi:10.1140/epjc/s10052-009-1208-7.
- [170] F. Januschek, Calculating common grids for inclusive jet events from H1 and ZEUS, ZEUS webpage, last visited 11.09.2011 (2008).
URL <http://www-zeus.desy.de/~fjanusch/Grids.ps>
- [171] F. Januschek, Combining inclusive jet data from H1 and ZEUS to include them in the PDF-Fits, talk presented at H1-ZEUS Combined Structure Functions Meeting (10 2008).
- [172] F. Januschek, Combination of jet data, talk presented at H1-ZEUS Combined Meeting (12 2008).
- [173] A. Cooper-Sarkar, HERAPDF1.5 at NNLO, Confronting HERAPDF with Tevatron and LHC data, Talk presented at PDF4LHC meeting (7 2011).
- [174] M. Klein, The LHeC conceptual design, PoS ICHEP2010 (2010) 520.
- [175] e. Altarelli, Massimo, e. Brinkmann, Reinhard, e. Chergui, Majed, e. Decking, Winfried, e. Dobson, Barry, et al., XFEL: The European X-Ray Free-Electron Laser. Technical design report (2006).
- [176] European XFEL, web page, last visited 17.10.2011.
URL <http://www.xfel.eu/>
- [177] J. Zhang, E. Fretwurst, R. Klanner, H. Perrey, J. Schwandt, I. Pintilie, Study of radiation damage induced by 12 keV X-rays in MOS structures built on high resistivity n-type silicon, submitted to *Journal of Synchrotron Radiation*. arXiv:1107.5949.
- [178] A. S. Grove, D. J. Fitzgerald, Surface effects on p-n junctions: Characteristics of surface space-charge regions under non-equilibrium conditions, *Solid-State Electronics* 9 (8) (1966) 783 – 806.
doi:DOI:10.1016/0038-1101(66)90118-3.
- [179] Rose Collaboration, Proposal for further work on radiation hardening on silicon detectors, CERN/LHCC 96-23, P62/LHC R&D (April 1996).
- [180] E. Fretwurst, F. Januschek, R. Klanner, H. Perrey, I. Pintilie, F. Renn, Study of the radiation hardness of silicon sensors for the XFEL, in: *Nuclear Science Symposium Conference Record, IEEE*, 2008, pp. 2535 – 2538.
- [181] M. Kohl, The OLYMPUS experiment at DESY, *AIP Conf.Proc.* 1160 (2009) 19–23.
doi:10.1063/1.3232027.
- [182] HASYLAB, DORIS III, last visited 24.09.2011 (2010).
URL http://hasylab.desy.de/facilities/doris_iii/index_eng.html
- [183] J. H. Hubbell, S. M. Seltzer, Tables of X-ray mass attenuation coefficients and mass energy-absorption coefficients from 1 keV to 20 MeV for elements $Z = 1$ to 92 and 48 additional substances of dosimetric interest, National Institute of Standards and Technology, NISTIR 5632, available online at <http://www.nist.gov/pml/data/xraycoef/index.cfm> (1996).

- [184] F. Renn, A practical guide for measuring and radiating diodes intended for research on intense x-ray radiation tolerant silicon detectors, DESY summer student report, available online at <http://www.desy.de/f/students/2007/reports/renn.pdf> (2007).
- [185] T. Tanaka, H. Kitamura, *SPECTRA*: a synchrotron radiation calculation code, *Journal of Synchrotron Radiation* 8 (6) (2001) 1221–1228.
doi:10.1107/S090904950101425X.
URL <http://dx.doi.org/10.1107/S090904950101425X>
- [186] R. Klanner, private communication (2007).
- [187] H. Feick, Radiation tolerance of silicon particle detectors for high-energy physics experiments, Ph.D. thesis, Hamburg University, Hamburg, DESY Internal Report: DESY F35D-97-08, available online at <http://cdsweb.cern.ch/record/335685> (1997).
- [188] S. M. Sze, *Physics of Semiconductor Devices*, Wiley, New York, 1969.
- [189] A. S. Grove, *Physics and Technology of Semiconductor Devices*, Wiley, John & Sons, 1967.
- [190] Adaptive gain integrating pixel detector, web page, last visited 05.10.2011 (2010).
URL http://hasylab.desy.de/instrumentation/detectors/projects/agipd/index_eng.html

Acknowledgements

A big *Thank you* goes to the ZEUS Collaboration and the ZEUS/CMS/Detector group of the University of Hamburg!

This thesis would never have been possible to write without the help of many people. The ZEUS collaboration and the group of Prof. Robert Klanner and Prof. Peter Schleper at the University of Hamburg have provided a great working environment, where people are always helpful and willing to share their knowledge. Unfortunately I cannot mention everybody here, so this list will necessarily be incomplete.

There are some people I need to thank personally though:

First of all, Robert Klanner has made it possible for me to study these exciting research topics and has been very supportive during my whole diploma and PhD research. Whichever physics question I had, he was always able to answer it with his profound physics knowledge.

Achim Geiser was able to provide me every information about ZEUS that I asked for; his insight has been invaluable for facing the challenges of the NC DIS analysis.

In addition, I want to thank both of them for volunteering to be referees of this thesis, as well as extend my thanks to Eckhard Elsen and Thomas Schörner-Sadenius for being willing to be the referees of my defense.

I have greatly profited from the discussions with Jolanta Sztuk-Dambietz, Monica Turcato, Eckhart Fretwurst, Enrico Tassi and Thomas Schörner-Sadenius. Jola has been of great help with the NC analysis and the ZEUS analysis environment. She has advised and accompanied me during my diploma and PhD time and I have learned a lot from her. Thomas and Monica have always found a way to fit helping me in their busy schedule. In the discussions with them one encounters their enthusiasm about particle physics at all times.

My stay in Oxford would not have been possible without Robin Devenish, Amanda Cooper-Sarkar and Claire Gwenlan.

Numerous lines of code, especially for making nice plots, were provided by Hanno Perrey, Thorben Theedt, Trevor Stewart, Jörg Behr and Jolanta Sztuk-Dambietz.

Working together on the NC analysis with Trevor has been a pleasure and I have profited a lot from the co-operation. A special thanks goes to him and the other proof-readers of this thesis for their helpful feedback within a very limited timeframe.

I have enjoyed many fruitful physics and non-physics discussions (especially during lunch not at the canteen) with Doris Eckstein, Thorben Theedt, Peter Buhmann, Katie Oliver, Trevor Stewart, Joachim Erfle, Matthias Schröder, Sebastian Naumann-Emme, Hanno Perrey and Alexandra Junkes.

Last, but definitely not least, I want to thank my family. Sabine, Franz, Steffi, Henning und Omi - vielen Dank für Eure liebevolle Unterstützung. Claudius and Alissa - Ihr seid einfach wundervoll!

